

Subsurface Fatigue Crack Growth in Glare Fibre Metal Laminates

Subsurface Fatigue Crack Growth in Glare Fibre Metal Laminates

Proefschrift

ter verkrijging van de graad van doctor
aan de Technische Universiteit Delft,
op gezag van de Rector Magnificus prof.dr.ir. J.T. Fokkema,
voorzitter van het College voor Promoties,
in het openbaar te verdedigen op donderdag 22 december 2005 om 13:00 uur

door

Christian Eugene RANDELL
Master of Science in Mechanical Engineering
Washington University in St Louis, St Louis, Missouri, Verenigde Staten
geboren te Fremont, Nebraska, Verenigde Staten

Dit proefschrift is goedgekeurd door de promotoren:
Prof.dr.ir. S. van der Zwaag

Samenstelling promotiecommissie:

Rector Magnificus,	voorzitter
Prof.dr.ir. S. van der Zwaag,	Technische Universiteit Delft, promotor
Prof.dr.ir. J. Schijve,	Technische Universiteit Delft
Ir. J.J. Homan,	Technische Universiteit Delft
Dr. S.A. Fawaz,	United States Air Force Academy
Prof.dr.ir. R. Benedictus,	Technische Universiteit Delft
Prof.dr.ir. A Bakker,	Technische Universiteit Delft
Prof.dr.ir. J.G. Rots,	Technische Universiteit Delft
Prof.dr. Z. Gürdal,	Technische Universiteit Delft, reservelid

ISBN-10: 9081025716
ISBN-13: 9789081025713

Keywords: Fibre Metal Laminate, Glare, crack propagation, fatigue, subsurface crack growth

Copyright © 2005 by Christian E. Randell

All rights reserved. No part of the material protected by this copyright notice may be reproduced or utilized in any form or by any means, electronic or mechanical, including photocopying, recording or by any information storage or retrieval system, without written permission from the copyright owner.

Printed in The Netherlands by PrintPartners Ipskamp, Enschede

Table of Contents

Nomenclature.....	x
Chapter 1 – Introduction	1
Chapter 2 – Literature Review	9
2.1 Introduction	9
2.2 Glare Essentials	10
2.2.1 Glare Construction	10
2.2.2 Glare Material Property Comparison	11
2.2.3 Physical Description of Fatigue Crack Growth in Glare.....	13
2.3 Fatigue Crack Growth Models for Glare	18
2.3.1 Analytical Model of Marissen	19
2.3.2 Mechanistic 2-D Model of Burianek.....	21
2.3.3 Analytical Model of Guo & Wu	22
2.3.4 Analytical Model of Alderliesten	24
2.3.5 Empirical Model of Toi	27
2.3.6 Phenomenological Model of Guo & Wu.....	28
2.3.7 Empirical Model of De Koning.....	30
2.3.8 Parametric Model of Rose.....	32
2.4 Summary	34
Chapter 3 – Experimentation	39
3.1 Introduction	39
3.2 Milled Open Hole Tension Bending	40
3.2.1 Specimen Configuration.....	44
3.2.2 Test Matrix and Test Specification	44
3.3 Four Point Bend.....	45
3.3.1 Specimen Configuration.....	45
3.3.2 Test Specification	47
3.4 Subsurface Crack Growth Measurement Techniques.....	48
3.4.1 Optical and Destructive Inspection	48
3.4.2 Eddy Current Trials	50

Chapter 4 – Development of Analytical/Numerical Crack Growth Model..... 57

4.1	Introduction	57
4.2	Finite Element Modelling.....	60
4.2.1	Uncracked Model Analysis	60
4.2.2	Cracked Model Analysis	63
4.2.3	Fibre Bridging Stress Extraction	68
4.2.4	FEM Results.....	69
4.3	Analytical Modelling.....	77
4.3.1	Crack Opening Stress Intensity Factor	78
4.3.2	Fibre Bridging Stress Intensity Factor.....	79
4.4	Numerical Calculations	81
4.5	Summary	83

Chapter 5 – Validation of Model Against Experimental Data 87

5.1	Introduction	87
5.2	MOHTB.....	88
5.2.1	Surface Crack Data.....	91
5.2.2	Subsurface Cracks and Their Relation to Surface Cracks.....	95
5.3	Four Point Bend.....	102
5.4	Model Sensitivity.....	106
5.5	Concluding Remarks	117

Chapter 6 – Extension to Model to Glare 3 121

6.1	Introduction	121
6.2	Experimentation	122
6.2.1	Material Orientation	123
6.2.2	Specimen Configuration.....	124
6.2.3	Test Specification	126
6.3	Hybrid Model	127
6.3.1	Modification to FEM.....	127
6.3.2	Modification to Analytical Model	134
6.4	Experimental Results.....	135
6.5	Validation of Model Against Experimental Data.....	137
6.6	Summary	138

Summary	141
Samenvatting	145
Appendix A – Finite Element Trials	149
A.1 Introduction	149
A.2 Finite Element Modelling.....	149
A.3 StressCheck™ Trials	151
A.4 ABAQUS™ Trials.....	153
A.5 Summary	154
Appendix B – Convergence Study	157
B.1 Introduction	157
B.2 Convergence Study.....	157
B.3 Summary	163
Appendix C – Finite Element Results	165
C.1 Introduction	165
C.2 Glare 2A	166
C.3 Glare 3	171
Appendix D – Experimental Results.....	173
D.1 Introduction	173
D.2 Glare 2A	174
D.3 Glare 3	186
Curriculum Vitae	195
Acknowledgements.....	196

Nomenclature

Symbol	Unit	Description
a	mm	Half crack length
a_o	mm	Initial crack size
a_{incr}	mm	Incremental crack size
a_{final} a_{fin}	mm	Final crack size
$a_{fin,target}$	mm	Targeted final crack size
b	mm	Delamination Height
C		Material Constant
COD	mm	Crack opening displacement
da/dN	mm/cycle	Crack growth rate
E	MPa	Young's Modulus
$f(g)$		Geometry Correction Factor
F	MPa mm	Stiffness
G	MPa	Shear Modulus
h	mm	Distance between vertical cracks
i, j		Integer Counters
k_b		Bending Factor
K	MPa \sqrt{mm}	Stress intensity factor
$K_{I(OH)}$	MPa \sqrt{mm}	Stress intensity factor due to open hole
K_{Ifb}	MPa \sqrt{mm}	Stress intensity factor due to fibre bridging
K_{tot}	MPa \sqrt{mm}	Total stress intensity factor
m, n		Material Constant
N	Cycles	Fatigue Cycles
N_{final}	cycles	Final number of fatigue cycles
N_{init}	cycles	Number of fatigue cycles to crack initiation
P	N/mm	Load per unit thickness
r	mm	Radius
S_{center}	mm	Stress at center of model
S_{corner}	MPa	Stress at corner of model
S_{max}	MPa	Maximum stress
S_{OHmax}	MPa	Stress at edge of open hole
t_{plate}	mm	Plate thickness
$t_{test\ section}$	mm	Test section thickness
u		Admissible solution to FEM
u_{FE}		Solution found by FEM
u_{EX}		Exact solution
x		

x, y, z		Ordinate directions
z_{max}	mm	Out of plane displacement
ε	mm/mm	Strain
ε_f	mm/mm	Strain in fibres due to loading
ε_{fb}	mm/mm	Strain in fibres due to fibre bridging
ε_{fd}	mm/mm	Strain in fibres due to loading and fibre bridging
ν		Poisson's Ratio
ϕ	mm	Diameter
σ_{logN}		Standard Deviation
σ, S	MPa	Stress
σ_{app}	MPa	Applied Stress
σ_{fb}	MPa	Fibre Bridging Stress
σ_{flank}	MPa	Flank Stress
σ_{max}	MPa	Maximum Stress
σ_{nom}	MPa	Nominal Stress
σ_{res}	MPa	Resultant Stress
σ_{tip}	MPa	Crack Tip Stress
σ_{BN}	MPa	Blunt Notch Strength

Abbreviations

Al	Aluminum
ARALL	Aramid Reinforced Aluminum Laminate
CCT	Center Cracked Tension
COD	Crack Opening Displacement
CTB	Combined Tension Bending
FEM	Finite Element Modelling
FML	Fibre Metal Laminate
Glare	Glass Reinforced Aluminium Laminate
LEFM	Linear Elastic Fracture Mechanics
MOHTB	Milled Open Hole Tension Bending
MSD	Multi Site Damage
MVF	Metal Volume Fraction
NLM	Neutral Line Model
OHTB	Open Hole Tension Bending
Prepreg	Pre-impregnated fibre layer

1

Introduction

Abstract – This chapter provides a brief introduction to the research problem investigated in this thesis. The statement of purpose is given, along with the hypothesis to be proven. A list of limitations to the research and a list of assumptions made in the research are provided. Lastly, a brief overview of the thesis content is given.



1.1. Introduction to the Research Problem

In the nineties, the fibre metal laminate (FML) family Glare was developed in the Structures and Materials Laboratory of the Faculty of Aerospace Engineering of the Delft University of Technology¹. The laminates are constructed of thin aluminum alloy sheets with alternating prepreg plies of long glass fibres in an adhesive. A cross-section is shown in Figure 1.1. The Glare FML concept encompasses a variety of laminates with the main variables being layer thickness, aluminum alloy type, and glass fibre orientation (e.g. uni-directional, cross ply).

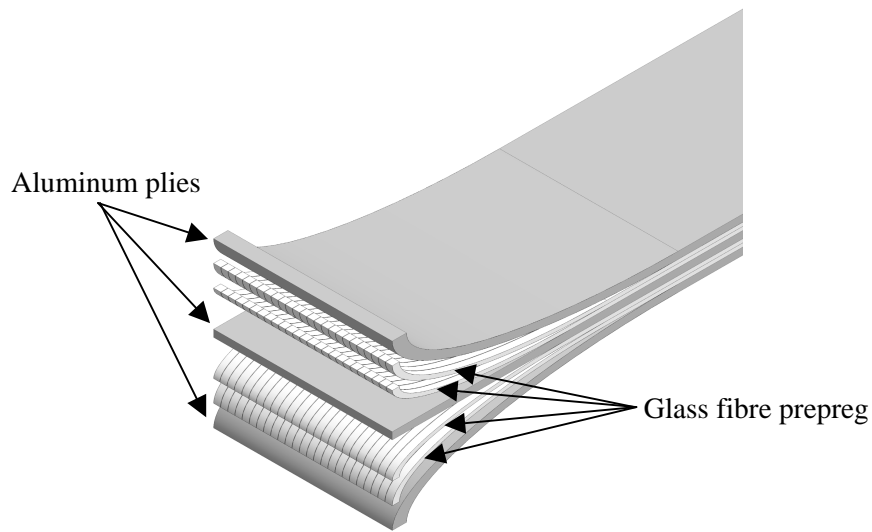


Figure 1.1: Glare fibre metal laminate construction.

The development of Glare was preceded² by fatigue investigations on laminates of bonded aluminum alloy sheets with no glass fibre prepreg layers, and on laminates of aluminum sheets layered with aramid fibres – a laminate called ARALL. ARALL laminates showed highly superior fatigue crack growth resistance compared to monolithic aluminum sheets of the same aluminum alloy. Later, the aramid fibres were replaced by advanced glass fibres, which further improved the fatigue properties. The superior fatigue properties of the fibre metal laminates are primarily obtained through a high crack growth resistance. After a crack has nucleated, the fibres constrain the opening of the crack – thus reducing the stress intensity of the tip of the crack. Furthermore, some load transmission can still occur due to the unbroken fibres in the cracked area, as shown in Figure 1.2. The FML Glare is the material on which the present investigation is focused.

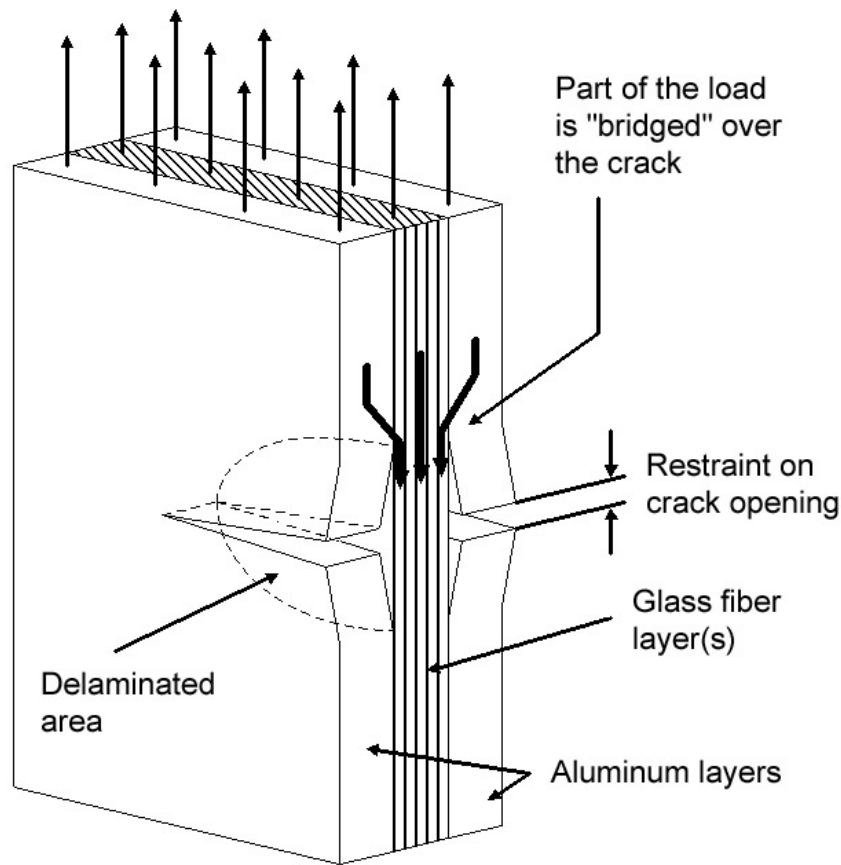


Figure 1.2: *Fibre bridging of fatigue crack in Glare. Load transfer and crack opening constraints illustrated.*

Various types of Glare were developed for application in components of aircraft structure where fatigue was a critical design issue. Because the specific mass of Glare is slightly lower than for monolithic aluminum alloys of the same thickness, the application of Glare can be very attractive as a skin material of pressurized fuselages. The riveted joints in the fuselage skin are well-known critical locations where fatigue cracks at the rivet holes can initiate. If fatigue cracks occur at many rivets in a row, the situation is labelled multi-site damage (MSD). A renowned accident³ occurred in 1988 when the fuselage of a passenger aircraft lost a large part of the skin panels at cruising altitude due to a failure along a longitudinal rivet row with MSD at numerous rivet holes.

Laboratory tests¹ have shown that the fatigue damage behaviour of riveted joints of FMLs differ from the behaviour of the riveted joint constructed of monolithic aluminum alloy sheets. In monolithic aluminum joints, crack initiation consumes a

large portion of the part's life. By the time a crack can be detected, the lifetime remaining is relatively short, due to fast crack growth. However, in riveted joints of FML construction, visible cracks are still growing rather slowly, due to the still intact fibres. As a result of these fibres, there is a long crack growth life, and the residual strength of the joint can still be sufficient.

Although the fatigue behaviour of riveted lap joints of Glare sheet material appears to be satisfactory, quantitative prediction of the development of fatigue damage in these joints is not yet possible. A few prediction models are presented in the literature^{4, 5, 6}; however, the validation of these models is limited and the validity is considered to be questionable in view of the assumptions made.

Riveted lap joints in an aircraft structure are loaded in tension. A major problem is the fact that a riveted lap joint under a tension load induces secondary bending due to the inherent eccentricity of neutral line of the joint⁷. As a consequence, the inner mating aluminum layer of the riveted Glare joint will see a larger stress than the other plies, and a fatigue crack will initiate in this layer, as shown in Figure 1.3. Only after considerable cracking in this surface layer of the laminate will cracks initiate in the second aluminum layer.

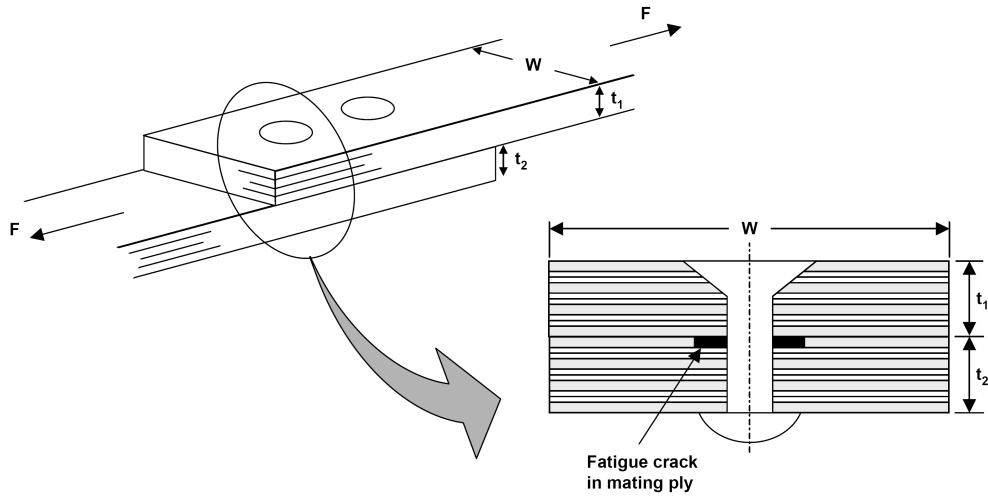


Figure 1.3: Example of riveted lap joint showing typical fatigue crack initiation location.

The major theme of this investigation is to obtain a better understanding of how fatigue damage in a riveted Glare joint is growing, initially in the first layer, and subsequently in the second and third layers. Obviously, such a study requires experimental observations on how the fatigue damage is developing in the laminate subjected to combined tension and bending. It then must be explored how crack growth in the second and third layers can be detected and monitored. Next, it will be studied how the growth of such cracks can be captured within a frame of predictions based on concepts of linear elastic fracture mechanics.

1.2. The Present Investigation

In order to refine the current theory on crack growth behavior of fibre metal laminates, the present investigation is focused on the propagation of fatigue cracks in surface and subsurface layers of various Glare laminates subjected to combined tension and bending. This study culminates in two products:

- 1) An analytical/numerical model to describe subsurface crack growth behaviour, and
- 2) The validation of the model through relevant experimentation

In the first part, stress intensity factors for cracks in subsurface layers of Glare are developed. Variables covered are

- Different ratios of surface to subsurface crack lengths
- Different ratios of bending to tensile stresses
- Different Glare configurations

Certain assumptions must be made at the onset of the analytical and numerical modelling. These assumptions include:

- Applicability of Linear Elastic Fracture Mechanics
- Delamination zone shapes
- Crack front shapes
- Applicability of the theory of superposition to stress intensity factors for FMLs

In the experimental part, the test matrix is constrained by the material (type of Glare), the specimen configuration (different types of open hole specimens), and the test conditions (tension and bending stress level and stress ratio).

1.3. Thesis Content

The investigation is described in the following chapters:

Chapter 2: Literature Review

This chapter is a brief review of current theories, with a focus on their applicability to the current investigation.

Chapter 3: Experimentation

This chapter details the materials, specimen configurations, and experimental techniques used to develop an insight into subsurface fatigue crack growth in Glare 2A specimens subjected to combined tension and bending.

Chapter 4: Development of Hybrid Crack Growth Model

This chapter describes the development of a hybrid analytical/numerical crack growth model for predicting fatigue crack growth in individual layers of Glare 2A laminates.

Chapter 5: Validation of the Model Against Experimental Data

This chapter compares the model developed in Chapter 4 against the experimental data generated in Chapter 3. Discussion of the model's sensitivity to various inputs is included.

Chapter 6: Extension of Model to Glare 3 laminates

This chapter investigates the applicability of the model developed in Chapter 4 to Glare 3 laminates. Details of the experimental program, and the adjustments to the model are discussed. Validation of the model against the experimental data is detailed, along with an assessment of the model's validity to Glare 3.

1.4. References

- ¹ **Vlot, A., Gunnink, J.W.**, *Fibre Metal Laminates an Introduction*, Kluwer Academic Publishers, 2001.
- ² **Vlot, A.**, *Glare – history of the development of a new aircraft material*, Kluwer Academic Publishers, 2001.
- ³ **NTSB**, *Aviation Accident Database Report*, DCA88MA054, 1990.
- ⁴ **Marissen, R.**, *Fatigue Crack Growth in ARALL, A hybrid Aluminium-Aramid Composite Material, crack growth mechanisms and quantitative predictions of the crack growth rate*, PhD Thesis, Delft University of Technology, 1988.
- ⁵ **De Koning, A.U., Schra, L.**, *Fatigue crack growth of part through the thickness cracks in Glare 3 and Glare 4B coupons*, NLR-CR-2000-078, 2000 (Restricted).
- ⁶ **Toi, R.**, *An Empirical Crack Growth Model for Fiber/Metal Laminates*, Proceedings of the 18th Symposium of the International Committee on Aeronautical Fatigue, Melbourne, Australia, 899-909 (1995).
- ⁷ **Schijve, J.**, *Some elementary calculations on secondary bending in simple lap joints*, NLR TR 72036 U, National Aerospace Laboratory NLR, 1972.

2

Literature Review

Abstract – This chapter provides a brief description of Glare structure and defines terminology related to that structure. Material properties of Glare laminates are compared to monolithic aluminum alloys to illustrate the advantages that FMLs represent. As the fatigue characteristics were key to the development of the laminate, a discussion of fatigue crack growth in Glare is described. Finally, several existing fatigue crack growth prediction models are described and evaluated for their applicability to the current research of surface and subsurface fatigue crack growth in Glare FMLs subjected to combined tension and bending.



2.1. Introduction

Fatigue crack growth in monolithic aluminum alloy sheet is relatively well documented^{1, 2}. Due to the alloy's compliance with the assumption of linear elastic fracture mechanics, a Paris law³ formulation to describe the crack growth is applicable. As part of this formulation, geometry effects must be taken into consideration – for example, width effects, stress concentrations due to notches, or thickness effects that determine plane strain versus plane stress conditions. Solutions to accommodate a wide range of geometry conditions are available⁴ that are applicable to monolithic metals.

To improve the fatigue behaviour of monolithic aluminum alloys, the fibre metal laminate (FML) concept was developed. The FML concept slows down the fatigue crack growth by introducing fibre bridging to restrain crack opening displacements. This fibre bridging is included by laminating fibre prepreg plies between metal sheets.

The FML Glare demonstrates an improvement in fatigue properties over monolithic aluminum; however, a crack growth prediction model is required to capitalize on the improvements. While FMLs are more complex than monolithic materials, due to the laminated structure of multiple materials and variable geometries, taking the concepts developed for monolithic material as a starting point makes sense.

To enable a proper appraisal of earlier literature models for fatigue crack growth in FML, it is necessary to discuss Glare structure and terminology, see Section 2.2. Earlier fatigue models for Glare (none of which are directly applicable to the current research for combined tension and bending conditions) are discussed in Section 2.3.

2.2. Glare essentials

The following section describes Glare construction and outlines some of the material properties that are important for aerospace applications. A complete description of Glare history and properties can be found in the literature^{5, 6}.

2.2.1. Glare Construction

Figure 2.1 illustrates the construction of a typical Glare laminate. All current Glare grades are constructed with 2024-T3 aluminum plies ranging in thickness from 0.2 to 0.5 mm. The fibre layers are made of S2-glass. They are adhered with FM-94 adhesive that acts as the matrix for the glass fibres and as an adhesive to bond the prepreg to the aluminum sheets. To maximize the performance of the bond, the aluminum sheets receive a tailored surface pre-treatment to increase adhesion and have controlled debonding. With these elements as the basic constituents, a variety of configurations can be assembled.

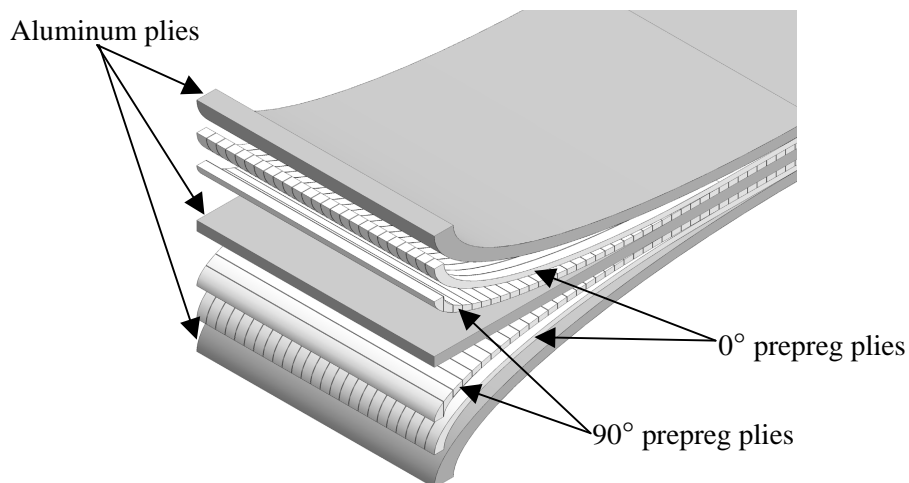


Figure 2.1: Notional Glare 3 construction.

The constituents of Glare can be configured in various ways to maximize the laminates performance for a given application (e.g. fatigue, strength, impact, shear). Table 2.1 lists the most common available Glare grades. The prepreg layers in Glare 2, 4 and 5 are stacked symmetrically. The prepreg layers in Glare 3 are stacked so that the fibres in the layer closest to the outer aluminum layer are orientated in the aluminum rolling direction. The rolling direction of the aluminum is defined as 0° , and the transverse rolling direction is defined as 90° . In order to concisely define Glare laminates, a coding system is implemented:

Glare Ax-B/C-t

Where:

- A defines the grade of laminate as defined in Table 2.1
- x gives information on the prepreg ply orientation
- B indicates the number of aluminum alloy plies
- C indicates the number of glass fibre prepreg layers
- t indicates the thickness of the aluminum alloy plies

Table 2.1: Standard Glare grades⁶

Glare Grade	Thickness of metal sheet (mm) & alloy	Prepreg orientation in each fibre layer	Main beneficial characteristic
Glare 2A	0.2-0.5 2024-T3	$0^\circ/0^\circ$	Fatigue, strength
Glare 2B	0.2-0.5 2024-T3	$90^\circ/90^\circ$	Fatigue, strength
Glare 3	0.2-0.5 2024-T3	$0^\circ/90^\circ$	Fatigue, impact
Glare 4A	0.2-0.5 2024-T3	$0^\circ/90^\circ/0^\circ$	Fatigue, strength in 0° direction
Glare 4B	0.2-0.5 2024-T3	$90^\circ/0^\circ/90^\circ$	Fatigue, strength in 90° direction
Glare 5	0.2-0.5 2024-T3	$0^\circ/90^\circ/90^\circ/0^\circ$	Impact

Where necessary, the number of layers has been increased, but the coding sequence as explained above can be used to derive the stack sequence.

2.2.2. Glare Material Property Comparison

Due to its laminated structure and fibre constituents, the material properties of Glare are different from those of monolithic aluminum. The following describes Glare properties compared to aluminum.

The properties of Glare are related directly to the ratio of its constituents. To fully exploit this relationship, the static properties of Glare have been expressed with an approach very similar to the rule of mixtures used for composites. This is called the Metal Volume Fraction (MVF) approach and has been validated and explained in detail in the literature⁶.

Figure 2.2 shows various material properties of four types of Glare indexed to the material properties of 2024-T3 aluminum. In this figure, the material properties of 2024-T3 aluminum represent the dotted line at 100.

In this figure, all of the basic material properties of Glare are lower than the aluminum alloy, save the ultimate strength. The low values of yield strength and Young's modulus are understood, as the Young's modulus of the prepreg is lower than that of the aluminum. The shear, or G-modulus of Glare is lower, as the prepreg is not effective in shear. The ultimate strength of Glare is higher, as the ultimate strength of the fibres is higher than that of aluminum.

Even with the lower specific weight that can balance out other lower material properties in a design, a significant additional advantage would be required to make Glare an attractive design choice. Glare displays several superior properties if compared to the monolithic aluminum alloy. They are associated with the glass fibres and the laminated construction of Glare. Glare shows advantages for corrosion resistance, impact behaviour and fire resistance⁶.

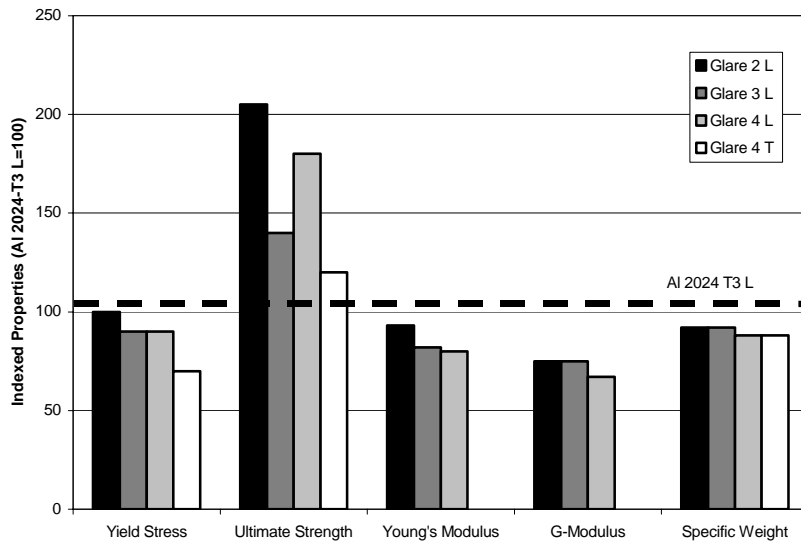


Figure 2.2: Indexed material properties of Glare compared to Al 2024 T3⁶.

However, the key advantage of Glare is its fatigue insensitivity. This insensitivity was the driving force behind the material system's development. Figure 2.3 illustrates this feature by comparing fatigue crack growth curves of monolithic aluminum alloy sheet to various Glare grades. Differences in the crack growth rates of the Glare grades are due to the differences in the laminate thickness and glass fibre orientations.

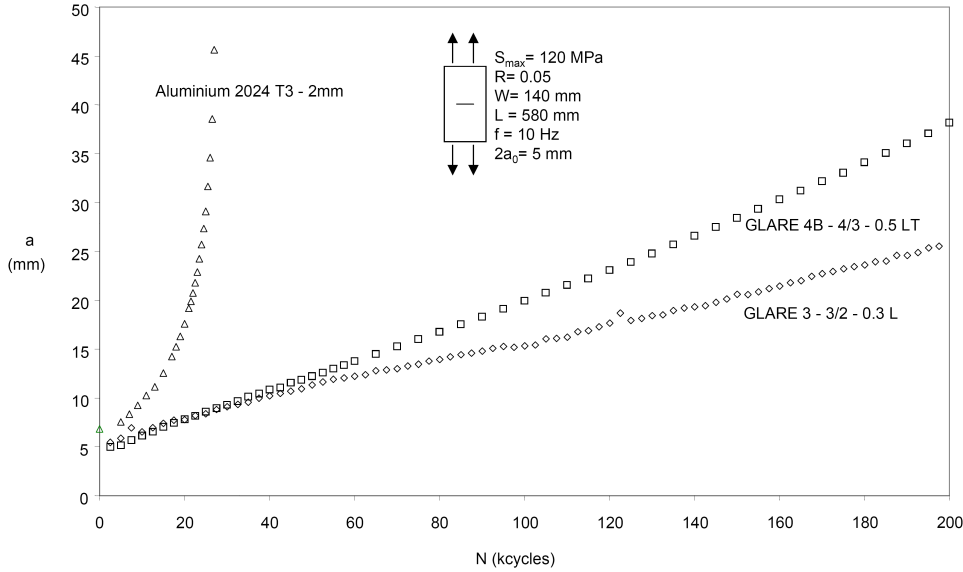


Figure 2.3: Fatigue characteristics comparison. Aluminum 2024 v. Glare 4B and 3⁶.

Cracks in Glare can generally be grouped into two categories: those cracks where the fibres in the laminate are broken, and those where the fibres remain intact. For through cracks where fibres are broken in the structure, Glare typically exhibits superior properties when compared to aluminum.

Fatigue cracks fall into the second category – the initiation and propagation of fatigue cracks leave the fibres unbroken. In this situation, the residual strength of Glare is superior to that of aluminum. This is due to the fact that the fibres in the structure of Glare are still in tact and offer an alternate load path⁷. As was previously mentioned, the superior fatigue behaviour of Glare was the driver behind its development. The development of a fatigue crack in Glare is discussed in detail in the next section.

2.2.3. Physical Description of Fatigue Crack Growth in Glare

The laminate constituents govern fatigue crack growth in Glare. Aspects of fatigue crack mechanics in Glare follow well-understood principals of the individual

materials in the laminate. Other aspects, owing to the interdependence of the constituents, require further understanding. Fatigue crack growth in Glare, as in any material, can be decomposed into crack initiation and crack propagation.

The fatigue crack initiation life is defined as the number of cycles required to show evidence of a minimum-sized crack. This minimum size is dependent upon the material and measurement technique employed. Micro crack nucleation and the initial crack growth are determined by surface conditions and stress concentrations. As these phenomena are not driven by a part's structure, micro crack growth mechanisms are the same for Glare and monolithic aluminum. In essence, the end of crack initiation occurs when a transition from micro crack growth to macro crack growth occurs. Homan⁸ proposed the crack initiation life for Glare as that number of cycles required for a crack to reach a length of 1mm. After this transition, the laws of linear elastic fracture mechanics become applicable.

While it has been shown^{8,9} that methodologies for monolithic aluminum can be used to study crack initiation in aluminum plies of Glare, the actual stress state in the aluminum ply must be known to quantify the data. The contributors to the stress state include the loading and the stress concentration due to the specimen geometry¹⁰. The glass fibre plies in Glare influence the stiffness of the laminate. Additionally, the curing¹¹ process imparts significant residual stresses. During crack nucleation, there is no fibre bridging contribution to the stress state of the aluminum plies, though the crack length at which the fibres become effective at restraining crack opening can be as short as 2mm^{12,13}.

The contributors to the stress state due to the presence of the glass fibres has the effect of increasing the actual stresses in the laminate above the applied stress levels. This decreases the crack initiation life of a Glare laminate. But while the initiation life is shorter, the fibre plies has a beneficial effect on the crack propagation life.

Once a crack has initiated in Glare, the crack growth mechanism is comprised of two phenomena – fatigue crack propagation in the aluminum plies, and the delamination of the glass fibre prepreg from the aluminum plies, as shown in Figure 1.2. As a crack opens in an aluminum ply, the adhesive bond between the aluminum and the prepreg ply fails locally. This local delamination allows the glass fibres to bridge the crack in the aluminum ply without failure. Without the delamination, the fibres would be subjected to large local strains due to the crack opening displacement such that they would fail⁶. By delaminating, a greater length of the fibres is available to absorb the crack opening displacement, thereby keeping the stresses in the fibres below failure. This fibre bridging acts to constrain the crack opening in the aluminum plies, and thus reduces the crack growth rate in the aluminum plies. The delamination and fatigue crack growth progress in a self-balancing manner¹³, i.e. the delamination growth and the fibre bridging stresses are linked, continuously balancing each other, which, in turn, effects the crack opening displacements.

Fatigue crack propagation in the aluminum plies in Glare can be defined using methodologies for monolithic materials. With the assumption of LEFM previously mentioned, the Paris law becomes a candidate for describing fatigue crack propagation.

$$\frac{da}{dN} = C(\Delta K)^m \quad (2.1)$$

Where C and m are material constants for aluminum. It is in the definition of the stress intensity factor range, ΔK , that the complexities of the laminate structure of Glare must be consolidated. The stress intensity is expressed:

$$K = f(g)\sigma\sqrt{\pi a} \quad (2.2)$$

Where $f(g)$ is a geometry correction factor, σ is the stress, and a is the crack length.

It is apparent that the stress state within the aluminum ply must be known. Within Glare, the stresses that affect the crack growth include not only those due to the applied load, but also those due to the adjacent fibre plies bridging the crack. As the fibres bridge over the crack, they offer an alternative load path that directly affects the stress state at the tip of the crack. Hence, in an FML, there is no global stress intensity factor for the laminate as a whole. Rather, the stress intensity must be found for each crack in every aluminum ply of the laminate, accounting for the local stress state due to the loading of the laminate and the fibre bridging.

Fatigue crack geometries in Glare can be grouped into three general types: through cracks, surface cracks, and part through cracks. Each type is generated as a result of specific conditions the laminate experiences. Each type of crack geometry can be encountered in practice.

A through crack, Figure 2.4, is constrained by fibre bridging, so the fatigue crack growth is slower in a part constructed of Glare than one of monolithic aluminum. If a through crack is introduced in a Glare part subjected to pure tension, the outer plies of aluminum will experience slightly faster crack growth than the inner plies. This is due to the fact that the inner plies have fibres bridging on both sides of the crack, compared to just one side for a surface ply¹⁴. A through crack can either result from the progression of a part-through crack to the opposite surface of the laminate, or from damage inflicted on a part.

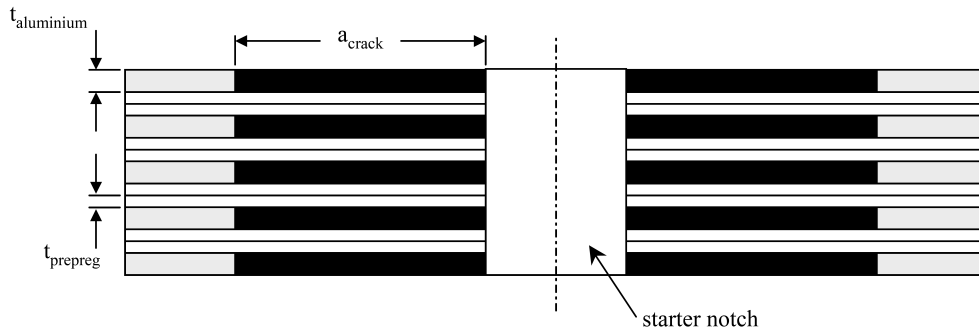


Figure 2.4: Through crack in notional Glare 2 laminate.

In a surface cracked condition, Figure 2.5, only one of the surface aluminum plies is cracked. This can occur, for instance, when the surface layer of a part has been damaged and a crack initiation site is provided. As the part is cyclically loaded, a crack will form. In this configuration, not only the adjacent fibres are acting to bridge the crack, but also the bulk of the laminate is acting in a bridging role.

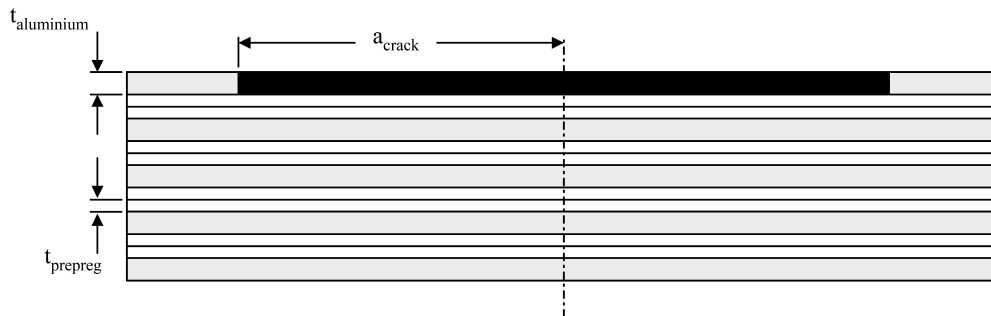


Figure 2.5: Surface crack in notional Glare 2 laminate.

The focus of the research described in this thesis is part-through cracks. A part-through crack, as shown in Figure 2.6, is the natural extension to the surface crack. This type of crack is regularly seen in parts subjected to combined tension and bending, Figure 2.7, as in an aircraft fuselage joint, or a part with a surface flaw. At the region of the crack, the laminate is loaded in combined tension and bending. The different plies in the laminate will experience differing levels of stress through the thickness. These different levels of stress will induce differing rates of crack growth.

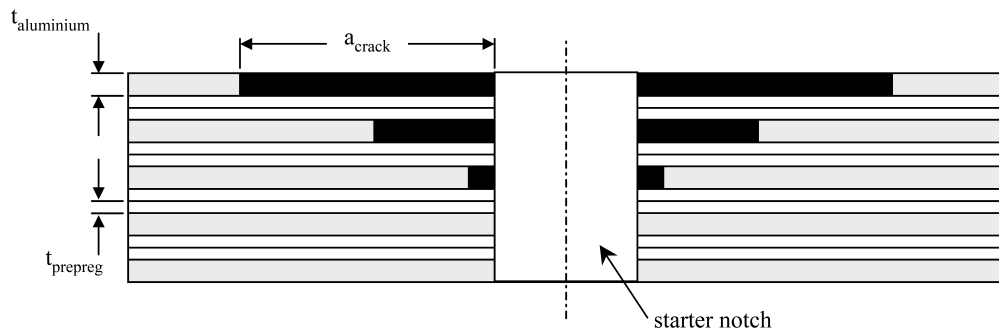


Figure 2.6: Part through crack in notional Glare 2 laminate.

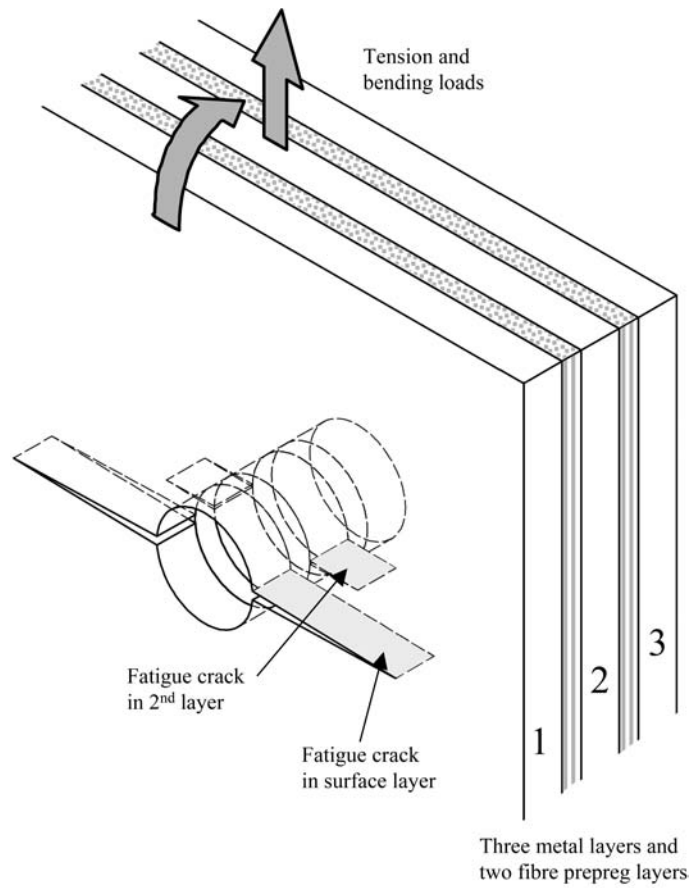


Figure 2.7: Part through crack in notional Glare 2-3/2 laminate subjected to combined tension and bending.

Fatigue cracks must initiate in each layer of aluminum for the crack system to progress through the thickness. This fact helps to retard the progression of the crack system through the thickness of a part. This effect has been shown by Schijve¹⁵ to be present in laminated aluminum sheets subjected to pure tension. Therefore, fatigue cracks in parts constructed of Glare are constrained from growing through the thickness due to this effect, and from growing in length due to the effects of the fibre bridging. This is in comparison to a similar part constructed of monolithic aluminum, which can not benefit from these effects.

For a crack emanating from a rivet hole, many additional factors must be considered, including the effects of pin loading, rivet squeeze force, fastener tilt, and the curvature of the joint⁶.

2.3. Fatigue Crack Growth Models for Glare

Any theory to predict fatigue crack growth in Glare must account for the simultaneous crack and delamination growth exhibited by the material. Several models exist to describe this behaviour, each following a different approach to the issue of fibre bridging. This section will outline and describe strengths and limitations of the models listed in Table 2.2. They will be assessed as to their applicability to the current research problem of predicting surface and subsurface crack growth in part-through cracks in Glare subjected to combined tension and bending.

Table 2.2: Fatigue crack growth models for Glare.

Model of	Type of Crack Modelled	Formulation
Marissen	Through	Analytical
Burianek	Through	Mechanistic
Guo & Wu	Through	Analytical
Alderliesten	Through	Analytical
Toi	Through, Surface	Empirical
Guo & Wu	Through	Phenomenological
De Koning	Surface	Empirical
Rose	Surface	Parametric

2.3.1. Analytical Model of Marissen

The model put forth by Marissen¹⁶ was a Paris Walker type crack growth relation. It was formulated to predict crack growth of through the thickness cracks in ARALL FMLs. ARALL is the predecessor of Glare, containing aramid fibres, rather than glass fibres, as the prepreg reinforcement. In this early FML version, prepreg quality was still imperfect, showing a resin-rich interface layer between the aluminum and prepreg plies of considerably lower stiffness. The model considers crack growth in the metal layers, fibre bridging and adhesive deformation as the three main mechanisms governing crack growth. Marissen developed an effective stress intensity factor for the metal layers by combining the effects of the applied stress and fibre bridging. He then found a stress intensity factor for the adhesive layer under shear deformation. He combined these two factors with superposition to achieve an effective stress intensity factor for the crack in the laminate as shown in the equations below.

$$K_{ARALL} = K_{Al} + K_{ad} \quad (2.3)$$

Where K_{ARALL} is the total effective stress intensity factor for the laminate, K_{Al} is the stress intensity factor for the aluminum layers, and K_{ad} is the stress intensity factor for the adhesive layers. Looking at each term on the right hand side of the equation:

$$K_{Al} = (S_{Al} - S_{br})\sqrt{\pi a} \quad (2.4)$$

Where S_{Al} is the stress in the metal layers and S_{br} is the stress taken up by the fibres as they bridge the crack in the metal layers. This bridging stress is not applied to the crack flank, but rather to the delamination boundary, so a correction factor, $C_{b/a}$, is introduced to suitable apply the stress. The variables a and b are the crack length and delamination height respectively. This factor was found by modifying a function found in Tada⁴ for a set of point forces applied to a crack a set distance from the crack flank. By integrating this function over the crack length along the delamination shape, the correction is found to account for the assumed constant fibre bridging stress applied at variable distances from the crack flank as a function of the stress in the laminate, S_{ARALL} .

$$K_{Al} = (S_{Al} - C_{b/a}S_{ARALL})\sqrt{\pi a} \quad (2.5)$$

The stress in the metal layers is related to the stress in the laminate by the ratio of stiffness:

$$S_{ARALL} = \left(\frac{1 + 2\frac{a}{b}}{\frac{F_{Al}}{F_{ARALL}} + 2\frac{a}{b}} \right) S_{Al} \quad (2.6)$$

The stress intensity in the adhesive layer is given by:

$$K_{ad} = C_{ad,d} (S_{Al} - S_{Al,0}) \sqrt{h \cdot \tanh(\pi a/h)} \quad (2.7)$$

The variable, h , in the above formula is derived from a solution for the stress intensity factor for a geometry with similar characteristics to the one investigated. This similar geometry is a row of parallel cracks in an infinite plate, with the distance between cracks denoted as $2h$. This geometry was found to express the same asymptotic behaviour for crack opening displacements as the geometry of interest. For the geometry of interest, the analogous expression for h is:

$$h = F_{Al} \sqrt{\frac{1}{jF_{ad}F_{Al}} + \frac{1}{jF_{ad}F_{ARALL}}} \quad (2.8)$$

Where j is the number of aluminum plies in the laminate. The variable $C_{ad,d}$ is a correction factor for the delamination of the adhesive near the crack tip, and is expressed as:

$$C_{ad,d} = \frac{S_{br}}{S_{ARALL}} \quad (2.9)$$

The stress intensity factor range found for the laminate was then introduced into a Paris law crack growth model.

$$\frac{da}{dN} = c(\Delta K_{ARALL})^n \quad (2.10)$$

Three issues are highlighted which make Marissen's model challenging for use in the current research. The first issue is the fact that Marissen imposed a simple elliptical delamination shape. This was an admitted approximation, and close to the crack tip, has been shown to be less than accurate¹⁷. Additionally, the fibre bridging stress distribution imposed on the delamination front was constant. This approximation, while justified as experimental data on the fibre bridging stresses are not experimentally measurable, was an oversimplification of the stress state¹⁸.

Finally, Marissen's work investigated ARALL, and a significant portion of the work deals with the adhesive deformation found in that fibre metal laminate around a fatigue crack. Glare does not display as pronounced an adhesive-rich layer between the aluminum plies and the glass fibres.

However, basic approach of Marissen is physically sound, with the stress intensity factor being comprised of super positioned factors accounting for sources of stress. Application to subsurface cracks should be possible, provided the stress sources for the plies can be determined. Augmentation to account for non-elliptical delamination fronts, and non-uniform fibre bridging stress distributions will be required.

2.3.2. Mechanistic 2-D Model of Burianek

The 2-D bridged crack growth model presented by Burianek¹⁹ is an empirical mechanism-based approach developed for titanium-graphite FMLs (TiGr). It developed an effective stress intensity range through superposition by following Marissen's model¹⁶:

$$\Delta K_{eff} = \Delta K_{applied} + \Delta K_{br} \quad (2.11)$$

$\Delta K_{applied}$ is the solution for a geometry of point loads applied away from a crack face given by Tada⁴.

$$\Delta K_{applied} = S_{metal} f(a/w) \sqrt{\pi a} \quad (2.12)$$

$f(a/w)$ is the geometry correction factor. S_{metal} is the stress in the metal layer found with classical laminate plate theory. To find the bridging stress intensity range, Burianek again followed Marissen in form:

$$\Delta K_{br} = S_{br} C_{b/a} \sqrt{\pi a} \quad (2.13)$$

$C_{b/a}$ is a correction factor for the fact that the bridging stresses act on the delamination boundary – not on the crack face. S_{br} was found through 2D finite element analysis. As delamination in TiGr were found to be triangular in shape, the appropriate angle of the triangular shape needed to be found. In order to accurately model the delamination shape in the finite element models, Burianek utilized a strip model to predict the energy release rate of delamination of one ply from another. With this he was able to find the energy associated with triangular delaminations with different angles at the crack tip. The angle that led to the maximum energy release was taken as the most likely delamination angle.

Crack growth rates took the form:

$$\frac{da}{dN} = C(\Delta K_{eff})^n \quad (2.14)$$

C and n are material constants for the metal layers. Burianek applied the model iteratively by solving for S_{br} with FEM for a given crack length and applying it to the crack growth model for a block of cycles. The block of cycles was kept to below 0.5% of the total predicted life of the specimen. With the new crack length, he solved for S_{br} with FEM and applied it again to the crack growth model. By repeating this process, he determined the crack growth rate.

The Burianek model predicted correct trends in crack growth rates. However, he did notice that the model broke down in the area around the crack tip and produced results that were not accurate for TiGr. These discrepancies were attributed to the 2-D model not accounting for realistic delamination shapes and their influence on S_{br} ; on the dramatic changes in S_{br} around the crack tip; and to a lesser extent to the possibility of the delamination front lagging the crack tip in TiGr.

While a promising approach, Burianek's results show that the 2-D finite element model employed did not capture the stress state in the fibres effectively. To employ finite element modelling to obtain fibre bridging stresses, the material system needs to be better represented.

2.3.3. Analytical Model of Guo & Wu

The method of Guo and Wu^{20, 21} is essentially an extension of Marissen's¹⁶ work in that the stress intensity factor in the aluminum plies of Glare is dependent upon the far field stress and the fibre bridging stress. The bridging stresses are derived from an analysis of the crack opening shapes and the factors that influence them.

The crack opening shape can be thought of as dependent upon fibre elongation over a delamination, the adhesive shear deformation, and any aluminum deformation. Each of these terms were derived for arbitrary delamination shapes.

Similarly, the crack opening shape can be thought of as dependent upon the applied load and the fibre bridging stress. The term for the remote applied load was also derived for arbitrary delamination shapes. This left the term for fibre bridging stress.

The crack opening due to fibre bridging was expressed by breaking the crack into bar elements and finding the contribution for each bar along the crack. This was expressed as:

$$u_{br}(x)_i = 2 \sum_{j=1}^N \sigma_{br,j} g(x_i, x_j) L(x_j, y_j) \quad (2.15)$$

The term $L(x_j, y_j)$ accounts for the bridging stress acting on the delamination front rather than the crack flank. The term $g(x_i, x_j)$ is expressed:

$$g(x_i, x_j) = G(-x_i, x_j) + G(x_i, x_j) \quad (2.16)$$

Where the term $G(x_i, x_j)$ is the Green's function, which takes into consideration the finite width of the plate.

As each of these representations for crack opening shape are equal to each other, Guo and Wu isolated the fibre bridging stress and solved the equation numerically.

$$H_{i,j} \sigma_{br,j} = Q_i \quad (2.17)$$

Where $H_{i,j}$ accounts for the crack opening due to applied load and aspects of the bridging stress, and Q_i accounts for the crack opening due to fibre elongation, adhesive shear deformation, and aluminum deformation.

By using the numerically calculated $\sigma_{br,j}$ in an expression for the nondimensional stress intensity factor, an expression for crack growth can be expressed:

$$f_{Al} = \frac{E_{Al}}{E_{la}} f \sqrt{\pi a} \quad (2.18)$$

Where f is the nondimensional stress intensity factor accounting for the applied stress and bridging stress, $\sigma_{br,j}$. The subscript Al refers to aluminum properties in the laminate, and la refers to the laminate as a whole.

$$\Delta K_{Al} = (S_{max} - S_{op}) f_{Al} \quad (2.19)$$

Where S_{max} is the maximum applied stress, and S_{op} is the stress required to open the fatigue crack. This expression is incorporated in the following equation for crack growth:

$$\frac{da}{dN} = C_1 \left[(1 - R_c)^{m-1} \Delta K_{Al} \right]^n \quad (2.20)$$

The key extension of the method was to calculate the fibre bridging stress distribution along the crack for every crack length in the crack growth analysis. This allowed for calculations of bridging stresses for a variety of delamination shapes.

While comparisons of crack opening shapes predicted by the model correlated well with experimental data²¹, there is no way of knowing if the model accurately predicts the actual bridging stress distributions. As the delamination shapes found experimentally were more triangular than elliptical, the bridging stress distribution calls into question why the delaminations did not grow faster near the crack tip. Nor was it explained how a faster delamination growth near the crack tip could preserve the triangular delamination shape.

Utilizing an incremental solution for the fibre bridging stress distribution over a non-elliptical delamination front is an augmentation to the Marissen model that should be applicable in principal to the current research.

2.3.4. Analytical Model of Alderliesten

Alderliesten proposed an analytical prediction model for constant-amplitude fatigue crack propagation of through cracks in Glare. Again, an extension of Marissen's model, Alderliesten incorporated similar augmentations as Guo and Wu, though in a different fashion.

The model describes the crack propagation of the fatigue cracks in the aluminium layers and the corresponding delamination growth at the aluminium/fibre interfaces perpendicular to the crack. The stress intensity factor at the crack tip consists of a stress intensity factor as function of the far field opening stress and a stress intensity factor as function of the crack closing bridging stress in the aluminium layers:

$$K_{tip} = K_{farfield} + K_{br} \quad (2.21)$$

The stress intensity factor related to the far field opening stresses is calculated similar to monolithic aluminium based on the actual stresses in the aluminium layers. These stresses are calculated with the Classical Laminate Theory based on the applied stresses and on the residual stresses present after curing.

$$K_{farfield} = S_{al} \sqrt{\pi a} \quad (2.22)$$

The stress intensity factor related to the bridging stresses, K_{br} , follows directly by integrating all the bridging stresses over the total crack length. The crack is divided into N bar elements. At the position of any bar element, the x -position is known, x_i , and the delamination height, b_i , is known, either from the initial delamination shape imposed, or from the calculated delamination growth.

$$K_{br} = 2 \sum_{i=1}^N \frac{S_{br,al}(x_i)w}{\sqrt{\pi a}} \frac{a}{\sqrt{a^2 - x_i^2 + b_i^2}} \left(1 + \frac{1}{2}(1 + \nu) \frac{b_i^2}{a^2 - x_i^2 + b_i^2} \right) \quad (2.23)$$

Where $S_{br,al}$ is the bridging stress along the crack length at position x_i , a is the crack length, and w is the width of a bar element.

The bridging stresses along the crack length are calculated on the basis of the crack opening relations for individual mechanisms. The reason is that the actual crack opening in the laminate can also be written as a crack opening due to the far field stresses and a crack closing effect due to the bridging stresses. Alderliesten equated the crack opening of a fatigue crack at any location along the crack, $v(x)$ to the elongation of the delaminated fibres bridging that crack at that location, $\delta_f(x)$, and the deformation of the prepreg layer, $\delta_{pp}(x)$:

$$v(x) = \delta_f(x) + \delta_{pp}(x) \quad (2.24)$$

The crack opening displacement was considered comprised of the effects due to the applied load $v_\infty(x)$ and the closure effect of the bridging fibres, $v_{br}(x)$:

$$v(x) = v_\infty(x) - v_{br}(x) \quad (2.25)$$

Expressions were found for appropriate terms:

$$v_\infty(x) = 2 \frac{S_{al}}{E_{al} \sqrt{a^2 - x^2}} \quad (2.26)$$

$$v_{br}(x) = \sum_{i=1}^N v(x_i, x_j) \quad (2.27)$$

$$\delta_f(x) = \frac{S_f + S_{br}(x)}{E_f} b(x) \quad (2.28)$$

$$\delta_{pp}(x) = C_b S_{al} t_{al} \sqrt{\frac{t_f}{G_f} \left(\frac{1}{F_{al}} + \frac{1}{F_f} \right)} \quad (2.29)$$

Where S indicated a stress, E is the Young's modulus, F is the stiffness, and G is the shear stiffness. The subscript al referred to aluminum, br to fibre bridging, and f to the fibres. The term C_b was a correction factor accounting for the dependency of the crack opening term on the delamination length. Equations 2.24-2.28 were equated and reduced to:

$$S_{br} = H^{-1} Q \quad (2.30)$$

Where, with the Kronecker delta, $\delta(i,j)$:

$$H = \sum_{j=1}^N \frac{v(x_i, x_j)}{S_{br}(x_j)} + \frac{b(i)}{E_f} \delta(i, j) \quad (2.31)$$

$$Q = v_{\infty}(i) - \delta_{pp}(i) - \frac{S_f}{E_f} b(i) \quad (2.32)$$

The bridging stresses are then used to calculate the delamination extension, using a correlation between the delamination growth rate and the energy release rate. By doing so, crack growth in the aluminium layers is calculated, while at the same time the delamination growth at the interfaces is calculated.

The prediction model was implemented in a numerical programme and was validated with a wide range of experimental data. A good correlation between predicted and experimental crack growth rates, crack opening contours and delamination shapes was obtained.

The Alderliesten model is an effective application of the basic concepts of Marissen, but with the advantage of numerically calculating the fibre bridging stress values at discrete points along the delamination boundary, rather than applying a constant value over the crack length. Additionally, the calculation of the delamination extension based upon the fibre bridging stresses is an aggressive step forward in describing analytically, the complex environment of fatigue crack growth in FMLs.

Alderliesten uses a Paris law formulation to describe the delamination extension. He conducted delamination experiments to determine appropriate material constants for the Mode II delamination growth of Glare. His investigations found that the material constants were not stress or Glare grade-dependent, but instead, dependent upon the adhesion of the constituents only. This means that to extend the Alderliesten model to other FMLs, these material constants must be found for that new laminate system.

The Alderliesten model was developed for through cracks only. Expanding the model to part through cracks would require investigating the effects of a long surface crack on the stress system of a shorter subsurface crack. Applying a combined tension and bending load could require analysing each aluminum ply individually at that ply's loading condition to assess the stress intensity factors. Again, the influence of one ply on another would need to be accounted for.

2.3.5. Empirical Model of Toi

Toi²² presented perhaps the simplest formulation of a fatigue crack growth model for Glare. This model assumed that through-crack growth in Glare could be correlated to crack growth in monolithic aluminum through the use of a correction factor. This factor would be employed in a similar manner to a geometry correction factor for the Paris crack growth law.

$$\frac{da}{dN} = C(\Delta K_{eff})^n \quad (2.33)$$

Toi used the Elber²³ formulation for ΔK_{eff} to account for the stress ratio, R :

$$\Delta K_{eff} = (0.5 + 0.4R)\Delta K_{Al} \quad (2.34)$$

Inserting the effective stress intensity range into the crack growth law and solving yields an expression for the aluminum plies in Glare:

$$\Delta K_{Al} = \frac{\left(\frac{da/dN}{C}\right)^{1/n}}{0.4 + 0.5R} \quad (2.35)$$

For the laminate as a whole, Toi assumed a form for the stress intensity factor range of:

$$\Delta K_{FML} = \beta_{geom} \Delta S \sqrt{\pi a} \quad (2.36)$$

The factor β_{geom} is a geometry correction factor, ΔS is the applied stress range, and a is the crack length. Toi then considered a correction factor to account for the contributions of the fibre metal laminate to the crack growth behaviour. β_{FML} was found empirically by comparing crack growth rates for aluminum and Glare at the same stress ranges leading to:

$$\beta_{FML} = \frac{\Delta K_{Al}}{\Delta K_{FML}} \quad (2.37)$$

By equating the above forms yields:

$$\beta_{FML} = \frac{\left(\frac{da/dN}{C} \right)^{1/n}}{\beta_{geom} \Delta S \sqrt{\pi a} (0.5 + 0.4R)} \quad (2.38)$$

This factor is dependent upon loading conditions, Glare type and configuration, and any other test conditions. Thus a corrective factor would need to be developed for every conceivable combination of the above dependencies. Toi tested the model for one test specimen configuration and various grades of Glare. From this he concluded that the fibre metal laminate correction factor has a unique value dependent only on the grade of Glare.

Alderliesten¹³ independently evaluated the conclusions of Toi by examining test results on Glare 1, 2 and 3 to determine the effects of Glare grade, applied stress, and the number of plies in the laminates on β_{FML} . These evaluations found significant influence due to the Glare grade, as expected. However, influences due to the applied stress values and the laminate thickness were found to be as significant as the Glare grade.

Gonesh²⁴ also investigated the applicability of the Toi model to surface cracks in Glare. He conducted tests on Glare 3 specimens with both a 2/1 and 3/2 lay up, with either a 5.0 or 25.0mm surface crack installed. He tested these configurations at constant amplitude of stress ranges of 5-150MPa and 5-180MPa. From these tests, Gonesh found dependence of β_{FML} to applied stress and laminate thickness to be of prime importance. The effects of the initial crack length were found to be negligible in the limited study conducted.

Because he did not test with other specimen configurations under different loading conditions, and through the independent evaluations described, the premise of a unique β_{FML} , dependent on the Glare grade alone is called into question. While a simple model that would be ideal for the design engineer to use as a design tool, the fact that it is merely a curve fitting practice means that the testing required to fill a matrix of all possible perturbations makes the model inapplicable to the current research.

2.3.6. Phenomenological Model of Guo & Wu

Guo and Wu²⁵ observed that fatigue crack growth in Glare in samples of sufficient width to exclude size effects attains a steady state under constant amplitude loading. This constant crack growth rate is independent of crack length and specimen type. The crack growth rate for through-cracks in FMLs loaded in pure tension is dependant upon the applied stress, stress ratio, Glare grade and laminate configuration. This observation prompted the development of a phenomenological model that would simplify the prediction of crack growth in Glare. An assumption was made that a single material constant could be defined that would enable the use

of a simple Walker-style analysis to predict crack growth. The Walker formulation was used to account for the effective applied stress range considering the influence of residual stresses in the laminate.

The development of this model again starts with simple LEFM definitions of the stress intensity. The equation for the stress intensity factor range due to applied constant amplitude stresses takes the form:

$$\Delta K = F\Delta S\sqrt{\pi a} \quad (2.39)$$

Due to fibre bridging, crack growth in FMLs bear no unique correlation to this stress intensity range. As the crack growth tends to steady state once fully developed, there is no geometry correction factor that can account for the crack growth behaviour. Guo and Wu defined an effective stress intensity range due to this applied stress that would be valid for steady state crack growth only. As this region of crack growth is independent of crack length and specimen configuration, no geometry correction factor is required. Only the applied stress and fibre bridging govern this region of crack growth. The two mechanisms are self-balancing and act to keep the effective stress intensity factor range constant during crack growth. The effective stress intensity factor range is defined as that constant range of values a crack will experience in Glare during steady-state crack growth and is expressed as:

$$\Delta K_{eff} = \Delta S\sqrt{\pi l_0} \quad (2.40)$$

The term l_0 is an equivalent crack length and is a material constant as all other terms in the equation are constant for the subject region of crack growth. This equivalent crack length is the proposed material constant that facilitates the definition of the effective stress intensity factor range. By using a Walker formulation of crack growth description, the effective stress intensity range could be isolated.

$$\frac{da}{dN} = C_1 \left[(1 - R_c)^{m-1} \Delta K_{eff} \right]^n \quad (2.41)$$

Crack growth rates were taken from experimental observations, and the effective stress intensity factor range was calculated. Looking at the ratio of Equation 2.39 to Equation 2.41:

$$\frac{\Delta K_{eff}}{\Delta K} = \frac{\sqrt[n]{da/dN}}{\sqrt[n]{C_1 (1 - R_c)^{m-1} (F\Delta S\sqrt{\pi a})}} \quad (2.42)$$

the equivalent crack length could be determined:

$$l_0 = \frac{\gamma^2}{1/F^2 - \gamma^2/F_o^2} (a - s) \quad (2.43)$$

Where F and F_o are configuration factors for the type of specimen investigated during the test, and when the crack length equalled the saw cut length, respectively. The term γ simply collects the terms from Equation 2.42. This accounts for short crack growth, where the fibre bridging has not yet become fully effective. Reordering:

$$\Delta K_{eff} = \frac{\sqrt{l_0}}{\sqrt{(a-s) + \frac{l_0}{F_o^2}}} \Delta S \sqrt{\pi a} \quad (2.44)$$

This formulation of the effective stress intensity factor range is valid over the entire crack growth regime – not just the steady crack growth rates of large cracks.

While shown to accurately predict the crack growth for through-cracks in the Glare types and specimen configurations studied, the methodology was found²⁶ to require a unique value for l_o for each Glare type and lay up. This was due to the fact that the equivalent crack size is dependent upon the geometry of the lay up, the stack up of the glass fibres, and the initial saw cut length. This made the model too restrictive for the current research.

2.3.7. Empirical Model of De Koning

De Koning's²⁷ model follows a Walker formulation for crack growth prediction. De Koning developed this model for surface cracks in Glare 3 and Glare 4B. This formulation was an attempt to explain why crack growth in Glare coupons was not sensitive to crack length, but was more sensitive to applied stress than monolithic aluminum coupons. De Koning found that crack growth in Glare was dependent on applied stress to a power of six, rather than to a power of about three, as found in monolithic aluminum²⁸. The derivation stems from the observation of nearly constant crack growth rates for much of the propagation life, which implies a constant stress intensity factor. To achieve this constant factor, a second loading system is assumed to travel with the crack tip along with the presence of the applied loads. This second loading system is fibre bridging. De Koning captured these relations in the following model.

The physical system is illustrated in Figure 2.8. Crack opening loads near the crack tip are represented by γS , where S is the remote applied load, and γ is a load transfer coefficient. These loads operate over a process zone defined as $\delta(S/\bar{\sigma})^2$. The term δ is a characteristic length parameter that depends on the metal sheet thickness, t ,

only. The correlation between δ and t is ε . The yield parameter, $\bar{\sigma}$, is analogous to the yield limit of metals used to determine plastic zone sizes. This parameter is considered to be a material constant of the prepreg in the laminate.

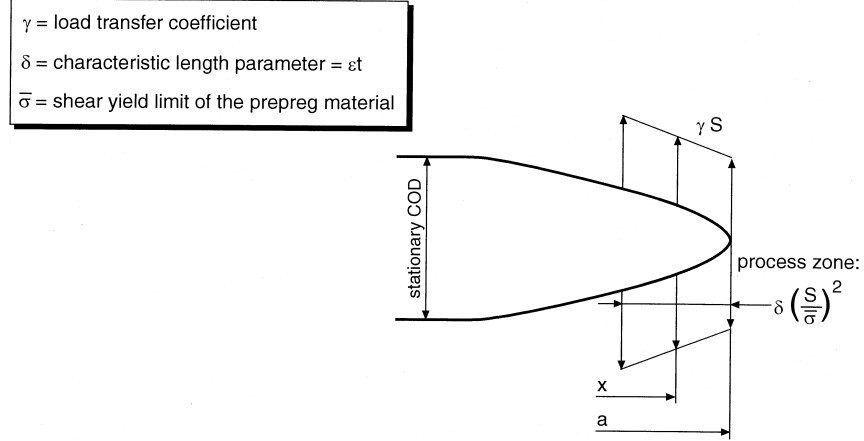


Figure 2.8: Local stress system near the crack tip²⁷.

Using this system for a centrally cracked specimen, the stress intensity can be found following Tada⁴:

$$K = \frac{4}{\sqrt{2\pi}} f\left(\frac{a}{w}\right) \left(\frac{\gamma \sqrt{\varepsilon}}{\bar{\sigma}} \right) S^2 \sqrt{t} \quad (2.45)$$

Where $f\left(\frac{a}{w}\right)$ is a geometry correction factor. Evaluating the system under maximum applied stress, a value for K_{max} is found. Inserting this into the empirical Paris crack growth law yields:

$$\frac{da}{dN} = C_1 (1 - R^2)^n \left[\frac{4 f\left(\frac{a}{w}\right)}{\sqrt{2\pi}} \left(\frac{\gamma \sqrt{\varepsilon}}{\bar{\sigma}} \right) S_{max}^2 \sqrt{t} \right]^n \quad (2.46)$$

The coefficients C_1 and n are standard material constants for the metal plies in the lay up. Noting that the S_{max} term is squared in the model, and then raised to n , shows how the relation of crack growth being tied to applied stress to the power of six is achieved. The term $\gamma \sqrt{\varepsilon} / \bar{\sigma}$ is a set of material parameters that only depend on the Glare configuration used. De Koning asserted that the three parameters could not be individually determined, but rather were grouped into a single material-configuration parameter. The value for this parameter was then found by fitting to da/dN versus S_{max} curves.

De Koning found the term $\gamma\sqrt{\varepsilon}/\bar{\sigma}$ to be dependent upon more than just the Glare type, but also on the laminate thickness and rolling direction of the aluminum plies in the laminate. This led to empirical correction factors being necessary to account for different configurations. This empirical nature, and the requirements of multiple correction factors to account for cracks in subsurface plies makes the approach inappropriate to apply for the current investigation.

2.3.8. Parametric Model of Rose

Gonesh²⁴ proposed utilizing the patching repair model developed by Rose²⁹ to describe the surface cracks in Glare. The Rose model predicts the reduction in the stress intensity factor, K , of a cracked metal plate due to the presence of a bonded patch repair. The model is parametric in that the bridging stress is linearly dependent on the crack opening displacement. The adhesive acts as a shear spring, and accounts for the bridging stress. The analysis is conducted in two steps, with the first calculating the redistribution of stress in an uncracked plate due to the local stiffening produced by the bonded reinforcement. This gives a formulation for the normal stress in the plate, σ_0 :

$$\sigma_0 = \frac{F}{t_p(1+S)} \quad (2.47)$$

Where F accounts for load transfer, t_p is the thickness of the plate, and S is the relative stiffness of the patched repair. The second step relaxes the normal stress in the location of the crack in the plate to zero. This simulates the effects of the crack, and the consequential stress transfer can be calculated. This requires considering the shear deformation of the adhesive bonding the patch and the secondary bending of the patched repair. The strain energy release rate for an assumed infinite patch overlap is:

$$G_\infty = \frac{\sigma_0^2}{E_p} \pi \Lambda (1 + \Omega) \quad (2.48)$$

Where Λ is the equivalent crack length, and $\pi\Lambda$ depends upon the relative stiffness of the patch and load transfer length required to transmit the stress redistribution through the adhesive. Beyond the load transfer length, the adhesive can be considered rigid. E_p is the Young's modulus for the plate, and Ω is a correction factor for secondary bending in the patched repair. The upper bound for the stress intensity is then:

$$K_\infty = \sqrt{G_\infty E_p} = \sigma_0 \sqrt{\pi \Lambda (1 + \Omega)} \quad (2.49)$$

Gonesh proposed implementing this model by considering a surface-cracked Glare plate as a cracked thin aluminum sheet with an infinite patch of the remainder of the Glare laminate. Gonesh used the definition of a constant stress intensity factor proposed by Guo and Wu:

$$K_{\infty} = \sigma_{\infty} \sqrt{\pi l_0} \quad (2.50)$$

Where σ_{∞} is the applied stress to the Glare plate, and l_0 is the equivalent crack length. Equating the two expressions for K_{∞} yields:

$$l_0 = \left(\frac{\sigma_0}{\sigma_{\infty}} \right)^2 \Lambda(1 + \Omega) \quad (2.51)$$

Equation 2.51 is used in Equation 2.50 to resolve the stress intensity factor for surface-cracked Glare, where so is defined for Glare as:

$$\sigma_0 = \frac{1 + \lambda}{1 + S} \sigma_{\infty} \quad (2.52)$$

Where λ and S are the relative thickness and relative stiffness of the Glare laminate, respectively.

Gonesh compared his Rose application to test results of surface cracked Glare and found that the model can be applied. However, the correction factor for secondary bending in the Rose model plays a significant role in determining the equivalent crack length. For surface cracks in thin Glare laminates, secondary bending can play a role, however, as the laminate thickness is increased, the effects of secondary bending diminish. Furthermore, the Rose model is dependent upon the transverse shear deformation of the adhesive only. This plays a minor role in Glare, as compared to patched repairs. More important to Glare would be the transverse shear deformation of the plate and patch, and the effects of the delamination of the prepreg from the aluminum around the fatigue crack.

Based upon these assessments, the applicability of the Rose model to subsurface crack growth is possible. Secondary bending will play a major role in driving the crack growth prediction for subsurface cracks. However, that secondary bending correction will be challenging to implement, as it will be determined not by the cracked geometry of the specimen local to the crack, but also to the geometry of the specimen as a whole, which will induce the secondary bending. Additionally, the effects of the delamination would need to be incorporated. Based upon these lacking features in the Rose model, its applicability to the current research is considered to be inappropriate.

2.4. Summary

To develop a predictive model for subsurface crack growth in Glare, the complexities involved must be accounted for. The physical system of fatigue in a fibre metal laminate is multivariate, dependent not only on the specimen geometry and loading, but also on the laminate construction.

Several models were evaluated for their applicability to the current research. They are outlined in Table 2.3. Based upon the evaluations of the models investigated, the models of Marissen, Burianek, Guo & Wu and Alderliesten all have aspects that are applicable to the current research.

Owing to the complexities of the physical environment studied in this research, the models discussed in this chapter that were empirical in nature^{22, 25, 27, 29} do not lend themselves to consideration in this research.

The approach of Marissen¹⁶ was the basis for many of the other models described here^{17, 19, 20}. Its basic premise of super positioning stress intensities to account for mechanisms effecting crack growth is logical. The stress intensity factor to account for fibre bridging reflects reality in that the stresses in his formulation act on the delamination boundary, rather than on the crack flank itself.

Burianek's¹⁹ use of finite element analysis was insightful, though a more accurate representation of the actual physical system than the two-dimensional model can provide is required. Aldersliesten's¹⁷ insights to delamination growth gave a first-time look at a formulation for the fibre bridging stress distributions based upon delamination fronts proposed from first principals, rather than empirical estimations. Guo and Wu's^{20, 21} numerical approach to calculate the fibre bridging stresses along a non-elliptical delamination front in an iterative fashion yielded remarkable potential in determining the changes in the stress distributions as cracks advance.

By focusing on the strengths of these approaches, support for the pursuit of a hybrid analytical/numerical model is gained. None of the models studied dealt with a part through crack, nor did any model consider a loading case of combined tension bending. The Rose model did deal with secondary bending, but its approach was not applicable to the current research. Finite element modelling is needed to gain insight into physical parameters not measurable experimentally – specifically the fibre bridging stress distribution. Using these results in an analytical framework similar to Marissen, Alderliesten and Guo and Wu, is expected to lead to a predictive model that can accurately describe fatigue crack growth in subsurface layers of Glare.

Table 2.3: Evaluation of fatigue crack growth models for Glare.

Model Author	Key Model Equation
<ul style="list-style-type: none"> • Type of Crack Modelled • Formulation 	<ul style="list-style-type: none"> • Aspects applicable to current research ○ Issues deemed inappropriate for current research
Marissen	$K_{ARALL} = K_{Al} + K_{ad}$
<ul style="list-style-type: none"> • Through • Analytical 	<ul style="list-style-type: none"> • Super positioning stress intensity factors to account for stress sources (far field, bridging) • Stress intensity factor formulation for bridging stresses acting on delamination front
Burianek	$\Delta K_{eff} = \Delta K_{applied} + \Delta K_{br}$
<ul style="list-style-type: none"> • Through • Mechanistic 	<ul style="list-style-type: none"> • Utilization of FEM to acquire information not accessible experimentally
Guo & Wu	$H_{i,j} \sigma_{br,j} = Q_i$
<ul style="list-style-type: none"> • Through • Analytical 	<ul style="list-style-type: none"> • Utilization of numerical solution to find fibre bridging stress distribution • Non-elliptical delamination front
Alderliesten	$S_{br} = H^{-1}Q$
<ul style="list-style-type: none"> • Through • Analytical 	<ul style="list-style-type: none"> • Utilization of numerical solution to find fibre bridging stress distribution • First-principals approach to predict delamination front shape
Toi	$\beta_{FML} = \frac{\Delta K_{Al}}{\Delta K_{FML}}$
<ul style="list-style-type: none"> • Through/Surf • Empirical 	<ul style="list-style-type: none"> ○ Empirical form makes model inapplicable to current research. ○ Dependence upon multiple parameters (appl stress, thickness, Glare grade, etc.) ○ Current research would add parameters (bending factor, ply depth, etc) making an empirical approach inefficient

Table 2.3 cont.: Evaluation of fatigue crack growth models for Glare.

Model Author	Key Model Equation
<ul style="list-style-type: none"> Type of Crack Modelled Formulation 	<ul style="list-style-type: none"> Aspects applicable to current research Issues deemed inappropriate for current research
Guo & Wu	$l_0 = \frac{\gamma^2}{1/F^2 - \gamma^2/F_o^2} (a - s)$
<ul style="list-style-type: none"> Through Phenom 	<ul style="list-style-type: none"> Empirical form makes model inapplicable to current research. Dependence upon multiple parameters (saw cut length, Glare grade, thickness, etc.) which makes an empirical approach inefficient Current research would add parameters to consider
De Koning	$K = \frac{4}{\sqrt{2\pi}} f\left(\frac{a}{w}\right) \left(\frac{\gamma\sqrt{\varepsilon}}{\bar{\sigma}}\right) S^2 \sqrt{t}$
<ul style="list-style-type: none"> Surface Empirical 	<ul style="list-style-type: none"> Need for empirical correction factors makes model inapplicable to current research. Factors dependent upon Glare grade, thickness, rolling direction Current research would add parameters to consider
Rose	$l_0 = \left(\frac{\sigma_0}{\sigma_\infty}\right)^2 \Lambda(1 + \Omega)$
<ul style="list-style-type: none"> Surface Parametric 	<ul style="list-style-type: none"> Secondary bending correction ill-formed for current research. Accounts for eccentricity due to crack only – no accounting for specimen geometry to induce secondary bending No accounting for delamination in model

2.5. References

- ¹ **Bannantine, J.A., Comer, J.J., Handrock, J.L.,** *Fundamentals of Metal fatigue Analysis*, Prentice-Hall. Inc., 1990.
- ² **Schijve, J.,** *Fatigue of Structures and Materials*, Kluwer Academic Publishers, 2001.
- ³ **Paris, P.C., Erdogan, F.,** *A Critical Analysis of Crack Propagation Laws*, Trans. ASME, J. Basic Eng., Vol. D85, 1963, pp. 528-534.
- ⁴ **Tada, H., P.C. Paris, G.R. Irwin,** *The Stress Analysis of Crack Handbook*, 3rd ed., The American Society of Mechanical Engineers, 2000.
- ⁵ **Vlot, A.,** *Glare – history of the development of a new aircraft material*, Kluwer Academic Publishers, 2001.
- ⁶ **Vlot, A., Gunnink, J.W.,** *Fibre Metal Laminates an Introduction*, Kluwer Academic Publishers, 2001.
- ⁷ **De Vries, T.J.,** *Blunt and sharp notch behaviour of Glare laminates*, PhD Thesis, Delft University Press, 2001.
- ⁸ **Homan, J.J.,** *Fatigue Initiation in Fibre Metal Laminates*, *International Journal of Fatigue*, submitted 2004.
- ⁹ **Beumler, T.,** *Flying Glare*, PhD Thesis, Delft University Press, 2005.
- ¹⁰ **Schijve, J.,** *Fatigue of Structures and Materials*, Kluwer Academic Publishers, 2001.
- ¹¹ **Kieboom, O.T.,** *Fatigue Crack Initiation and Early Crack Growth in Glare at Different Temperatures*, Masters Thesis, Delft University of Technology, 2000.
- ¹² **Papakyriacou, M., Stanzl-Tschegg, S.E., Mayer, H.R, Schijve, J.,** *Fatigue crack growth in Glare, role of glass fibers, Structural Integrity: Experiments, Models and Applications*, (Eds. K.-H. Schwalbe and C. Berger), Proc. ECF 10, EMAS, Warley, 1193-1199, 1994.
- ¹³ **Alderliesten, R.C.,** *Development of an empirical fatigue crack growth prediction method for the Fibre Metal Laminate Glare*, Masters Thesis, Delft University of Technology, 1999.
- ¹⁴ **Takamatsu, T., Matsumura, T., Ogura, N., Shimokawa, T., Kakuta, Y.,** *Fatigue crack growth properties of a GLARE 3-5/4 Fiber Metal Laminate*, *Engineering Fracture Mechanics* 63 253-272, 1999.
- ¹⁵ **Schijve, J., Van Lipzig, H.T.M., Van Gestel, G.F.J.A., Hoeymakers, A.H.W.,** *Fatigue Properties of Adhesive-Bonded Laminated Sheet Material of Aluminum Alloys*, *Engineering Fracture Mechanics*, 12 561-579, 1979.

- ¹⁶ **Marissen, R.**, *Fatigue Crack Growth in ARALL, A hybrid Aluminium-Aramid Composite Material, crack growth mechanisms and quantitative predictions of the crack growth rate*, PhD Thesis, Delft University of Technology, 1988.
- ¹⁷ **Alderliesten, R.C.**, *Fatigue Crack Propagation and Delamination Growth in Glare*, PhD Thesis, Delft University Press, 2005.
- ¹⁸ **Randell, C.E., Zwaag, S. van der**, *On Subsurface Crack Growth in Fibre Metal Laminate Materials*, Proceedings of the International SAMPE Technical Conference, Dayton, OH, 2003.
- ¹⁹ **Burianek, B.A.**, *Mechanics of Fatigue Damage in Titanium-Graphite Hybrid Laminates*, PhD Thesis, Massachusetts Institute of Technology, 2001.
- ²⁰ **Guo Y.J., X.R. Wu**, *A theoretical model for predicting fatigue crack growth rates in Fibre-reinforced Metal Laminates*, *Fatigue & Fracture of Engineering Materials & Structures*, **21** 1133-1145 (1998).
- ²¹ **Guo Y.J., X.R. Wu**, *Bridging stress distribution in center-cracked fiber reinforced metal laminates: modelling and experiment*, *Engineering Fracture Mechanics*, **63** 147-163 (1999).
- ²² **Toi, R.**, *An Empirical Crack Growth Model for Fiber/Metal Laminates*, Proceedings of the 18th Symposium of the International Committee on Aeronautical Fatigue, Melbourne, Australia, 899-909 (1995).
- ²³ **Elber, W.**, *The Significance of Fatigue Crack Closure*, Damage Tolerance in Aircraft Structures, ASTM STP 486, American Society for Testing and Material, Philadelphia, 230-242, 1971.
- ²⁴ **Gonesh, K.A.M.**, *Development of a fatigue crack growth model for surface cracks in GLARE*, Master Thesis, Delft University of Technology, 2000.
- ²⁵ **Guo Y.J., Wu X.R.**, *A phenomenological model for predicting crack growth in Fiber-reinforced metal laminates under constant-amplitude loading*, *Composites Science and Technology*, **59** 1825-1831 (1999).
- ²⁶ **Alderliesten, R.C.**, *Development of an empirical fatigue crack growth prediction model for the Fibre Metal Laminate Glare*, Master Thesis, Delft University of Technology, 1999.
- ²⁷ **De Koning, A.U., Schra, L.**, *Fatigue crack growth of part through the thickness cracks in Glare 3 and Glare 4B coupons*, NLR-CR-2000-078, 2000 (Restricted).
- ²⁸ **Homan, J.J.**, *Crack growth properties of thin aluminum sheets*, Delft University of Technology, Report BV2-01-16, issue 2, 2002.
- ²⁹ **Rose, L.R.F.**, *An application of the inclusion analogy for bonded reinforcements*, *International Journal of Solid Structures*, **17** 827-838, 1981.

3

Experimentation

Abstract – This chapter provides an overview of the experimental programs that provided the critical data on which to build the hybrid model described in this thesis, as well as the standard against which the model was validated. Development of the experimental fatigue specimen geometry is discussed, and the test specifications used to generate fatigue data. Inspection methods used to gather that fatigue data are described.



3.1. Introduction

Fuselage joints are exposed to a combined tension bending stress state due to the shift in the neutral line of the aluminum as it passes from one side of a joint to the other. For pressurized fuselages, many components are loaded in tension. Joints in the fuselage are also loaded in bending, as the neutral line must shift. This induced bending can increase the stress in the joint significantly.

The magnitude of the secondary bending is indicated by the bending factor, k_b , defined here as:

$$k_b = \frac{\sigma_{\max}}{\sigma_{nom}} \quad (3.1)$$

Where σ_{nom} is the nominal tensile stress in the far field away from the overlap, and σ_{\max} is the resultant maximum stress in the surface of the specimen due to the secondary bending.

A bending factor of at least 2.0 was targeted in this research to achieve bending stresses as significant as those that can be seen in fuselage joints. A bending factor of at least 2.0 also ensured that there was a significant difference in stress levels in each ply of the laminate. The tension-side surface ply of aluminum would have the highest resulting stress and would initiate a fatigue crack first. As the stress levels were lower for deeper plies in the laminate, fatigue cracks would initiate later, and grow at a slower rate, though the change in the neutral line as plies cracked did affect the crack growth rates of deeper plies. As deeper plies had progressively longer crack initiation lives, the crack tips would be a maximum distance from each other. This helped to ensure that each crack tip would have as minimal an influence on the surrounding plies as possible for finite element modelling purposes.

The test programs described here are focused on obtaining surface and subsurface crack growth data, as well as information regarding delamination growth around fatigue cracks in Glare 2A. Section 3.2 details the development of fatigue specimens targeted at achieving combined tension and bending stress states in a test section. Section 3.3 details fatigue testing conducted in a pure bending environment. Section 3.4 details standard and novel approaches used in this research to acquire subsurface crack growth data.

3.2. Milled Open Hole Tension Bending

Fawaz¹ developed the Open Hole Tension Bending (OHTB) specimen, shown in Figure 3.1, to generate a controllable combined tension and bending stress state within a specimen. The bending stress state is due to the secondary bending in the original design. Three individual plates of monolithic aluminum are bonded together with a high strength adhesive. The ratio of tension to bending stresses induced is controlled through the geometry of the overlap of the three pieces of the specimen.

Due to the ability to control the stress state in the specimen, and its ease of manufacture, a modification of the OHTB specimen was first chosen for this research. The modification involved using fasteners instead of an adhesive bond as shown in Figure 3.2. Unfortunately, cracks emanated from the fastener holes of all OHTB specimens, and subsequently, plastic bending deformation occurred in the overlaps. This made it impossible to safeguard the stress state in the test section of the specimen throughout the fatigue tests. As a result of the plastic deformation and the resulting drop in bending stresses during the fatigue testing, anomalous crack growth behaviour was observed.

3 Experimentation

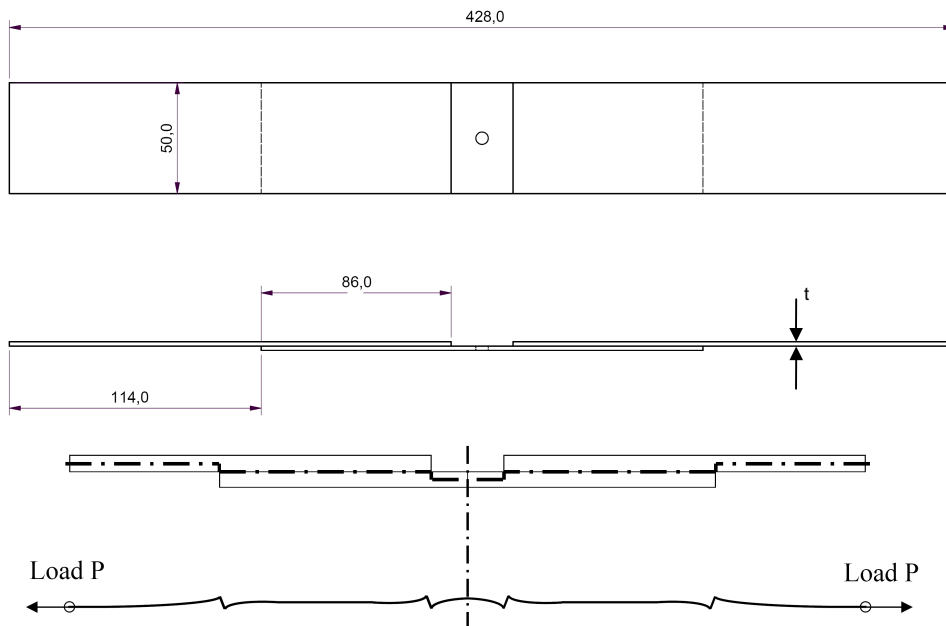


Figure 3.1: Original open hole tension bending (OHTB) specimen showing idealized shift in neutral line. From top to bottom: top view, side view, notional shift in neutral line position, and displacement of neutral line in loaded specimen.

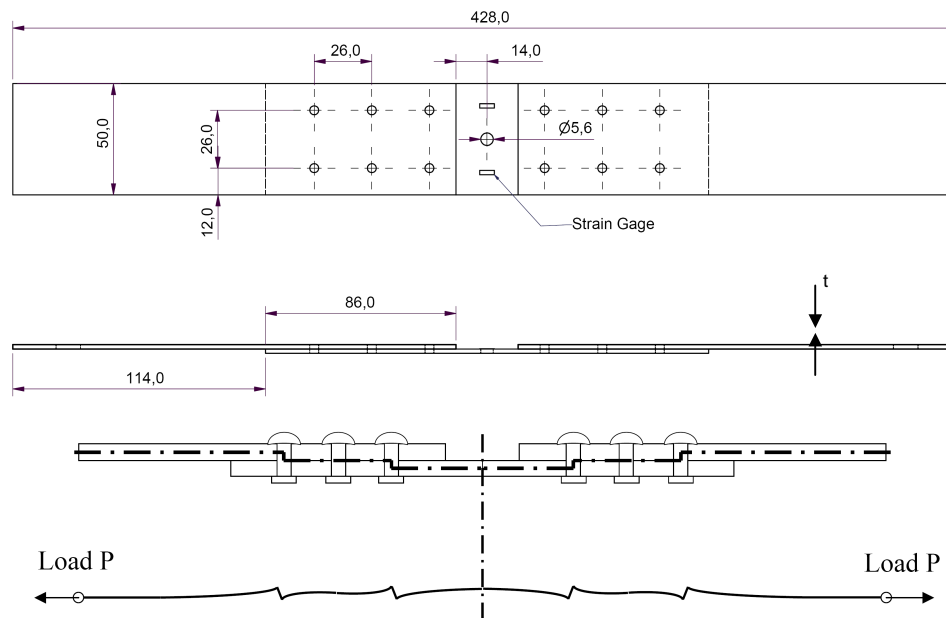


Figure 3.2: Modified OHTB Specimen showing idealized shift in neutral line. From top to bottom: top view, side view, shift in neutral line position, and displacement of neutral line in loaded specimen.

In order to overcome the issues associated with the bolted OHTB specimen, a new specimen geometry was required for which excellent control over the bending state as well as a relatively inexpensive manufacturing process for FML specimens could be realized. A combined tension-bending environment was still required, as was the ability to easily define the specimen to achieve predictable combinations of tension and bending. While other specimens are available to achieve a combined stress state^{2,3}, none fit the needs of the test requirements at reasonable costs as well as the OHTB specimen.

Previous works on secondary bending in Glare⁴ investigated modifying the overlaps of a Combined Tension Bending specimen. This was intended to reduce the stress riser at the overlap, while having minimal effect on the bending behaviour of the specimen. As shown in Figure 3.2, the shift in the neutral line, and hence, bending stress is locally abrupt if the stepped geometry for the overlap is used.

The configuration finally chosen in Figure 3.3 was a tapered overlap. This configuration made the shift of the neutral line more gradual – ensuring that the sharp stress riser inherent in at overlap of the non-tapered was mitigated. The tapered overlap made calculating the bending factor more challenging, though adequate analytical and numerical predictions exist to design the tapered overlaps into the specimen and still achieve the required stress state in the test section.

This specimen can be obtained by machining from a single large thickness plate, t_{plate} , or by assembling from three thinner plate sections as in the situation of the original Fawaz OHTB specimen. The bolted joints are thus eliminated, and the tapered sections avoid the abrupt thickness changes of the bonded OHTB specimen of Figure 3.1. The resulting thickness of the test section, $t_{test\ section}$, is fully adjustable in the specimen design.

The first tapered overlap design for the MOHTB specimen was made using the neutral line model (NLM). The NLM, developed by Schijve⁵, is a one-dimensional analytic formulation using beam theory to estimate the displacement of the neutral line. With the displacement along the length of the specimen known, the stresses can be calculated. This method has been validated with monolithic aluminum joints, though joints constructed with Glare pose challenges, including more complicated calculations to estimate the shift in the neutral line⁶. Additionally, the NLM does not take variability in stresses in the width direction into account.

Incorporating a taper in the overlap within the NLM model would have required extensive numerical approximations. Therefore, the NLM was used only as a first predictor of the stress state within the MOHTB specimen. The NLM was used to gain initial rough values for the stresses in a representative un-tapered configuration of a specimen. Any later conceived configuration refinement was then modelled in FEM to evaluate the stresses at the overlap to ensure no plastic deformations would occur, and in the test section to ensure required stress levels were met.

3 Experimentation

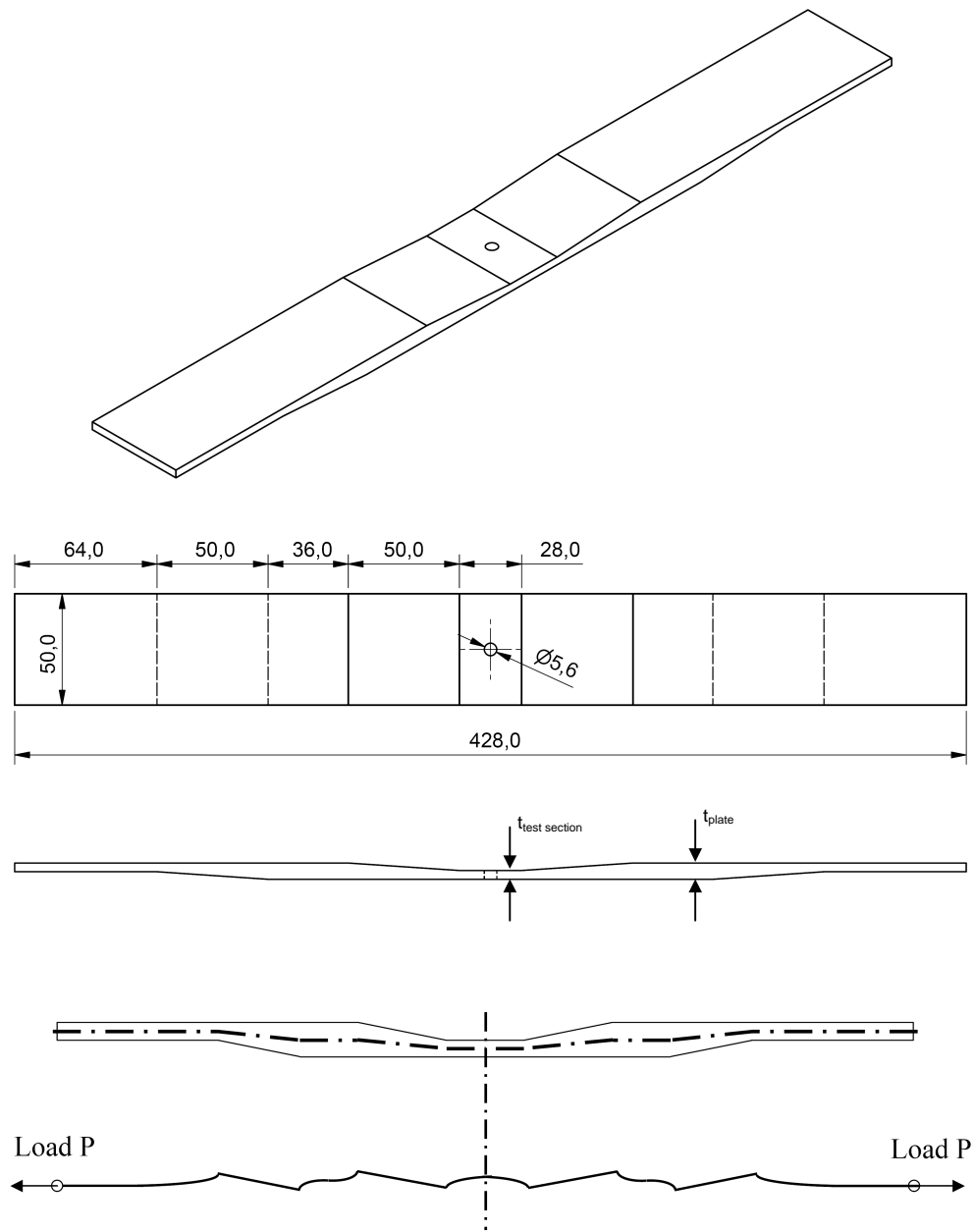


Figure 3.3: Milled Open Hole Tension Bending (MOHTB) Specimen showing idealized shift in neutral line. From top to bottom: isometric view, top view, side view, shift in neutral line position, and displacement of neutral line in loaded OHTB specimen.

A minimum bending factor of 2.0 was the target for the test sections in the new MOHTB specimens. This value represents severe secondary bending, but is not unheard of in aircraft fuselage joints, where the bending factor can reach values even greater than 2.5. The final taper dimensions chosen were a 50mm run-out to the end of the overlap on both sides. The resulting bending factor in the test sections of the specimens were evaluated to ensure the target value was met.

3.2.1. Specimen Configuration

The MOHTB specimen configuration shown in Figure 3.3 incorporated the taper as defined above, and eliminated the fasteners. All specimens were manufactured at Delft University of Technology. Specimens had widths of either 50mm or 100mm depending upon the predetermined crack length required. The length of the test section for each specimen was 28mm.

Each specimen was milled out of a single sheet of Glare 2A-11/10-0.4. The tapered overlaps were cut directly into the sheet. The original test matrix called for all specimens to have a 6/5 configuration in the test section. However, manufacturing variability resulted in specimens with either a 5/4 or a 6/5 configuration in the test section. This added variable in the lay up of the test section served to provide another data point of a different Glare configuration to compare an analytical model against. An open hole was milled in the center of the test section of each specimen. This open hole served as a fatigue crack initiation site, and enabled detection of subsurface fatigue crack initiation.

Selected specimens were instrumented with strain gages to ensure that resulting stresses generated in the specimen agreed with FE predictions. The strain gages were positioned on both the tension and compression sides of the specimens, at the edge of the specimens, in line with the center of the open hole in the test section. This was the same instrumentation configuration used for the OHTB specimens, in the test section at the same location adopted for the OHTB specimens, see Figure 3.2.

3.2.2. Test Matrix and Test Specifications

In total, eight specimens were fatigue tested to investigate subsurface crack growth. The specimen Glare type and configuration are given in Table 3.1 including targeted values for final surface crack length, a_{fin} , and estimated values of k_b . All tests were conducted on a 100kN servo-hydraulic, closed loop computer controlled MTS test machine. All specimens were tested at constant amplitude and stress ratio of $R=0.1$, at a frequency of 10Hz, at room temperature and laboratory humidity. A ninth specimen was damaged during testing and yielded no results.

Table 3.1: Test matrix of the Milled Open Hole Tension Bending Specimens.

Configuration	# Specimens	σ_{app} (MPa)	Width (mm)	a_{fin} (mm)	k_b
G2A-5/4-0.4	2	80	50	10.0, 15.0	2.7
G2A-5/4-0.4	1	80	100	30.0	2.7
G2A-5/4-0.4	2	100	50	15.0, 30.0	2.5
G2A-6/5-0.4	1	100	50	10.0	2.0
G2A-6/5-0.4	2	100	100	20.0, 40.0	2.0

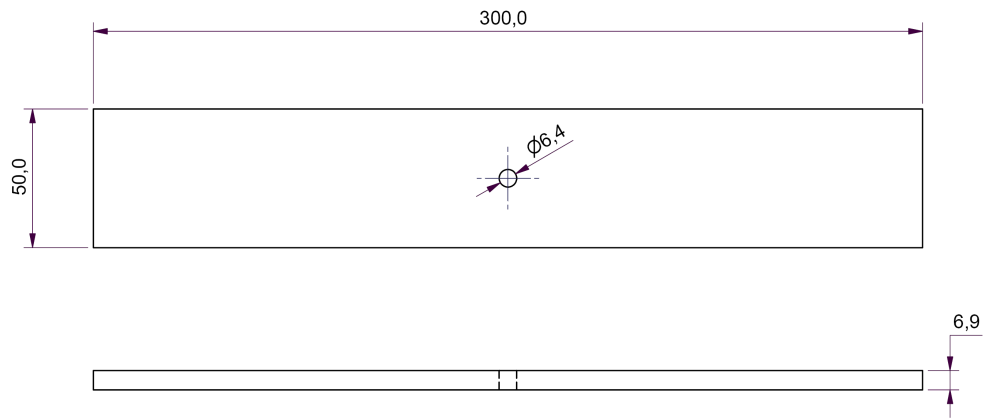
Two applied stress levels, σ_{app} were used in the test matrix, 80 and 100 MPa. Once surface cracks had grown in the specimens to preset lengths, a_{fin} , the specimens were destructively inspected to obtain crack length and delamination shape information. All inspections followed the procedures outlined in Section 3.4.1.

3.3. Four Point Bend

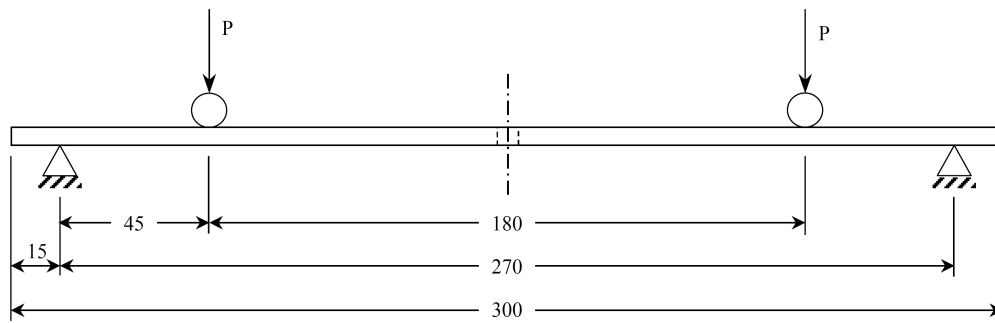
A series of four point bend tests were carried out on simple beam specimens of constant thickness to obtain surface and subsurface fatigue crack growth data on Glare 2A subjected to pure bending. To further validate the analytical model to be described in Chapter 4, this type of loading was chosen, although it is not typical for aircraft structures. If the model could adequately estimate crack growth rates in this specimen, then its potential for applications to other configurations than the MOHTB condition would seem justified.

3.3.1. Specimen Configuration

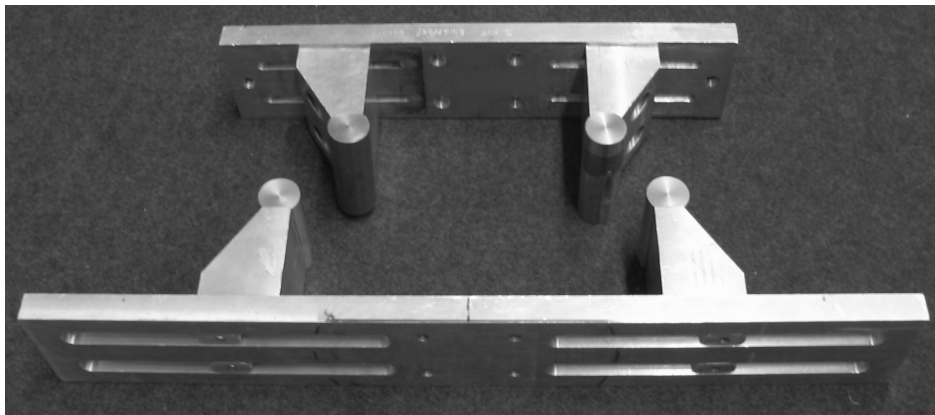
The four-point bend specimen is shown in Figure 3.4a. The test setup is shown in Figure 3.4b. The specimen selected was a Glare 2A-11/10-0.4. A thick laminate was chosen to maximize the distance from the neutral line to the outermost ply. By maximizing this distance, the stress gradient from the outer ply to the neutral line was made as smooth as possible when the specimen was under full bending displacement. Having several aluminum plies above the neutral line meant that those plies experienced tensile stresses in the test section ranging from a maximum at the surface, to zero at the center of the specimen. This helped to ensure a gradient of crack growth rates in the different plies, with the surface ply cracks growing the fastest.



a. Specimen configuration



b. Test Setup



c. Test fixture uninstalled from test machine. Supports are adjustable.

Figure 3.4: Four point bending specimen.

The specimens were 50mm wide and 300mm long. An open hole was carefully milled in the center of each specimen to induce crack initiation, and to allow for subsurface crack monitoring. The open-hole diameter was increased from 5.6mm as used in the MOHTB specimen, to 6.35mm. This was done to accommodate a prototype eddy-current probe. This probe is discussed in Section 3.4.2.

3.3.2. Test Specification

Four specimens were tested to various surface crack lengths. All tests were conducted on a 100kN servo-hydraulic, closed loop computer controlled MTS test machine. All specimens were tested under displacement control with an induced tensile stress, σ_{max} , of 200MPa on the tension side of the specimens. The induced tensile stress was monitored with strain gages installed on the surface of the specimens. The tests were conducted at a frequency of 5Hz, at room temperature and laboratory humidity. The tests were conducted according to standard test procedures for a four-point bend test⁷. For each sample a different number of cycles was imposed in order to create samples with different final crack lengths ranging from 8.0 to 15.0mm. This range of final surface and subsurface cracks would yield a sufficiently broad data set of crack length combinations to validate the model to be presented in Chapter 4.

Specimens were fatigued with a constant amplitude with an R-ratio of 0.1 for a preset block of 10,000 cycles. The four point bend test rig did not allow for direct observation of the fatigue cracks, as there was no room to fit the digital camera or endoscope. Therefore, at the end of each block of cycles, the specimen was removed from the test rig and installed in a measurement fixture.

In the measurement rig the specimen is loaded with a predefined three-point bending load, see Figure 3.5. The bending load used to open the fatigue cracks for measurement induced 90% of the maximum applied fatigue load, or 180MPa, measured with the strain gages on the specimens. The rig was essentially a simple three point bend apparatus that easily opened any fatigue cracks present. A digital camera was then used to measure the surface crack length. An optical endoscope was used to peer inside the open hole of the specimen to discern if fatigue cracks had formed in any subsurface ply. These cameras are detailed in Section 3.4.1. Specimens were then removed from the measurement rig and an eddy current probe was used to try and determine if fatigue cracks had formed in subsurface aluminum plies, as described in Section 3.4.2. Following crack measurements, the specimen was reinstalled in the test rig and fatigue cycling continued.

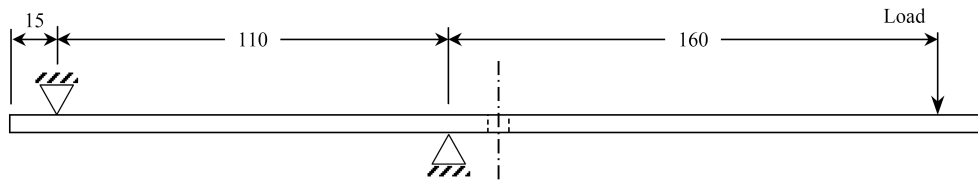


Figure 3.5: *Measurement fixture setup for measuring cracks from four point bend tests.*

Once the surface crack was grown to the assigned length, the specimen was destructively inspected to obtain fatigue crack lengths and delamination shape information as outlined in Section 3.4.1.

3.4. Subsurface Crack Growth Measurement

3.4.1. Optical and Destructive Inspection

An AIX MX5 digital camera⁸ was used to measure the surface crack length, yielding well-defined pictures such as shown in Figure 3.6. This camera was mounted on a digitally controlled 3-axis translation table to accurately measure the surface crack lengths. Surface crack lengths are accurate to 0.01mm.

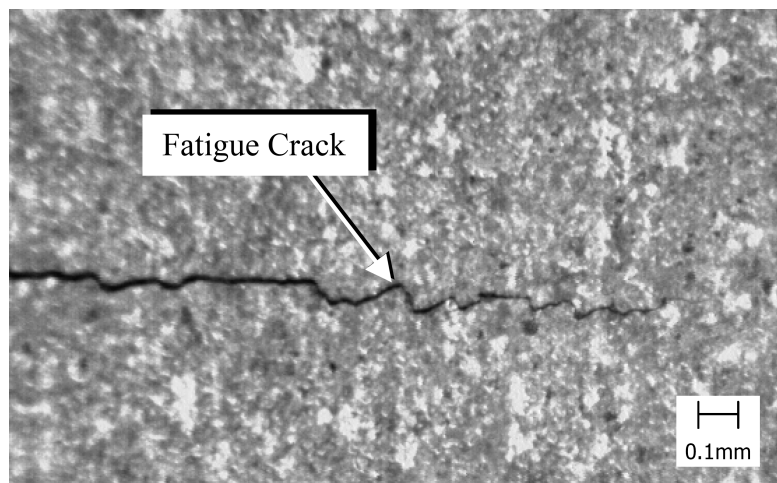


Figure 3.6: *Typical digital microscope view of surface cracks.*

An optical endoscope was used to determine subsurface crack initiation. The magnification of the endoscope was sufficient to discern if fatigue cracks had formed in any subsurface ply as shown in Figure 3.7. Data taken at the end of each block of cycles included number of cycles, surface crack length, and whether a

subsurface fatigue crack had formed and in which ply. Inspections were made at every 5000 or 10000 cycles, depending on the specimen. This placed the accuracy of the measurements of the cycles to crack initiation in any ply at 2500 or 5000 cycles.

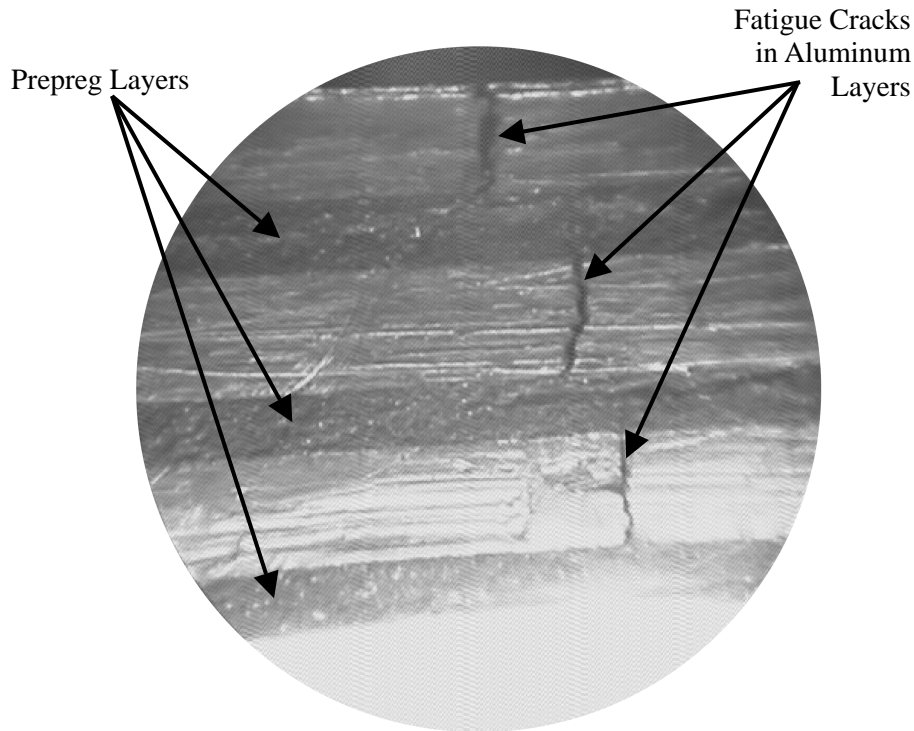


Figure 3.7: *Typical endoscope perspective of subsurface cracks on interior of the open hole.*

Once a surface crack had grown to its preassigned length, the fatigue test was stopped and the specimen was destructively inspected. To destructively inspect the specimens, they were first statically failed by applying a tensile load large enough to pull the specimen apart. If the specimen still had enough residual strength left to withstand the maximum load capacity of the test machine, then the laminate was cut along the centreline from the outer edge in to within approximately 5.0mm of the tip of the surface cracks. The static failure of the specimen started at the tips of the fatigue cracks and continued generally along the centreline of the specimens to the outer edges. This process exposed the crack faces along the centreline of the specimens. While the crack faces were exposed, the failed glass fibres made detailed measurements of the crack lengths impossible. Additionally, no information could yet be gained about the delamination zone, which was still encased in the laminate. The glass fibres needed to be separated from the aluminum plies for measurements to be made.

One possible method to separate the aluminum from the glass fibres is to chemically etch the aluminum plies away. This method was not used as all crack length data is lost when the aluminum etches away, and this crack length data was of prime importance for the research. The main advantage of etching is that it gives a good indication of the delamination zone, as the etching process leaves a definitive etch mark in the prepreg layer where the aluminum was delaminated from the prepreg.

In the method used for this research, the specimens were placed in an oven at 350 degrees Celsius for four hours to slowly burn away the adhesive in the prepreg layers. The aluminum layers were then free for inspection. Crack lengths in each layer were then measured with an optical microscope, and average crack growth rates were calculated using the initiation point derived from the endoscopic measurements.

By growing surface cracks to different final lengths in each type of fatigue specimen, differing lengths of subsurface cracks were generated. By plotting the data from the various samples on a single graph, a more complete da/dN curve could be drawn for each type of specimen.

Delamination zone size measurements were also made on the burned specimens. If the fibres in the prepreg layer next to an aluminum ply were perpendicular to the fatigue crack, the burning process also left a scorch mark on the aluminum where the prepreg was delaminated from the aluminum. These marks varied in intensity, with most being easy to obtain precise measurements of the delamination size and shape. However, in some instances, the marks were quite faint making the measurements difficult for those delaminations. For fibres running parallel to the fatigue crack, as on one side of an aluminum ply in a Glare 3 specimen, the delamination-scorch marks left on the aluminum were very difficult to see.

3.4.2. Eddy Current Trials

The eddy current non-destructive test uses the physical phenomenon of electromagnetic induction, which is the interaction of a magnetic field with an electrically conductive object. It occurs when a changing magnetic field is present around a conductive object, like the aluminum layers in Glare. In an eddy current probe, the magnetic field is generated by passing alternating current through a conductive coil Figure 3.8a. If the coils are brought near a conductive material, and the coil windings are parallel to the material's surface, then the alternating magnetic field penetrates the object. This penetration will induce currents in the material that flow in circular loops perpendicular to the magnetic field. These are eddy currents, and they generate their own secondary magnetic field that is in opposition to the primary field generated by the coil.

When eddy currents are disturbed by the presence of a flaw in the surface of the conductive material, Figure 3.8b, then the circular loops of flow change shape. This

change of flow path of the eddy current changes the secondary magnetic field. As the secondary field is in opposition to the primary field, any change in the secondary field will affect the primary field. These changes result in changes in impedance in the coil. The coil then produces a voltage according to the change in impedance, which can be measured by a voltmeter.

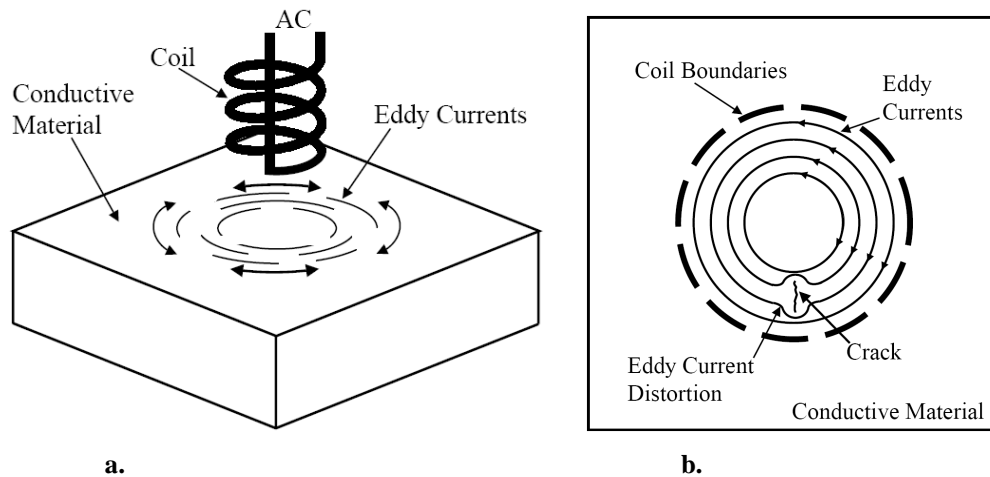


Figure 3.8: Eddy currents in conductive material. a. Coil orientation. b. Defect interfering with normal path of eddy currents.

There are several parameters that affect the performance of an eddy current probe⁹. Of interest in this discussion is the coil size and shielding. The coil diameter has an important influence on the primary magnetic field; the depth of penetration into the conductive material is directly proportional to the diameter of the coil, while the sensitivity of the probe to defect size is inversely proportional to the coil diameter. The primary magnetic field size generated by a probe starts with the same diameter as the core of the coil in the probe. This field then expands in a conical shape. Including shielding around the coil can narrow the expansion of the field – much like shining light through a pinhole. Shielding the coil with conductive or magnetic material can increase the penetration of the primary field into the conductive material, and at the same time focus the primary field to improve the sensitivity to smaller defects.

To inspect for the presence of cracks in the individual plies of aluminum initiating from the open hole in the specimens, a bolthole eddy current probe was used. This configuration of probe has the coil oriented such that the surface of the conductive material being inspected is the hole wall.

For inspecting a part constructed of Glare, the laminated structure poses a significant challenge. Any defect in one ply of aluminum tends to be seen by the probe as

extending to adjacent plies, as the width of the electromagnetic field generated by the coils in the probe head is larger than the individual aluminum plies in the laminate. For instance, if a fatigue crack is in the surface layer, the probe may see that crack even as it is inspecting the second or third layer, as the electromagnetic field generated shines out in an arc.

For this application, a smaller set of coils was required to focus the arc to the width of just one aluminum ply. The trial was conducted on the 4 Point Bend specimens detailed in Section 3.3 using a Nortec 19E Eddy Current Tester fitted with a prototype Rohmann¹⁰ spinning bolthole non-contact probe. Typical bolthole probes have coil diameters of approximately 1.0mm. The prototype probe had a coil diameter of 0.3mm. The proprietary metal shielding around the probe was also increased to further focus the field. This generated a field narrow enough to discern defects in one cracked aluminum ply alone. The penalty for this narrow field was very shallow penetration. This was not an issue for this test, as only the presence of a crack at the hole wall was required for detection, and minimal depth of penetration was required.

This probe had an external probe head diameter of 6.2mm, which drove the diameter of the open hole in the fatigue specimens. The probe operated in a frequency range of 0.5-2.0MHz. A spinning bolthole non-contact probe is typically used to inspect individual fastener holes with the fastener removed. The probe is attached to a stepper motor and is rotated at approximately 100 RPM. The non-contact probe travels along the surface of the wall of the hole, and any defects in the wall register as an induced change in the electromagnetic field generated by the probe.

The physical condition of subsurface cracks present in Glare, are illustrated in Figure 3.9. Results of the eddy current trial are shown in Figure 3.10 a-d. The horizontal axis shows the angular placement of the crack along the open hole. The angular reference had 0 and 180 degrees pointing in the loading direction, and 90 and 270 degrees aligned with the fatigue cracks. This set of data represents the right hand crack set on the 4 Point Bend specimen, 4PtBnd-02, which lie at 90 degrees for the measurements. The y-axis indicates the vertical position of the probe with respect to the surface.

These figures clearly show the formation of fatigue cracks in different layers as the fatigue test progressed. The resolution of the probe was such that cracks that formed on one layer could be attributed to another layer as well. However, the fact that the fatigue cracks in different layers did not form at the same angular position in the hole, as typified in Figure 3.9, meant that the different cracks could be distinguished with the eddy current probe. If the cracks had formed at the same angular position for two layers, then distinguishing them with the probe would be very difficult without further focusing of the electromagnetic field generated by the probe.

Table 3.2 shows surface crack length data and subsurface crack detection data. If a crack in a subsurface ply had been detected with the optical endoscope, then an “x” is shown in the data column, else a “0” is shown. Comparing the tabular data to the eddy current graphs shows that the eddy current detected cracks in the aluminum plies prior to detection with the digital microscope and the optical endoscope. For a crack detected in any one ply, cracks were registered in adjacent plies. This supports the idea that the focus of the probe was wide enough to look at one ply and see a crack in an adjacent ply. If the probe depth was aligned with the middle of a ply, however, the probe typically only detected cracks in that ply. With this tool, crack initiation in subsurface plies could be observed with both the eddy current probe and with the optical endoscope. This helped to more accurately capture the crack initiation lives of subsurface plies.

With the methodologies described in this chapter, we now have a set of tools to reliably measure surface and subsurface fatigue cracks accurately.

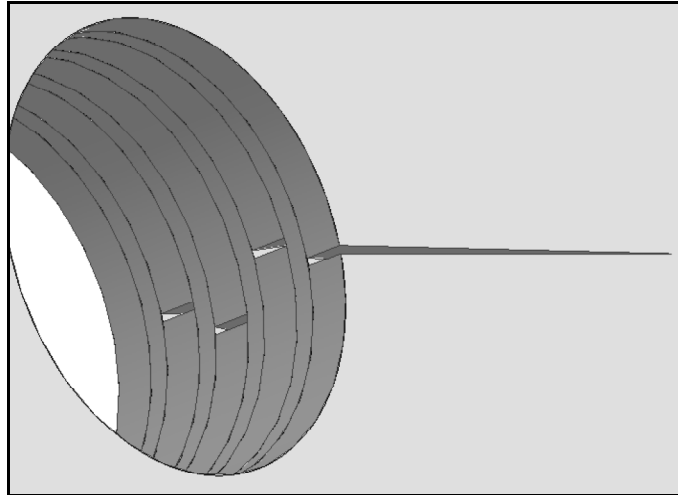


Figure 3.9: Typical angular placement of fatigue cracks in multiple layers of an FML emanating from an open hole. Fatigue cracks shown running in the 90-direction, corresponding to data shown in Figure 3.10.

Table 3.2: Crack data from optical sources. a_1 is the surface crack, a_2 is the 2nd layer, and a_3 is the 3rd layer. “x” indicates a subsurface crack was detected with the endoscope.

N (kcycles)	a_1 (mm)	a_2 (mm)	a_3 (mm)
70	0.0	0	0
110	0.0	0	0
190	7.8	0	0
220	8.5	x	0
380	14.5	x	x

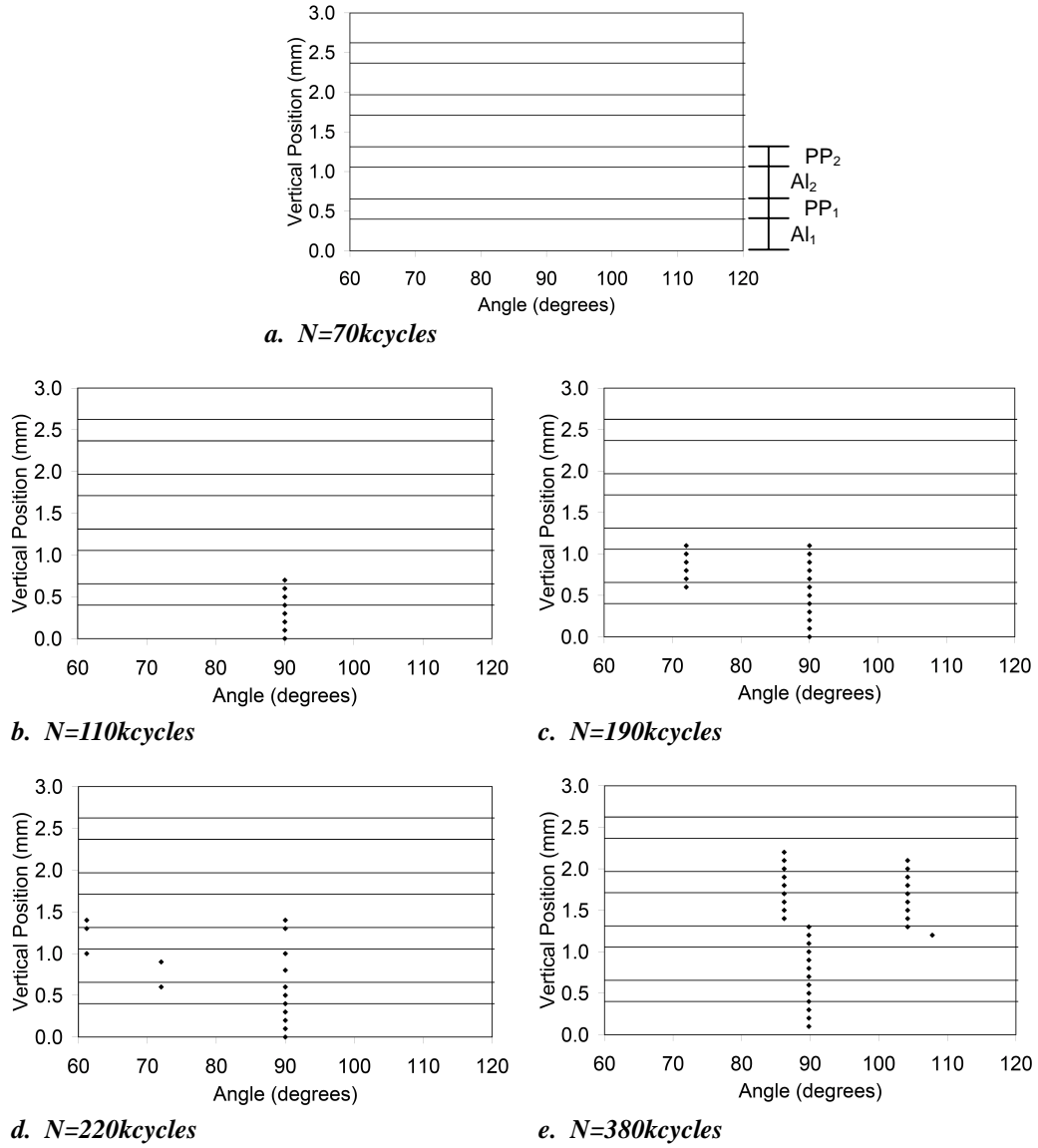


Figure 3.10: Eddy Current results for different numbers of fatigue cycles. Vertical position in open hole indicated on vertical axis, where $y=0$ corresponds to the surface loaded in tension. Horizontal axis indicates the angular position around the open hole, with the fatigue cracks running in the 90 and 270 directions (see Figure 3.9).

3.5. References

- ¹ **Fawaz, S.**, *Fatigue Crack Growth in Riveted Joints*, PhD Thesis, Delft University Press, 1997.
- ² **Nam, K. W., Ando K., Ogura, N., Matte, K.**, *Fatigue Life and Penetration Behaviour of a Surface-Cracked Plate Under Combined Tension and Bending*, *Fatigue and Fracture of Engineering Materials and Structures*, **17** (1994): 873:882.
- ³ **ASTM E647-95a**, *Standard Test Method for Measurement of Fatigue Crack Growth Rates*, Annual Book of ASTM Standards, American Society for Testing and Materials, 1995.
- ⁴ **Pellenkoff, F.**, *Secondary Bending in Glare*, Masters Thesis, TU Delft, 2000.
- ⁵ **Schijve, J.**, *Some elementary calculations on secondary bending in simple lap joints*, NLR TR 72036 U, National Aerospace Laboratory NLR, 1972.
- ⁶ **De Rijck, J.J.M.**, *Stress Analysis of Fatigue Cracks in Mechanically Fastened Joints*, PhD Thesis, Delft University Press, 2005.
- ⁷ **ASTM E855-90**, *Standard Test Methods for Bend Testing of Metallic Flat Materials for Spring Applications Involving Static Loading*, Annual Book of ASTM Standards, American Society for Testing and Materials, 1995.
- ⁸ **De Vries, T.**, *Blunt and sharp notch behaviour of Glare laminates*, PhD Thesis, Delft University Press, 2001.
- ⁹ **Borsboom, C.**, *Eddy Current Testing of Fibre Metal Laminates*, Report TD-R-93-008, Structural Laminates Company, 1993.
- ¹⁰ **Gans, M.**, *Endabnahmeprotokoll*, Report FB-BM-010-R00, Rohmann GmbH, 2004.

Development of Analytical / Numerical Crack Growth Model

Abstract – This chapter details a hybrid analytical/numerical crack growth model developed for surface and subsurface fatigue crack growth in Glare 2A fibre metal laminates. The construction of stress intensity factors accounting for far field stresses and the effects of fibre bridging are explained. The process of extracting fibre bridging stress distributions from finite element analysis is shown. These distributions are then expressed with mathematical approximations for insertion into the stress intensity factors. These factors are then used in a Paris law crack growth model. Details of the process for numerically calculating the crack growth rates are shown.



4.1 Introduction

To achieve the research goal of accurately predicting fatigue crack growth in surface and subsurface plies of Glare fibre metal laminates, a hybrid analytical/numerical model was developed. This chapter details the development of that model by identifying those parameters important in the fatigue phenomenon, and the approach to modelling them.

The choice in the approach to modelling fatigue crack growth identifies the parameters that must be defined. This research takes as a starting point the approach of Marissen¹, as discussed in Chapter 2. Two principal assumptions were made in order to justify the use of Marissen's approach. The first assumption was in applying linear elastic fracture mechanics (LEFM) to crack growth in Glare. As

LEFM is based upon the theory of elasticity, assumptions of small displacements and general linearity between stress and strains are also carried along. Past research^{2, 3, 4} has shown that these assumptions are justified for Glare when the effects of the presence of the glass fibres and delaminations are accounted for.

The second important assumption is that the Paris relationship⁵ between the stress intensity factor and crack growth rate for thin monolithic aluminum alloys^{1, 6} is applicable to the even thinner sheets of aluminum in Glare. The presence of the glass fibres does not change the nature of the aluminum sheets, but only the stress intensities the aluminum plies experience. The fundamental Paris relationship is written as:

$$\frac{da}{dN} = C(\Delta K)^m \quad (4.1)$$

where C and m are material constants of the aluminum sheets in Glare, and ΔK is the stress intensity range. The stress intensity has the general form

$$K = f(g)\sigma\sqrt{\pi a} \quad (4.2)$$

where σ is the remote applied stress in the aluminum layers, a is the crack length, and $f(g)$ is a geometry correction factor.

To find the stress intensity range in Glare, the complexities of the stress state around a crack must be accounted for. These complexities are condensed to two primary sources of stress: the stress generated due to the applied load, the specimen geometry, and the presence of a fatigue crack; and the stress resulting from the glass fibres bridging the fatigue crack^{1, 3, 4}. These two sources are presented as two separate Mode I stress intensity factors, $K_{farfield}$ and $K_{fibrebridging}$. The Principle of Superposition⁷ is used to incorporate these two disparate stress intensity factors into a single Paris relationship to represent fatigue crack growth in Glare.

$$K_{Glare} = K_{farfield} + K_{fibrebridging} \quad (4.3)$$

Recalling the process of crack growth in Glare, the glass fibre plies delaminate in a controlled and reproducible manner away from the vicinity of a fatigue crack as it grows. As the fibres are not in contact with the aluminum at the crack flank, the fibre bridging stresses act away from the crack at the delamination front. To obtain values for $K_{fibrebridging}$, the fibre bridging stress distribution and delamination shape must be known. The fibre bridging stresses are then applied at the delamination front.

For this research, the stress state of the specimen is fairly complex. As the research was to investigate subsurface fatigue crack growth in Glare, the decision was made

to induce an environment of combined tension and bending. This decision was made for two reasons. The first reason was to more accurately mimic the stress state in an aircraft joint, which can experience significant secondary bending. The second reason was to induce different crack growth rates in the different layers of aluminum in the laminate. With the bending included, a faster crack growth rate was expected for the surface ply on one side of the specimen. Crack growth rates were expected to decrease for deeper subsurface plies – reaching a minimum on the opposite surface ply, or at the deepest layer where a crack can still nucleate and grow.

Additionally, all specimens featured an open hole – both to induce fatigue cracking in the test sections of the specimens, and to facilitate the monitoring of fatigue crack initiation in subsurface plies. The open hole was a stress concentration that further complicated the stress state within the test sections of the specimens.

With the inherent complexities of the fatigue crack environment in an FML, the decision was made to develop the model initially for Glare 2A laminates only. This decision meant that only the simplest Glare configuration would be used to investigate this modelling approach to subsurface fatigue crack growth. As the model is physically-based, and not phenomenologically-based, if the approach was successful, it would be expandable to other Glare configurations.

As the formulation of an expression for the stress intensity factor due to fibre bridging, $K_{fibrebridging}$, was a key requirement for this research, insights to its nature were required. In order to gain knowledge of the fibre bridging stress distributions within a cracked Glare laminate, finite element (FE) analyses were used, as actual bridging stresses in the glass fibres cannot be measured experimentally.

The stress distributions extracted from the FE analyses were used as an input to an analytical crack growth model. These data were incorporated into a stress intensity factor formulation, which is an accurate analytical description of the system. The final step in developing the model was to incorporate the two stress intensity factors into a Paris relation and generate crack growth curves.

This hybrid approach, combining FEM and an analytical approach, was chosen as it combines established methodologies for describing fatigue crack growth with flexible and reproducible means of gaining numerical approximations of physical data within the laminates that, to date, can be acquired no other way. Using FEM to acquire data meant that variations to the materials, laminate, and specimens could be accommodated.

This chapter is divided into three general sections. Section 4.2 details the finite element modelling that was required to determine various parameters affecting fatigue crack growth in Glare. Section 4.3 describes the analytical models for the stress intensity factors that contribute to the Paris law formulation for the fatigue crack growth. Section 4.4 illustrates the hybrid nature of this modelling approach by

taking the FE results and incorporating them numerically into the analytical stress intensity factor solutions, and then calculating crack growth rates.

4.2 Finite Element Modelling

Based upon the results of the FEM package trials detailed in Appendix A, ABAQUS™ was selected to model the Milled Open Hole Tension Bending (MOHTB) specimen. ABAQUS was selected due to its ability to accurately estimate the non-linear response of Glare subjected to combined tension and bending. All bending problems are by nature non-linear, and the laminated structure of Glare made the secondary bending calculations required all the more complex. ABAQUS versions 6.3 through 6.5 were used for the research.

The strategy used to acquire fibre bridging stress distributions through finite element modelling followed three general stages: undamaged model analysis, damaged model analysis, and data extraction. The first stage ensured that the global model was an accurate representation of the physical specimen. The second stage introduced fatigue cracks and delaminations of well-selected dimensions to the model in an orderly sequence to allow for the third stage, data extraction. To extract the fibre bridging stress information from the damaged model analyses, strains were recorded from the models for incrementally imposed fatigue damage. By incrementally imposing the damage, two contributors to the total strain in the delaminated fibres of the model can be identified.

- The first contributor is the strain in the fibres due to applied loads and the resultant strains in the fibres due to damage away from the ply of interest.
- The second contributor is the strain due to the fibres bridging the fatigue crack in the ply of interest. This second contributor is the value of interest in the research, as this acts to restrain fatigue cracks from growing.

The following sections detail the development of each of these stages of FE modelling.

4.2.1 Uncracked Model Analysis

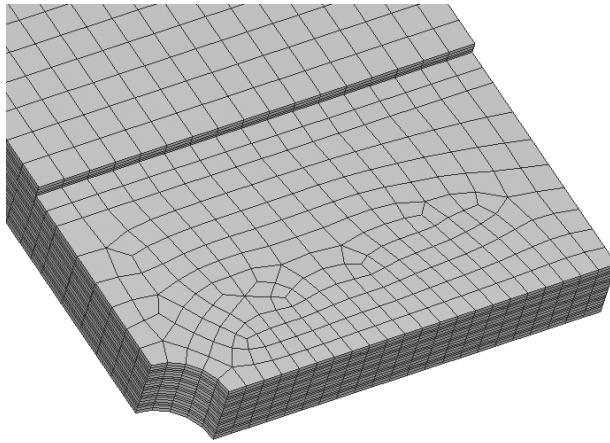
An example of a MOHTB model and its coordinate system is shown in Figure 4.1. One quarter of the specimen was modelled, with symmetry constraints applied along the length (y-direction) and width (x-direction) of the model. An ABAQUS C3D8R-type element was used for this research. The C3D8R element is a hexagonal reduced integration element with hourglass controls built in⁸.

Reduced integration elements use a lower-order integration when forming the element stiffness matrix. It uses a lower-order integration by reducing the number of

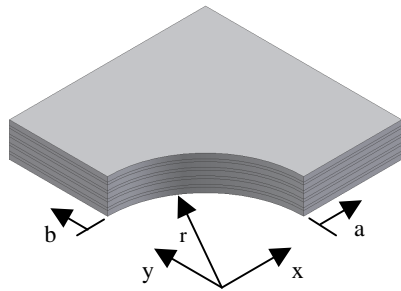
integration points within an element that are used to form the element stiffness matrix. The benefit of using reduced integration elements is the reduction in the number of calculations required due to the reduction in the size of the matrix. This reduction is not performed on the mass or loading matrices.

Hourglass controls are needed for reduced integration elements, as it is possible for them to distort such that the strains calculated at the integration points are all zero. If this spurious distortion occurs, then uncontrolled distortion of the entire model mesh can occur. This happens as the program attempts to balance strains between elements. Hourglass controls work to avoid these zero-strain distortions within an element.

Each ply of the Glare laminate was modelled individually. The tapers in the MOHTB specimen were not modelled precisely, but rather were approximated by a stepped-taper. The lengths of plies in the taper were decreased appropriately to achieve this stepped-approximation of the taper. This was done as a trade off of the benefits of modelling the taper precisely versus the benefits of the stepped-approximation. As the region of the overlaps was not a region of interest for extracting model data, the stepped-taper approximation was deemed sufficient.



a. Detail of MOHTB specimen.



b. origin convention.

Figure 4.1: *a. Typical FEM mesh of uncracked MOHTB specimen G2A-5/4-0.4. b. Origin convention used to define crack and delamination measurements.*

Material properties were assigned to each ply of the model. As each specimen was constructed of Glare 2A, only two material properties definitions were required – one for the aluminum plies, and one for the glass fibre prepreg plies. The glass fibre prepreg plies are all orientated with the fibres running in the y-direction for these Glare 2A MOHTB specimens. The material definitions are shown in Table 4.1. The aluminum was modelled as an elastic isotropic material. The glass fibre prepreg was modelled as an elastic orthotropic material. Residual stresses due to the curing of Glare are not included in these formulations. No plasticity was included in the models.

Table 4.1: Finite element model material property definitions⁹.

Material	E_1 (MPa)	E_2 (MPa)	E_3 (MPa)	ν_{12}	ν_{23}	ν_{31}	G_{12} (MPa)	G_{13} (MPa)	G_{23} (MPa)
Aluminum	72000	72000	72000	0.33	0.33	0.33	N/A	N/A	N/A
Prepreg	54000	9400	9400	0.33	0.0574	0.0574	5548	5548	5548

To assemble the full laminate, individual plies were bound together using tie constraints, which in effect, models a perfect adhesive. Tie constraints will not fail regardless of the loads applied. This is not realistic, for in Glare the act of delamination through adhesive failure plays a crucial role in its stable fatigue characteristics. For undamaged regions, however, the tie constraint was a simple and effective means of constructing the laminates.

The model was loaded by applying uniform stress to the end of the specimen. Due to the overlaps in the specimen, secondary bending was induced, which resulted in a combined tension and bending stress state in the test section. In the region where the far field stress was applied to the model, a single node was constrained from moving out of plane to avoid rigid-body displacements of the model.

A convergence study was conducted to confirm that the element size used resulted in consistent solutions. The model used for the convergence study was a MOHTB model constructed of G2A-6/5-0.4. Increasing mesh densities were analyzed to evaluate the displacements and stresses in the model, focusing on the appropriate global mesh size for the majority of the specimen. A convergence study focusing on the test section is discussed in Appendix B. Results showed that a global element size of 2.5mm, with local refinement in the test section yielded good results. Comparisons of the resulting stresses in the test section of the model at the same location as experimental strain gage data taken at the specimen surface yielded less than 5% error in the FEM prediction. The final models contained up to 50k elements, with approximately 220k degrees of freedom.

4.2.2 Cracked Model Analysis

With an uncracked model of the Glare MOHTB specimen in hand, cracked models were constructed. To model cracked specimens, both the cracks in the aluminum and the delaminations of the glass fibre prepreg had to be introduced.

A cracked configuration of the model was built based upon experimental observations that gave crack and delamination data for a given instant in the fatigue life of a specimen. From these cracked models, data was taken that gave insight into the stress in the Glare at that snapshot in the fatigue life of the specimen. The FE model was a static analysis – so the cracks in the model did not initiate or propagate.

As each specimen was taken to a different surface crack length, a range of damage distributions was acquired – with subsurface crack lengths increasing for increasing surface crack length. This allowed for multiple FE models to be run for progressively increasing damage to the models. By taking these modelling snapshots in time as damage progressed in the specimens, the changes in fibre bridging stress could be tracked and associated with a given damage scenario. Crack surveys were taken of each specimen to determine the length of cracks in each aluminum layer. Typical data are shown graphically in Figure 4.2, showing the crack length in the various layers with progressive loading cycles and resulting crack length increases. Complete data sets for all specimens tested are given in Appendix D.

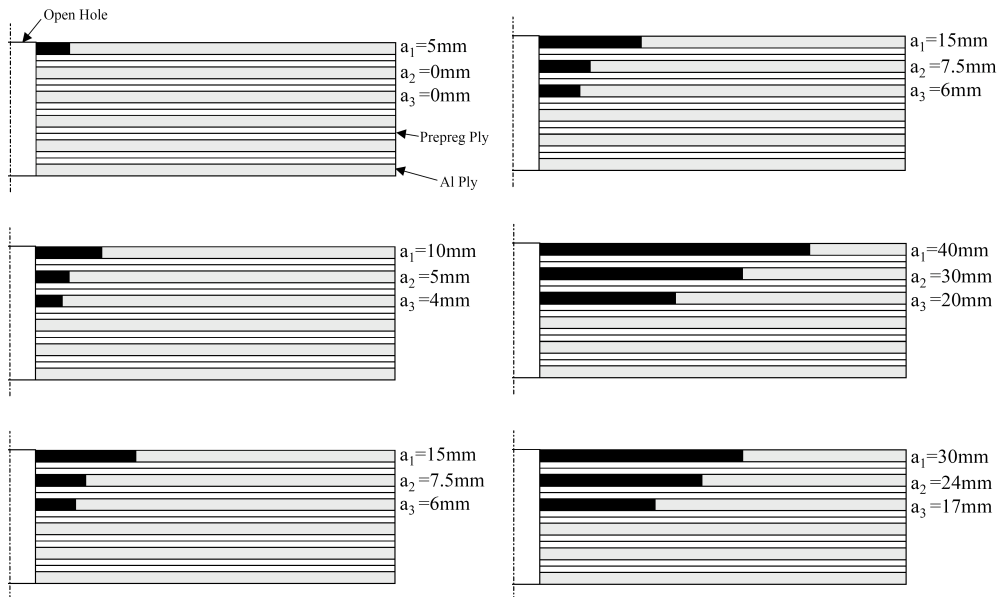


Figure 4.2: Typical fatigue crack distributions for Glare 2A-6/5-0.4 specimens tested at $\sigma_{app}=100\text{MPa}$ at various stages of crack growth. Only one side of the specimen is shown.

Similar to the crack surveys described above, delamination surveys were also taken of the specimens after tear-down. An optical microscope was used to record the delamination heights along the crack lengths for each cracked aluminum ply in each specimen. This data is shown graphically in Figure 4.3, for increasing crack length values and a number of loading and sample constructions.

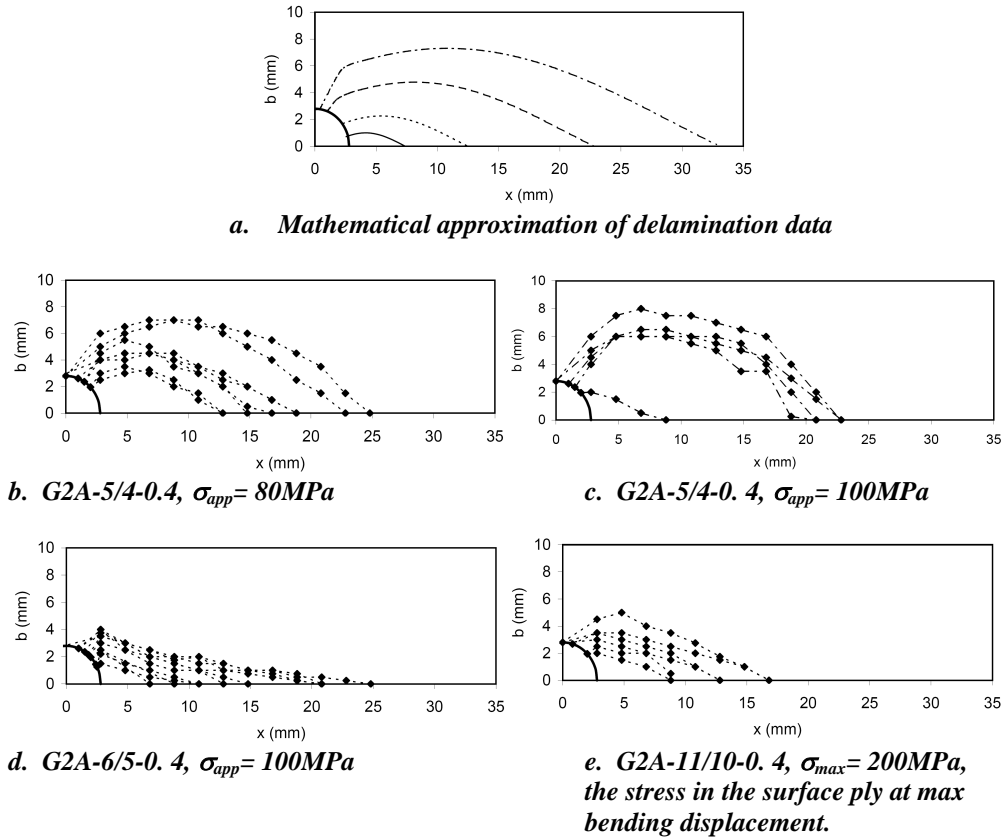


Figure 4.3: Glare 2A delamination shape survey. Each curve represents one ply of one specimen. Data taken from multiple specimens and ply levels. Each specimen was fatigued to a different number of cycles. Only one side of the specimen is shown.

From the experimental investigations, the delaminations were found to start with a triangular shape up to a crack length of approximately 5mm, then to take a cosine shape for longer cracks. This is an assessment of all delamination data available, and variability in the delamination shapes was apparent. The delaminations could be described with anything between a triangle and an ellipse, and Alderliesten⁴ found through analytical modelling that the delaminations indeed tend towards a stable shape in this regime.

The shape of the delamination zone was defined in this research using Equation 4.4, with the height of the zone, b , in the y -direction. The delamination shape curve started at the intersection with the open hole, and ended at the crack tip. This formulation for the delamination shape is a curve fit for all delamination data.

$$b(x) = \left(0.065 + 0.187 \cos \left(2.53 \frac{x}{a+r} - 0.676 \right) \right) a \quad 0 \leq x \leq a+r \quad (4.4)$$

For cracks longer than 20mm, Equation 4.4 does not intersect the open hole. However, experimental data shows that the delamination front always intersected the open hole. Therefore, the delamination approximation was modified for longer cracks by forcing the delamination front to cross the open hole boundary. This was done for portions of the delamination front where $x < r$ only. This kept the main body of the delamination shape the same, and only affected that region in the shadow of the open hole. This is shown graphically in Figure 4.3a.

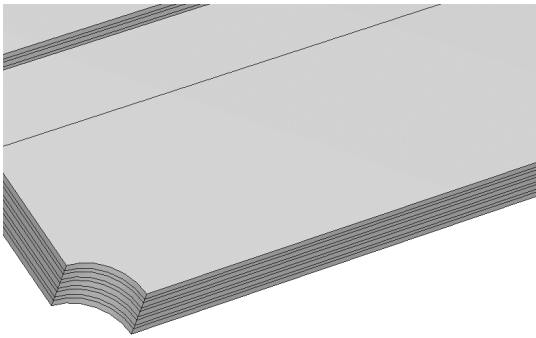
It should be admitted that Equation 4.4 is a modest approximation to the delamination profile tailored to the delamination shape of the surface layer. For a deeper aluminum ply, the delaminations above and below a crack should not be identical due to the stress distribution through the thickness of the laminate. This depth dependence is not incorporated in the model as the delamination survey showed this effect to be modest and inconsistent. Some specimens had identical delamination profiles above and below the fatigue crack, and delamination data was not available for every delamination in every specimen.

Sensitivity studies were conducted to evaluate the effects of the delamination shape on the predicted crack growth. These studies, detailed in Chapter 5, show that the cosine approximation was the best representation of the data. In light of the above observations, Equation 4.4 is considered an adequate approximation to the physical system.

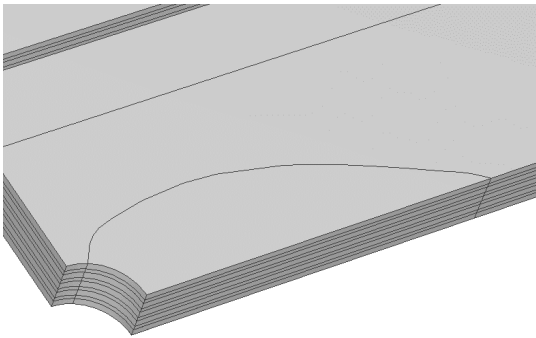
These cracks and delaminations were incorporated into the uncracked models. This created the damaged model that provided the fibre bridging stresses as inputs for the analytical model. To introduce these cracks and delaminations to the uncracked model, three modelling steps were required: partitioning, modification of constraints, and re-meshing. Each step is described below.

Partitioning:

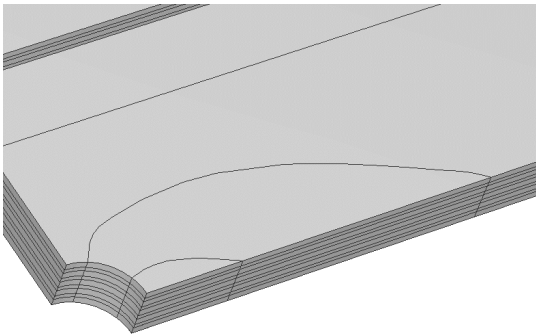
Partitioning is a modelling procedure in ABAQUS that divides a part into sections. Partitioning has no effect on a part's material properties or response to loading, but is rather an aide to modelling complex geometries. When a part is partitioned, the mesh of that part will conform to the contours of the partition. Partitioning was used in this research to define the crack lengths and delamination shapes in a model.



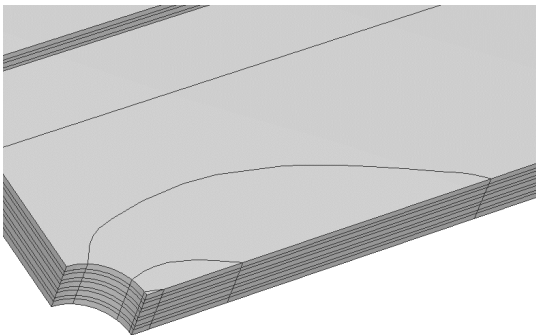
a. Uncracked MOHTB model.



b. MOHTB model partitioned for single surface crack.



c. MOHTB model partitioned for surface and one subsurface crack.



d. MOHTB model partitioned for surface and two subsurface cracks.

Figure 4.4: Modelling procedure to introduce fatigue crack damage to a G2A-6/5-0.4 MOHTB specimen.

The process started with an undamaged model as shown in Figure 4.4a. Partitions were imposed that took the shape of the delaminated regions, as shown in Figure 4.4b. The delamination shape was placed on the surface of the model and extruded through all plies. This allowed the partition to define both the delamination front and the crack front. This process was repeated until all surface and subsurface cracks were introduced as shown in Figure 4.4c-d. The partition for one layer was imposed on every layer in the laminate. This was a requirement of the tie constraints imposed and is explained in detail in the discussion on modification of constraints below.

Modification of Constraints:

Fatigue cracks were introduced to the partitioned undamaged model by removing the y-symmetry constraint on the crack faces defined by the partition - as seen for a surface crack in Figure 4.5. When loads were then applied, the cracks were allowed to open, as the y-direction symmetry constraint no longer restrained crack opening displacements.

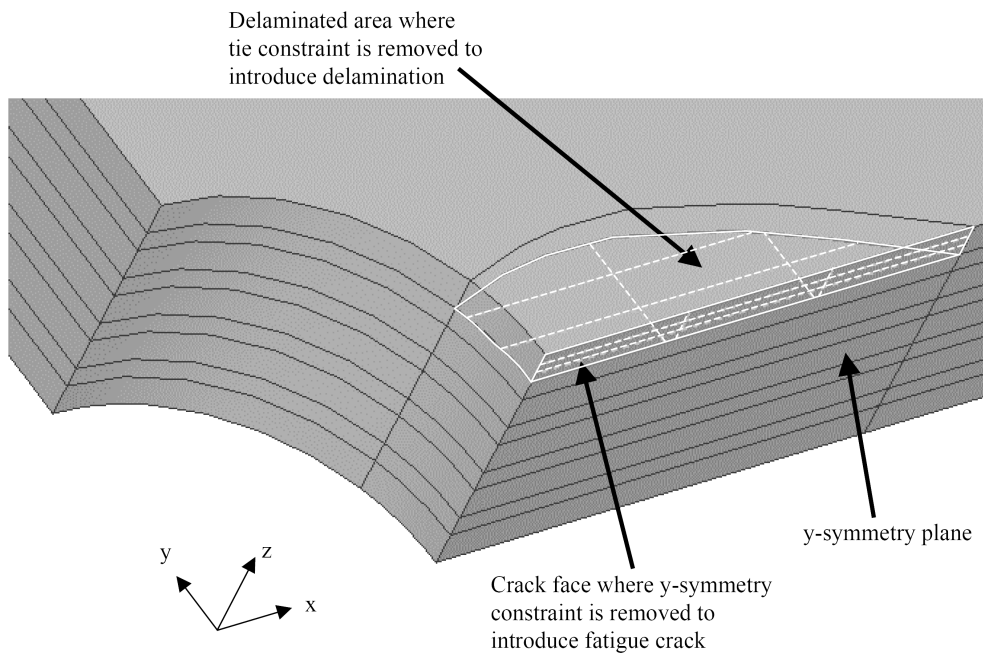


Figure 4.5: *Illustration of constraint modification to introduce a surface fatigue crack and delamination zone into an uncracked model.*

This method of crack modelling meant that the crack path was always a straight line, aligned with the x-axis of the specimen. Additionally, the crack front was a straight

line in a ply aligned with the z-axis. While these implementations are approximations, the loss of accuracy is deemed small in comparison to the gains made in modelling simplicity.

To introduce the delamination, the tie constraints between the cracked aluminum ply and its adjacent prepreg layers were removed in the delaminated region as shown in Figure 4.5. This freed the prepreg from the aluminum in the delamination region, and allowed the glass fibre prepreg to bridge over the crack flanks. For subsurface cracks, the delamination regions above and below the crack in the aluminum ply were assumed to be identical.

Due to the bending load induced, the fibres on one side of a cracked aluminum ply carry a slightly different load than the fibres on the other side of the ply. This should induce a different delamination shape on either side of an aluminum ply. For this research, however, the delamination shapes were kept identical above and below the cracked aluminum ply. The delamination survey supported this approximation.

As tie constraints require nearly identical meshes on adjacent parts to link nodes together, the partitions for every crack/delamination were imposed on every ply in the model. This is shown in Figure 4.4c and d for a model with a surface and one or two subsurface cracks. This ensured the meshes for every ply would be identical and the tie constraints in undamaged regions would be unaffected.

Remeshing:

The final step to introducing damage to the FE model was to re-mesh. As the tip of the fatigue cracks represented a severe stress concentration, the mesh was locally refined to ensure accurate results. A convergence study was conducted to find the appropriate mesh size in the test section of the specimen. The study used the MOHTB model constructed of G2A-6/5-0.4 taken from the undamaged model convergence study. Details of this study are found in Appendix B. Results showed that localized graded refinement of the mesh in the test section down to 0.25mm in the vicinity of the crack tip was justified and was used throughout the remainder of the investigations.

4.2.3 Fibre Bridging Stress Extraction

The final stage in finite element modelling was to extract the required information from the model runs. The data required for the analytical model was the fibre bridging stress distribution. To develop this data, the strain in the fibres bridging the fatigue cracks was extracted. The expression for the total strain in the fibres, $\varepsilon_{fd}(x)$, was considered to be composed of two parts:

- The strain due to the applied load, secondary bending and the response due to damage in plies above the ply of interest, $\varepsilon_f(x)$

- The strain induced due to the fibres bridging the crack of interest, $\varepsilon_{fb}(x)$

So the total strain in the fibres was expressed:

$$\varepsilon_{fd}(x) = \varepsilon_f(x) + \varepsilon_{fb}(x) \quad (4.5)$$

To extract the required fibres bridging strain, $\varepsilon_{fb}(x)$, two modelling steps were required. The first step was to extract the total strain data from fibres bridging a crack in a ply of interest, $\varepsilon_{fd}(x)$. The second modelling step involved finding the values of $\varepsilon_f(x)$ by running a model with damage introduced down to, but not including the ply of interest.

With values of $\varepsilon_{fd}(x)$ and $\varepsilon_f(x)$ in hand, Equation 4.5 was used to find $\varepsilon_{fb}(x)$. The fibre bridging strain was then converted to the fibre bridging stress, σ_{fb} . Given the nature of the glass fibres, the fibre bridging stress distribution resulting from the fibre bridging strains were determined through simple elastic material properties:

$$\sigma_{fb}(x) = E_f \varepsilon_{fb}(x) \quad (4.6)$$

4.2.4 FEM Results

FEM analyses were conducted for all cracked configurations of specimens referenced in Figure 4.2 and Appendix D, with delaminations imposed according to Equation 4.4. As this represents a large volume of data, only typical and summary data will be presented here. Data for all analyses are given in Appendix C. By conducting these analyses on all cracked configurations of specimens available, a more complete picture was drawn of the changes to the fibre bridging stress distributions within a specimen as damage progressed in the test section.

For any one analysis, the data gained were the fibre bridging stress distributions over fatigue cracks in every cracked ply of the model. Such a data set is given in Figure 4.6. This data set is for a MOHTB specimen of Glare 2A-6/5-0.4 tested at an applied stress of 100MPa. The horizontal-axis shows the x-location along the specimen, with $x=0$ representing the center of the open hole. As cracks in this research were measured from the edge of the open hole, $x=2.8\text{mm}$, the length of a crack in the figure is equal to the x-position of the tip of the crack minus the open hole radius. The vertical-axis shows the fibre bridging stress, σ_{fb} . The data set shows the surface crack imposed was 15.0mm, the first subsurface crack was 7.5mm, and the second subsurface crack was 6.0mm. This set of cracks applied was chosen to match a configuration from the experimental crack survey previously mentioned.

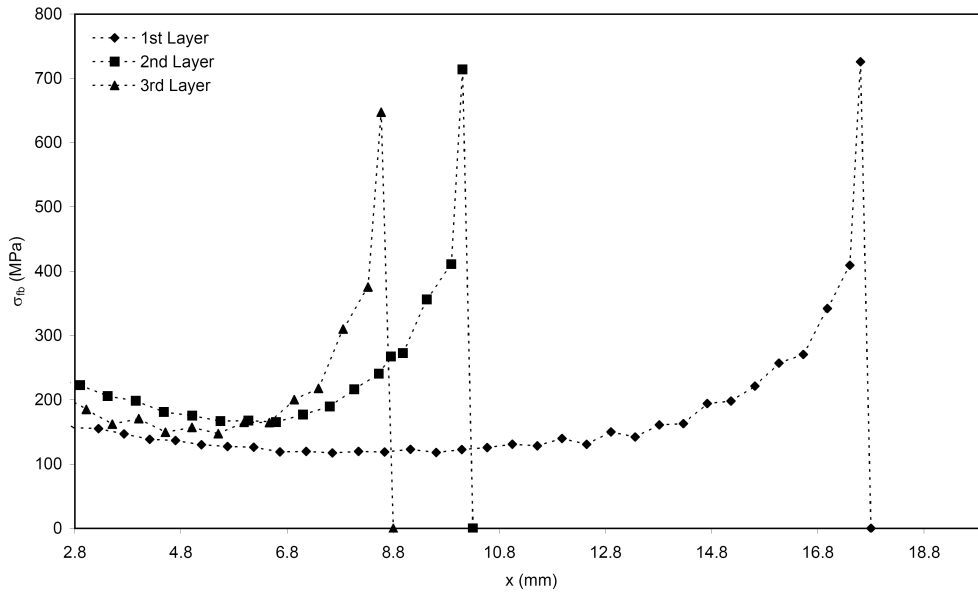


Figure 4.6: Fibre bridging stress distributions for three cracked plies of Glare 2A-6/5-0.4 MOHTB specimen. $\sigma_{app} = 100$ MPa. Surface crack length, $a_1 = 15.0$ mm.

The chart clearly shows that each stress distribution has similar characteristics. The curves start at a slightly higher level close to the open hole, drop to a lower level over the flank of the cracks, and then peak at the crack tip. The rise in fibre bridging stress near the open hole is to be expected and is due to the stress rising action of the open hole. The stress along the flank of the crack drops to a nearly constant level and remains there for the majority of the length of the crack. This is clearly evident in the curve of the long surface crack. This observation holds for all surface and subsurface cracks analyzed – though for short cracks, the effects of the open hole dominate the curve over the flank of the crack, as can be seen for the 3rd layer crack, and to a lesser extent, the 2nd layer crack in Figure 4.6.

The peak at the tip of the crack has the same shape for all cracks, surface and subsurface. The width of the peak remains fairly constant for all cracks observed. The differences in the peak stress at the tip show variation from crack to crack. As this is a measure at the crack tip, which represents a stress singularity, differences in the meshes at the tips of the cracks plays the dominant role in the variation in calculated stress levels. The convergence study in Appendix B illustrates the mesh insensitivity of the data extracted along the crack flank.

In order to assess how the fibre bridging stress distributions changed as damaged progressed in the specimens, multiple analyses were conducted for progressively extensive damage. Figure 4.7 - Figure 4.9 give insight to how the distributions changed as damaged progressed. Figure 4.7 shows surface crack data for eight

damage sets. These damage sets had damage that progressed to multiple plies of aluminum in the specimen. Figure 4.8 and Figure 4.9 show 2nd and 3rd layer fibre bridging distributions for increasing crack lengths in the models. The specimen analyzed in the figures was a Glare 2A-6/5-0.4 MOHTB specimen tested at an applied stress of 100MPa. The axes in the figures are the same as in Figure 4.6.

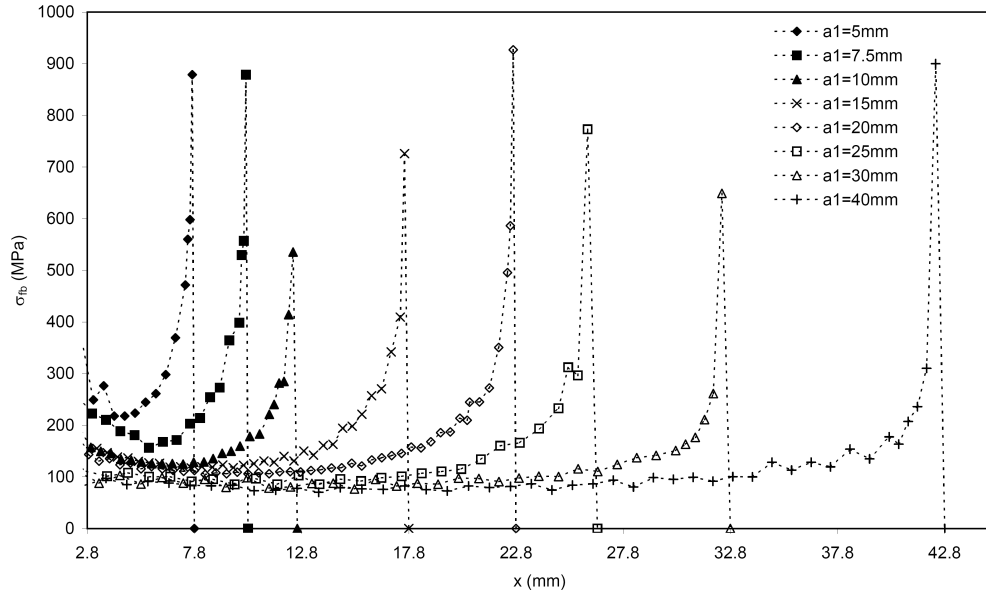


Figure 4.7: Typical fibre bridging stress distributions for surface cracks. Glare 2A-6/5-0.4, $\sigma_{app} = 100$ MPa.

Subsurface Fatigue Crack Growth in Glare Fibre Metal Laminates

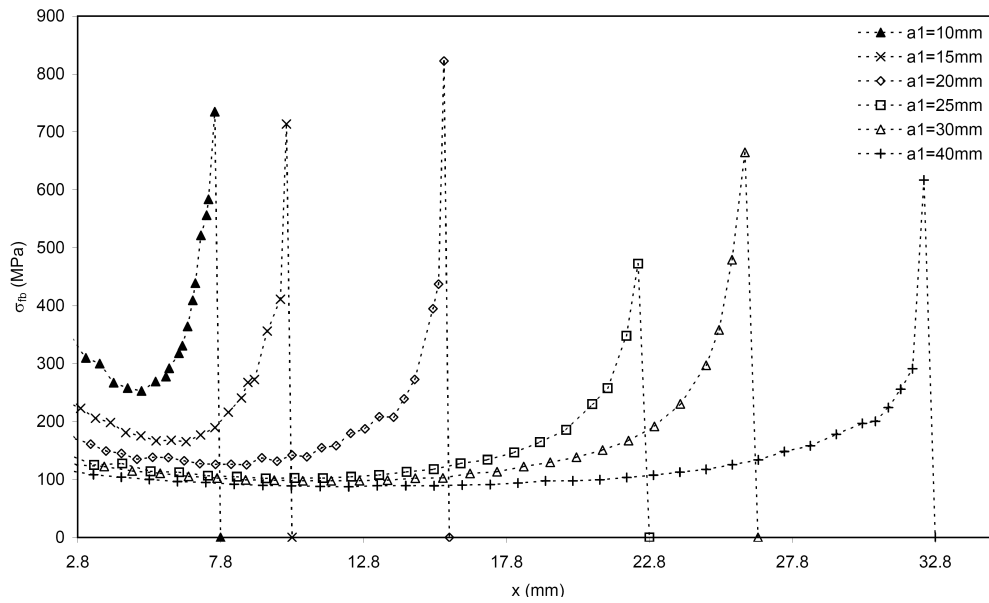


Figure 4.8: 2nd layer fibre bridging stress distributions. Data labelled with associated surface crack length for comparison to data in Figure 4.7. Glare 2A-6/5-0.4, $\sigma_{app} = 100$ MPa.

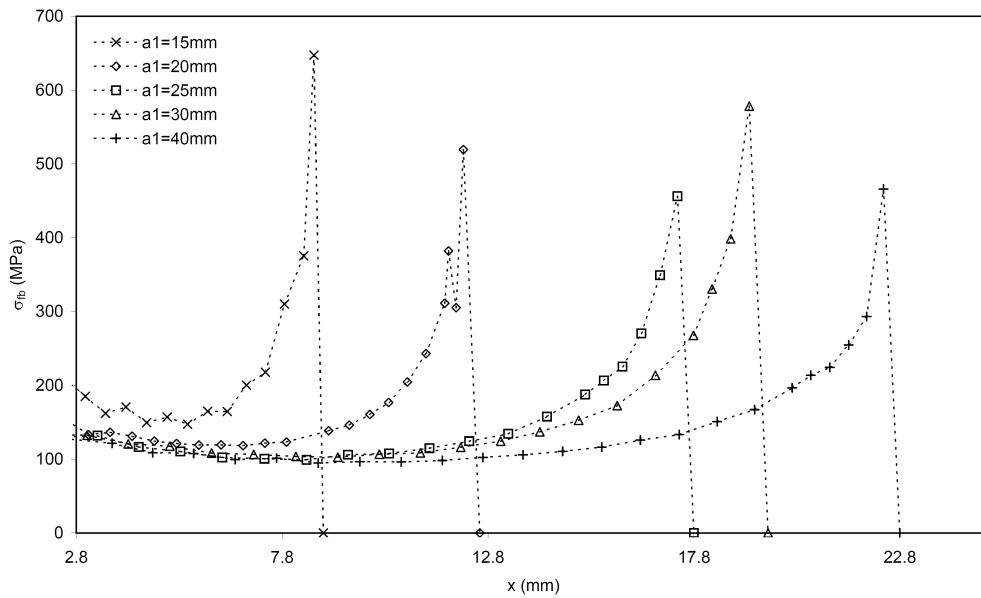


Figure 4.9: 3rd layer fibre bridging stress distributions. Data labelled with associated surface crack length for comparison to data in Figure 4.7. Glare 2A-6/5-0.4, $\sigma_{app} = 100$ MPa.

The plots of the fibre bridging stresses for progressively longer cracks again show the same characteristics as described in Figure 4.6. The rise in stress close to the open hole, the consistent stress level over the majority of the flank of the crack, and the sharp peak at the crack tip are evident in each plot. Each of these characteristics is described in more detail below.

The rise in stress at the open hole is attributed to the stress concentration the hole represents. Had the analysis been conducted on a crack emanating from a saw cut, the stress concentration would be different, and thus characteristics of the initial portion of the curve would be markedly different. This section is considered to be a function of the geometry of the specimen, rather than a feature characteristic of fatigue crack growth in Glare.

The fibre bridging stress over the flank of the crack, or flank stress, is a feature characteristic of fatigue cracks in Glare. Similar characteristics have been shown in other research^{1, 4, 10} on fibre bridging stress distributions, and its behaviour directly affects the crack growth in Glare. The flank stress, σ_{flank} , to be used in the analytical model is defined as the consistent value the stress distribution dropped to away from the open hole and crack tip. It was determined by averaging the values of the stress from 4mm away from the open hole to 2mm before the crack tip. For short cracks, the flank stress value was determined to be the lowest consistent value on the stress distribution. This analysis resulted in a single value of flank stress for a given crack. This range was selected to ensure that the peaks at the crack tips and the influence of the open hole were not included in the assessment of the flank stress.

The flank stress showed a marked decline for increasing crack lengths as shown in Figure 4.7 through Figure 4.9. This trend held for cracks in every layer of every specimen analyzed. This drop in σ_{flank} as the cracks grow has a direct effect on the crack growth prediction.

An important trend was noticed in the FEM results of σ_{flank} values versus modelled crack length. For a given specimen, the σ_{flank} values always fell around the same shaped curve – regardless of the ply investigated. This is shown graphically in Figure 4.10 for Glare 2A-6/5-0.4 MOHTB specimens tested at an applied stress of 100MPa. Three data curves are shown for the three cracked aluminum plies modelled.

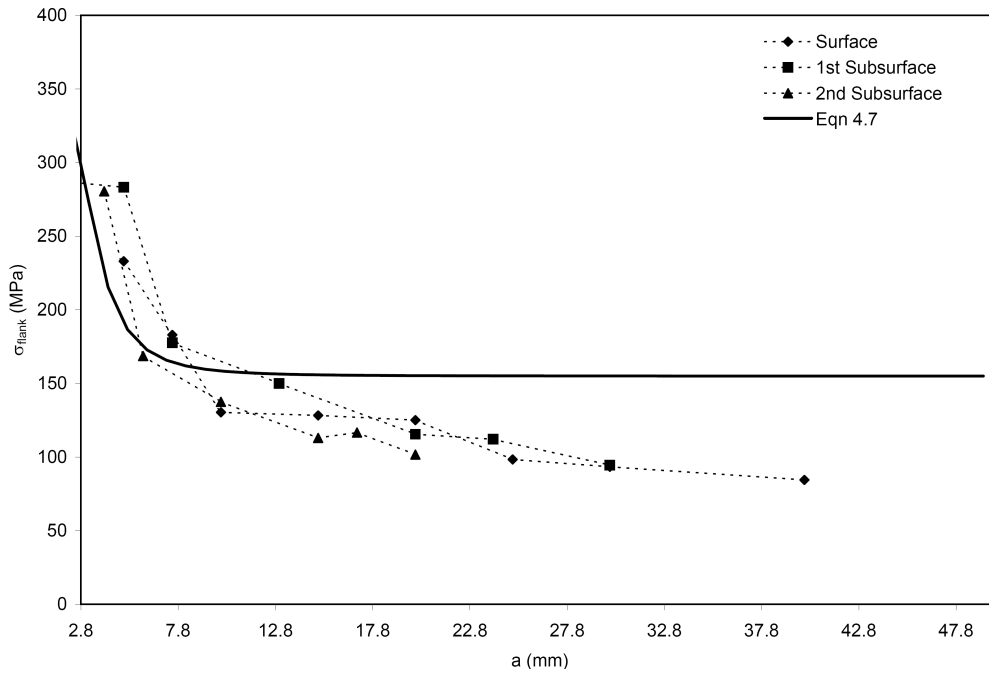


Figure 4.10: Flank stress versus final crack length for Glare 2A-6/5-0.4 with $\sigma_{app} = 100$ MPa, where a is the length of the fatigue crack from open hole to tip. Data points represent the constant value recorded of fibre bridging stresses along the flank of a crack.

The plot shows that the flank stress values for all modelled cracks in the three aluminum plies fell near the same curve. The data plots also clearly show that the length of the crack and the proximity of the crack tip to the open hole are the dominant parameters in determining the value of σ_{flank} . The layer the crack is in, surface or subsurface, does not play a significant role in determining the flank stress level. This runs counter to intuition, as the more subsurface a ply is in a specimen undergoing bending, the lower the resultant stress.

It would be expected that subsurface plies would experience lower fibre bridging stresses for the same crack length, however, the analysis does not bear this assumption out. Mitigating this effect is the fact that the neutral line is also shifting as aluminum plies are cracked. For the bending factors evaluated, these effects appear to balance out and result in flank stress values falling near the same curve.

Similar analyses were conducted for all specimens tested and are shown in Appendix C. For each of these different specimens, the same shape and magnitude of curve of σ_{flank} versus crack length was observed. The only marked difference was the overall placement of the curve, which was shifted either up or down in stress, depending upon the resultant stress in the aluminum layers due to the applied stress.

There are many parameters that affect the flank stress distribution. Five of these parameters are focused on here to evaluate the influence on the stress distribution:

- Specimen Geometry and Applied Stress: The eccentricity of the neutral line and the applied stress play obvious roles in determining the resulting stress in a ply of aluminum in the laminate. Various values of k_b and σ_{app} were evaluated, and all flank stress distributions fell on the same shaped curve. Other than the vertical placement of the curve on the σ_{flank} versus a chart as in Figure 4.10, the k_b and σ_{app} values did not appear to affect the shape or range of stresses in the distribution.
- Stress Concentrations: Here defined as the open hole in the specimen, this is closely related to the Specimen Geometry discussed above. Effects of the open hole can clearly be seen in the distributions, as the stress levels rise close to the hole, and drop to a near-constant level away from the hole. Calculations¹¹ based on monolithic aluminum sheet under pure tension with a circular hole return a stress concentration factor of 3, and a stress gradient that dissipates the effects of the open hole within three times the radius of the open hole. This matches well with the FE results presented in Figure 4.7 to Figure 4.9.
- Ply depth position: As the resultant stresses in the plies of the MOHTB specimen drops for increasing depths, it is expected that the flank stress levels would drop for increasing depths as well. However, this is not the case, as the plots for flank stress for each ply in the laminates fall on top of each other. Mitigating the effect of dropping stress for deeper layers is the fact that for a given crack length in a subsurface ply, the cracks in the plies closer to the surface are longer. This has the effect of causing the subsurface ply of interest to carry more load – which would drive up the flank stresses. Additionally, as the plies closer to the surface crack, the neutral line shifts – inducing more bending and driving up the stresses in the deeper layers.
- Crack Length: Crack length plays a role in determining the flank stress distribution. For longer cracks, the COD is greater, which induces greater strain on the fibres near the open hole, causing the delamination to grow a commensurate amount to maintain the self balancing nature of crack growth with delamination growth. As the stresses in the fibres at the edge of the open hole reach a near constant value for crack lengths larger than approximately twice the diameter of the open hole, the concept of the balance of crack and delamination growth is supported.

Based upon the above discussion, the stress concentration of the open hole was considered to be the primary driving factor in determining the shape of the flank stress trend for short cracks. The plots of the flank stress for each cracked aluminum ply in Figure 4.10 all rise in the same manner close to the open hole. Additionally,

all the plots fall along the same shaped curve away from the open hole. The flank stress dropped to a nominal value away from the open hole for each cracked aluminum ply. The last point in Figure 4.10 where data from all three layers are available is for a crack length of approximately 20mm. At this point, the mean value of the flank stress for the three layers was 93.6MPa with a standard deviation of 8.6MPa.

To incorporate these results in an analytical model, two choices were readily apparent. Individual curve fits could be generated for each type of specimen, or a single, general curve fit could be used. Utilizing multiple, sample-modified curve fits would have required rationales to justify the customizations of the curves. As no consistent set of criteria was evident on which to base changes to the curves, the second option was chosen. To make the model as simple as possible, a single curve fit was applied to match each of these distributions, as shown in Figure 4.10 and expressed in Equation 4.7.

$$\sigma_{flank}(a) = (0.6\sigma_{res} + 220) - 185e^{-60*a^{-3.5}} \quad (4.7)$$

Where a is the crack length being investigated. The resulting stress, σ_{res} , is found with FE analysis of an uncracked model. The value of σ_{res} is the net stress found in the test section of the surface aluminum ply of that FE model. While not the best curve fit for any one set of data, this shape was found to be a good representation all data sets. Basing the equation on σ_{res} shifted the curve up or down in stress, based upon the configuration and load level of the specimen being analyzed.

Equation 4.7 captures the effects of the stress concentration of the open hole, and allows the flank stress value to arrive at a constant value away from the open hole. The form of the equation clips the maximum value of the distribution at the open hole and has sharp enough gradients to match the flank stress values found in the FE models.

The sharp rise in stress at the crack tip, the tip stress, is denoted as σ_{tip} . This rise is expected as the length of the fibres that have delaminated close to the crack tip is short and any COD in the metal plies imparts a large strain in the adjacent fibres. As can be seen in Figure 4.7, the widths of the peaks were essentially the same for all crack lengths. The peak stresses found at the tips of the cracks varied from crack length to crack length. This peak level of the fibre bridging stress distribution was difficult to assess, as it was very dependant upon the FEM mesh.

The sensitivity of the results to delamination shape were discussed by Alderliesten⁴. There he discussed the strengths of a delamination shape between a triangle and ellipse yielding well-behaved fibre bridging stress distributions. The delamination shape used in this research fell within the recommendations, and the same shape was used for all analyses, therefore, it is concluded that the variances in the peak tip

stress were not due to the delamination shape used. The cracks in the different plies of a specimen were significantly different. Because the crack tips in the various layers were so far apart, any mutual influence of one ply's crack tip on another was minimal. As the same shape was used for all delaminations, the difference in the mesh configurations near the tips of the cracks was the sole contributor to the variances.

To incorporate these results in an analytical model, some simplifying assumptions were needed to derive a sensible value for σ_{tip} . As many of the results of the FEM show values well above the failure limit of the fibres, a fixed and constant value of 90% of the failure stress of the fibres was utilized for the peak stress level. This was deemed appropriate as the FEM results do show a spike in stress at the crack tip, but experimental results do not show fibre breakage. Therefore, the value of σ_{tip} must be less than the failure limit. There was no relation found from FE analysis between tip stress and crack length, so a constant value was used.

The tip stress distribution ramped from the flank stress value to the peak stress value over the final 0.5mm of the crack to ensure inclusion of the plastic zone at the tip of the crack. Sensitivity studies of the effects of σ_{tip} on the predicted crack growth rates show that the term plays a smaller role in comparison to the flank stress, hence we define σ_{tip} as follows:

$$\sigma_{tip} = 0.9\sigma_{BN} \quad (4.8)$$

where $\sigma_{BN} = 1193\text{MPa}$, is the blunt notch strength of the glass fibres¹².

With each section of the fibre bridging stress distribution defined, the total fibre bridging stress distribution is merely the sum of the components:

$$\sigma_{fb}(x) = \begin{cases} \sigma_{flank} & r \leq x < (a+r) - 0.5 \\ \sigma_{tip} & (a+r) - 0.5 \leq x \leq (a+r) \end{cases} \quad (4.9)$$

4.3 Analytical Modelling

Unlike in monolithic materials, two types of stresses govern the local stresses around a crack tip in Glare. The first is the remote stress resulting from the applied load. The applied load and specimen geometry govern the resulting stress intensity. The second stress, typical for FMLs, is the stress in the fibres passing over the crack: the fibre-bridging stress. These two stress types are superimposed to develop a total stress intensity factor for the specimen. In view of the assumed elastic behaviour, the superposition is justified.

4.3.1 Crack Opening Stress Intensity Factor

Tada⁷ gives the Mode I stress intensity factor for a crack emanating from an open hole in an infinite sheet undergoing pure tension, shown in Figure 4.11, as:

$$K_{I(OH)} = \sigma \sqrt{\pi a} \left\{ 0.5 \left(3 - \frac{a}{a+r} \right) \left[1 + 1.243 \left(1 - \frac{a}{a+r} \right)^3 \right] \right\} \quad (4.10)$$

where a is the crack length and r is the open hole radius. This formulation is applicable to the present tension-bending configuration as each ply is considered individually. The stress state varies through the thickness of the laminate due to the combined tension-bending, but an individual ply is considered to be at its own stress level, derived from FE modelling.

The stress level in any given ply of aluminum in the laminate, σ in Equation 4.10, is taken to be the net stress in the test section of the undamaged aluminum ply of interest, σ_{res} . Therefore, σ_{res} depends on macroscopic far field stress levels and ply depth. No finite width corrections were incorporated into this formulation of the analytical model.

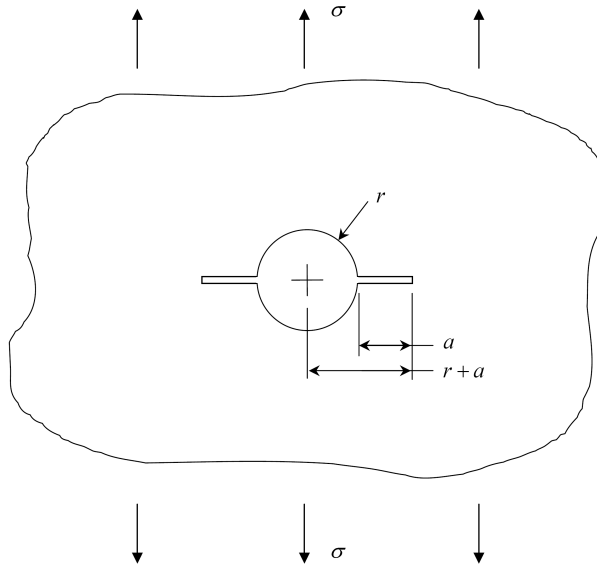


Figure 4.11: Stress intensity factor geometry definition for a crack emanating from an open hole.

4.3.2 Fibre Bridging Stress Intensity Factor

The second, and more complicated stress intensity formulation is generated from the effects of the fibre bridging. An important feature of the stress intensity factor formulation for fibre bridging is that the fibre bridging stresses act at the delamination front – not on the crack face. Similarly, the fibre bridging stress distribution is not uniform – the fibres bridging the crack do not all carry the same load. To incorporate these two non-uniform aspects that comprise the fibre bridging, the stress intensity factor for a symmetric set of point loads arrayed around a crack is used. Tada⁷ gives the basic formulation for the Mode I stress intensity factor for an array of point loads around a crack in an infinite sheet, as shown in Figure 4.12. Marissen¹ rewrote the expression in a form with only real variables:

$$K = P \sqrt{\frac{2a}{\pi}} \left\{ \frac{B}{A} + y_o^2 (1 + \nu) \left(\frac{BC}{A^{3/2}} - \frac{\sqrt{A} + C}{2AB} \right) \right\} \quad (4.11)$$

where:

$$A = (a^2 - x_o^2 + y_o^2)^2 + 4x_o^2 y_o^2 \quad (4.12)$$

$$B = \sqrt{a^2 - x_o^2 + y_o^2} + \sqrt{A} \quad (4.13)$$

$$C = a^2 + x_o^2 + y_o^2 \quad (4.14)$$

where x_o and y_o locate the point of application of the stress – here the fibre bridging stress applied at the delamination front, defined with Equation 4.4.

The term P is the applied load per unit thickness and ν is the Poisson's ratio of the aluminum plies. While Eq. 4.11 applies to an infinite sheet without a hole, its use is justified here as the effect of the open hole may be expected to be small for longer cracks. Sensitivity studies of the effects of the use of this stress intensity factor formulation on the predicted crack growth rate show that the effects of the lack of open hole are modest. These studies are described in detail in Chapter 5. No finite width corrections were incorporated into this formulation of the analytical model.

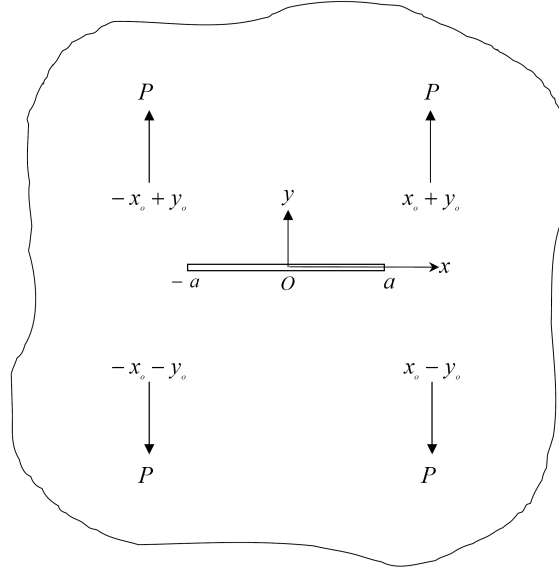


Figure 4.12: *Stress intensity factor geometry definition for a crack with a symmetrical array of point loads.*

Substituting the fibre bridging stress distribution from Equation 4.9 into Equation 4.11 for P , and using the delamination shape defined in Equation 4.4 to define y_o , the stress intensity factor was determined. Marissen¹ integrated the stress intensity, $K_{I(fb)}$, expression over an elliptical delamination shape with a constant fibre bridging load. This allowed him to arrive at a relation between the stress intensity factor due to fibre bridging and a constant fibre-bridging load applied to a center-cracked tension specimen. Incorporating the non-uniform stress distribution and the appropriate approximation of the delamination shape to his expansion yields:

$$K_{I(fb)} = \sqrt{\frac{2a}{\pi}} \int_r^{a+r} \sigma_{fb} \left\{ \frac{B}{A} + y_o^2 (1 + \nu) \left(\frac{BC}{A^{3/2}} - \frac{\sqrt{A} + C}{2AB} \right) \right\} dx \quad (4.15)$$

with

$$x_o = x \quad r < x < a+r \quad (4.16)$$

$$y_o = b(x) \quad r < x < a+r \quad (4.17)$$

The terms A , B and C are identical to those defined in Equations 4.12 - 4.14. The limits on the above integration range from $x = r$ (the edge of the open hole, where the crack length is zero), to the final crack length, $x = a+r$. The fibre bridging stress

term, σ_{fb} , is dependent upon both the length of crack being analyzed, a , and the position on that crack, x , as described by Equation 4.9.

Using both contributing Mode I stress intensity factor formulations found in Equations 4.10 and 4.15, the principal of superposition is used to arrive at a total stress intensity factor for the fatigue crack in the MOHTB specimen.

$$K_{I(tot)} = K_{I(OH)} - K_{I(fb)} \quad (4.18)$$

$$K_{I(tot)} = \sigma_{res} \sqrt{\pi a} \left\{ 0.5(3-s) \left[1 + 1.243(1-s)^3 \right] - \sqrt{\frac{2a}{\pi}} \int_r^{a+r} \sigma_{fb} \left\{ \frac{B}{A} + y_o^2(1+\nu) \left(\frac{BC}{A^{3/2}} - \frac{\sqrt{A+C}}{2AB} \right) \right\} dx \right\} \quad (4.19)$$

Where σ_{fb} is the flank stress given by Equation 4.7 for $r < x < (r+a)-0.5$ and the tip stress for $(r+a)-0.5 < x < (r+a)$. From this a stress intensity factor range can be developed to allow for crack growth predictions using simple Paris law formulations.

$$\frac{da}{dN} = C(\Delta K_{I(tot)})^n \quad (4.20)$$

where C and n are the material constants for the metal constituents. For the aluminum alloys used in this study, C and n values are taken from literature⁹ on through-crack modelling and are 2.17×10^{-12} and 2.94, respectively for da/dN in mm/cycle and ΔK in MPa $\sqrt{\text{mm}}$.

4.4 Numerical Calculations

The formulation for $\Delta K_{I(tot)}$ was intentionally posed for a numerical solution. The numerical package MathCADTM was used to produce crack growth predictions. The numerical model program structure is shown in Figure 4.13. The crack propagation data for each ply is calculated individually. Each ply can be calculated independent of the other plies in the laminate, as influences of surrounding plies were accounted for in the FE modelling. The approach used can be summarized as follows:

- Delamination front shapes are taken from experimental investigations. Curve fits of the shapes are applied based upon the investigated crack length.

- Resultant stresses to applied loads are taken from FEM for each aluminum and prepreg ply.
- Stress intensity factors are calculated for an initial fatigue crack based upon the analytical approximations to the local stress field.
- The fatigue crack is grown a predefined amount. The number of cycles to achieve that predefined amount is calculated based upon the stress intensity factors using a Paris law relation.
- Material parameters for the model include the material constants for the metal plies in the laminate. Loading parameters are the resultant stresses found in each aluminum ply from FE analysis. These parameters set the fibre bridging stress distribution for the aluminum ply. Geometry parameters are tied to the far field stress intensity factor and include the open hole radius in the specimens. The modelling parameters required include a_{incr} , which sets the crack growth step size the analysis follows. The parameter a_o is the initial crack size used as a starting point for the analysis, and a_{final} is the final desired crack length.

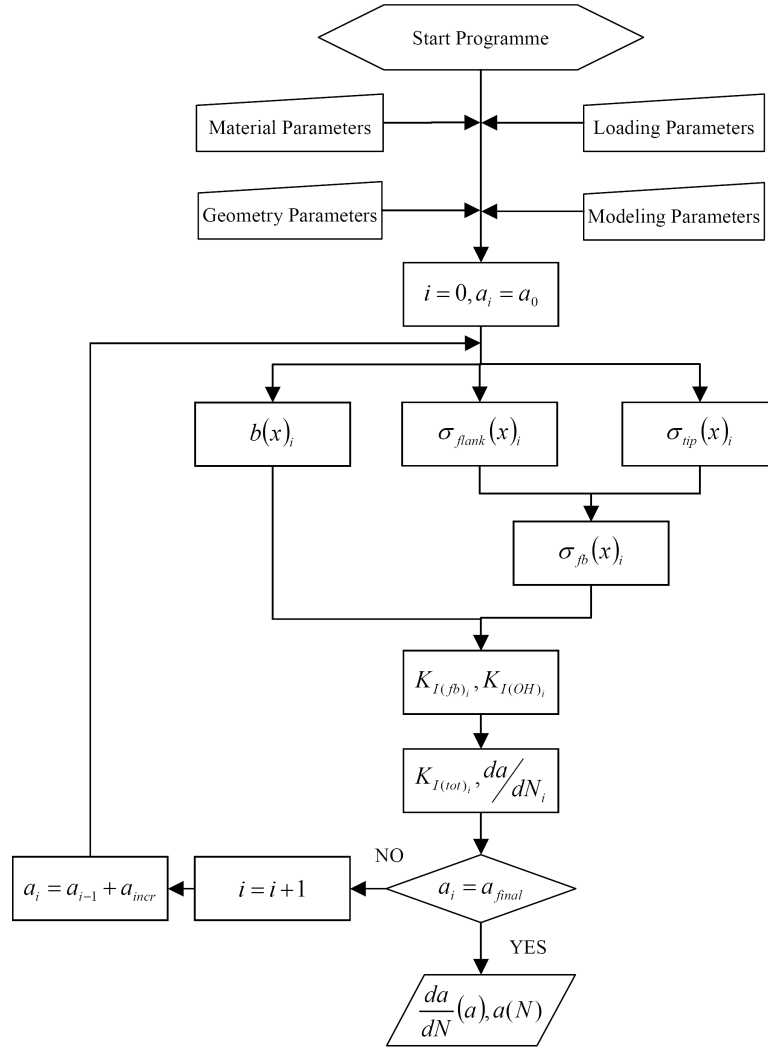


Figure 4.13: Flow diagram for the crack growth prediction model

4.5 Summary

A hybrid analytical/numerical fatigue crack growth prediction model was presented for surface and subsurface cracks in Glare 2A. The methodology for acquiring fibre bridging stress distributions with FEM was discussed. FEM results were presented in the form of σ_{fb} versus a diagrams. Strong trends were observed in the fibre bridging responses of the various configurations of specimens analysed. This led to a mathematical approximation to the σ_{fb} distribution that could easily be

incorporated into an analytical formulation for the stress intensity factors for fatigue cracks in any layer of the laminate.

The total stress intensity factor that describes surface and subsurface crack growth was shown to be comprised of two parts, a far field part, $K_{farfield}$, and a part accounting for the effects of fibre bridging, K_{fb} . The far field stress intensity factor accounts for the applied load, the specimen geometry and any geometry correction factors required (e.g. crack emanating from an open hole). The fibre bridging stress intensity factor accounts for the fibres acting to restrain crack opening. As the stress distribution driving K_{fb} was taken from FE models of cracked configurations of the laminates observed from experimentation, interactions between the cracked plies are accounted for in the model.

4.6 References

- ¹ **Marissen, R.**, *Fatigue Crack Growth in ARALL, A Hybrid Aluminum-Aramid Composite Material, Crack Growth Mechanisms and Quantitative Predictions of the Crack Growth Rates*, PhD Thesis, Delft University Press, 1988.
- ² **Guo Y.J., Wu, X.R.**, *A theoretical model for predicting fatigue crack growth rates in Fibre-reinforced Metal Laminates*, *Fatigue & Fracture of Engineering Materials & Structures*, **21** 1133-1145 (1998).
- ³ **De Koning, A.U., Schra, L.**, *Fatigue crack growth of part through the thickness cracks in Glare 3 and Glare 4B coupons*, NLR-CR-2000-078, 2000 (Restricted).
- ⁴ **Alderliesten, R.C.**, *Fatigue Crack Propagation and Delamination Growth in Glare*, PhD Thesis, Delft University Press, 2005.
- ⁵ **Bannantine, J., Comer, J., Handrock, J.**, *Fundamentals of Metal Fatigue Analysis*, Prentice Hall, 1990.
- ⁶ **Schijve, J., Van Lipzig, H., Van Gestel, G. Hoeymakers, A.**, *Fatigue Properties of Adhesive-Bonded Laminated Sheet Material of Aluminum Alloys*, *Engineering Fracture Mechanics*, Vol 12, pp. 561-579, 1979.
- ⁷ **Tada, H., Paris, P., Irwin, G.**, *The Stress Analysis of Cracks Handbook*, 2nd edition, Paris Productions Inc., 1985.
- ⁸ **ABAQUS, Inc.**, *ABAQUS Version 6.4 Users Manual*, ABAQUS™, Inc., 2003.
- ⁹ **Vlot A., Gunnink J.**, *Fiber Metal Laminates an Introduction*, Kluwer Academic Publishers, 2001.
- ¹⁰ **Guo Y.J., Wu, X.R.**, *Bridging stress distribution in center-cracked fiber reinforced metal laminates: modelling and experiment*, *Engineering Fracture Mechanics*, **63** 147-163 (1999).
- ¹¹ **Schijve, J.**, *Fatigue of Structures and Materials*, Kluwer Academic Publishers, 2001.
- ¹² **Roebroeks, G.**, *The Metal Volume Fraction Approach*, Structural Laminates Industries Report TD-R-00-003, 2000.

5

Validation of Model Against Experimental Data

Abstract – This chapter provides an assessment of the experimental fatigue crack data generated from the test programs detailed in Chapter 3. Experimental results show that the new MOHTB specimen developed in this investigation performed well. Experimental data was repeatable, and scatter amongst the specimens was within expected tolerances of $\sigma_{\log_N} < 0.20$. These experimental results were compared to model predictions, with good results. The hybrid analytical/numerical model effectively estimated fatigue crack propagation for surface and subsurface plies in MOHTB specimens constructed of Glare 2A-5/4-0.4 and 2A-6/5-0.4 tested at 80 and 100MPa, and in four point bend specimens constructed of Glare 2A-11/10-0.4 at 200MPa outer fibre stress. Studies were conducted on the sensitivity of the model to various input parameters. Parameters with a high sensitivity were identified.



5.1. Introduction

Having presented the model in Chapter 4 and the experimental conditions in Chapter 3, this chapter is dedicated to comparing the observed crack life data to model predictions. Two data sets of different natures are available: the MOHTB data and four point bend data. In the MOHTB specimens, all layers experienced an imposed tensile stress and an imposed layer-position dependent bending stress. In the four point bend tests, no applied tension is imposed, and only bending stresses are present.

To validate the analytical model described in Chapter 4, the accuracy of the model is investigated. Chapter 4 detailed the construction of the analytical model and its physical basis was judged to be sound. Therefore, a comparison of the model to experimental data seems justified. Additionally, the sensitivity of the model is investigated by adjusting the input parameters by set amounts and observing the resultant model predictions.

5.2. MOHTB

The test matrix of all MOHTB specimens tested is given again in Table 5.1. Using the recorded data sets of surface and subsurface crack length versus the number of cycles, crack growth data were generated, which are listed in Table 5.2.

Table 5.1: Test matrix of the Milled Open Hole Tension Bending (MOHTB) specimens.

Configuration	# Specimens	σ_{app} (MPa)	Width (mm)	$a_{fin, target}$ (mm)	k_b
G2A-5/4-0.4	2	80	50	10.0, 15.0	2.7
G2A-5/4-0.4	1	80	100	30.0	2.7
G2A-5/4-0.4	2	100	50	15.0, 30.0	2.5
G2A-6/5-0.4	1	100	50	10.0	2.0
G2A-6/5-0.4	2	100	100	20.0, 40.0	2.0

In Table 5.1, σ_{app} is the applied stress to the specimen during the fatigue tests, $a_{fin, target}$ is the targeted final surface crack length for the specimen, and k_b is the bending factor, defined as $\sigma_{max}/\sigma_{nom}$, found through FE analysis. In Table 5.2, a_{init} is the actual initial crack length for the surface aluminum ply; a_{fin} is the actual final crack length for the cracked aluminum plies. N_{init} and N_{final} are the numbers of fatigue cycles to crack initiation and to the final crack length respectively.

For a given specimen configuration, loading condition and aluminum ply, fatigue cracks initiated at a reasonably consistent number of cycles. This is evidenced by the frequent occurrence of the same number of cycles to crack initiation shown for the various layers in Table 5.2. The problems associated with the OHTB specimens discussed in Chapter 3 were not present. No plastic deformations or fatigue cracks were present in the tapered overlaps of the MOHTB specimens. The gradual shift in the neutral line was effective in removing the intense stress riser present in the sharp overlap of the OHTB specimen, and using a bonded attachment rather than a bolted one removed the stress risers of the fastener holes in the overlaps.

Table 5.2: Fatigue test results for the MOHTB specimens. N_{init} , N_{final} , a_{init} and a_{final} data shown for left and right cracks.

Configuration		Layer 1		Layer 2		Layer 3	
Specimen ID	Side	N_{init} N_{final} (kcycles)	a_{init} a_{fin} (mm)	N_{init} N_{final} (kcycles)	a_{fin} (mm)	N_{init} N_{final} (kcycles)	a_{fin} (mm)
G2A-5/4-0.4 - 80MPa							
MOHTB-1	L	66 526	0.5 29.1	108 526	7.9	258 526	4.5
	R	66 526	0.4 23.6	150 526	7.5	300 526	3.8
MOHTB-2	L	40 195	0.7 9.7	100 195	3.7	150 195	1.6
	R	40 195	0.7 10.7	70 195	3.5	130 195	1.4
MOHTB-4*	L	35 225	0.3 12.6	110 225	4.3	**	**
	R	30 225	0.2 13.2	140 225	3.1	**	**
G2A-5/4-0.4, 100MPa							
MOHTB-5	L	30 155	0.7 17.4	40 155	5.5	100 155	2.3
	R	20 155	0.8 18.6	55 155	3.8	80 155	2.5
MOHTB-6	L	25 160	0.6 17.6	45 160	5.7	80 160	3.3
	R	25 160	0.3 16.9	55 160	4.0	95 160	2.8
G2A-6/5-0.4 - 100MPa							
MOHTB-7	L	40 240	0.5 9.1	45 240	6.9	80 240	3.9
	R	50 240	0.3 9.4	50 240	6.5	50 240	5.0
MOHTB-8	L	70 1331	0.7 39.4	70 1331	28.8	80 1331	21.6
	R	50 1331	0.8 40.2	60 1331	30.1	60 1331	21.6
MOHTB-9	L	40 1170	0.1 25.3	60 1170	21.8	70 1170	15.0
	R	40 1170	0.2 33.0	60 1170	24.9	70 1170	17.7

*: Sample MOHTB-3 was damaged during testing. **: Data unavailable due to damage to ply during teardown.

After completing the fatigue tests, the specimens were destructively inspected following the procedure outlined in Chapter 3. The destructive inspection, depicted in Figure 5.1, showed fatigue cracks in several aluminum plies of the specimens. The fatigue crack is easily identified in the figure. As the specimens were pulled apart in a static failure at the end of the fatigue tests to expose the fatigue crack surfaces, a visible transition from fatigue crack to static failure is present in each fatigue-cracked ply. This transition to the static failure is identifiable by the sudden shift in the crack path of each ply. Under the optical microscope, the transition from fatigue to static cracking was equally evident as the crack surface changed from perpendicular to the specimen surface for the fatigue crack, to angled at approximately 45° for the static failure. These cracks were progressively shorter the more subsurface the aluminum ply was. This was expected, as the tensile load on the aluminum plies is smaller for subsurface plies than for the surface ply. This was further evidenced by the fact that deeper subsurface aluminum plies initiated fatigue cracks later in the fatigue test than plies closer to the surface.

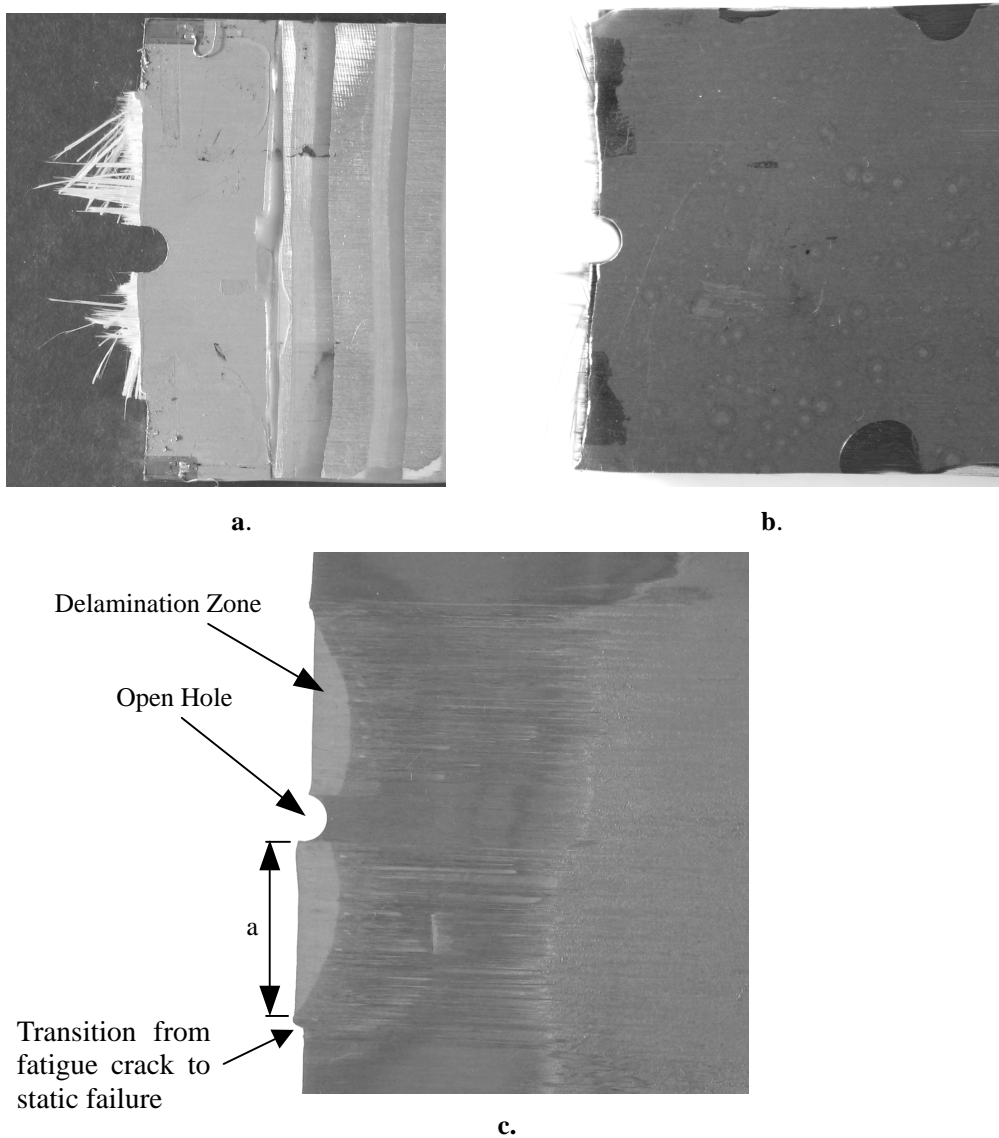


Figure 5.1: *MOHTB specimen destructive inspection. Following fatigue tests, the specimens were pulled apart (a) to expose the crack surfaces. The specimens were then heated to burn away the adhesive in the laminate (b). This allowed the aluminum plies to be separated and inspected (c).*

The large amount of crack growth data will not be presented here, but rather in Appendix D. To aid in the understanding of the experimental programs, summaries of the relevant data are given. As surface crack growth data is most plentiful, this data is presented first to offer a comparison to the analytical model. The quality of the comparison will lend confidence to the capabilities of the model to estimate

fatigue crack growth in a MOHTB specimen. Following the comparison of the surface crack data to the model prediction, all cracked plies of each specimen configuration will be compared to the analytical model.

5.2.1. Surface Crack Data

Typical surface crack propagation data is given in Figure 5.2 as crack length versus numbers of cycles for each specimen type tested. Surface crack propagation curves showed good repeatability, with standard deviations of the log of the number of cycles to reach a crack 20mm in length less than 0.2 for all specimen types. Scatter was apparent from specimen to specimen, but was well within the expected¹ variability experienced in fatigue testing. Two exceptions were MOHTB-1 and MOHTB-9, both of which had one side of the specimen crack at a somewhat lower rate than the rest of the like specimens. These deviations were not significant enough to deem them as outliers^{1,2}, and they were therefore left in the data sets. The standard deviations of the log of the number of cycles to propagate surface cracks to 10, 15 and 20mm were all less than 0.20, which is an indication of low scatter in the fatigue data sets.

The specimens selected for Figure 5.2 were those specimens with the longest surface crack length. Crack growth rates for the surface cracks were calculated using the Seven Point Polynomial Incremental method³. This method uses a second order polynomial to fit through seven successive data points. The midpoint of the curve designates the new placement of the fourth point in the data set. This process is repeated by advancing the set of seven data points by one, and is continued through all data points. The final data set of crack growth rates is truncated by three points at the beginning and end of the series by this method. This process smoothes the conditioned data set and can greatly reduce scatter. Engineering judgement must be used with this method, however, as any outlier in a data set will skew the smoothing process as long as the outlier is in the series of seven points.

As the majority of the specimens tested were 50mm wide, the greatest amount of surface crack data are for cracks less than 20mm. One G2A-5/4-0.4 specimen and two G2A-6/5-0.4 specimens were 100mm wide and provide the crack data beyond 20mm. Crack lengths were kept at or below 80% of the total specimen widths for all specimens. This helped to ensure that edge effects did not dominate the crack growth of the specimens. As the crack propagation curves show no acceleration in the surface fatigue cracks during the tests, the position taken that edge effects were minimal is supported.

Crack initiation values for the models of the three specimen types were taken as the initiation lives of the typical specimens plotted in the figure. The influence of subsurface crack initiation on surface crack propagation is discussed in each section pertaining to specific specimen configurations.

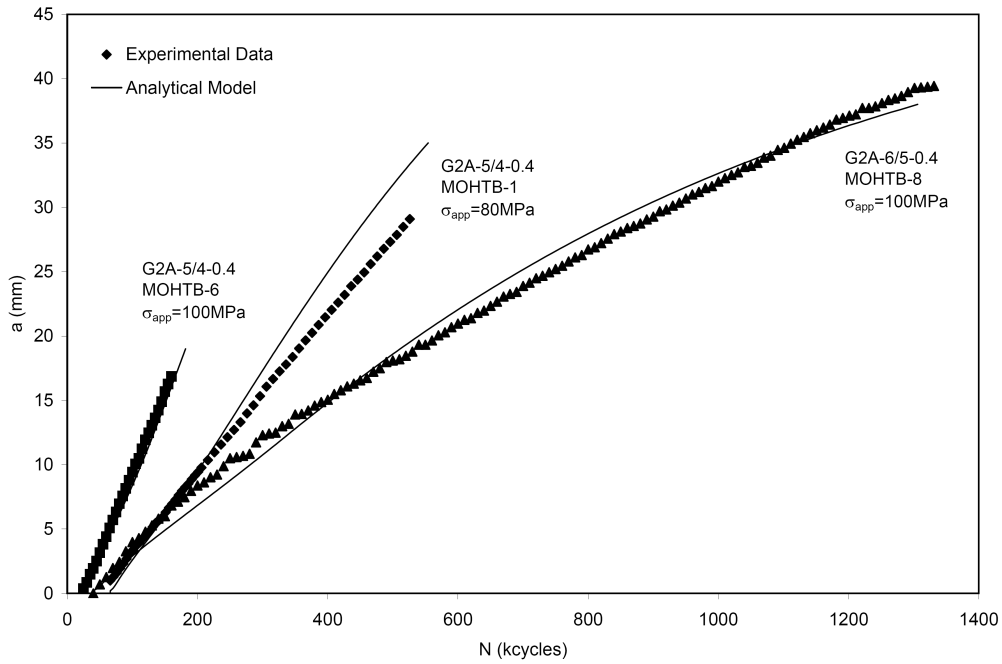


Figure 5.2: Surface crack propagation data for Glare 2 specimens. Data points taken from typical experimental data, and solid lines represent the analytical model.

The surface crack propagation data behave as one would expect. Comparing the 5/4 laminates, the specimens tested at 80MPa exhibit a slower crack growth rate than the laminates tested at 100MPa. As the cross-sections of the laminates are identical, resulting stresses in the aluminum plies in the test sections only differ due to the differences between the applied stresses. The 80MPa-applied stress generated resulting stresses of 225MPa, compared to the resulting stress of 250MPa generated by the 100MPa-applied stress. With the lower stresses in the specimens tested at 80MPa, the crack growth rates were correspondingly lower.

The laminates tested at 100MPa show similar trends, with the 6/5 laminates exhibiting slower crack growth rates than the 5/4 laminates. As the applied stresses are identical, the difference in crack growth rates must be explained by the cross section of the two laminates. The 6/5 laminate was thicker than the 5/4 laminate and therefore was stiffer in bending. This induced less secondary bending at the test section and resulted in lower stresses in the surface ply of the 6/5 laminate (200MPa). Additionally, both the 5/4 and 6/5 specimens were milled from a single sheet of 11/10 laminate. Therefore, the eccentricity of the 6/5 specimens was lower as the shift in the neutral line was less. This helped to induce less bending in the 6/5 specimens. This trend is to be expected, as the bending factor for the 6/5 specimens was 2.0, while the bending factor for the 5/4 laminate was 2.5.

An additional factor to explain the lower crack growth rate of the 6/5 laminate is the number of aluminum to fibre interfaces. For the thicker laminate, there were more interfaces, which resulted in more load transfer paths as more subsurface plies were cracked⁴. The greater the number of cracked aluminum plies, the greater the number of delaminations that offer load transfer paths. This resulted in less load transfer required per interface. While not as significant an effect for early part-through cracks, the significance increases as more plies are cracked.

The comparison of the analytical model overlaid on the surface crack cases in Figure 5.2 through Figure 5.5 show good agreement. As the analytical model only predicts crack propagation and not cycles to initiation, the model was started at the average number of cycles to crack initiation for the surface ply of each specimen. Comparing the G2A-5/4-0.4 specimens tested at 80MPa to the model in Figure 5.3 shows the weakest correlation of the group. While shorter crack behaviour is well predicted, the model over estimates the crack growth rate for cracks longer than approximately 10mm. Some of this deviation can be explained by looking at specimen MOHTB-1. The left hand crack on this specimen grew at a lower rate than the right hand crack. MOHTB-1 was the only 100mm wide specimen tested in this configuration. Therefore, the lower crack growth rate played a significant role in generating the surface crack growth averages for cracks longer than 20mm, as its data were the only ones used in forming the average.

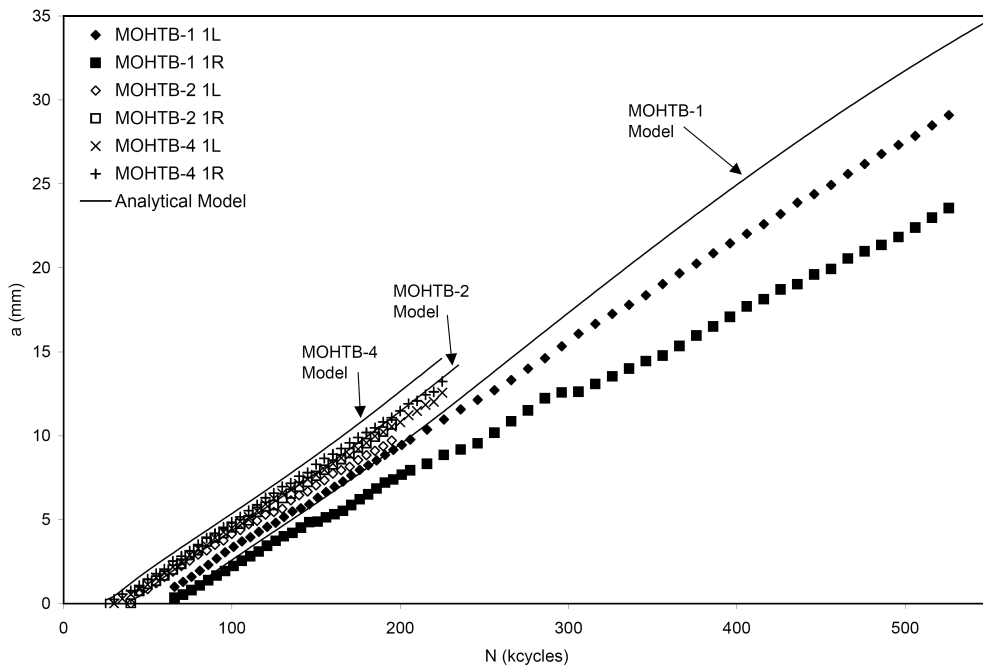


Figure 5.3: Surface crack propagation of G2A-5/4-0.4 MOHTB specimens tested at 80MPa. “L” and “R” are left and right-hand cracks. The solid lines represent the analytical model, started at the average crack initiation value.

Comparing the G2A-5/4-0.4 specimens tested at 100MPa to the model in Figure 5.4 shows a very tight correlation. However, as no 100mm-wide specimens were tested at this load level, the crack growth average only extends to 20mm. The model does track extremely well with the averaged data, as well as with each individual experimental data set.

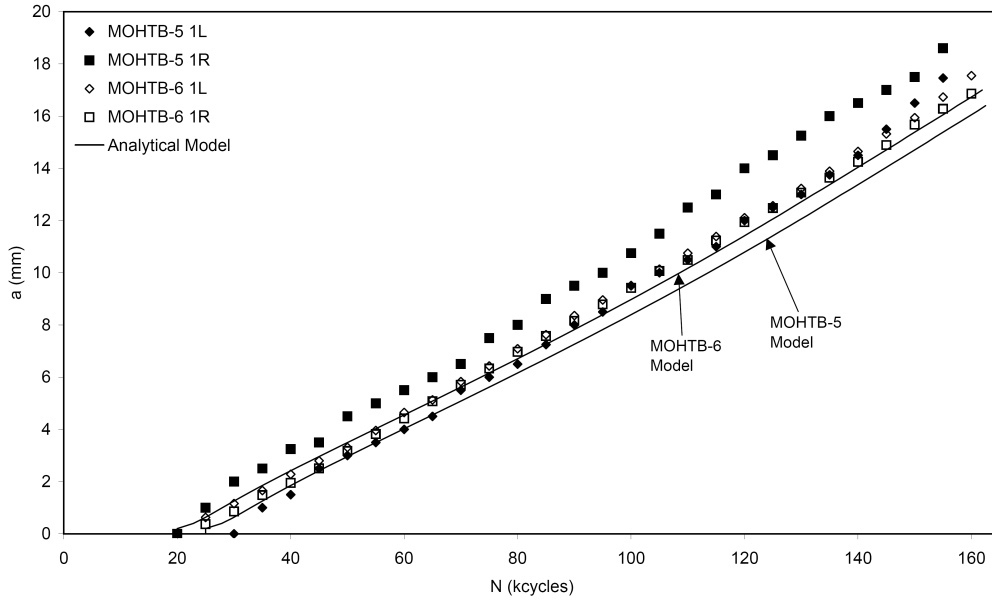


Figure 5.4: Surface crack propagation of G2A-5/4-0.4 MOHTB specimens tested at 100MPa. “L” and “R” are left and right-hand cracks. The solid lines represent the analytical model, started at the average crack initiation value.

Comparing the 5/4 laminate models, it is seen that the model accurately captures the increase in crack growth rate in going from 80MPa to 100MPa. This lends confidence to the idea that the fibre bridging stress distributions utilized in the model have been accurately described. While much of the shift in the slope of the experimental crack growth curves is due to the change in applied stress, the other contributing factor is the resulting fibre bridging stress distribution. The applied stress was well defined – both in the experiments and in the analytical model. The uncertainty was in the definition of the fibre bridging stress. Offsetting the shape of the fibre bridging stress distributions based on the resulting stress in a pristine specimen yielded accurate estimations. As the prediction was accurate for both stress levels, this supports the definitions of the shape and the magnitude of the distributions.

Comparing the G2A-6/5-0.4 specimens tested at 100MPa in Figure 5.5 to the model shows good correlation as well. All three specimens had nearly identical crack initiation lives, therefore, only one model prediction curve is presented. Similar to the G2A-5/4-0.4 specimens tested at 80MPa, one specimen had one crack that grew at a lower rate than the others that affected the data set. Without the slower crack included in the aggregate, the model prediction would slightly underestimate the whole of the experimental data. Regardless, the model tracks well with the experimental data.

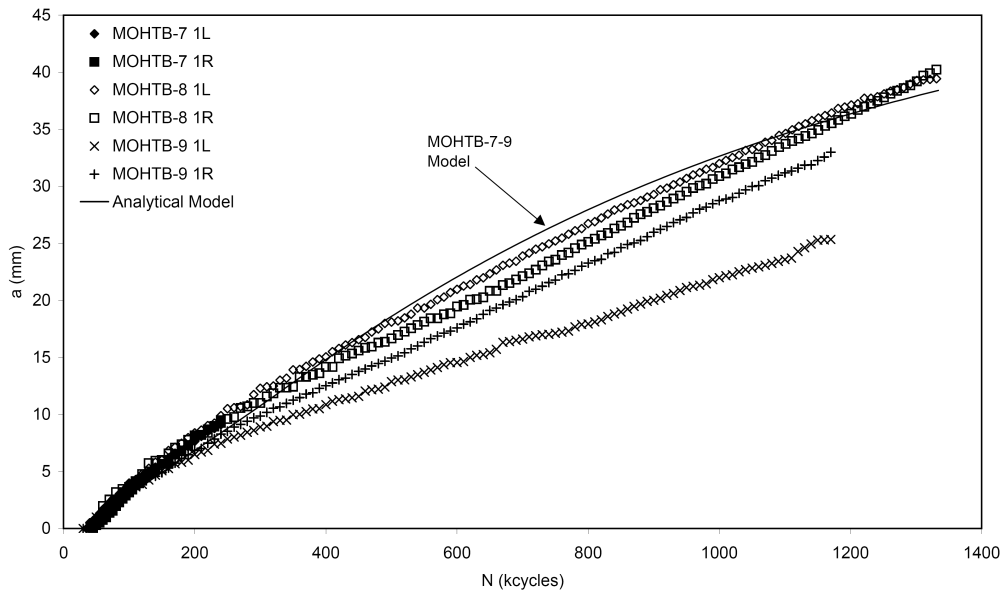


Figure 5.5: Surface crack propagation of G2A-6/5-0.4 MOHTB specimens tested at 100MPa. “L” and “R” are left and right-hand cracks. The solid line represents the analytical model, started at the average crack initiation value.

Comparing the laminate models tested at 100MPa, the drop in crack growth rate in going from a 5/4 laminate to a 6/5 laminate is accurately captured. This too lends confidence to the modelling approach of the using a single fibre bridging stress distribution shape regardless of applied stress or number of plies. The offsetting technique tied to the resultant stress in an aluminum ply to set the fibre bridging stress levels was effective in capturing the surface crack growth of tested configurations of Glare 2A.

5.2.2. Subsurface Cracks and Their Relation to Surface Cracks

Subsurface crack growth data consisted of only two points per aluminum ply: an initial crack length at the observed initiation point and the final crack length after the total number of cycles imposed. As samples were taken to various numbers of cycles (and crack length values), a relatively good indication of the subsurface crack

growth behaviour can be obtained by plotting the data from various samples in a single graph. To plot these data on a single graph, the cycles to crack initiation for each subsurface crack were normalized to a common value. That value was the average number of cycles beyond the initiation of a crack in the layer above. Subsurface crack data showed good repeatability, with crack initiation and growth rates tracking well from specimen to specimen. Scatter was again acceptable.

Figure 5.6 to Figure 5.10 show both surface and subsurface crack growth data. The surface data is taken from Figure 5.2 for the appropriate specimen. Subsurface crack data has been normalized to a common initiation life based upon the average time to initiate a crack in one ply from the initiation time in the previous ply.

Looking at the crack propagation data in Figure 5.6 for the G2A-5/4-0.4 specimens tested at 80MPa, the crack propagation distribution from surface to subsurface layers follows predictable trends. As expected, surface cracks initiated well before cracks in subsurface plies. Once surface cracks grew to approximately 5mm, a crack in the first subsurface ply would initiate. Once surface cracks grew to approximately 10mm and the first subsurface crack had grown to 4mm, a crack in the second subsurface ply would initiate. The amount of scatter in the subsurface cracks is evident in the figure, and is well within expected norms for fatigue testing. Crack initiation values for layer 2 were established by taking the average time from crack initiation in the surface ply to the initiation of a crack in the second ply. For the third layer, the crack initiation values were established by taking the average time from crack initiation in layer 2 to the initiation of a crack in the third ply.

One would expect to see an influence of subsurface crack initiation on surface crack propagation. As a crack initiates in a subsurface ply, more load would be transferred⁵ to the remaining net section of the surface aluminum ply – which should cause an increase in crack growth rate. However, no evidence of crack acceleration or deceleration was seen, either in the a versus N chart of Figure 5.6, or in the da/dN versus a chart of Figure 5.7. As the surface crack tip has grown away from the open hole by the time a subsurface crack has initiated, the influence of the subsurface crack tip is minimal. Any load transfer that would theoretically be seen on the surface aluminum ply is carried by the prepreg plies in the wake of the surface ply delamination zone.

5 Validation of Model Against Experimental Data

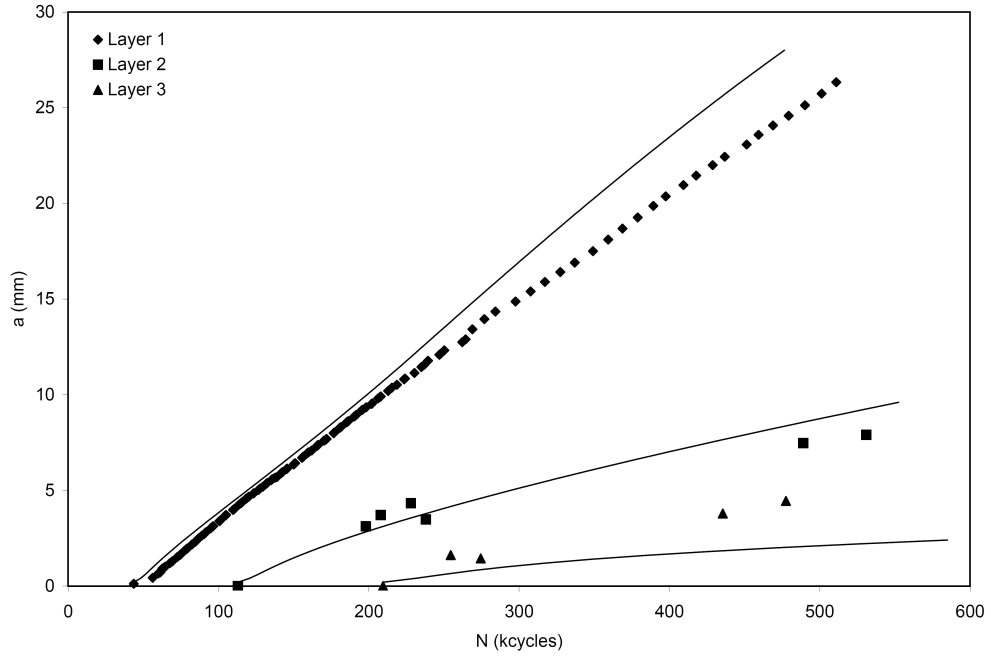


Figure 5.6: *G2A-5/4-0.4, $\sigma_{app}=80\text{MPa}$. Typical surface crack data, all subsurface data from normalized crack initiation values. Solid lines represent the analytical model for each ply.*

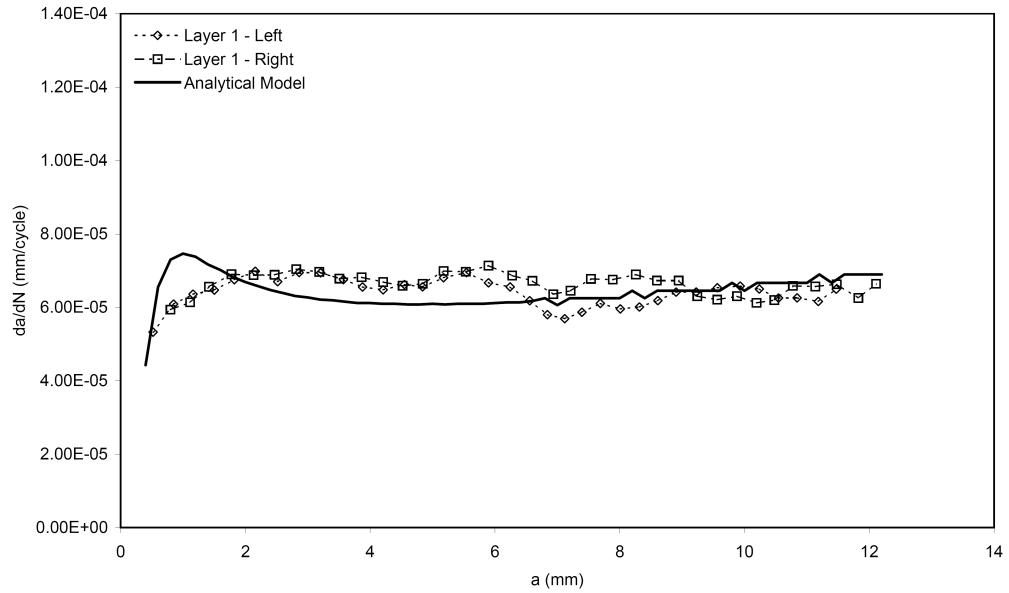


Figure 5.7: *Typical da/dN vs. a curves for G2A-5/4-0.4 MOHTB tested at 80MPa. Data points are conditioned with the Seven Point Polynomial Incremental method³. Solid line is analytical prediction.*

Comparing the analytical model to subsurface crack data shows good correlation. Looking specifically at the first subsurface crack data, the model accurately estimates the slightly more rapid crack growth rate for the crack up to approximately 3mm, and slowing down to match the crack growth rates for longer cracks. This change in the crack growth rate can be attributed to the fact that for very short cracks, the stress riser due to the open hole⁶ causes faster crack growth. Additionally, in Glare, cracks less than approximately 2mm in length have not developed a significant delamination from the glass fibre plies. Without the delamination the fibres cannot effectively bridge the crack and slow the crack growth rate¹. For these short cracks, the crack growth behaviour matches that of monolithic aluminum, rather than that of a fibre metal laminate.

Looking at the second subsurface crack data, the model underestimates the actual crack growth. The model does trend correctly, showing a very slight decrease in the crack growth rate similar to that seen in the model for the first subsurface crack. The second subsurface crack represents a ply with much lower stress resulting from the applied load due to the secondary bending in the MOHTB specimen. With the lower resultant stress near the open hole in this ply the relative drop in stress away from the open hole will be less than that seen in the surface or first subsurface ply.

Looking at the crack growth data for the G2A-5/4-0.4 specimens tested at 100MPa in Figure 5.8, the crack growth distribution from surface to subsurface layers follows the same trends discussed for the 5/4 specimens tested at 80MPa. Again, good repeatability and consistency is apparent for the subsurface data. All specimens tested in this configuration were 50mm wide. Therefore, no surface crack data exists for cracks longer than 20mm, and consequently subsurface crack data is for a small range of crack lengths. The same methodology for finding the average subsurface crack initiation values as was used for the previous specimens was used.

No influence of subsurface crack initiation on surface crack propagation is seen in this series of specimens. As can be seen in the a versus N chart of Figure 5.8 and in the da/dN versus a chart of Figure 5.9, no crack acceleration is apparent due to subsurface crack initiation.

5 Validation of Model Against Experimental Data

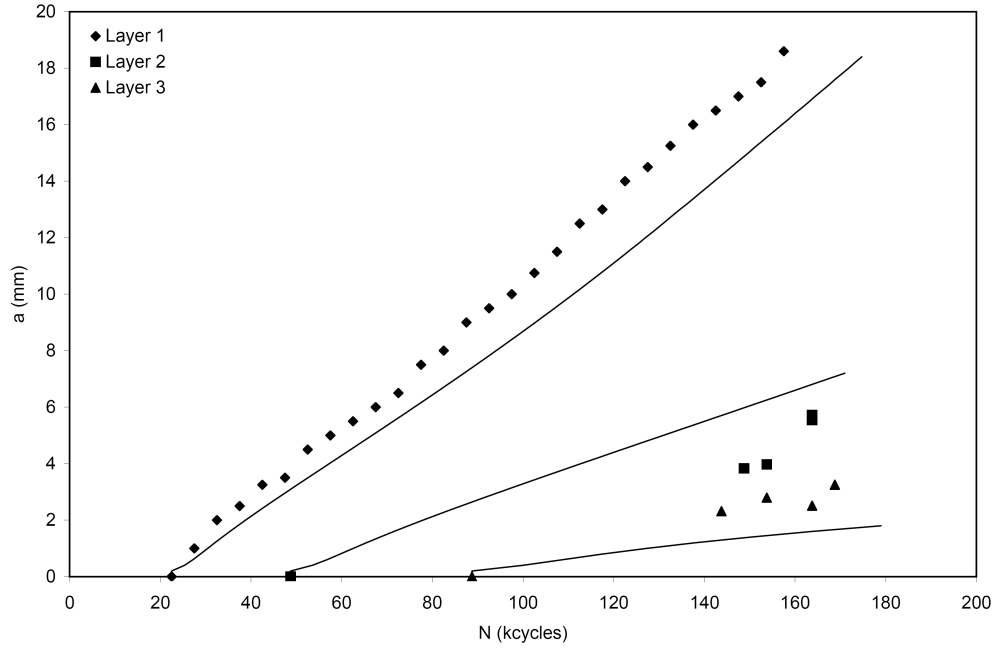


Figure 5.8: Crack growth curve; G2A-5/4-0.4, $\sigma_{app}=100\text{MPa}$. Typical surface crack data, all subsurface data from normalized crack initiation value. Solid lines represent the analytical model for each ply.

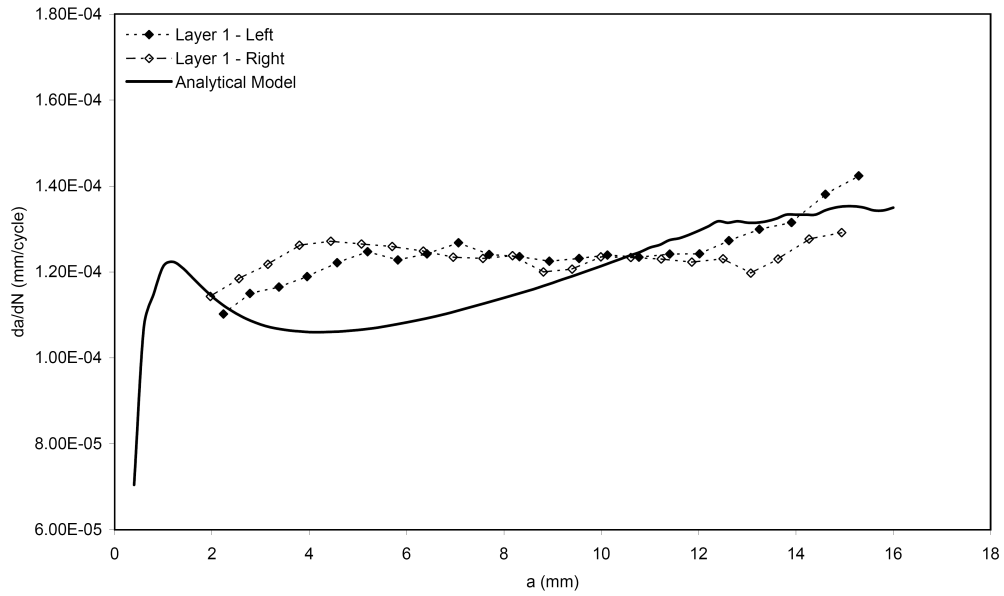


Figure 5.9: Typical da/dN vs. a curves for G2A-5/4-0.4 MOHTB tested at 100MPa. Data points are conditioned with the Seven Point Polynomial Incremental method³. Solid line is analytical prediction.

Comparing the analytical model to subsurface crack data again shows good correlation. For the first subsurface crack, the model overestimated the crack growth rate. The decrease in crack growth rate apparent in the first subsurface ply in the 5/4 specimen tested at 80MPa is not present in the specimen tested at 100MPa. This is most likely due to the fact that the crack had not yet grown away from the stress riser of the open hole. The model underestimated the crack growth rate for the second subsurface crack. The same discussion from the 5/4 specimen tested at 80MPa applies to this analysis.

Looking at the crack growth data for the G2A-6/5-0.4 specimens tested at 100MPa in Figure 5.10, the crack growth distribution from surface to subsurface layers follows the same trends discussed previously. Again, good repeatability and consistency is apparent for the subsurface data. Specimens tested in this configuration were both 50mm and 100mm wide. Therefore, subsurface crack data is available for both shorter and longer crack lengths. The same methodology for finding the average subsurface crack initiation values in previous specimens was used.

Similar arguments as to the influence of subsurface crack initiation on surface crack growth rates can be made for the 6/5 specimens as were made for the 5/4 specimens. Again no evidence of crack acceleration are apparent in the a versus N , or da/dN versus a charts in Figure 5.10 and Figure 5.11 due to subsurface influence. Crack initiation times were closer together for the 6/5 laminates than for the 5/4 laminates. However, this can be explained by the fact that the differences between the net stresses in the three plies of aluminum in the 6/5 laminate were less than in the 5/4 lay-up. With these stresses being closer in value to each other, similar crack initiation times are expected.

5 Validation of Model Against Experimental Data

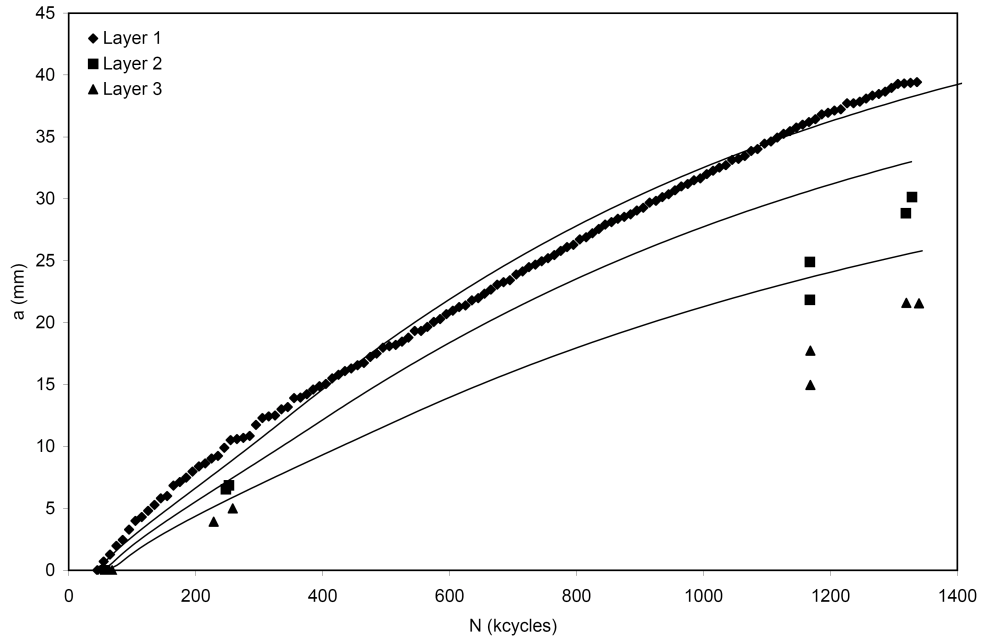


Figure 5.10: Crack growth curve; G2A-6/5-0.4, $\sigma_{app}=100\text{MPa}$. Typical surface crack data, all subsurface data from normalized crack initiation value. Solid lines represent the analytical model for each ply.

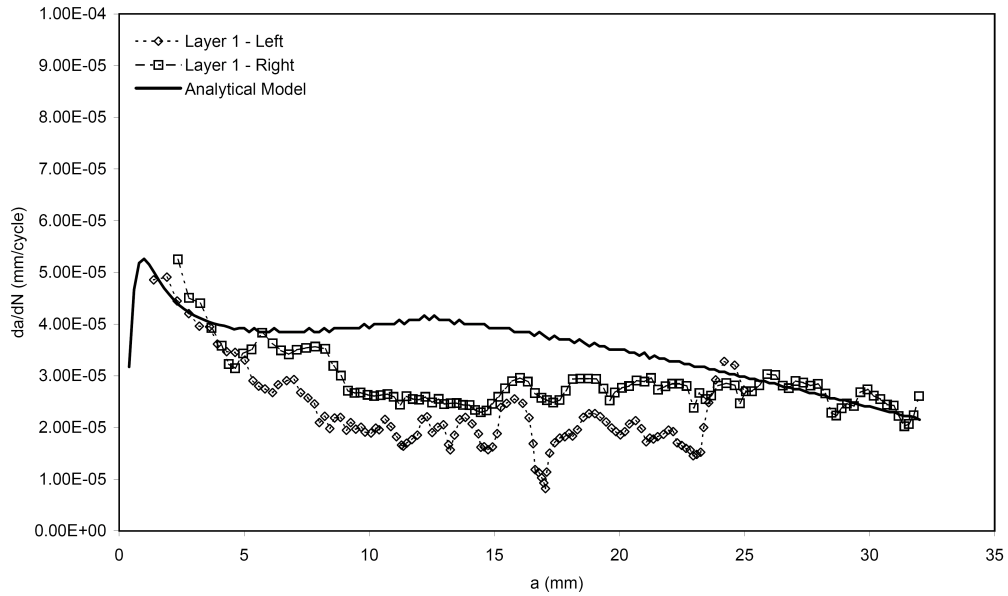


Figure 5.11: Typical da/dN vs. a curves for G2A-6/5-0.4 MOHTB tested at 100MPa. Data points are conditioned with the Seven Point Polynomial Incremental method³. Solid line is analytical prediction.

Comparing the analytical model to subsurface crack data again shows good correlation. For second layer subsurface cracks, the model accurately predicted the shorter crack growth and then slightly overestimates the longer crack growth rates. The deceleration of the crack growth rate is again apparent in these specimens, evidenced by both the experimental data and the analytical prediction.

Looking at the model for the third layer subsurface cracks, the model overestimates the crack growth rate – slightly for the shorter cracks, and more significantly for longer cracks. The same trend to decelerate for longer cracks is again illustrated in the experimental data and analytical prediction.

In total, the analytical model effectively predicted the crack growth in all plies of each specimen tested. The model utilized no correction factors for lay-up or depth location. The simple tuning of the model to the resultant stress in the ply of interest effectively calibrated the model to all of the test conditions investigated.

A complete listing of all test data acquired and crack growth curves generated for all MOHTB specimens is found in Appendix D.

5.3. Four Point Bend

From the recorded data sets of surface and subsurface crack length versus the number of cycles, crack growth data were generated, as shown in Table 5.3. Crack growth rates for the surface cracks were calculated using the Seven Point Polynomial Incremental method³. The time to crack initiation for each layer was reasonably consistent across the specimens, taking into consideration the scatter expected from fatigue tests.

Table 5.3: *Recorded fatigue crack results for four point bend tests. G2A-11/10-0.4, $\sigma_{resultant} = 200\text{MPa}$.*

Specimen ID	Side	Layer 1		Layer 2		Layer 3	
		$N_{init} N_{final}$ (kcycles)	$a_{init} a_{fin}$ (mm)	$N_{init} N_{final}$ (kcycles)	a_{fin} (mm)	$N_{init} N_{final}$ (kcycles)	a_{fin} (mm)
4PT-01	L	58 248	1.0 10.2	138 248	3.4	168 248	2.1
	R	118* 248	2.5 9.1	148 248	3.3	198 248	1.5
4PT-02	L	90 350	0.4 14.7	200 350	3.4	220 350	2.6
	R	100 350	0.5 15.0	200 350	3.5	220 350	2.7
4PT-03	L	50 310	0.6 13.4	80 310	4.4	170 310	1.5
	R	40 310	0.6 13.8	120 310	2.7	230 310	0.9
4PT-04	L	80 290	0.5 7.3	190 290	2.6	280 290	0.5
	R	80 290	0.9 8.5	190 290	3.3	220 290	2.1

*: Cycles to crack initiation not captured accurately. Most likely occurred between $N=75$ -100kcycles.

Each specimen was destructively inspected, following the techniques detailed in Chapter 3. Tear down of the specimens showed fatigue cracks in several aluminum plies of the specimens. Figure 5.12 illustrates this, with one quarter of a specimen

shown. The surface cracked ply is furthest to the right. One quarter of the open hole can be seen in the bottom corner of each ply. The surface fatigue crack is identified in the figure. Subsurface fatigue cracks are in similar positions in subsequent plies. The specimens were pulled apart in a static failure at the end of the fatigue tests in the same manner as the MOHTB specimens. This exposed the fatigue cracks for measurement, following the procedures discussed in Chapter 3.

Similar to the fatigue cracks in the MOHTB specimens described in Section 5.2, the cracks in the four point bend specimens were longest at the surface ply and grew progressively shorter for the deeper subsurface plies. For the four point bend test, the load applied is entirely of a bending nature – no additional tensile load is applied. The specimens were loaded until strain gage measurements showed the surface ply of the specimens had reached 200MPa. This value was chosen to approximate the stress level found in the surface plies of the MOHTB specimens.

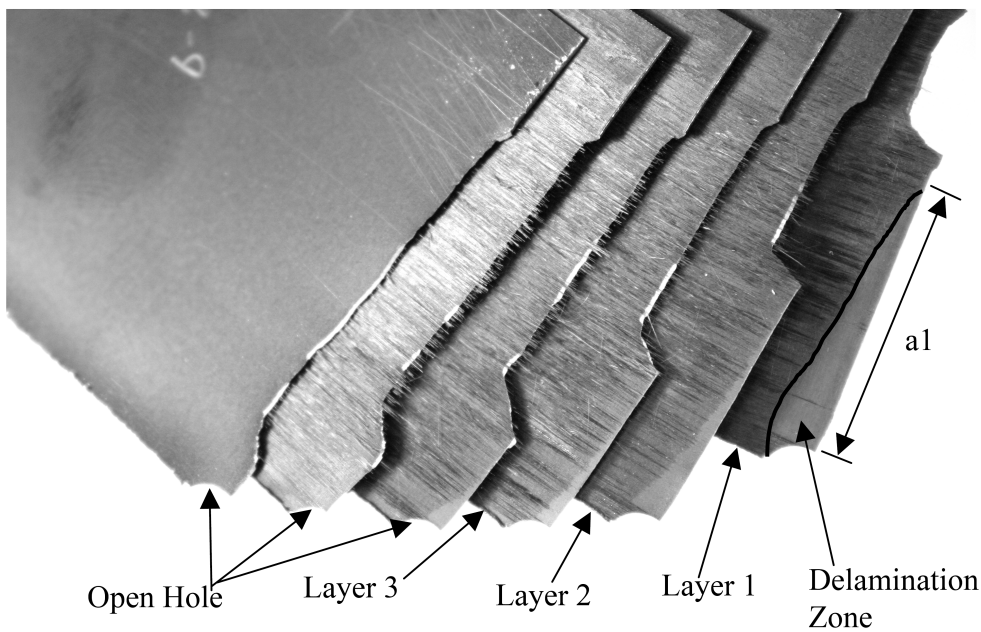


Figure 5.12 Teardown of four point bend specimen. One quarter of the specimen is shown. Surface cracked ply is furthest right.

The specimens were constructed from Glare 2A-11/10-0.4, and therefore were significantly thicker than the test sections of the MOHTB specimens. This increase in thickness was intentional to maximize the distance from the surface of the specimen to the neutral line. This allowed for higher stresses in the second and third subsurface plies of aluminum than would have been seen in a laminate with fewer

plies. These higher stresses were desired to generate significant crack growth rates in the subsurface plies.

Fatigue cracks initiated at a reasonably consistent number of cycles for each layer. Crack growth rates did not exhibit the same trend of rapid short crack growth and tapering off to slower levels as shown in MOHTB specimens, detailed in Section 5.2. All specimens were 50mm wide, and the open hole diameter was increased to 6.8mm diameter to accommodate an eddy current probe as discussed in Chapter 3. During testing, strain gage data was recorded to ensure the resulting stress at the center of the specimen remained consistent and that no significant plastic deformations occurred in the specimens.

Similar to Section 5.2, the individual crack propagation data will not be presented here, but rather in Appendix D. Summaries of the relevant data are given in Figure 5.13. The figure shows a typical surface crack propagation curve from specimen 4PT-03. Subsurface crack growth data points are superimposed for each specimen tested. The subsurface data show points for every crack - both cycles to crack initiation and final crack lengths. Cycles to crack initiation for a given subsurface ply are the average value for all the specimens.

Average crack initiation time for the surface ply are about 3.25 times shorter than literature data⁷. For the second ply the comparison fell within a factor of 1.8, and for the third ply the experimental data was off by a factor of 0.87. The literature data was for aluminum sheet subjected to pure tension, with comparable stress concentrations. The above factors were calculated by comparing the average crack initiation values for the plies of all the specimens.

Subsurface crack data showed good repeatability, with crack initiation and growth rates tracking well from specimen to specimen. Scatter was apparent from specimen to specimen, but was well within the expected variability experienced in fatigue testing, with the standard deviation of the propagation lives to 10.0mm cracks less than published limits¹, $\sigma_{\log_{N_{10}}} < 0.20$. Looking at the data, the crack growth distribution from surface to subsurface layers follows the same trends discussed for the MOHTB specimens of a cascade of fatigue cracks forming, starting with the surface ply and proceeding to the subsurface plies.

5 Validation of Model Against Experimental Data

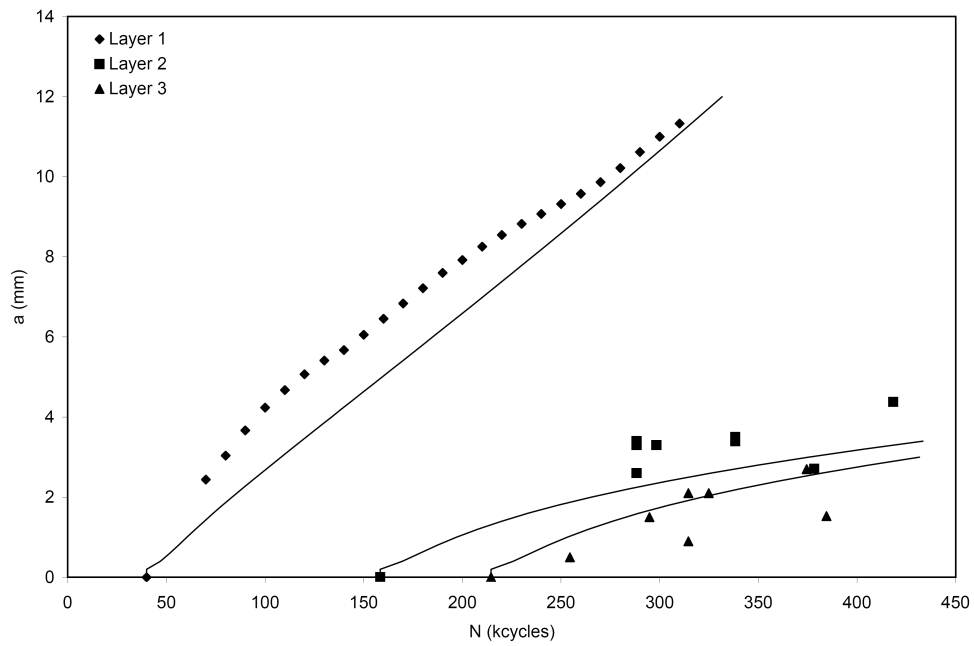


Figure 5.13: Four point bend crack growth curves. Typical surface crack data, all subsurface data from normalized crack initiation value. Solid lines represent the analytical model for each ply.

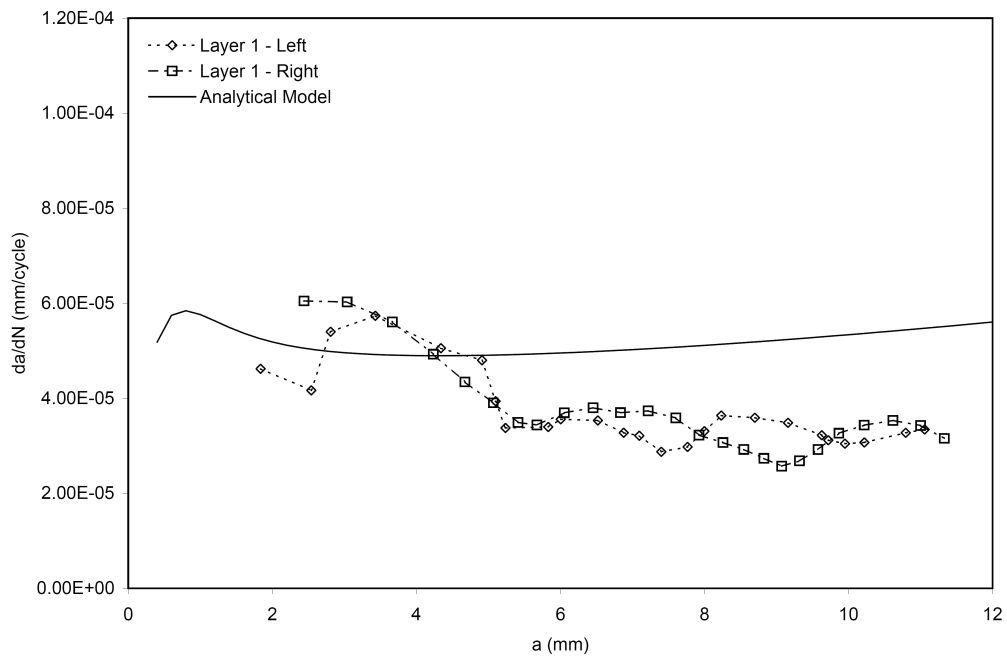


Figure 5.14: Typical da/dN vs. a curves for G2A-11/10-0.4 four point bend specimen 4PT-03 tested at 200MPa. Data points are conditioned with the Seven Point Polynomial Incremental method³.

Comparing the analytical model to the experimental data, a good correlation is found. The model matches the surface crack growth in the slope of the crack growth curve, though the initially more rapid crack growth shown in the experimental data is not reflected in the model.

Looking at the model prediction for the second layer subsurface cracks, the model accurately estimates the crack growth rate of the experimental data, with the model passing through the bottom of the crack data. The trend of the crack growth rate to decelerate for longer cracks is again illustrated in the analytical prediction, but is not as evident in the experimental data.

Looking at the model for the third layer subsurface cracks, the model accurately estimates the crack growth rate of the experimental data, with the model passing through the top of the crack data.

5.4. Model Sensitivity

As discussed in Chapter 4, the crack lengths and delamination shape surveys from each specimen tested were used as FEM inputs. The FEM runs generated fibre bridging stress distributions. These distributions were used to define the stress intensities within the analytical model. The fibre bridging stress distributions were all represented by the same shaped curve in the analytical model – only offset by a constant factor of the resultant stress in the aluminum ply of interest. This allowed for the stress intensity factor generation in the model to be defined with minimal required knowledge of the stress state within the laminate.

To gain insight into the model's sensitivity, the G2A-6/5-0.4 MOHTB specimen tested at 100MPa was used as a reference. A variety of parameters were investigated to establish the effects of changes to the model's accuracy. Six studies were conducted, as shown in Table 5.4, and each is described below.

Table 5.4: Sensitivity study parameters. Parameter variations with respect to base model settings.

Model Parameter	Lower Bound	Upper Bound
σ_{res}	-10%	10%
$\Delta\sigma_{flank}$ due to ΔN_i	Varied by layer	Varied by layer
σ_{flank}	- 5%	+5%
σ_{tip}	-50%	+10%
$b(x)$	Triangular	Elliptical
K_{OH} to K_{CC}		

Resultant Stress

The model's sensitivity was determined by adjusting the input parameter of the resultant stress, σ_{res} , in the aluminum ply of interest. For the surface crack, Figure 5.15 shows this sensitivity for σ_{res} values deviating from the FEM results by 0.0%, 1.0%, 5.0%, and 10%.

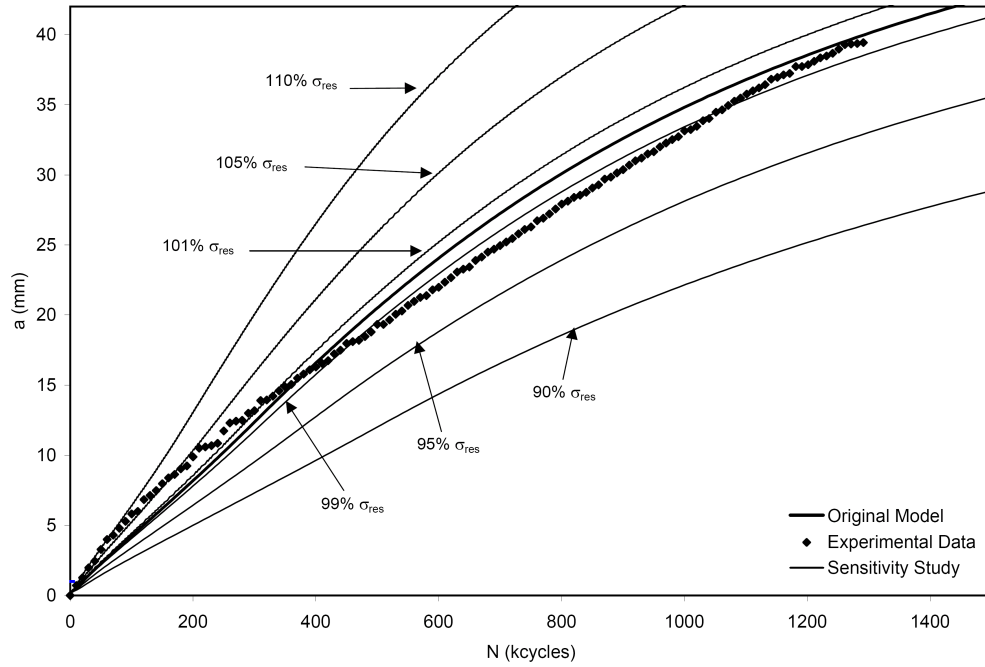


Figure 5.15: Crack propagation predictions for varied input values of resultant stress. Surface crack data for G2A-6/5-0.4 MOHTB specimen tested at 100MPa.

An alternate way of viewing the above data is given in Figure 5.16, which shows the number of cycles for the analytical model to reach a range of crack lengths for each of the cases displayed in Figure 5.15. This figure shows the near-linearity of the variance in the predictions for shorter cracks. The variance increases in severity for longer cracks, as would be expected as the variance is simply a result of the Paris law formulation for the crack growth prediction. By varying the applied stress to an aluminum ply, the crack growth rate will change, and the longer that applied stress is varied from the true value, the greater the deviation from the experimental data. The amount of that deviation also plays a dominant role, and it can be seen that for small deviations from the true value, the predicted crack growth rate is close to the experimental data. This lends confidence to the assertion that the model is stable, and that for a known deviation from the σ_{res} value found in the FEM, the change to the crack growth rate is predictable.

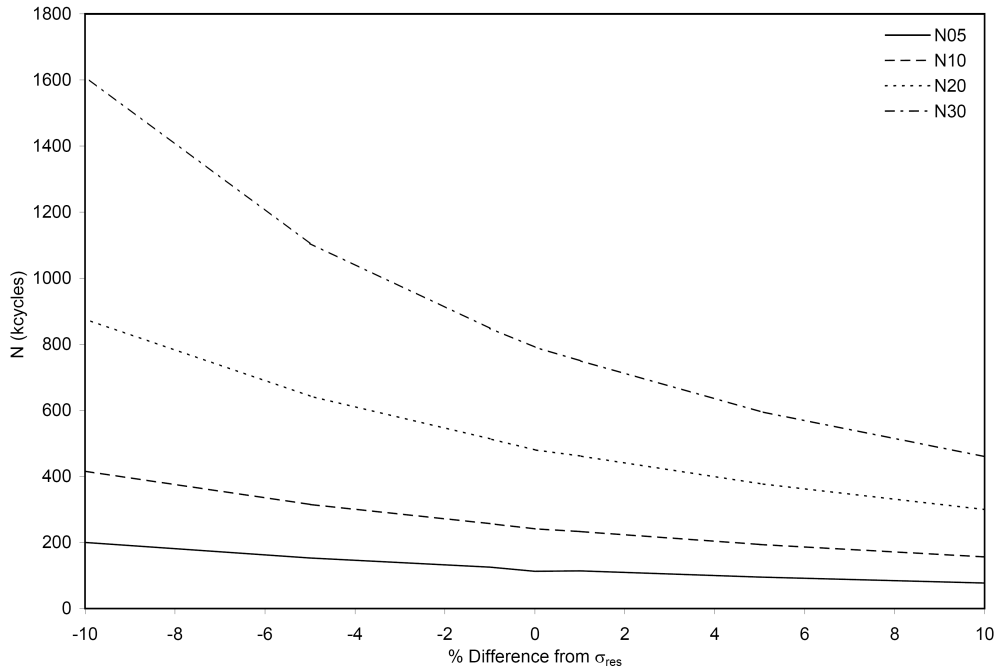


Figure 5.16: Plot of predicted number of cycles to reach surface crack lengths of 5, 10, 20, and 30mm in G2A-6/5-0.4 MOHTB specimen tested at 100MPa for different input values of σ_{res} .

For all surface crack models, it must be noted that the predicted crack growth rates eventually reduce to zero, i.e. the crack propagation curves in Figure 5.15 all eventually reach a horizontal asymptote. This is due to an overestimation in the fibre bridging stress distribution for longer cracks used as an input by the model – specifically the flank stress. This is unrealistic and can only be corrected by extending the fibre bridging stress distributions in the model for cracks longer than those investigated. To legitimately extend these distributions, experiments would be required to generate cracks in the surface and subsurface plies longer than those tested here. With those longer crack lengths in hand, FEM models could be generated to determine how to appropriately modify the fibre bridging stress distributions.

Varying Initiation Life

In addition to varying the resultant stresses in the aluminum layers to determine the model's sensitivity, effects of the crack initiation times and crack propagation rates in the sub layers were also investigated. This, in effect, investigated the sensitivity of the fibre bridging stress distribution to the crack distributions. To determine appropriate variations in fibre bridging stresses, the experimental data was reviewed to determine the extreme scenarios for fatigue crack distributions in the various specimens. Finite element models were constructed for these extremes, and fibre bridging stress distributions were extracted.

For the first extreme scenario, cracks were inserted in the FE models that corresponded to the shortest time to crack initiation and fastest crack growth. Conversely, for the second extreme scenario, cracks were inserted in the FE models that corresponded to the longest time to crack initiation and slowest crack growth. This methodology was used to develop a set of FE models for each specimen type. These sets of extreme-case models had surface and subsurface crack sets introduced with surface cracks ranging from 5.0mm to 30mm.

The fibre bridging stress distributions were extracted from each model, and the same methodology to determine analytical approximations for σ_{flank} and σ_{tip} were used. The same shape of stress distribution was observed for both scenarios. The same formulation for σ_{flank} was found – though offset from the base formulation. These two case studies resulted in variations in σ_{flank} of +/- 5.0%, and no variation in σ_{tip} . These variations in σ_{flank} were introduced into the analytical model, and crack propagation predictions acquired. The crack initiation lives for these predictions were kept the same as that for the base model. This allowed an evaluation of the effects of the investigated fibre bridging stress distributions on the crack propagation characteristics of the model. These predictions are shown for the G2A-6/5-0.4 MOHTB specimens tested at 100MPa in Figure 5.17 to Figure 5.19 for the surface layer, layer 2 and layer 3 respectively. Similar variations were evident in all specimens.

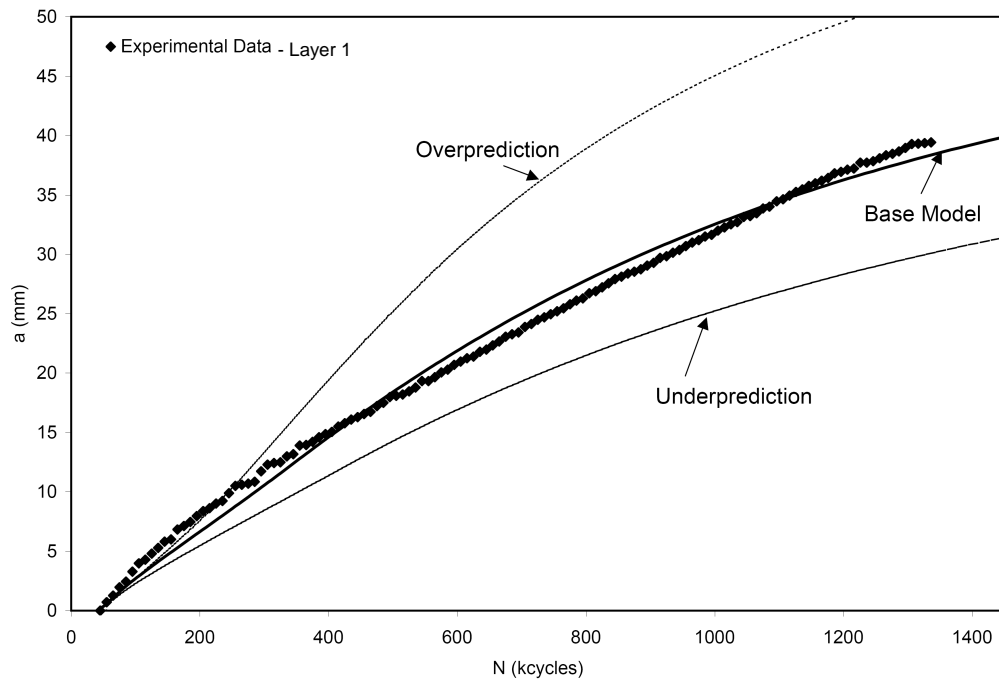


Figure 5.17: Analytical model sensitivity to +/- 5% variation in σ_{fibre} . Surface crack propagation prediction for G2A-6/5-0.4 tested at 100 MPa. $N_{init}=45$ kcycles.

For all layers, the model shows sensitivity to underestimating the fibre bridging stresses. Overestimating the fibre bridging stresses also has a marked effect on the model.

This sensitivity study lends confidence to the formulation of the fibre bridging stress used for the base model. The base formulation was a fit of all experimental data, and not a fit on the extremes of the experimental data. As the base formulation more accurately predicts crack propagation for all specimens, it follows that the base formulation is the best fit of the experimental data available.

5 Validation of Model Against Experimental Data

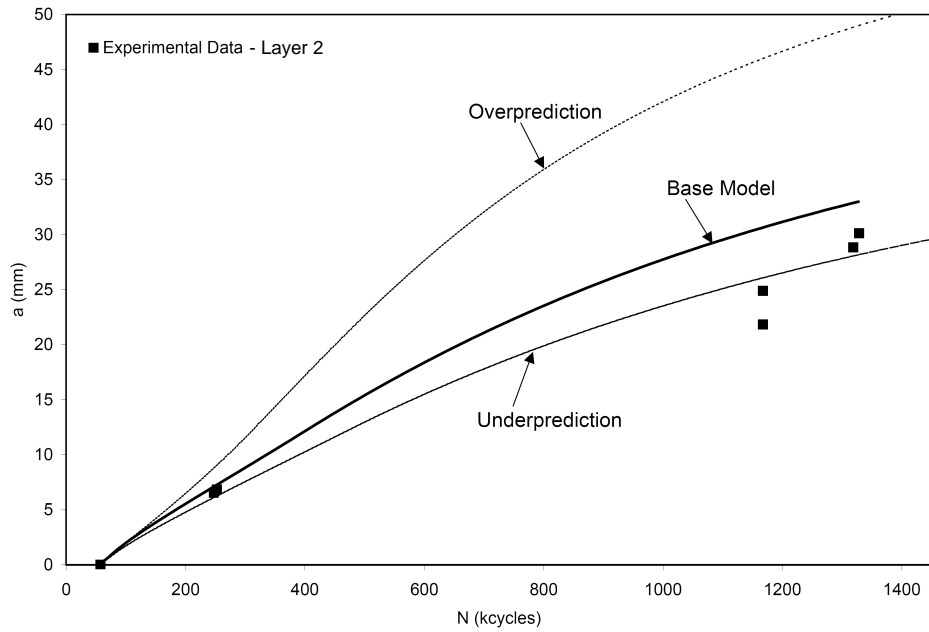


Figure 5.18: Analytical model sensitivity to $\pm 5\%$ variation in σ_{flank} . Layer 2 crack propagation prediction for G2A-6/5-0.4 tested at 100 MPa. $N_{init}=58$ kcycles.

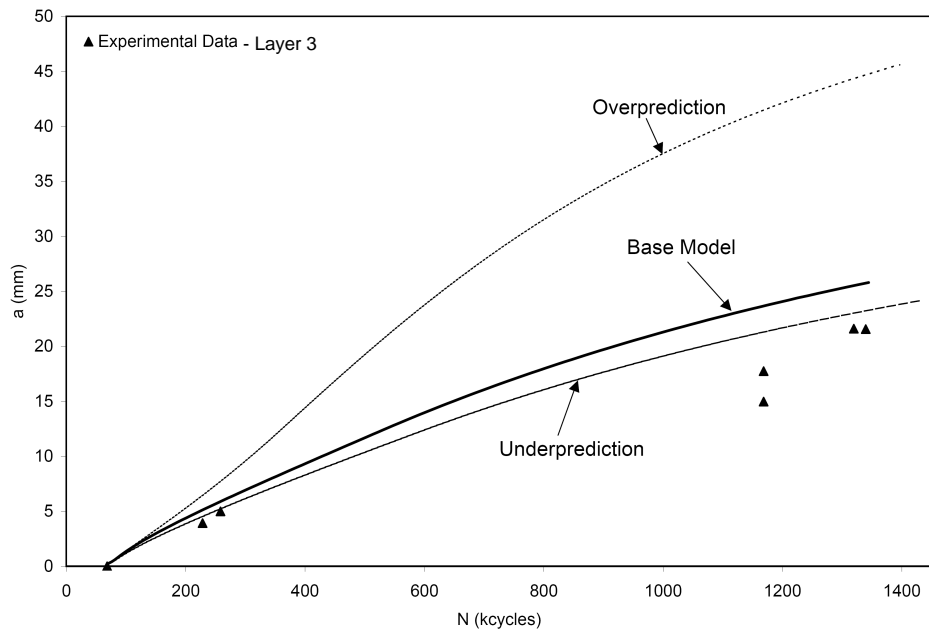


Figure 5.19: Analytical model sensitivity to $\pm 5\%$ variation in σ_{flank} . Layer 3 crack propagation prediction for G2A-6/5-0.4 tested at 100 MPa. $N_{init}=68$ kcycles.

Flank Stress

From Figure 4.10, variations in the shape of the flank stress curves are evident. A sensitivity study was conducted to evaluate the effects of utilizing the upper and lower bounds of the data in Figure 4.10 as the basis for the formulation of σ_{flank} . The bounds were determined by applying the same fitting procedure through the flank stress data obtained from FEA. The upper and lower bounds were found by fitting to the extremes of the data. A $\pm 5\%$ shift in the σ_{res} term in Equation 4.7 was required to capture the limits of the data.

Figure 5.20 clearly shows a strong dependence of the crack growth rate on the flank stress for all lengths of cracks. This response is expected, as the fibres bridging the flank of the crack resist the crack from opening. Variations to that resistance will effect the fatigue propagation characteristics of the laminate. While sensitive to variations, the figure shows that the approximation incorporated in the model was justified.

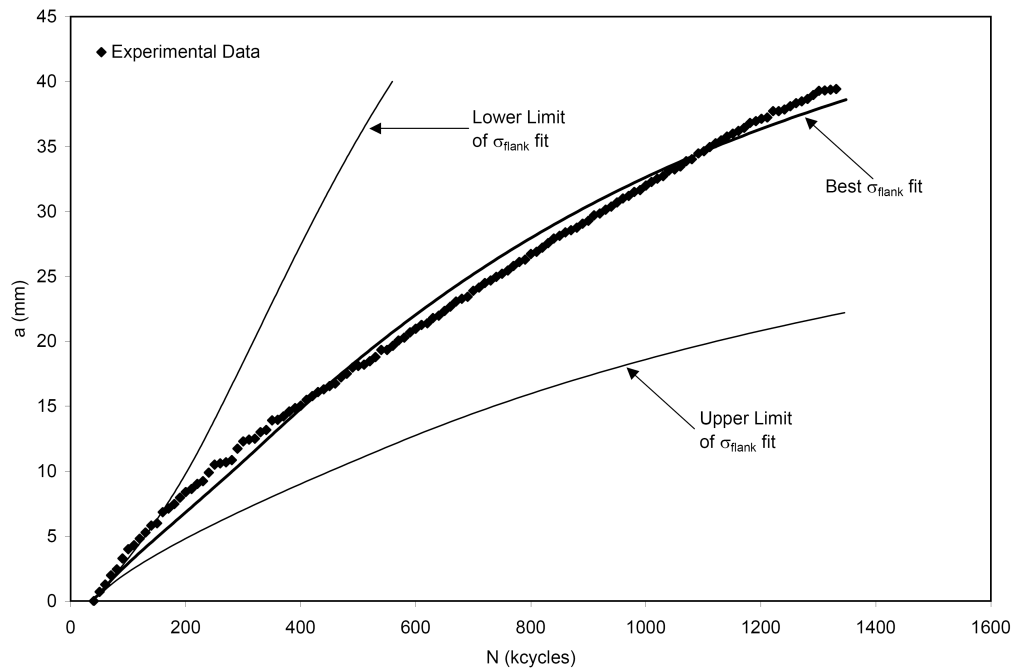


Figure 5.20: Effects of changes to the flank stress approximation on the crack propagation model.

Tip Stress

A sensitivity study was conducted to evaluate the effects of changing the tip stress approximation on the crack growth prediction. The original approximation was 90% of the blunt notch strength of the glass fibres. This was deemed justified from the FE analyses, which showed tip stress in excess of the failure strength of the fibres in many cases. Conversely, several models showed tip stresses well below the failure strength. Information from the FE analyses regarding the state of the fibres in the region of the tip of the crack were dependent upon the FE model itself, though all showed a sharp spike in the stress values in the vicinity of the crack tip. An engineering judgement was required to establish the tip stress, and thus a value of 90% was selected, as this value was below the failure limit of the fibres, but still significantly higher than the flank stress values found in all FE analyses.

For the study, the value of the tip stress was varied. The upper bound of the study had the tip stress at the failure limit of the fibres. The lower limit was 45% of the failure limit of the fibres. The results of the study, shown in Figure 5.21, show the effects of changing the tip stress values. By comparing Figure 5.21 to Figure 5.20, the effects of changes to the tip stress are seen to be less than those due to changes to the flank stress. A reduction in the tip stress of ten percent resulted in a 10.1% increase in crack length at 1.4 million cycles over the original prediction.

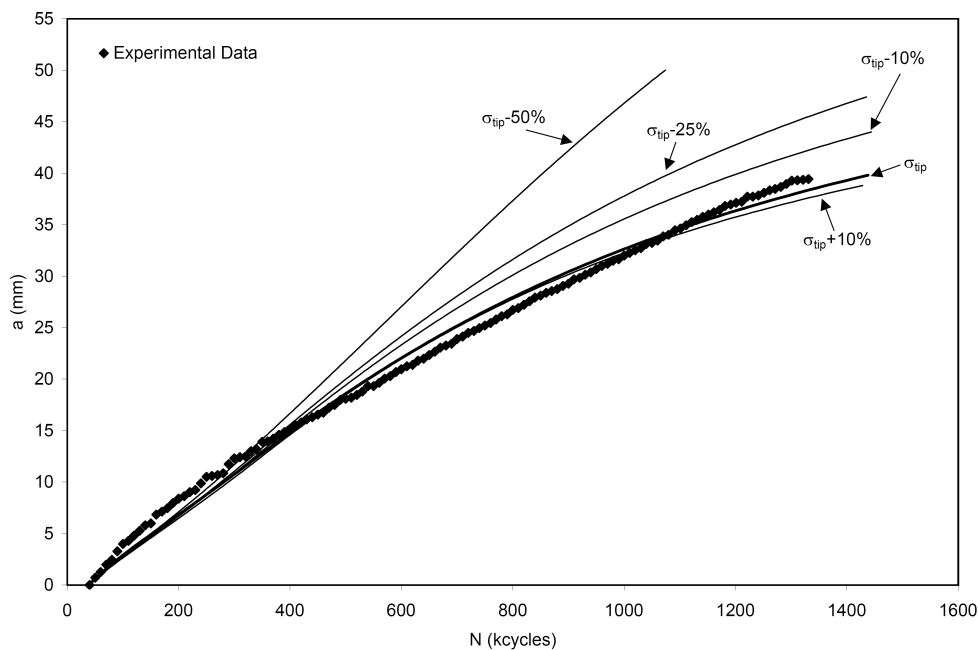


Figure 5.21: *Effects of changing the tip stress approximation on the crack growth prediction.*

Delamination Shape

Figures 4.3 b-e show variations in the shape of the delamination, based upon the specimen type tested. A cosine approximation was selected to represent all the data from the investigation. A sensitivity study was conducted to evaluate the effects of that approximation on the crack growth prediction model. Prior models^{8, 9, 10} have utilized either an ellipse or triangle to describe the delamination shape in FMLs, and Alderliesten¹¹ showed analytically that the delamination shape for Glare does fall between these two shapes. The sensitivity study used these two shapes as bounds for determining the sensitivity of the current model to the delamination shape.

The elliptical approximation had a major axis equal to the crack length, and a minor axis of 0.2 times the crack length. The triangular approximation had a slope of 0.2. Both of these approximations have been used in the past as representations of the delamination shape in Glare. Figure 5.22 shows the effects on the crack growth prediction of the delamination assumptions. As expected, the triangular delamination shape had a lower crack growth rate – as the shorter lengths of delaminated fibres would result in greater fibre bridging stress for a given COD. Conversely, the elliptical delamination shape had longer lengths of delaminated fibres in comparison to the cosine shape in the regions away from the open hole. As the delamination shape used in the model was a better representation of all the experimental data, its use in the model is justified.

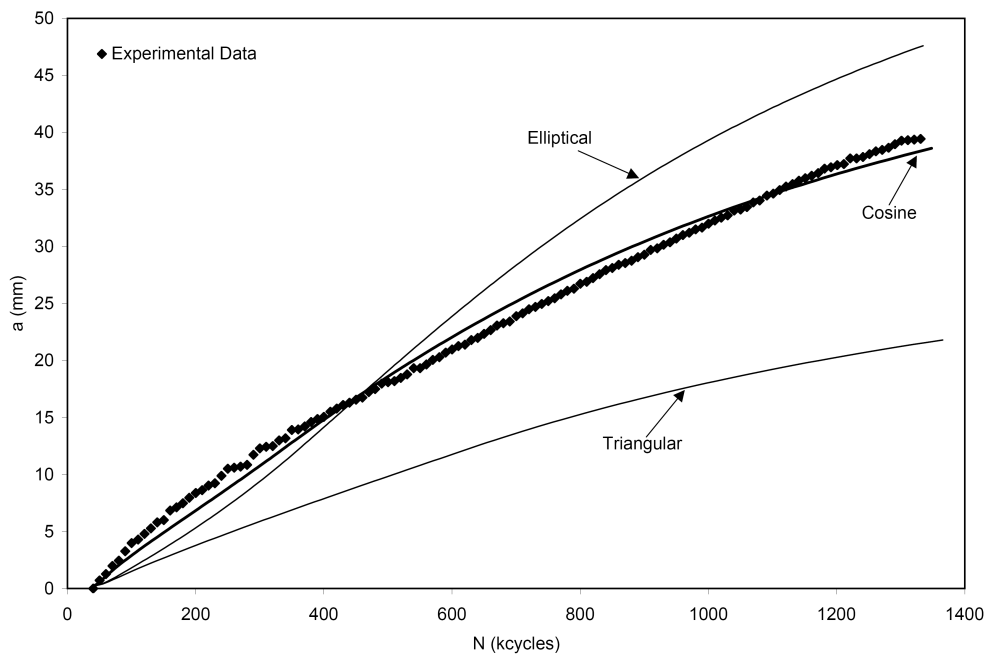


Figure 5.22: Effects of changing the delamination shape on the crack growth prediction.

Stress Intensity Factor

The stress intensity factor formulations for the far field and fibre bridging contributions were based upon the geometries shown in Figures 4.11 and 4.12. The fact that the far field geometry includes an open hole, while the fibre bridging geometry does not was studied to evaluate the effects on the crack growth prediction. To this aim, the far field stress intensity factor was replaced in the model with a formulation for an infinite sheet with a crack, as shown in Figure 5.23.

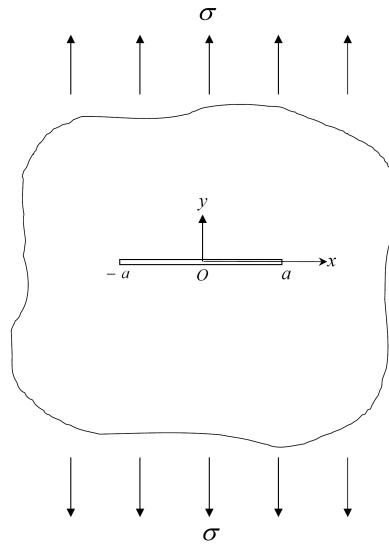


Figure 5.23: *Stress intensity factor geometry for crack in an infinite sheet used in determining the far field stress intensity factor sensitivity.*

The effects of the open hole are shown in Figure 5.24 and Figure 5.25, and are seen to be small – with immediate effects apparent for cracks less than 5mm in length. The differences in final crack length varied by 5.4% between the two models, and bracketed the actual crack length. This justifies the stress intensity factor formulations used in the model, as the effects of the open hole are modest.

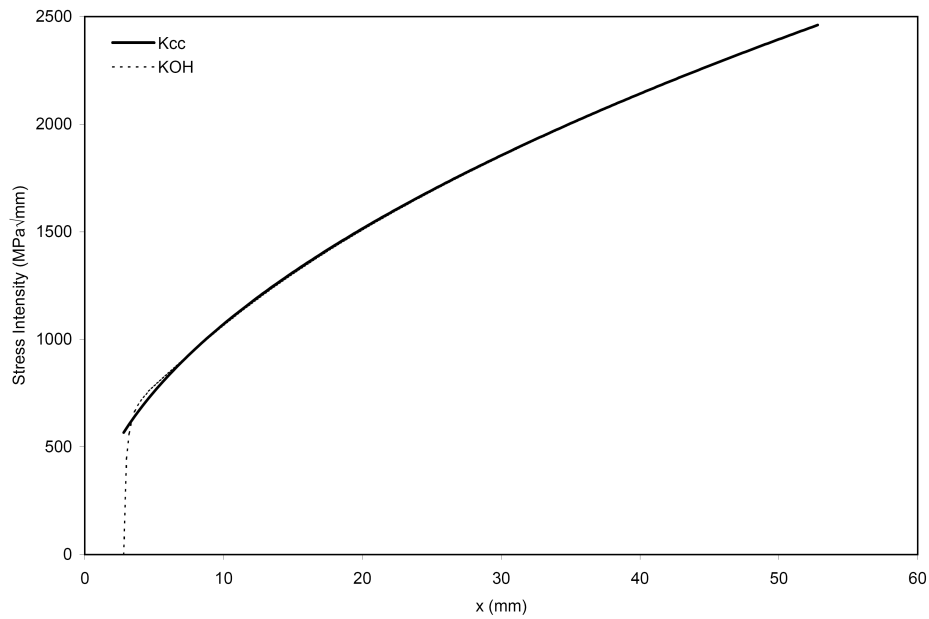


Figure 5.24: Comparison of stress intensities for infinite sheet with a through crack, K_{CC} , to stress intensity for infinite sheet with a through crack emanating from an open hole, K_{OH} .

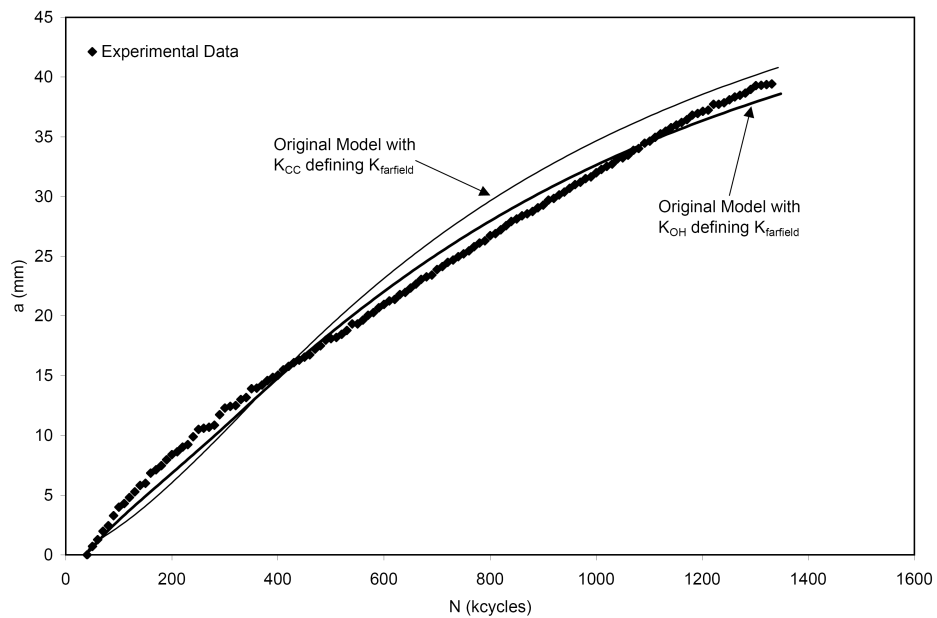


Figure 5.25: Effects of changing the stress intensity factor formulation for the far field contribution to the crack growth model.

Finally, it should be pointed out that in the experiments and the model validation study, a number of base parameters were fixed, hence defining the center of gravity of the model validation. These fixed parameters fall into the categories of the material, the geometry of the specimen, and the load case, and are described below. By identifying the extents of the parameters used in validating the model, the range of applicability of the model can be assessed.

The material parameters can be divided into the laminate type, the number of plies, and the aluminum ply thicknesses. The laminate type tested here has been Glare 2A exclusively. The range on the number of plies tested was from a 5/4 to an 11/10 lay up. The aluminum ply thickness tested was 0.4mm exclusively.

The geometry parameters can be divided into specimen width, crack length, and open hole diameter. The specimen widths tested were 50mm to 100mm. No width effects were evident in the experimental data, though the model is dependant upon the width of the fibre bridging stress distribution. The crack lengths ranged from 0.5mm to 40.2mm. The open hole diameters ranged from 5.6mm to 6.5mm.

The loading parameters can be divided into the maximum applied stress, the stress ratio, and the bending factor. The load cases investigated had applied stresses to the MOHTB specimens of 80MPa and 100MPa. The four point bend specimen resulted in stresses in the surface ply of aluminum of 200MPa. Stress ratios were kept at $R=0.1$ for all tests. Bending factors ranged from 2.0 to 2.5 for the MOHTB specimens. The bending factor is not applicable to the four point bend specimens.

5.5. Concluding Remarks

Based upon the results reported in Chapters 3 – 5, the following concluding remarks can be made. Experimental fatigue crack growth data is evaluated for a novel new fatigue specimen constructed of Glare fibre metal laminate. The new MOHTB specimen was designed to provide a combined tension and bending environment for fatigue crack growth investigations. The new specimen displayed stable and repeatable crack growth, with no plastic deformations in the regions of the overlaps typical of the Open Hole Tension Bending specimen. The specimen design is easily adjusted to tailor the stress state in the test section of the specimen, which allows for a wide range of bending factors.

A hybrid analytical/numerical crack growth model for Glare is compared to experimental data for a set of specimen configurations and loading conditions. The model requires as an input the fibre bridging stress distribution for each cracked ply in a specimen. This distribution was extracted from FEM analyses. These distributions were found to have marked similarities from ply to ply and specimen to specimen. These similarities were capitalized and a single formulation for the fibre

bridging stress distribution was used which varied by situation based upon the stress in the aluminum ply being investigated. This single formulation was found to be a good interpretation of the physical situation, as the crack propagation predictions followed the experimental data well.

Taking all Glare 2 data presented here, the analytical model performed well in predicting surface and subsurface crack growth. The model neither consistently over- nor underestimated the crack growth for any one layer modelled. For surface cracks, for example, the model slightly underestimated for two specimen types, more significantly overestimated for another, and was quite accurate for the fourth. Based upon these results, the model is deemed accurate for surface and subsurface fatigue crack growth in Glare 2A laminates.

Sensitivity studies were conducted to evaluate the effects on the crack growth predictions of changes to various input parameters. The model was found to be sensitive to the inputs of resultant stress in the aluminum plies, the formulation of the flank stress distribution, and to the representation of the delamination shape imposed around a fatigue crack. Accurate knowledge of these parameters is essential for the success of the model. Through this sensitivity study, the formulation arrived at for the fibre bridging stress distribution and delamination shape were found to be the best interpretation of the experimental data set, as deviations from those approximation yielded inaccurate results.

The sensitivity studies also investigated the effect of the use of the open hole geometry for determining the far field stress intensity of the system. The use of this geometry, rather than a geometry without the open hole was found to have minimal effect on the predicted crack growth behaviour of the model.

With the hybrid model in hand and validated for various specimens constructed of Glare 2A, an expansion of the model to other configurations is justified to further investigate the range of applicability of the model. This investigation is presented in Chapter 6.

5.6. References

- ¹ **Schijve, J.**, *Fatigue of Structures and Materials*, Kluwer Academic Publishers, 2001.
- ² **Stevens, J.S.**, *Theory of Measurements*, D. van Nostrand Co., 1916.
- ³ **ASTM E647-95a**, *Standard Test Method for Measurement of Fatigue Crack Growth Rates*, Annual Book of ASTM Standards, American Society for Testing and Materials, 1995.
- ⁴ **Alderliesten, R.C.**, *Development of an empirical fatigue crack growth prediction method for the Fibre Metal Laminate Glare*, Masters Thesis, Delft University of Technology, 1999.
- ⁵ **Vlot, A., Gunnink, J.W.**, *Fibre Metal Laminates an Introduction*, Kluwer Academic Publishers, 2001.
- ⁶ **Bannantine, J.A., Comer, J.J., Handrock, J.L.**, *Fundamentals of Metal fatigue Analysis*, Prentice-Hall. Inc., 1990.
- ⁷ **Homan, J.J.**, *Fatigue Initiation in Fibre Metal Laminates*, International Journal of Fatigue, 2005.
- ⁸ **Marissen, R.**, *Fatigue Crack Growth in ARALL, A hybrid Aluminium-Aramid Composite Material, crack growth mechanisms and quantitative predictions of the crack growth rate*, PhD Thesis, Delft University of Technology, 1988.
- ⁹ **Guo Y.J., X.R. Wu**, *A theoretical model for predicting fatigue crack growth rates in Fibre-reinforced Metal Laminates*, Fatigue & Fracture of Engineering Materials & Structures, **21** 1133-1145 (1998).
- ¹⁰ **Burianek, B.A.**, *Mechanics of Fatigue Damage in Titanium-Graphite Hybrid Laminates*, PhD Thesis, Massachusetts Institute of Technology, 2001.
- ¹¹ **Alderliesten, R.C.**, *Fatigue Crack Propagation and Delamination Growth in Glare*, PhD Thesis, Delft University Press, 2005.

6

Extension of Model to Glare 3

Abstract – This chapter details the extension of the hybrid crack propagation model developed in Chapter 4 for Glare 2A to Glare 3 laminates. An experimental program is detailed which returned fatigue crack data for modified MOHTB specimens constructed of Glare 3. This data was used to construct FE models that gave inputs to the analytical portion of the model, and the experimental data was used to validate that model for Glare 3. The hybrid analytical/numerical model effectively predicted fatigue crack propagation for surface and subsurface plies in MOHTB specimens constructed of Glare 3-7/6-0.3 tested at 100MPa.



6.1. Introduction

The hybrid analytical/numerical model developed in Chapter 4, and validated in Chapter 5, was developed around the Glare 2A laminate. The use of the simplest configuration of Glare, with its alternating plies of aluminum and prepreg oriented in the rolling direction of the aluminum sheets, to develop the model was a conscious decision. Having achieved good results in predicting surface and subsurface crack growth in Glare 2A specimens subjected to combined tension and bending, an extension to the model is warranted.

The model's basic construction is generic in nature – nothing in the model prevents its use on other Glare laminate types. Stress intensities were developed for a Paris law-based model to describe the two major sources of stress in the laminate that dictate fatigue crack propagation in the aluminum plies: the far field stress and the fibre bridging stress. The formulation of these stress intensities is based upon the state of individual plies in the laminate. Therefore, once sufficient knowledge is

acquired about the stress states within other laminate configurations, the model can be adapted for those laminates.

To evaluate the plausibility of extending the developed model, it was used to predict the crack propagation of a MOHTB specimen constructed of Glare 3. Glare 3 was chosen as it is a more complex laminate, with two prepreg plies oriented perpendicular to each other, laminated between the aluminum sheets.

If the model can be successfully adapted to Glare 3, then its generality can be expected in its adaptability to other fibre metal laminates. In Section 6.3.1, three primary features were explored that must be accounted for in the extension:

- Material orientation: the transition from Glare 2A to Glare 3 requires one of the glass fibre layers in each prepreg ply to be turned 90 degrees. This has an obvious impact on the crack propagation properties of the laminate. The FE models must accurately capture the effects on the stress state in each ply of the laminate.
- Delamination zone shape and size: As with the Glare 2A specimens, experimental data is required to accurately model the delamination in the FE and analytical model. A delamination survey is discussed.
- Fatigue crack length distribution: To construct the FE models for Glare 3 specimens, experimental data was required to know the lengths of fatigue cracks in each layer of the laminate after different numbers of fatigue cycles. A fatigue crack survey is discussed.

Once the fibre bridging stress distributions were extracted from the Glare 3 FE models, trends were analyzed in the distributions. These trends were analysed to establish if they were similar to the trends found in the Glare 2 models. If the same trends were found, then the same form of mathematical approximation used in Glare 2A could be used for the Glare 3 to introduce the fibre bridging stresses into the crack growth model.

6.2. Experimentation

In order to validate the extension of the fatigue crack growth model discussed in Chapter 4 to Glare 3 laminates, an experimental database of sufficient magnitude and detail was required. As in the development of the model for Glare 2A laminates, this experimental data was necessary for obtaining crack growth data for use in the formulation of the crack growth model for Glare 3.

6.2.1. Material Orientation

Glare 3 differs from Glare 2A in its glass fibre orientation. Glare 2A is constructed by alternating plies of aluminum and two layers of glass fibre prepreg. In Glare 2A these layers of glass fibres are oriented in the rolling direction of the aluminum, as shown in Figure 6.1. In Glare 3, one of the two layers of glass fibres is oriented perpendicular to the rolling direction of the aluminum. The layer that is oriented perpendicular to the rolling direction is the one closest to the center of the lay up. This gives Glare 3 superior fatigue performance under bi-axial loading, as in aircraft fuselage applications³.

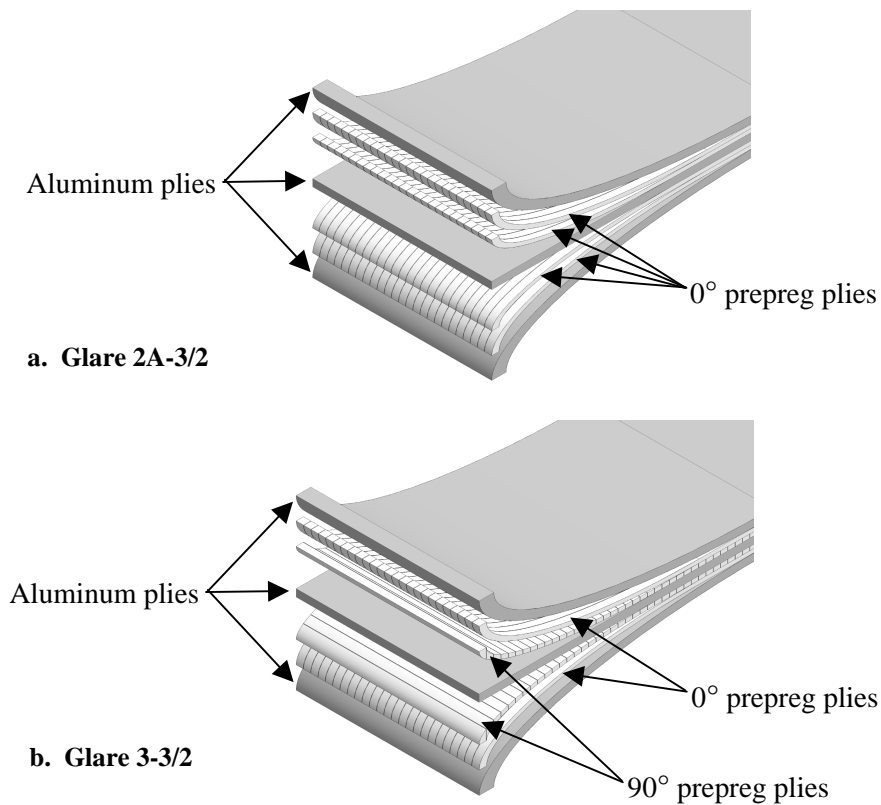


Figure 6.1: Comparison of notional Glare lay ups. *Prepreg ply orientation relative to rolling direction of the aluminum plies.*

6.2.2. Specimen Configuration

The same general Milled Open Hole Tension Bending (MOHTB), Figure 6.2, specimen as described in Chapter 3 was used for this test series. In total, eight specimens were fatigue tested to investigate subsurface crack growth in Glare 3. Each specimen was taken to a different targeted surface crack length, ranging from 5.0 to 30.0mm.

Specimens were 100mm wide. The manufacture of the Glare 3 MOHTB specimens differed from that used in construction of the Glare 2A MOHTB specimens. While the Glare 2A specimens were milled from a single sheet of Glare 2A-11/10-0.4 to achieve the shifts in the neutral line, the Glare 3 specimens were constructed from three separate parts and bonded together. This allowed for thinner sheets of Glare to be used, which made material acquisition much easier.

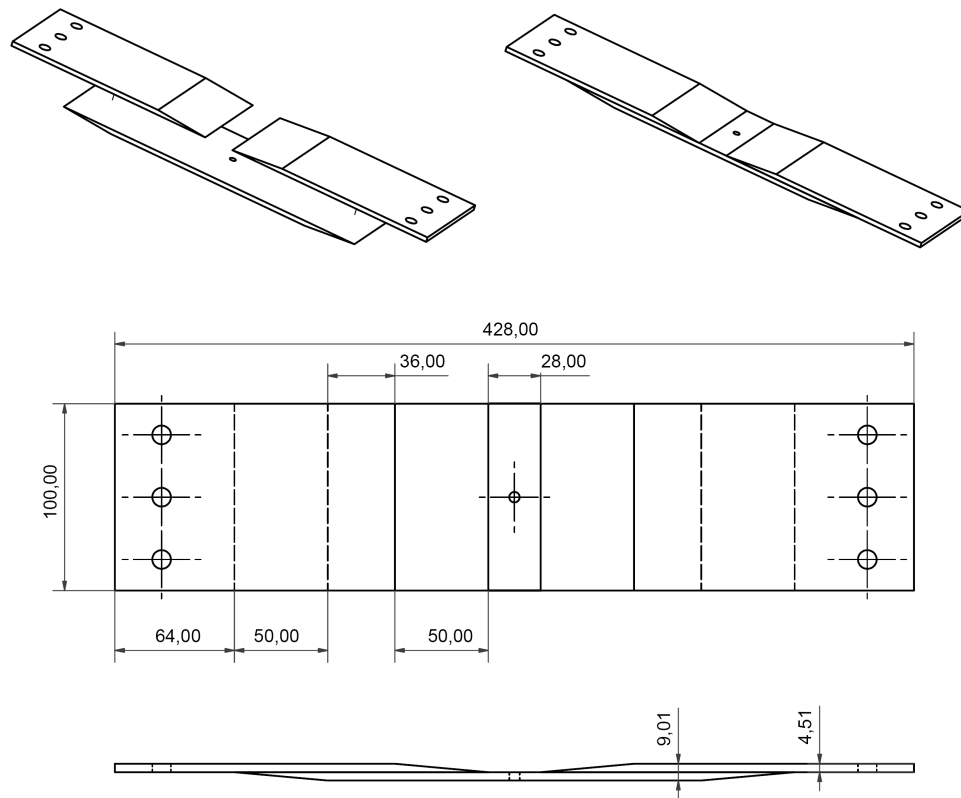


Figure 6.2: Milled Open Hole Tension Bending (MOHTB) specimen.

The three parts were milled individually out of Glare 3-7/6-0.3 sheet. The milling process imparted a 50mm taper at one or both ends of the parts. The parts were

bonded using 3M AF-9323 two-part adhesive with glass microbeads blended in, Figure 6.3. The microbeads acted to ensure proper bond line thicknesses for the specimens during lay up. This adhesive¹ had sufficient strength, a long working time, and allowed for room temperature curing. No special surface treatment was required, other than cleaning and degreasing of the already primed surfaces. All specimens were cured at room temperature. The specimens were assembled to leave a 28.0mm test section at the center of the specimen. This was the identical configuration to the Glare 2A MOHTB specimens. An open hole 5.6mm in diameter was milled through the center of the test section, again, identical to the Glare 2A specimens.

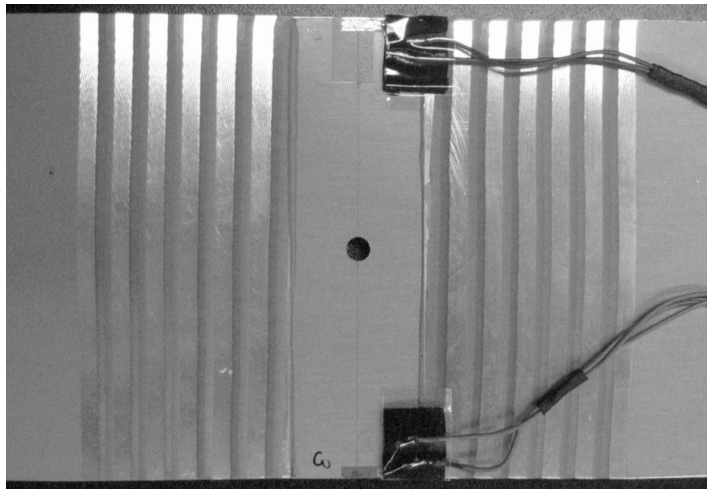


Figure 6.3: *G3-7/6-0.3 MOHTB specimen. Strain gages installed.*

As the lay-up sequence is different in Glare 3 compared to Glare 2A, a slightly different bending response is expected. Bonding three sheets of Glare 3-7/6-0.3 together to form the MOHTB specimen has a different secondary bending response than a single-piece MOHTB specimen milled of a single sheet of Glare 3-11/10-0.3. Manufacturing the specimen out of three sheets also maintained the symmetric lay-up of Glare 3 in the test section. Additionally, if the part had been milled from a single, thick sheet of 14/13 to arrive at the final 7/6 configuration, the prepreg plies in the test section would have been non-symmetrical.

In order to correctly design the three-piece MOHTB specimen, FE models were constructed to gain insight into the bending response of the assembly. The overall geometry of the test section and overlaps were kept identical to those of the single-piece specimens. FEM estimations put the resulting bending factor, k_b , of the three-piece specimen at 2.3, which was within the range of bending factors found for the Glare 2 specimens.

Selected specimens were outfitted with strain gages to ensure that the resulting stresses generated in the specimen fit with analytical and numerical estimations. The strain gages were positioned on both the tension and compression sides of the specimens, at the edge of the specimens, in line with the center of the open hole in the test section.

6.2.3. Test Specification

The tests for the Glare 3 MOHTB specimens were conducted in a similar manner to those conducted for the Glare 2A MOHTB specimens. Details of those tests are given in Chapter 3. All tests were conducted on a 100kN servo-hydraulic, closed loop mechanical and computer controlled MTS test machine. All specimens were tested at constant amplitude, at a frequency of 10Hz, at room temperature and laboratory humidity. All specimens were tested at 100 MPa and a stress ratio of 0.1.

Specimens were fatigued for preset blocks of 10,000 cycles. At the end of each block of cycles, the surface ply under the greatest amount of tension was observed to determine if a fatigue crack had initiated. A digital camera was used to measure the surface crack length. An optical endoscope was used to peer inside the open hole of the specimen. The magnification of the endoscope was sufficient to discern if fatigue cracks had formed in any subsurface ply. Data taken at the end of each block of cycles included number of cycles, surface crack length, and whether a subsurface fatigue crack had formed and in which ply.

Once the surface crack was grown to the assigned length, a_{fin} , the specimen was destructively inspected. Each specimen was pulled apart, exposing the fatigue crack surfaces emanating from the open hole. The specimen was then placed in an oven at 350 degrees Celsius for four hours to burn away the adhesive in the prepreg layers. The aluminum layers were then free for inspection. Crack lengths in each layer were then measured with an optical microscope, and crack growth rates calculated.

Subsurface crack growth data consisted of only two points per aluminum ply: an initial crack length at the observed initiation point and the final crack length after the total number of cycles imposed. As samples were taken to various numbers of cycles (and crack length values), a relatively good indication of the subsurface crack growth behaviour can be obtained by plotting the data from various samples in a single graph. This aided in the construction of the fibre bridging stress distributions needed for the analytical model.

If the fibres in the prepreg layer next to an aluminum ply were perpendicular to the fatigue crack, the burning process also left a scorch mark on the aluminum where the prepreg was delaminated from the aluminum. These scorch marks were quite faint in several instances, and made it difficult to obtain precise measurements of the delamination size and shape. For fibres running parallel to the fatigue crack, it was very difficult to see delamination-scorch marks left on the aluminum. The

aluminum plies in Glare 3 specimens had fibres running parallel to the fatigue crack on one surface, and perpendicular on the other. This meant that delamination data was primarily available for one side only of the cracked aluminum plies.

6.3. Hybrid Model

This section details the process followed to apply the hybrid analytical/numerical crack growth model to Glare 3 MOHTB specimens. The modifications to the finite element models are described, along with the requisite assumptions made to model the damaged laminate. The results of the FE models and the fibre bridging stress distributions are discussed. The incorporation of the FE results into the analytical model is also outlined.

6.3.1. Modification to FEM

No changes were made to the FE model construction techniques used for the Glare 2A specimens. The general nature of the fibre metal laminate was not changed, and the requirements necessary for modelling the Glare 2A and Glare 3 specimens were identical. Therefore, the findings of the convergence studies in Appendix B, conducted for the Glare 2A analyses were considered applicable to the Glare 3 models. Consequently, identical mesh densities were used in the Glare 3 models. Far field mesh densities away from the test section of the specimens were held at 2.5mm, and densities around the crack tip were graded down to 0.25mm.

As each specimen was constructed of Glare 3, an additional material property definition was required for the glass fibre prepreg ply running perpendicular to the rolling direction of the aluminum. The material definitions are shown in Table 6.1. The rolling direction of the aluminum was the loading direction of the specimen. This was defined as 0°. The 90° ply runs parallel to the crack paths. The aluminum was modelled as an elastic isotropic material. The glass fibre prepreg was modelled as an elastic orthotropic material. No plasticity was included in the models.

Table 6.1: Finite element model material property definitions³.

Material	E_1 (MPa)	E_2 (MPa)	E_3 (MPa)	ν_{12}	ν_{23}	ν_{31}	G_{12} (MPa)	G_{13} (MPa)	G_{23} (MPa)
Aluminum	72000	72000	72000	0.33	0.33	0.33	N/A	N/A	N/A
PP 0°	54000	9400	9400	0.33	0.0574	0.0574	5548	5548	5548
PP 90°	9400	54000	9400	0.0574	0.33	0.0574	5548	5548	5548

At the mating interface between the three parts of the specimen, an aluminum ply was in contact with an aluminum ply. As in the Glare 2 models, all adhesives were modelled with tie constraints. The tie constraint models a perfect adhesive, which does not fail regardless of the applied load.

A stress of $\sigma_{app}=100\text{MPa}$ was applied to the model in an identical fashion as that applied to the Glare 2A model. Experimental strain gage data, extracted in the same location on the Glare 3 specimens, as shown in Figure 3.2, returned net stress values of 240.84MPa, and the uncracked model returned net stress values of 232.36MPa in the strain gage region, which represents a difference within 5%.

With the baseline model constructed, damage was introduced to extract fibre-bridging data. Crack and delamination surveys were taken from experimental data to determine sets of crack lengths to apply in the models in order to simulate damage propagating through a specimen as it was fatigued. Models were constructed with progressively longer sets of cracks in the surface and subsurface plies. The crack length distributions used in the finite element models are given in Figure 6.4. These distributions correlate to values found in the surveys of the Glare 3 samples. Delamination surveys are shown in Figure 6.5. This incrementally imposed damage produced fibre bridging stress distributions for each step of increasing crack length. With these distributions, trends could be observed in the response of the fibre bridging stress to increasing damage in the laminate.

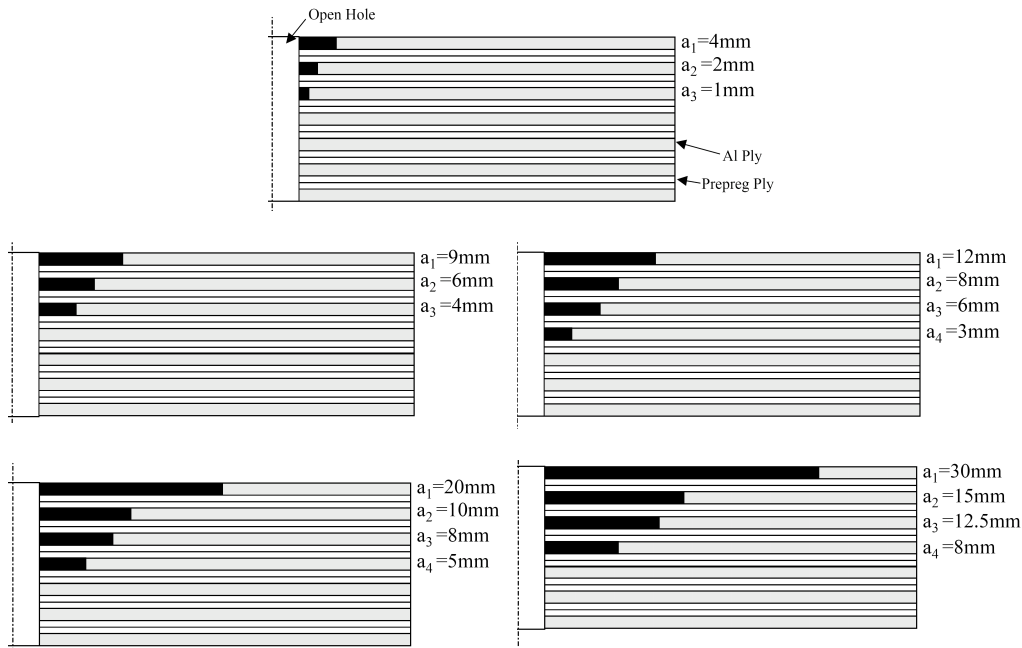


Figure 6.4: Crack survey data used in FE modelling of Glare 3-7/6-0.3 MOHTB specimens tested at $\sigma_{app}=100\text{MPa}$.

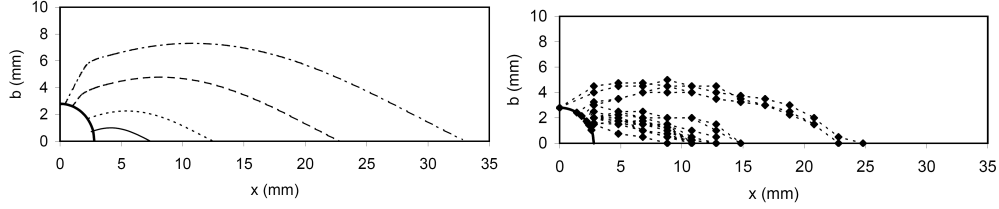


Figure 6.5: Delamination survey of Glare 3-7/6-0.3 MOHTB specimens tested at $\sigma_{app}=100\text{MPa}$. Left-hand figure shows mathematical approximations of Equation 6.1. Right-hand figure shows experimental data.

The delamination survey showed similar delamination shape distributions as those observed for the Glare 2 specimens. Therefore, the same delamination expression was applied:

$$b(x) = 0.065 + 0.187 \cos\left(2.53 \frac{x}{a+r} - 0.676\right)a \quad (6.1)$$

For cracks longer than 20mm, Equation 6.1 does not intersect the open hole. However, experimental data shows that for the cracks investigated, the delamination front always intersected the open hole. While data about the fibres at locations of $x < r$ are not used as inputs to the analytical model, it was important to physically model the delamination correctly. Therefore, the delamination approximation was modified for longer cracks by forcing the delamination front to cross the open hole boundary. This was done for portions of the delamination front where $x < r$ only. This kept the main body of the delamination shape the same, and only affected that region in the shadow of the open hole. This is shown graphically in Figure 6.5, and was identical to the procedure followed for the Glare 2A specimens.

The cracks and delaminations were introduced to the undamaged model in the same manner as done for the Glare 2A model, detailed in Chapter 4. Due to the construction of Glare 3, the perpendicular fibres on one side of a cracked aluminum ply carry a significantly different load than the fibres in the loading direction on the other side of the ply. This should induce a different delamination shape on either side of an aluminum ply. However, as the perpendicular fibres are bonded to the adjacent ply of fibres in the loading direction, the perpendicular fibres still delaminate. For this research the delamination shapes were kept identical above and below the cracked aluminum ply, similar to the modelling of Glare 2A in Chapter 4. The delamination survey supports this approximation.

For each model run, the relevant fibre strain data was extracted in the same manner as for the Glare 2A analyses. The first step was to extract the strain data from fibres

bridging a crack in a ply of interest, $\varepsilon_{fd}(x)$ with damage introduced to all the appropriate plies. The second modelling step extracted the strain data from the fibres bridging the same crack, $\varepsilon_f(x)$, but with damage introduced to all but the ply of interest. FEM analyses were conducted for all cracked configurations of specimens referenced in Figure 6.4. The fibre bridging strain, $\varepsilon_{fb}(x)$, was the difference between $\varepsilon_{fd}(x)$ and $\varepsilon_f(x)$. As this represents a large volume of data, only typical and summary data will be presented here. Data for all analyses are given in Appendix C.

For any one analysis, the data gained were the fibre bridging stress distributions over fatigue cracks in every cracked ply of the model. Such a data set is given in Figure 6.6. The x-axis shows the x-location along the specimen, with $x=0$ representing the center of the open hole. The y-axis shows the fibre bridging stress, σ_{fb} . The data set shows the surface crack imposed was 20.0mm, the second layer crack was 10.0mm, and the third layer crack was 8.0mm. This set of cracks applied was chosen to match a configuration from the experimental crack survey previously mentioned.

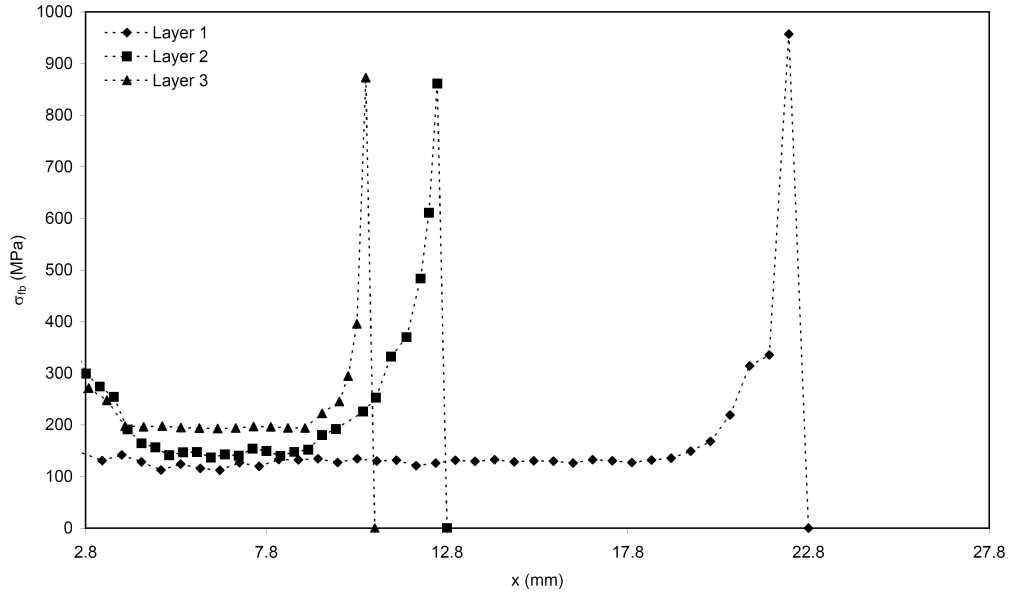


Figure 6.6: *Fibre bridging stress distributions for three cracked plies of Glare 3-7/6-0.3 MOHTB specimen. $\sigma_{app} = 100$ MPa. Surface crack length, $a_I=20.0$ mm. Taken from FEM analysis.*

Figure 6.6 shows the same characteristics displayed by the Glare 2A specimens. Each distribution starts at a high value close to the open hole, decreases to a minimum value over the majority of the flank of the crack, and then peaks near the tip of the crack. The same convention was used to describe the sections of the distribution, with the flank stress, σ_{flank} , describing the distribution over the majority of the crack length, and the tip stress, denoted as σ_{tip} .

Figure 6.7 to Figure 6.9 show all the fibre bridging stress distributions for the first, second and third layer cracked plies, respectively. The characteristic trend of decreasing values of σ_{flank} for increasing crack lengths is evident for each ply.

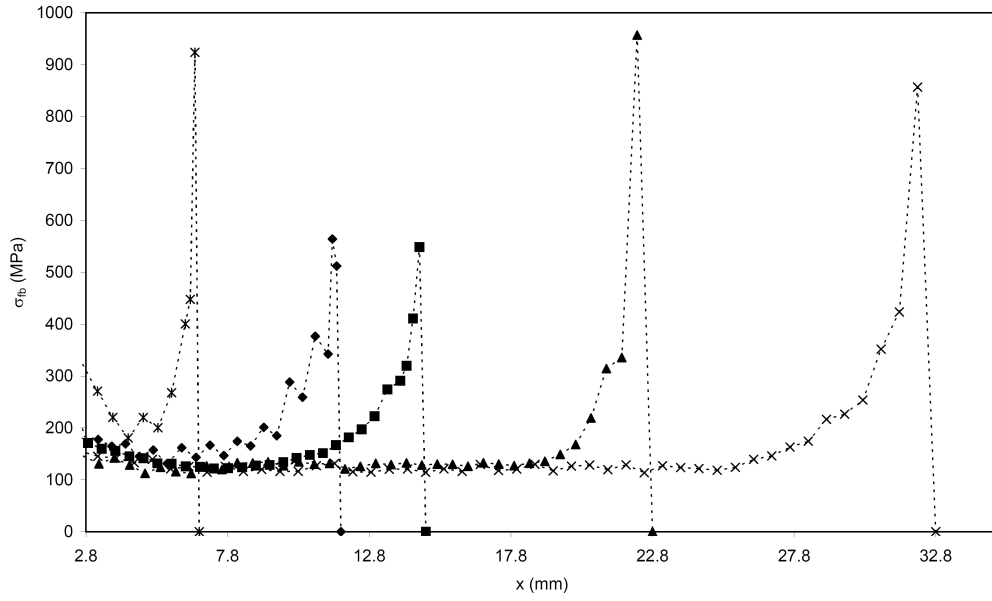


Figure 6.7: Fibre bridging stress distributions for surface cracks. Glare 3-7/6-0.3, $\sigma_{app} = 100$ MPa. Taken from FEM analysis.

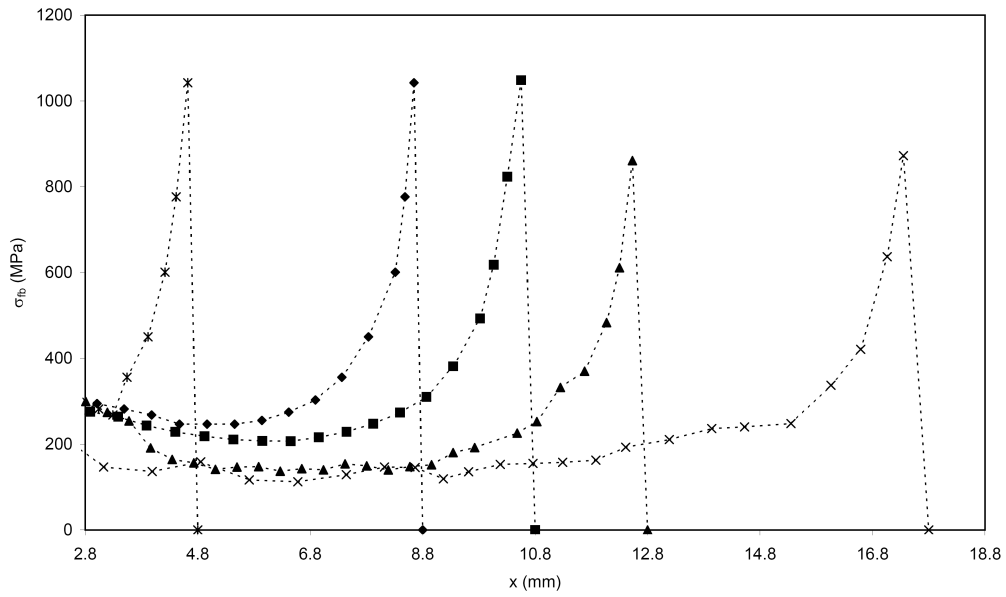


Figure 6.8: Fibre bridging stress distributions for layer 2 cracks. Glare 3-7/6-0.3, $\sigma_{app} = 100$ MPa. Taken from FEM analysis.

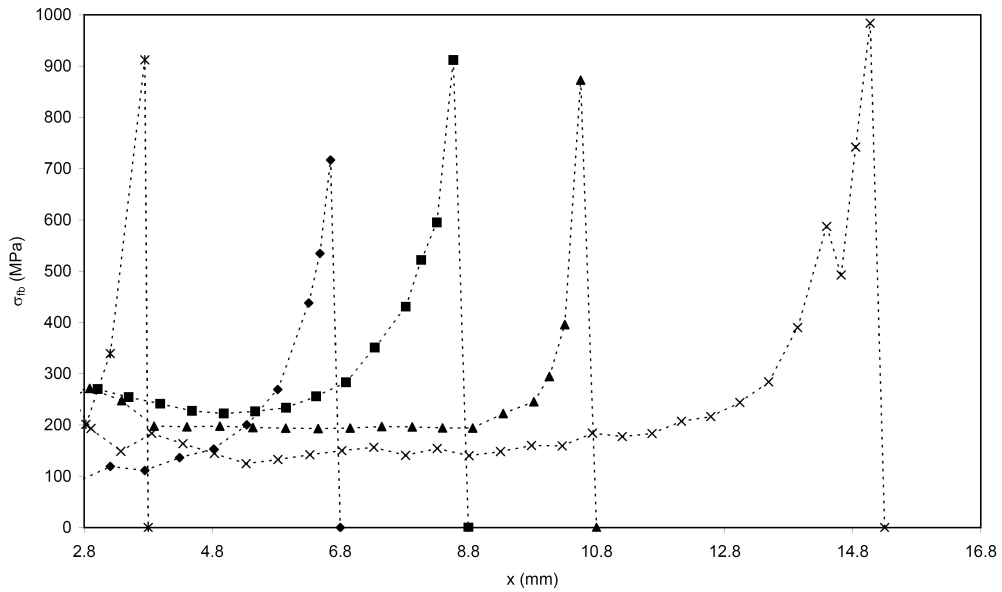


Figure 6.9: Fibre bridging stress distributions for layer 3 cracks. Glare 3-7/6-0.3, $\sigma_{app} = 100$ MPa. Taken from FEM analysis.

As the flank stress distribution followed the same trend as that of the Glare 2A specimens, that trend was investigated to establish if a similar mathematical

expression could be used to describe σ_{flank} . The flank stress is shown graphically in Figure 6.10 for all surface and subsurface cracks analysed.

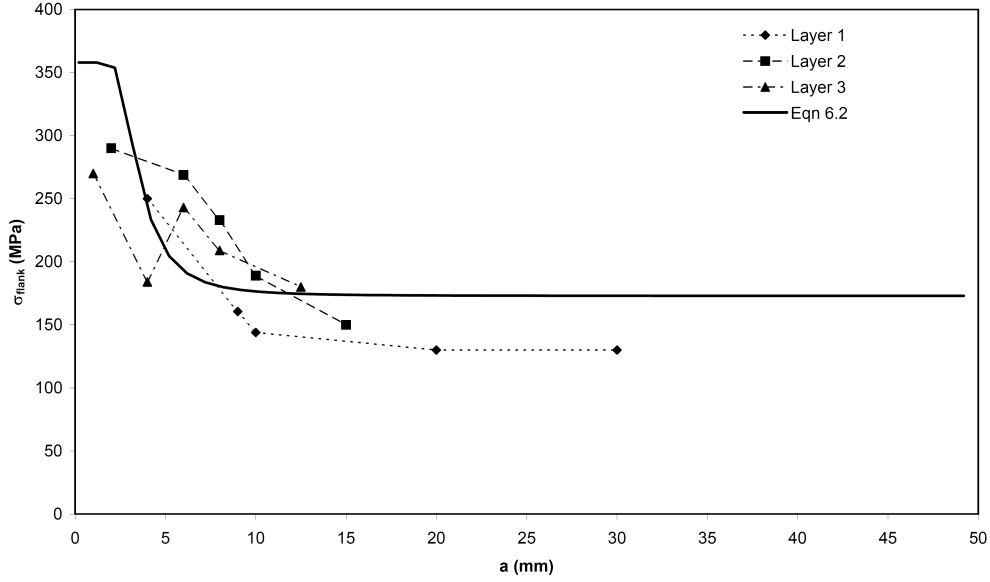


Figure 6.10: Flank stress vs. final crack length for Glare 3-6/5-0.4 with $\sigma_{app} = 100$ MPa.

To incorporate the flank stress distribution into an expression for the total fibre bridging stress distribution, a mathematical expression was required to describe the nature of σ_{flank} . The same expression for the flank stress used for the Glare 2A specimens was found to be a good fit with the Glare 3 specimens. The same form of offset was used, based upon the resulting net stress, σ_{res} , found in the surface aluminum ply of the appropriate loaded undamaged model. The expression for the flank stress is expressed in Equation 6.2, and superimposed on the FEM data in Figure 6.10.

$$\sigma_{flank}(a) = (0.6\sigma_{res} + 220) - 185e^{-60*a^{-3.5}} \quad (6.2)$$

where a is the crack length being investigated. Again, while this is not the best curve fit for any one set of flank stress distributions for a specific specimen, this was the best fit for all the data taken as a whole.

The same methodology to incorporate the tip stress, σ_{tip} , used for the Glare 2A specimens was used for the Glare 3 specimens. With $\sigma_{BN}=1193$ MPa, the blunt notch strength of the glass fibres² was applied at the tip of the crack:

$$\sigma_{tip}(x) = 0.9\sigma_{BN} \quad (6.3)$$

With each section of the fibre bridging stress distribution defined, the total fibre bridging stress distribution is merely the sum of the components:

$$\sigma_{fb}(x) = \begin{cases} \sigma_{flank} & r \leq x < (a+r)-0.5 \\ \sigma_{tip} & (a+r)-0.5 < x \leq (a+r) \end{cases} \quad (6.4)$$

6.3.2. Modification to Analytical Model

The analytical model used for Glare 2A was the same as for Glare 3. Only the stress intensity factors changed to account for the different laminate. As previously detailed, the analytical model is a Paris law formulation:

$$\frac{da}{dN} = C(\Delta K_{I(tot)})^n \quad (6.5)$$

where C and n are the material constants for the metal constituents. For the aluminum alloys used in this study, C equals $2.17\text{E-}12$, and n equals 2.94 . These values are taken from literature³ on through crack modelling for da/dN in mm/cycle and ΔK in $\text{MPa}\sqrt{\text{mm}}$.

The term $\Delta K_{I(tot)}$ is the total stress intensity range. This term is comprised of two components, the crack opening term applicable for a crack emanating from an open hole, $\Delta K_{I(OH)}$, and the fibre bridging term, $\Delta K_{I(fb)}$:

$$K_{I(tot)} = K_{I(OH)} - K_{I(fb)} \quad (6.6)$$

These terms are defined in detail in Chapter 4. The fibre bridging stress distribution from Equation 6.4 is used in the $\Delta K_{I(fb)}$ term. As the same formulation for σ_{fb} was found to be applicable for Glare 3, no changes were required to the model to implement it for this different lay up.

6.4. Experimental Results

A complete listing of fatigue crack growth data is given in Appendix D. The data is presented here in summary and with typical results. From the recorded data sets of surface and subsurface crack length versus the number of cycles, crack growth data were generated, as shown in Table 6.2. Crack growth rates for the surface cracks were calculated using the Seven Point Polynomial Incremental method⁴.

Table 6.2: *Experimental results, G3-7/6-0.3 MOHTB specimens tested at 100MPa. N_{init} and a_{final} data shown for left and right-hand cracks.*

Specimen ID	Side	Layer 1		Layer 2		Layer 3	
		N_{init} N_{final} (kcycles)	a_{fin} a_{fin} (mm)	N_{init} N_{final} (kcycles)	a_{fin} (mm)	N_{init} N_{final} (kcycles)	a_{fin} (mm)
MOHTB -10	L	40 150	0.6 8.0	50 150	6.0	60 150	5.1
	R	30 150	0.2 8.0	40 150	6.2	50 150	5.1
MOHTB -11	L	30 140	0.8 8.8	30 140	5.9	50 140	3.5
	R	30 140	0.4 8.8	40 140	6.1	50 140	4.8
MOHTB -12	L	20 240	0.3 14.6	30 240	10.5	40 240	8.5
	R	20 240	0.3 15.2	30 240	10.5	40 240	9.0
MOHTB -13	L	20 190	0.9 11.9	40 190	8.0	50 190	6.5
	R	20 190	0.9 12.7	40 190	8.5	50 190	7.0
MOHTB -14	L	20 300	0.1 19.3	40 300	11.5	50 300	8.0
	R	20 300	0.3 19.7	40 300	11.0	60 300	9.5
MOHTB -15	L	20 60	0.2 4.1	40 60	1.8		
	R	20 60	0.2 4.2	40 60	2.0		
MOHTB -16	L	20 300	0.6 23.9	30 300	11.8	40 300	10.5
	R	30 300	0.8 23.6	40 300	11.5	40 300	10.1
MOHTB -17	L	10 390	1.0 30.9	40 390	13.8	50 390	12.3
	R	10 390	0.1 31.6	40 390	14.2	60 390	11.9

The specimen response followed the trends set by the Glare 2A specimens. The three-part Glare 3 MOHTB specimen performed well, with no plastic deformations or spurious fatigue damage noted.

Figure 6.11 shows surface crack propagation curves for the Glare 3 MOHTB specimens. Figure 6.12 is a da/dN versus a curve for specimen MOHTB-17. The surface crack data shows good repeatability, with acceptable scatter between specimens.

Subsurface Fatigue Crack Growth in Glare Fibre Metal Laminates

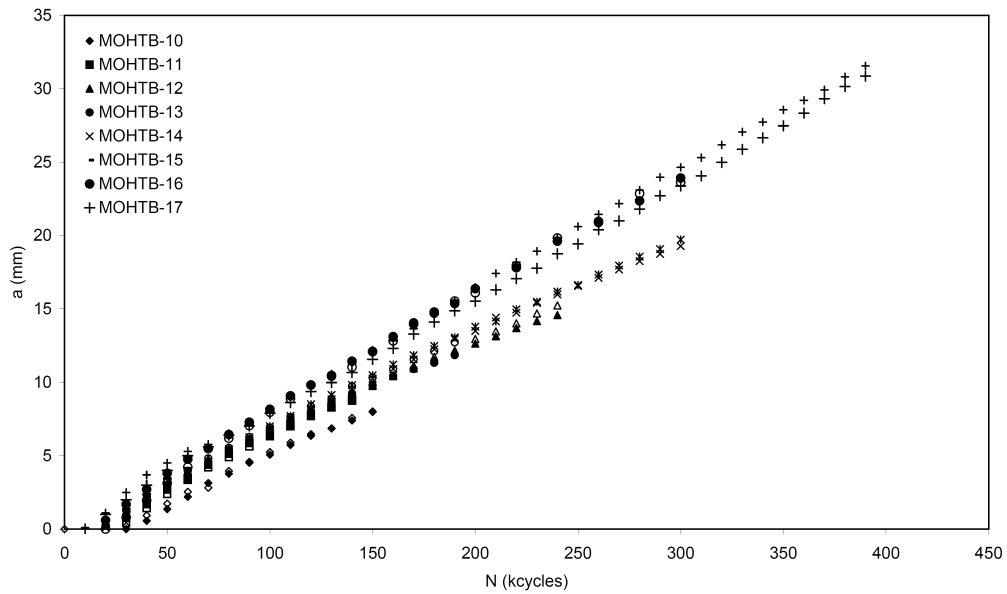


Figure 6.11: Surface crack growth curves for MOHTB specimens constructed of Glare 3-7/6-0.3 tested at 100MPa. Filled data points are for right-hand cracks, unfilled data points are for left-hand cracks.

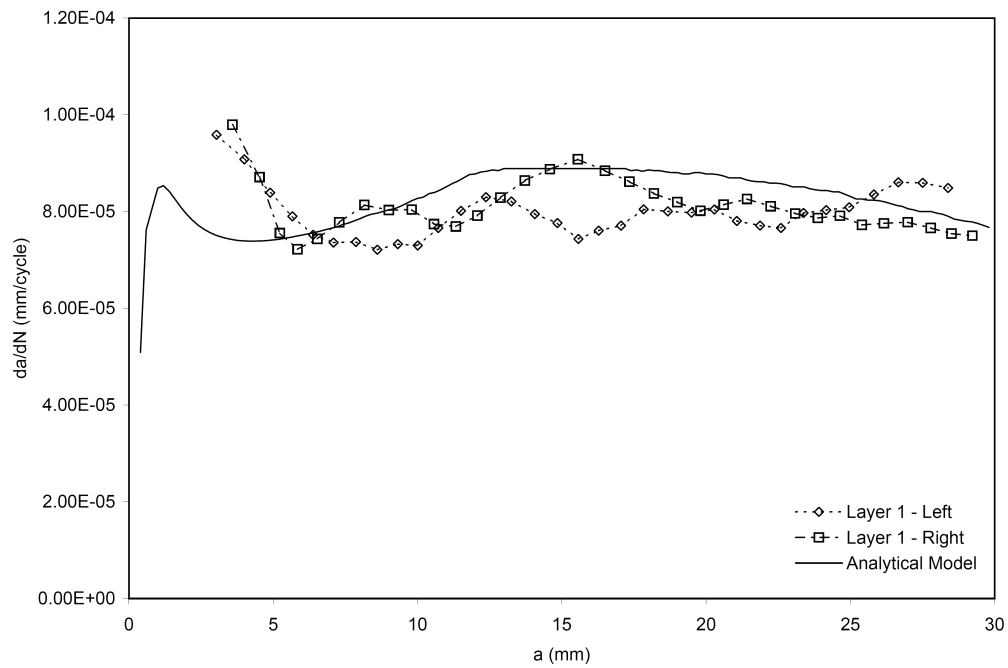


Figure 6.12: Typical da/dN vs. a curve, G3-7/6-0.3 MOHTB-17 specimen tested at 100MPa. Data conditioned with the Seven Point Polynomial Incremental method⁴.

Surface crack data was much more plentiful, as the cracks were directly observable with the digital microscope. Subsurface crack data consists of only two points per aluminum ply: the number of cycles to initiation, and the number of cycles to final crack length. Following the process used for the Glare 2A specimens, each specimen was taken to a different surface crack length. This resulted in a range of surface and subsurface crack length data sets, shown in Table 6.2. These sets were used in the FEM analysis described in Section 6.3.1.

6.5. Validation of Model Against Experimental Data

Figure 6.13 shows a summary of crack growth data for the Glare 3 MOHTB specimens compared to the prediction of the analytical model. The data points are for the aluminum plies layer 1, layer 2 and layer 3. The surface crack data is typical of all specimens tested. The subsurface data points are discrete data points for all specimens tested. Cycles to crack initiation for each ply are the normalized value for all specimens. The normalization techniques used for the surface crack propagation and subsurface crack initiation are discussed in Section 5.2.

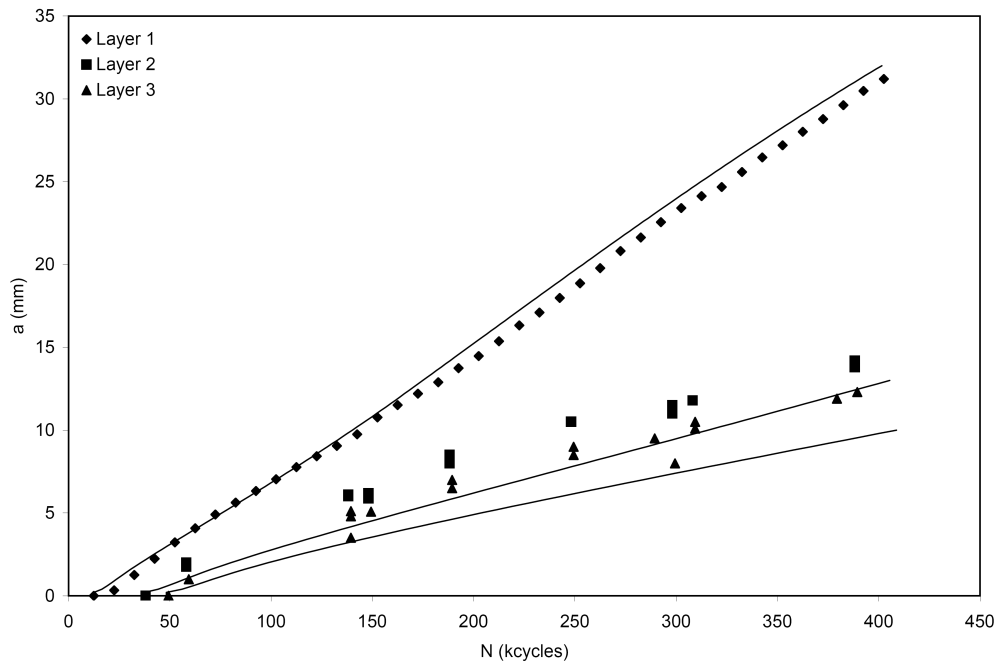


Figure 6.13: Crack growth curve; Glare 3-7/6-0.3, $\sigma_{app}=100\text{MPa}$. Typical surface crack data, all subsurface data from normalized crack initiation value. Solid lines represent the analytical model predictions for each ply.

The comparison of the analytical model overlaid on the surface crack data in Figure 6.13 show good agreement. As specimens tested were 100mm wide, subsurface crack data is available for both shorter and longer crack lengths. Comparing the analytical model to subsurface crack data again shows good correlation. The second layer model underestimated the crack growth for shorter cracks and then the slope of the crack growth curve turned to reasonably match that of the longer crack growth rates.

Looking at the model for the third layer cracks, the model underestimates the crack growth rate – slightly for the shorter cracks, and more significantly for longer cracks. The same trend to decelerate for longer cracks is again illustrated in the experimental data and analytical prediction, though for the experimental data, the shift is slight.

In total, the analytical model effectively predicted the crack growth in all plies of each specimen tested. The model utilized no correction factors for lay-up or depth location. The simple tuning of the model to the resultant stress in the ply of interest effectively calibrated the model to all of the test conditions investigated. Taking all Glare 3 data presented here as a whole, the analytical model performed well in predicting surface and subsurface crack growth.

The model performed quite well in estimating surface crack growth, though it consistently under estimated the crack growth for subsurface cracks. Much of this underestimation occurred due to crack growth rates being faster than predicted for shorter cracks in particular. Comparing crack growth rates from experimental data to those estimated by the model shows the majority of the over or under estimation occurred for shorter cracks, and the agreement was reasonable for longer cracks. Based upon these results, the model is deemed accurate for surface and subsurface fatigue crack growth in Glare 3 laminates.

6.6. Summary

The applicability of the hybrid analytical/numerical crack growth model to Glare 3 was investigated. An experimental program was conducted to acquire fatigue crack growth data for surface and subsurface plies. This data was used to generate finite element models of cracked MOHTB specimens. Fibre bridging stress distributions were extracted from these FE models.

Trends in the fibre bridging stress distributions of the Glare 3 specimens had the same characteristics as those found in the Glare 2A specimens. Based upon these identical trends, the same mathematical formulation to approximate the fibre bridging stress distribution for Glare 2A was used for Glare 3. Comparing the model predictions to experimental data showed good agreement.

6.7. References

- ¹ **3M**, *Material Datasheet: AF-9323 two-part structural adhesive*, 3M, 2003.
- ² **Roebroeks, G.**, *The Metal Volume Fraction Approach*, Structural Laminates Industries Report TD-R-00-003, 2000.
- ³ **Vlot A., Gunnink J.**, *Fiber Metal Laminates an Introduction*, Kluwer Academic Publishers, 2001
- ⁴ **ASTM E647-95a**, *Standard Test Method for Measurement of Fatigue Crack Growth Rates*, Annual Book of ASTM Standards, American Society for Testing and Materials, 1995.

Summary



The investigation of the present thesis is concerned with the fatigue crack growth behaviour of part through cracks in Glare fibre metal laminate subjected to combined tension and bending. To develop a predictive model for subsurface crack growth in Glare, the complexities involved must be accounted for. The physical system of fatigue in a fibre metal laminate is multivariate, dependent not only on the specimen geometry and loading, but also on the laminate construction.

The following provides summaries of the findings of each chapter in this thesis, which culminated in the development of a hybrid analytical/numerical model to describe surface and subsurface fatigue crack growth. This model has been validated against an experimental program.

In Chapter 2, a literature was conducted on crack growth prediction models. Several models were evaluated for their applicability to the current research. In general, the models that were empirical in nature were found to be inapplicable to the loading environment analysed in this thesis.

The approach of Marissen, which was the basis for many of the models reviewed, was taken as the starting point for the current research. Its basic premise of super positioning stress intensities to account for mechanisms affecting crack growth is logical. The stress intensity factor to account for fibre bridging reflects reality in that the stresses in his formulation act on the delamination boundary, rather than on the crack flank itself. Extensions to the Marissen approach were required to account for non-elliptical delamination fronts and non-uniform fibre bridging stress distributions over that delamination front.

To acquire the fibre bridging stress distributions, the approach of Burianek was consulted. His use of finite element modelling was instructive, though a more accurate representation of the actual physical system than the two-dimensional model he employed was required. To establish the shape of delamination front to incorporate into the model, the work of Alderliesten was referenced. A similar approach to Alderliesten and Guo and Wu was employed to numerically calculate the stress intensity factor due to fibre bridging stresses.

Based upon the strengths of these approaches, a hybrid analytical/numerical model was developed. None of the literature models dealt with a part through crack, nor did any model consider a loading case of combined tension bending. Finite element modelling was used to establish the fibre bridging stress distributions for the surface and subsurface layers.

In Chapter 3, the development of a novel tension bending fatigue specimen, the Milled Open Hole Tension Bending specimen, was detailed. This was developed as to have a specimen that can easily be designed with desired combined tension and bending stress states in a test section, and to ensure the stability of the stress levels during fatigue loading. An experimental program for this specimen and four point bend specimens was discussed. The destructive and non-destructive inspection techniques required by the research for gathering surface and subsurface fatigue crack initiation and crack lengths were outlined.

Test results for these experimental programs are reported for applied stress levels of up to 100MPa and bending factors on the order of 2.2 for the MOHTB specimens, and resultant stresses in the four point bend specimens of 200MPa. These results showed rapid short crack growth for all layers; followed by slower and stable crack growth. Time to crack initiation was consistent between specimens of the same type and loading, and compared well with published predictions.

On the topic of the subsurface fatigue crack growth behaviour of Glare, it can be concluded that the relationship between crack growth and delamination extension is of an identical nature as that for a surface crack, in that they both progress in a self-balancing nature. Crack growth rates for cracks less than 3mm in the MOHTB specimen are dominated by a lack of effective fibre bridging, and by the effects of the stress concentration of the open hole. Once a crack has grown to a sufficient length, the fibre bridging plays the key role. Delamination front shapes fall between a triangle and an ellipse – a cosine function was an adequate approximation of the experimental data.

In Chapter 4, the hybrid analytical/numerical fatigue crack growth prediction model for surface and subsurface cracks in Glare 2A was developed. The finite element modelling required gathering fibre bridging stress distributions for the various plies of the laminate was detailed. Data analysis of these distributions led to a mathematical approximation that lent itself to incorporation into the stress intensity factor formulation for the crack closing effects of the fibre bridging. This stress intensity factor, along with one to account for the specimen geometry and far field loading, were superimposed into a Paris law crack growth model and were solved numerically. With this crack growth model, crack propagation curves were predicted correlating to experimental conditions observed in the laboratory.

Results of the finite element analyses are reported for models of the experimental specimens and conditions studied in Chapter 3. Results of the crack growth model for surface and subsurface cracks are likewise reported for the MOHTB specimens and for the four point bend specimens.

On the topic of the use of finite element modelling as a tool for assessing stress states within Glare, it can be concluded that fibre bridging stress distributions over a crack can be determined through FE analysis. Those fibre bridging stress

distributions can be characterized by two components: flank stresses and tip stresses. In a specimen subjected to combined tension and bending, the values of the flank stress fall to a single shaped curve, regardless of aluminum ply investigated. That curve of flank stresses decreases in value for increasing crack lengths.

In Chapter 5, the hybrid crack growth model developed in Chapter 4 was evaluated against experimental results acquired in Chapter 3. The results of the comparison showed good agreement between the prediction and the experimental data. For all specimens tested, the model tended to over predict crack growth rates for very short cracks (less than 3mm), but then matched the crack growth rates well for cracks in the range of 3 – 30mm. For very long cracks (greater than 30mm) the model predicts crack growth rates slowing to unrealistic levels. This is due to a lack of information about fibre bridging stress distributions for very long cracks, which is needed for the mathematical approximation used in the stress intensity factor formulation.

Sensitivity studies were conducted to evaluate the effects of changes to various input parameters on the crack growth predictions. The model was found to be sensitive to the inputs of resultant stress in the aluminum plies, the formulation of the flank stress distribution, and to the representation of the delamination shape imposed around a fatigue crack. Accurate knowledge of these parameters is essential for the success of the model. Through this sensitivity study, the formulation arrived at for the fibre bridging stress distribution and delamination shape were found to be the best interpretation of the experimental data set, as deviations from those approximation yielded inaccurate results.

On the topic of the validity of the stress intensity factor formulations proposed in this research, it can be concluded that the formulation for the stress intensity factor due to fibre bridging is physically sound. That formulation is based upon experimental observations of the delamination front shapes and finite element analysis of the fibre bridging stress distributions. And finally, the analytical model based upon those stress intensity factors is sensitive to stress values used as inputs to the model. Those input parameters are the resultant net stress in the aluminum plies of the laminate under applied load, and the fibre bridging stress distribution around a fatigue crack in the laminate under applied load.

In Chapter 6, the applicability of the hybrid analytical/numerical crack growth model to Glare 3 was investigated. Following the same methodology used in developing the model for Glare 2A, the model was employed against MOHTB specimens constructed of Glare 3. Trends in the fibre bridging stress distributions of the Glare 3 specimens were found to have the same characteristics as those found in the Glare 2A specimens. Comparing the model predictions to experimental data showed excellent agreement. Characterizations applicable to the model's performance on Glare 2A were also found for Glare 3. It can be concluded that the nature of the model developed is such that it can be applied to other Glare and fibre metal laminate variants.

Samenvatting



Dit proefschrift behandelt het vermoeiingsscheurgroei gedrag van scheuren deels door de dikte in Glare vezel-metaal laminaten onder een gecombineerde trek en buig belasting. Om een voorspellings model voor scheuren in metaal lagen onder de oppervlakte laag te ontwikkelen zal op een juiste manier rekening gehouden moeten worden met de complexiteit van het scheurgroei gedrag. Het scheurgroei mechanisme in een vezel-metaal laminaat is afhankelijk van vele variabelen, de genoemde complexiteit is niet alleen gerelateerd aan proefstuk geometrie en belasting, maar ook aan de laminaatopbouw.

In het volgende worden de bevindingen uit ieder hoofdstuk samengevat welke hebben geleid tot de ontwikkeling van een gemengd analytisch/numeriek model ter beschrijving van scheurgroei in oppervlakte lagen en lagen onder de oppervlakte. Dit model is gevalideerd met experimenten.

Hoofdstuk 2 geeft een overzicht van bestaande scheurgroeimodellen voor vezel-metaal laminaten. De modellen zijn geëvalueerd op hun toepasbaarheid voor dit onderzoek. In het algemeen bleek dat de empirische modellen ongeschikt zijn voor dit onderzoek, met name met betrekking tot de aard van de onderzochte belastingsvorm (trek en buiging).

De aanpak van Marissen, basis voor veel reeds bestaande modellen, is als startpunt gebruikt voor dit onderzoek. De basis van dit model is superpositie van verschillende spannings intensiteits factoren die ieder een deel van het scheurgroei mechanisme beschrijven. De spannings intensiteits factor voor scheuroverbrugging door de vezels kan als realistisch worden beschouwd in de zin dat dat de scheuroverbruggende vezelspanningen op het delaminatie front werken, en niet op de scheurflanken. Uitbreidingen van het Marissen model waren noodzakelijk om niet ellips vormige delaminatiefront geometriën alsook niet-uniform verdeelde scheuroverbruggende vezelspanningen te verdisconteren.

De aanpak van Burianek is gebruikt om tot een bruikbare verdeling van scheuroverbruggende vezelspanningen te komen. De manier van eindige elementen modellering was informatief, doch onvoldoende om het feitelijke mechanisme van partiele scheurgroei door de dikte afdoende te beschrijven. Een uitbreiding op het twee-dimensionale model was daarom noodzakelijk. Het werk van Alderliesten is benut om de vorm van het delaminatiefront te beschrijven. Een vergelijkbare benadering van Alderliesten en Guo & Wu is gebruikt om op numerieke wijze de spanningsintensiteits- factor voor scheuroverbrugging door de vezels te berekenen.

De sterke punten van genoemde benaderingen in ogenschouw nemend is er voor gekozen een gemengd analytisch/numeriek model te ontwikkelen. Echter geen van

de bestaande modellen voorziet in deels door-de-dikte scheurgroei, noch in gecombineerde trek/buiging belastingsgevallen. Eindige elementen modellen werden gebruikt om scheuroverbruggende vezelspanningen in de afzonderlijke aluminium lagen te bepalen.

In Hoofdstuk 3 wordt de ontwikkeling van een nieuw type trek/buig proefstuk, het “Milled Open Hole Tension Bending” (MOHTB) proefstuk, behandeld. Dit proefstuk is ontwikkeld om de gewenste combinatie van trek- en buigspanningen te verkrijgen en te behouden op de plaats waar scheurgroei zal optreden gedurende het hele vermoeiingsleven. Het MOHTB proefstuk en een vierpunts-buigproefstuk worden gebruikt in het experimentele programma. De opzet van dit programma wordt beschreven. De gebruikte destructieve en niet-destructieve inspectie methodes worden uiteengezet.

Resultaten van vermoeiingsproeven zijn gerapporteerd. MOHTB proefstukken werden belast tot maximaal 100 MPa met een buigfactor van 2.2. De vierpunts buigproefstukken werden belast tot een spanning van 200 MPa in de uiterste vezel. Alle proeven lieten snelle scheurgroei zien voor korte scheurtjes, gevolgd door langzame en stabiele scheurgroei naarmate de scheuren langer werden. Dit beeld was aanwezig in alle aluminium lagen. De initiatie levensduur was consistent voor proefstukken van gelijk type en met gelijke belasting en kwam goed overeen met gegevens uit de literatuur.

De relatie tussen scheurgroei en delaminatiegroei bleek gelijk te zijn voor de oppervlakte- laag en de aluminium lagen onder het oppervlak. In beide gevallen ontstaat een zichzelf instellend evenwicht tussen scheurgroei en delaminatiegroei. In scheuren korter dan 3 mm in de MOHTB proefstukken was vrijwel geen invloed van de aanwezigheid van de vezels. Scheurgroei in deze scheuren werd gedomineerd door de aanwezigheid van het gat in het proefstuk. Bij langere scheuren werd door scheuroverbruggende werking van de vezels dominant. Delaminatie front vormen varieerden tussen die van een driehoek en een kwart ellips. Een cosinus bleek een goede benadering van de gevonden vormen.

Hoofdstuk 4 beschrijft de ontwikkeling van het gemengde analytische/numerieke model voor de voorspelling van scheurgroei in de verschillende aluminium lagen in Glare 2A. Het eindige elementen model dat nauwkeurig de spanningsverdelingen in de verschillende lagen beschrijft is uiteengezet. Op basis van de analyse van deze spannings- verdelingen is een mathematische benadering afgeleid voor deze verdelingen. Deze benadering is verwerkt in de mathematische beschrijving voor de spanningsintensiteits- factor voor scheuroverbrugging door de vezels. Deze factor wordt gecombineerd met die voor een proefstuk met eindige breedte voor het geval van spanningen aangezet aan de uiteinden. De resulterende spanningsintensiteitsfactor wordt gebruikt om met behulp van de ‘Paris’ scheurgroeirelatie scheurgroei krommes te bepalen geldend voor de beproefde proefstukken.

Uitkomsten van de eindige elementen analyse zijn gerapporteerd voor de proefstukken en belastingscondities beschreven in Hoofdstuk 3. Resultaten van het scheurgroeimodel voor de verschillende lagen zijn eveneens gerapporteerd voor de MOHTB en vierpunts-buigproefstukken.

Het is gebleken dat eindige elementen analyse geschikt is voor het bepalen van spanningstoestanden, met name scheuroverbruggende spanningsverdelingen, in Glare. Deze scheuroverbruggende spanningsverdelingen in de vezels worden gekarakteriseerd door twee componenten: flank- en tipspanningen. In het geval van gecombineerde trek/buig spanningen blijkt de flankspanning gerepresenteerd te worden door een enkele kromme die onafhankelijk van de laminaatopbouw is. De waarde van de flankspanningen zakt met toenemende scheurlengte.

In Hoofdstuk 5 wordt het in Hoofdstuk 4 geëvalueerde model beschreven aan de hand van testresultaten die in Hoofdstuk 3 zijn gepresenteerd. Deze testresultaten komen goed overeen met voorspellingen met behulp van het model. Voor alle proefstukken bleken de scheurgroeisnelheden voor korte scheuren (korter dan 3 mm) in de voorspelling lager te zijn dan in de experimenten, echter voor langere scheuren (3 tot 30 mm) bleek de overeenkomst goed te zijn. Voor zeer lange scheuren (langer dan 30 mm) geeft het model scheurgroeisnelheden die tot onrealistisch lage waarden zakken. Dit is te wijten aan een gebrek aan informatie over de scheuroverbruggende spanningsverdeling voor deze scheurlengtes.

Gevoeligheidsstudies zijn uitgevoerd om het effect van variatie in inputparameters op de berekende scheurgroeisnelheid te bepalen. Het model bleek gevoelig voor de spanning in de aluminiumlaag, de scheuroverbruggende spanningsverdeling en de delaminatievorm rond de scheur. Kennis van deze parameters is essentieel voor het succesvol toepassen van het model. Uit de gevoeligheidsstudies bleek dat de voorgestelde scheuroverbruggende spanningsverdelingen de beste resultaten gaven. Variaties op deze verdelingen leidden tot onnauwkeurige resultaten.

Naar aanleiding van de validatie van de spannings-intensiteitsfactoren die in het model worden gebruikt mag worden geconcludeerd dat de spannings-intensiteitsfactor voor de scheuroverbruggende vezelspanningen een goede fysische basis heeft. De formulering van deze factor is gebaseerd op waarnemingen van de vorm van delaminatiefronten in proefstukken en op resultaten van eindige elementen berekeningen. Het op deze spannings-intensiteitsfactoren gebaseerde analytische model is ook gevoelig voor de spanning in het aluminium en de scheuroverbruggende spanningen in de vezellaag rond de scheur.

In Hoofdstuk 6 is onderzocht in hoeverre het model toepasbaar is voor Glare 3. Het model voor Glare 3 is op vergelijkbare wijze ontwikkeld als voor Glare 2A en gevalideerd met Glare 3 MOHTB proefstukken. De scheuroverbruggende spanningsverdelingen in de vezels hebben in Glare 3 dezelfde karakteristieke vorm als in Glare 2A. De voorspellingen aan de hand van het model komen zeer goed overeen met de testresultaten. Geconcludeerd kan worden dat het ontwikkelde model van dien aard is dat het toegepast kan worden op andere Glare en vezel-metaal laminaten.

Finite Element Modelling Trials



A.1. Introduction

Attempts were made with FEM packages to accurately represent cracked Glare under applied tension and bending. The trials investigated material definitions within the programs, evaluated their abilities to accurately predict non-linear problems such as combined tension and bending environments, and their capabilities at accurately modelling laminated structures like Glare laminates. Those attempts are described here.

A.2. Finite Element Modelling

As fatigue cracks grow in aluminum sheets in Glare, the glass fibres delaminate away from a region around the crack. These delamination shapes were experimentally observed and are described in Chapter 4. As loads are applied to a cracked Glare specimen, the fibres bridge over the crack and act to restrain the crack from opening. The stresses generated in the glass fibres are not experimentally observable. To obtain the stresses in the glass fibres bridging over the crack, finite element modelling approaches were used.

To decide which FEM package to use, the strengths and weaknesses of different FEM approaches were evaluated. Achieving a numerical model that accurately represents physical actuality is not a trivial task. Assumptions must be made, as exact solutions of the physical system are not known. If care is not taken in these assumptions, results from the numerical models will inaccurately represent the physical system, and poor engineering decisions can be the result.

The engineering purpose of a finite element model is to obtain information regarding the response of a physical system to stimuli (generally applied loads). The results of

the finite element model must be representative of the physical system in order to confidently apply those results to engineering decisions. This condition is best achieved for a given FE model if the error in the energy norm is minimized¹. Or:

$$\|u_{EX} - u_{FE}\| = \min \|u_{EX} - u\| \quad (A.1)$$

Where u_{EX} is the actual displacement of an element within the physical system, u_{FE} is the displacement of the element found in the finite element solution, and u is any non-infinite admissible solution for displacement within the system.

Finding the solution with the minimum error is not a guarantee that the results of the FE model are adequately representative of the physical system. If the FE model is over-simplified, responses of the physical system may not be captured. This is referred to as discretization error.

Consider the example of finding a curve fit through a set of non-linear data points. One can find a linear curve fit through the data, but its representation is less than optimal, or its discretization error is large. To improve on the representation, one can use the linear curve fitting process through subsets of the data and connect them, or increase the order of the equation used to describe the data. Either method will improve the results, and each comes with its own computational requirements.

The above example of curve fitting is analogous to refining an FE model. There are two general methods of refining a finite element model to improve its representation of a physical system: h-element extensions and p-element extensions. Both are described below with discussions of the comparative advantages and disadvantages.

In p-element extensions, the polynomial order of the solution used to resolve the displacements between nodes of elements is increased. This means that the number of elements can be kept relatively small, and the degrees of freedom of the model are governed by the order of the solutions for u_{FE} for each node on the boundaries of the elements. The decrease in discretization error through the use of p-element extensions are found to be equal to, or better than, the rate found with h-element extensions for most engineering problems. The non-linear solutions require more computing time for each node – though timesavings are achieved through the reduced number of elements required. The p-element extension is the approach utilized by the FEM package StressCheck™.

In h-element extensions, the sizes of elements are refined to arrive at a solution for a model. By subdividing the elements of a model, the number of finite element spaces is increased. This increases the degrees of freedom of the FE model. Each element will better approximate the displacement of the boundaries of the element, u_{FE} , as the linear solution will be more appropriate over the element's smaller size.

By making the elements smaller, the error associated with assuming a linear solution between nodes is reduced. Once sufficiently small, the difference between the FE solution and the exact solution will be acceptable. Finding the refinement level that yields the optimal balance between accuracy and affordability requires successive runs at increased refinement until the improvement in resolution is deemed negligible. This process can represent a large requirement for computing power, especially for larger models, as an increase in refinement means an increase in the degrees of freedom of the model. The h-element extension is the approach utilized by the FEM package ABAQUS™.

A.3. StressCheck Trials

The materials investigated here are the constituents of Glare – isotropic aluminum and orthotropic glass fibres. These materials are defined within StressCheck² by defining Young's modulus and Poisson ratios for the constituents. These material properties are applied to elements that define the geometries of the lamina within Glare. An additional feature present in StressCheck, however, is the ability to define sub-laminates. A sub-laminate is defined in StressCheck as a group of plies combined in a single element. When working with composite structured models, the user is able to define properties for each material in the laminate. The user can then define the stack up sequence and orientation of each ply, as well as the number of sequences to arrive at the final sub-laminate thickness. StressCheck then homogenizes all the plies in the sub-laminate together into one layer with one set of material properties that represents the sub-laminate stack up. By minimizing the number of elements within a model through sub-laminates, a significant reduction in computing can be achieved.

An additional advantage of p-element extension use in finite element modelling is the inherent error estimation capabilities. By calculating the error in the energy norm as shown in Equation A.1, as the order of the polynomials are raised, the convergence of the finite element solution can be seen. This gives a qualitative measure of the accuracy of the model, as a rapid convergence to a solution is an indication that no discontinuities exist in the model. StressCheck also identifies those elements that contribute to the overall error in the model the most. This assists in targeting the user to those areas in the model that require attention.

Another powerful feature in StressCheck is its parametric architecture. By assigning geometries and material properties as variables, rather than discrete values, sensitivity studies are easily carried out. This can include investigations on the effects of changing thicknesses of plies, or defect geometries, or aluminum rolling directions on the stress predictions in the model. This allows the user to develop one model for a given Glare type and specimen configuration, and then define sensitivity studies to capture fibre bridging stress distributions for various crack lengths, and for various aluminum-ply thicknesses. For the research conducted here, this was a very desirable feature.

To evaluate whether StressCheck could be used to extract the data required for this research, two general trials were performed. The first was an investigation into linear problems. These simpler problems would determine if StressCheck could predict the reactions in a complex laminate such as Glare. The second trial was a set of non-linear problems. These were posed to evaluate StressCheck's ability to deal with bending in a specimen. The problems were increasingly complex, culminating in a close approximation of the problem faced by this research.

The linear tests consisted of two parts: a simple tensile test, and a Center-Cracked Tension (CCT) Specimen subjected to a tensile load. The specimens were 50mm wide, and 200mm long. One quarter of the specimens were modelled, with symmetry boundary conditions applied to the symmetry planes. Individual plies were bound together by having adjacent elements share nodes on the interface surfaces. The mesh was designed so that the elements had the same shape for each ply – only the thicknesses and material properties of the elements were varied. Cracks were introduced by removing the symmetry boundary condition over the faces of the desired crack shapes.

The specimen configurations were analyzed for Glare 2-5/4-0.4 and for monolithic aluminum of the same thickness. The Glare was modelled both with individual plies, and as a combination of individual plies and sub-laminates. All model runs were conducted with p-extensions allowed up to $p=8^2$.

As expected, StressCheck performed well in predicting the resultant displacements and stresses in the tensile tests. The aluminium specimen model had results less than 2% different than expected from the theory of linear elasticity³. The Glare models using individual plies varied less than 5% from published values⁴. The models of Glare using sub-laminates also varied less than 5%, although values for the stresses in the sub-laminate could not be correlated to stresses in individual plies. The stresses in the surface plies, and the overall displacements were accurate.

The CCT model was run to evaluate displacements and to see if stresses around a crack tip fell within reasonable values. For both the aluminum and Glare specimens, the models resulted in stresses and displacements that fell in line with published results^{5,6}.

The non-linear trial consisted of two problems: a cantilevered beam and a combined tension-bending (CTB) specimen. Both problems were posed with monolithic aluminum and with Glare. The Glare was modelled both with individual plies and sub-laminates. Non-linear problems in StressCheck are solved by conducting two model runs. The first is strictly a linear solution to a given problem. This establishes the various stiffness matrix sizes and provides a starting point for the non-linear run. Errors in the energy norm for the linear run must be minimized to achieve accurate solutions to a non-linear run. For a given percentage error in a

linear run, the error in the non-linear run can be expected to be between 50 and 100% higher.

The aluminum cantilevered beam model returned results within 10% of expected results³. The Glare cantilevered beam with individual plies returned results within 17% of expected results. Using sub-laminates, the results were within 20%.

The loss of accuracy for the non-linear cantilevered beam problems was concerning, but not sufficient to warrant discontinuing the use of StressCheck. It was thought that different meshing schemes might have brought the results to within acceptable levels.

The aluminum CTB model returned results within 12% of expected results⁷. The Glare CTB model could not converge to a solution. Attempts were made with discrete plies and with sub-laminates to achieve convergence. Regardless of the meshing scheme, for Glare laminates with more than four aluminum plies, the models would not converge. Based upon that limitation, other FEM packages were investigated.

A.4. ABAQUS Trials

ABAQUS⁸ is an FEM package that utilizes h-element extensions to refine models. This requires the user to reduce the size of elements to achieve increased accuracy in results. It is possible to locally refine the mesh in ABAQUS so as to balance the increased computing requirements that mesh refinement entails with the increased accuracy it offers. An additional feature of ABAQUS is global and local modelling, in which a coarse model of an entire component can be run to extract general responses from the component. Subsections of the component can then be modelled as a local model. The results from the global model are applied to the local model as applied displacements or loads. The local model is by definition smaller geometrically than the global. Mesh refinements can then be carried out with less computing impact on the local model than if carried out on the global model.

Similar trials were carried out on ABAQUS models as those conducted on StressCheck. A series of linear and non-linear trials to ultimately establish the capacity of ABAQUS to accurately predict the forced response of a specimen constructed of Glare. The same problems were modelled in the ABAQUS trials as described in the previous section.

The linear trial consisted of again, a simple tensile specimen and a CCT specimen, each constructed of both aluminum and Glare 2-5/4-0.4. The tensile model produced results within 3.5% of expected values for monolithic aluminum. Similar results were produced for specimens modelled of Glare. The CCT models also produced results that matched well with published results.

The non-linear trial again consisted of two problems: a cantilevered beam and a combined tension-bending (CTB) specimen. The aluminum cantilevered beam model returned results within 2% of expected results³. The Glare cantilevered beam with individual plies returned results within 3% of expected results.

The aluminum CTB model returned results within 3% of expected results⁷. The Glare CTB model returned results within 5% of expected results⁵.

Submodelling trials were conducted to establish their effectiveness in the current research. The Glare CTB model described above was used as the global model. A submodel was constructed by partitioning an elliptical section into the center of the global model at the location fatigue cracks would be introduced in a damaged model (described in Chapter 4). The global model was run with the elliptical partition in place. Once results were obtained for the global model, the responses at the ellipse boundary were applied to the submodel of only the elliptical section of Glare.

The results of the submodel showed that the transfer of the stress state from the global model to the boundary of the submodel was hampered by the laminated structure of Glare. The output from the global model appeared smoothed over the interfaces between plies of the laminate and between nodes in any one ply. This resulted in unreasonable responses from the local model. Various attempts were made with different meshing schemes with no improvement to the outcome.

A.5. Summary

Based upon the results of the FEM trials, ABAQUS was selected as the FE package to continue the investigations with. Local modelling of the crack and delamination was discontinued, based upon the unsuccessful local modelling trials of the Glare CTB specimens.

A.6. References

- ¹ **Szabó, B., Babuška, I.**, *Finite Element Analysis*, John Wiley & Sons, Inc., 1991.
- ² **Engineering Software Research & Development, Inc.**, *Stress Check Users Manual*, 2001.
- ³ **Beer, F., Johnston, R.**, *Vector Mechanics for Engineers*, 5th ed., McGraw Hill, 1988.
- ⁴ **Roebroeks, G.**, *The Metal Volume Fraction Approach*, TD-R-00-003, SLI, Delft, 2000.
- ⁵ **Randell, C.**, SAMPE Conference Proceedings, 2003.
- ⁶ **Alderliesten, R.C.**, *Development of an empirical fatigue crack growth prediction method for the Fibre Metal Laminate Glare*, Masters Thesis, Delft University of Technology, 1999.
- ⁷ **De Rijck, J.J.M.**, *Stress Analysis of Fatigue Cracks in Mechanically Fastened Joints*, PhD Thesis, Delft University Press, 2005.
- ⁸ **ABAQUS, Inc.**, *ABAQUS Version 6.4 Users Manual*, ABAQUSTM, Inc., 2003.

B

Convergence Study



B.1. Introduction

A convergence study was conducted to confirm that the element size used in the FE modelling resulted in consistent solutions. The model used for the convergence study was a MOHTB model constructed of G2A-6/5-0.4. Increasing mesh densities were analysed to evaluate the displacements and stresses in the model, focusing on the appropriate global mesh size for the majority of the specimen.

B.2. Convergence Study

Selecting a global mesh size required balancing between a mesh fine enough to discern the physical response of the specimen and still as course as possible to minimize computing requirements. A G2A-6/5-0.4 MOHTB model with an applied stress of 100MPa described in Chapter 4 was used for the study. This model had no cracks or delaminations imposed. This allowed for a very simple, uniform mesh over the model. The C3D8R element required two elements through the thickness of each ply to ensure accurate response to secondary bending.

In the length and width directions, a baseline value for element sizes of 5.0mm was selected. The mesh was refined in these two directions and various locations on the model were selected to extract stress and displacement information. The results of these model runs are shown in Figure B.1. Meshes were refined from 5.0mm down to 1.5mm uniformly. Mesh sizes less than 1.5mm resulted in models with degrees of freedom higher than could be calculated with the available computing resources.

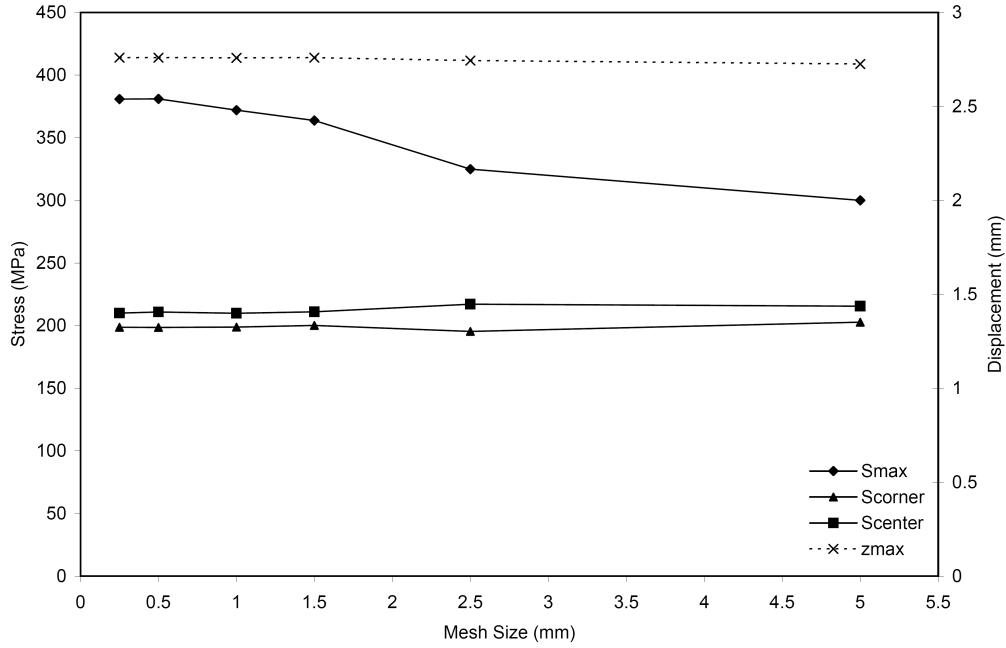


Figure B.1: Model responses for various uniform meshing configurations. MOHTB, G2A-6/5-0.4, $\sigma_{app}=100\text{MPa}$.

The extraction points for this data are shown in Figure B.2. All stresses displayed in Figure B.1 are stresses in the loading direction. The value S_{max} was the maximum stress in the model. This was located at the edge of the open hole in the specimen on the surface ply of aluminum. The value S_{corner} was taken on the surface ply of aluminum, at the corner of the model on the symmetry plane opposite the open hole. The value S_{center} was likewise taken on the surface ply of aluminum, in the center of the model on the symmetry plane between the open hole and the corner. The value z_{max} was the maximum out of plane displacement of the model.

The results show that for the stresses along the centreline of the specimen away from the open hole remained reasonably constant regardless of the mesh size selected. Stresses at the open hole and maximum out of plane displacements increased from a mesh size of 5.0mm to 1.5mm. As the values for S_{max} and z_{max} were still increasing, a localized refinement was used to ascertain if constant levels could be reached. For this localized refinement, the far field mesh size was placed at 2.5mm, and in the test section along the symmetry plane, the mesh was refined to 1.0mm and 0.5mm. With this localized refinement, the values of z_{max} stabilized and the values of S_{max} increased by less than 5%.

Comparing the FE results to strain gage data yielded good results. Strain gage data was taken from the experimental program detailed in Chapter 3. The FE prediction for the stress at the location of the strain gage was 223MPa while strain gage measurements placed the value at 232MPa – a difference of less than 4%.

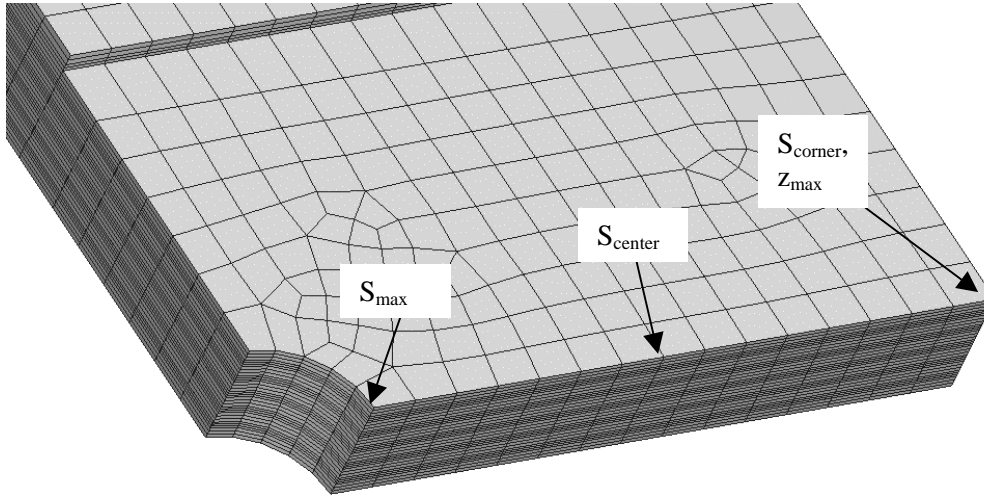


Figure B.2: Data extraction locations for global mesh convergence study. MOHTB, G2A-6/5-0.4, $\sigma_{app}=100\text{MPa}$.

This localized refinement showed that gradating the mesh was an effective means to arrive at converged solutions. Having the model converge with far field mesh sizes of 2.5mm indicated that as an appropriate far field mesh size to continue the local refinement in the test section.

A convergence study was conducted to find the appropriate mesh size in the test section of the specimen. The study used the MOHTB model constructed of G2A-6/5-0.4 taken from the above convergence study.

A surface crack and delamination were introduced to the model in the same manner as detailed in Chapter 4. This imparted the sharp stress riser at the crack tip, as well as offering insights into the fibre bridging stress distributions around the delamination fronts. As previously mentioned, the far field mesh size was held at 2.5mm. Increasing mesh densities were analyzed to evaluate the displacements and stresses in the test section of the model.

In the test section, the baseline mesh size was a uniform 1.0mm. This mesh size was decreased uniformly to 0.5mm. A graded mesh was then analyzed with the mesh uniformly dense around the crack tip to the delamination front at 0.25mm,

increasing to 1.0mm in the rest of the test section. A second graded mesh was analyzed with the mesh density set at 0.25 around the crack tip, increasing to 0.5 to the delamination front, and then further increasing to 1.0 in the test section.

The extraction points for this data are shown in Figure B.3. The value S_{OHmax} was located at the edge of the open hole in the specimen on the surface ply of aluminum. The value S_{corner} was taken on the surface ply of aluminum, at the corner of the model on the symmetry plane opposite the open hole. The value S_{tip} was likewise taken on the surface ply of aluminum, at the tip of the crack. The value z_{max} was the maximum out of plane displacement of the model, and COD was the crack opening displacement measured at the root of the crack at the open hole.

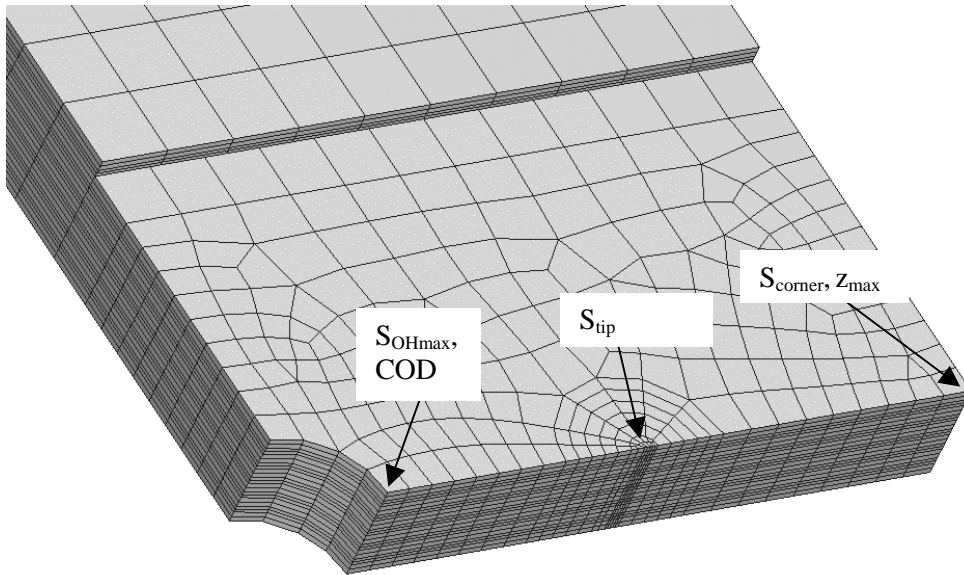


Figure B.3: Data extraction locations for local mesh convergence study. MOHTB, G2A-6/5-0.4, $\sigma_{app}=100\text{MPa}$.

The results of these models are shown in Figure B.4 and Figure B.5. All stresses displayed in Figure B.5 are stresses in the loading direction. The displacement and COD results show excellent convergence, with values shifting less than 1.0% from a uniform mesh of 0.5mm to either graded mesh. Stresses probed away from the crack tip remained consistent regardless of the mesh refinement. Stresses at the crack tip continued to rise with increased mesh density, but as will be discussed later in the next section, this was not considered to be as important as the fibre bridging stress responses.

B Convergence Study

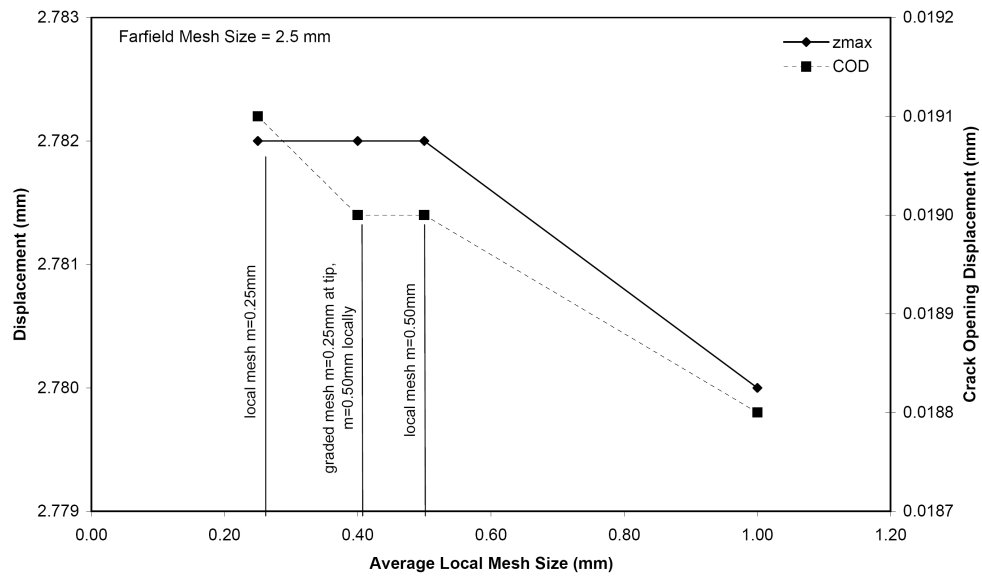


Figure B.4: Model displacement responses for uniform far field meshing and various densified local meshing. MOHTB, G2A-6/5-0.4, $\sigma_{app}=100\text{MPa}$.

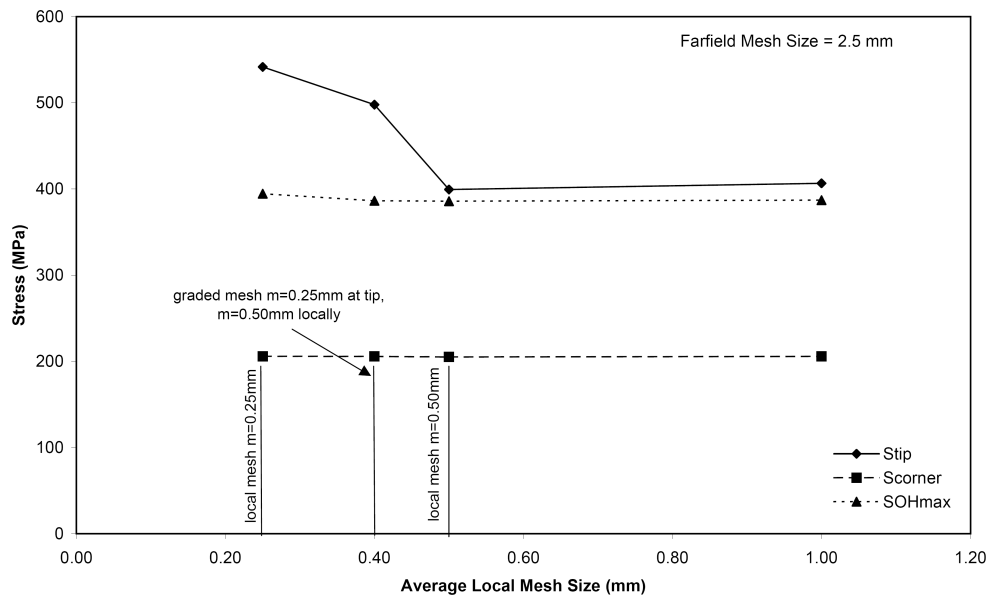


Figure B.5: Model stress responses for uniform far field meshing and various densified local meshing. MOHTB, G2A-6/5-0.4, $\sigma_{app}=100\text{MPa}$.

The stress in the delaminated fibres, σ_{fd} , includes both the stress due to the applied load and secondary bending, and the stress induced due to the fibres bridging the crack. Any mesh sensitivity of the stress in the delaminated fibres would be apparent in Figure B.6. This would manifest itself in changes in the shape of the curve as the mesh was refined. Changes would be expected in the region of the crack tip – where the short length of delaminated fibre would be most sensitive to any COD induced. Figure B.6 shows no appreciable difference in stress distribution with respect to mesh refinement, save at the node located directly over the crack tip.

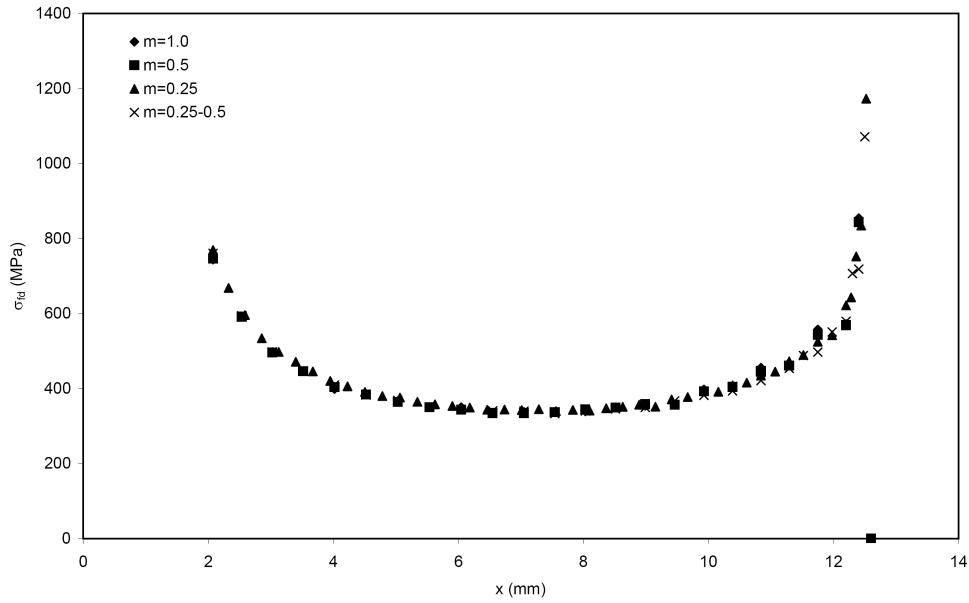


Figure B.6: Stresses in delaminated fibres, σ_{fd} MOHTB, G2A-6/5-0.4, $\sigma_{app}=100\text{MPa}$.

Data in the delaminated fibres was taken at the delamination front. As the fibres were not modelled explicitly, data was evaluated at various locations in the y-direction for different positions along the crack length. Values should be consistent along the direction from the crack flank to the delamination front.

Figure B.7 evaluates the consistency of the data in the fibre layers. Series of data represent data taken at different points in the fibre layer from the crack flank up to the delamination front. Variances in position of the data points in a series in the crack length direction are due to differences in the x-position of the nodes in the mesh.

The data in Figure B.7 represents a maximum error of 2.9% in Series3 with a standard deviation of 5.6MPa for a mean value of σ_f of 195MPa. This shows that the stresses evaluated in the fibre layers for a given position along the crack flank

are consistent in the y-direction from the crack flank up to the delamination front. Therefore the approach of extracting data on the fibres at the delamination front is justified.

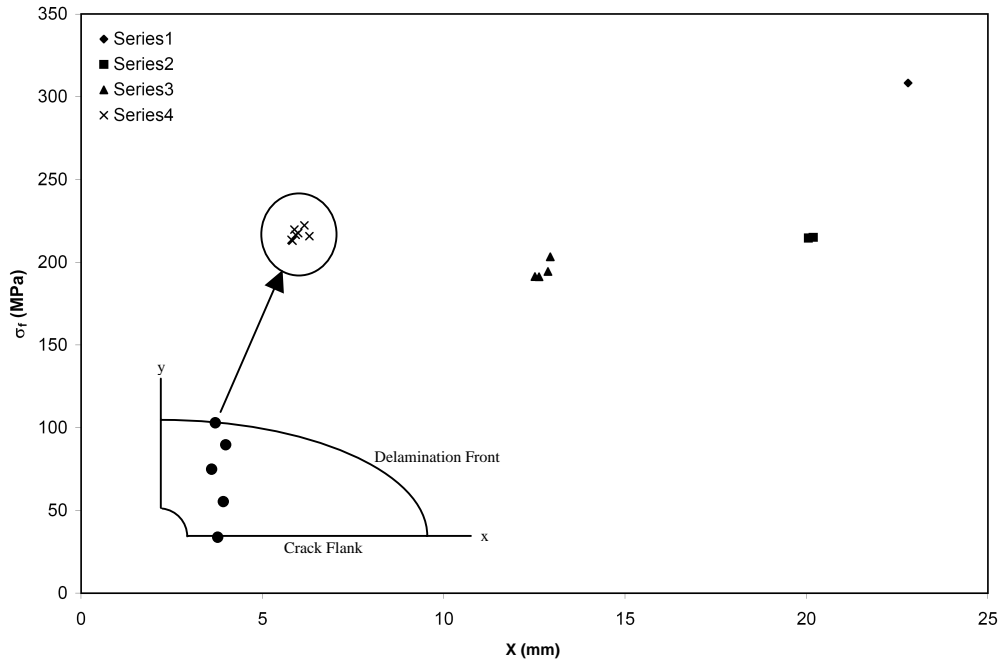


Figure B.7: Stress in delaminated fibres at various points along the crack length.

B.3. Summary

Based upon the convergence study, a far field mesh size of 2.5mm and local mesh graded to 0.25mm in the vicinity of the crack tip were justified and used throughout the rest of the investigations. Data extraction locations were also established.

C

Finite Element Results



C.1. Introduction

The results of the finite element modelling detailed in Chapters 4 and 6 are presented here. Each specimen has fibre bridging stress data presented in stress versus a format for three cracked aluminum plies, for various crack lengths.

The data is arranged in the same order as presented in the main body of the manuscript. Starting with Glare 2A specimens, the first to be presented are the 5/4 lay-ups tested at 80 and 100MPa. Next is the 6/5 lay-up tested at 100MPa, followed by the four point bend specimens. The last portion of data is for the Glare 3-7/6-0.3 specimens tested at 100MPa.

C.2. Glare 2A

C.2.1. MOHTB G2A-5/4-0.4 @ 80MPa

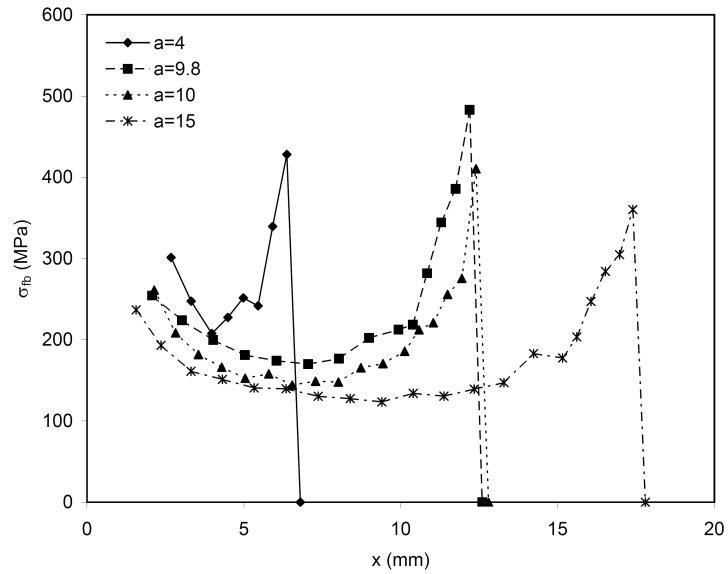


Figure C.1: Layer 1 fibre bridging stress distributions for various crack lengths. G2A-5/4-0.4 MOHTB specimen with $\sigma_{app}=80\text{MPa}$.

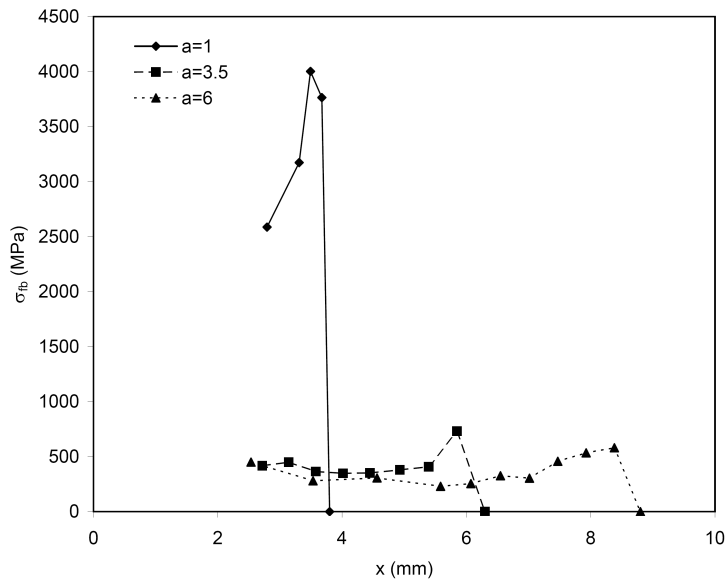


Figure C.2: Layer 2 fibre bridging stress distributions for various crack lengths. G2A-5/4-0.4 MOHTB specimen with $\sigma_{app}=80\text{MPa}$.

C Finite Element Results

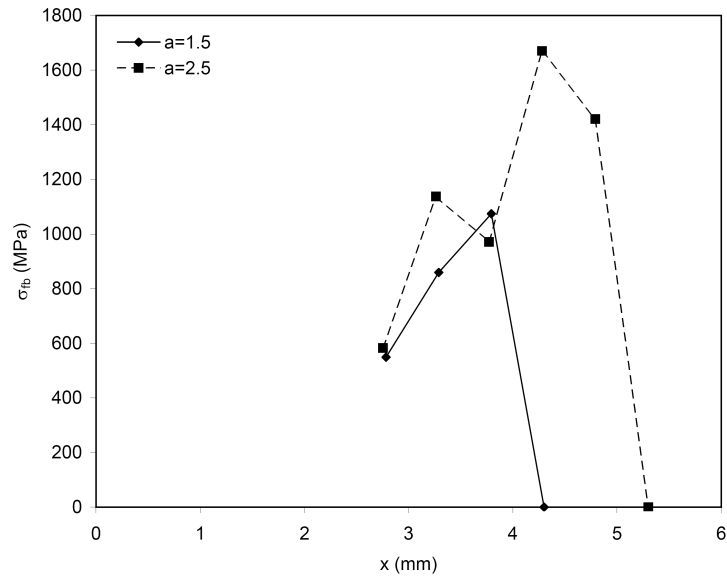


Figure C.3: Layer 3 fibre bridging stress distributions for various crack lengths. G2A-5/4-0.4 MOHTB specimen with $\sigma_{app}=80\text{MPa}$.

C.2.2. MOHTB G2A-5/4-0.4 @ 100MPa

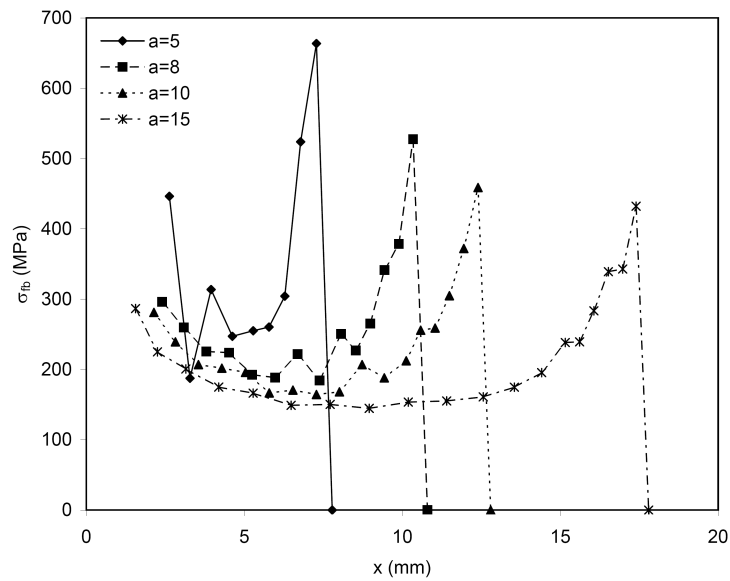


Figure C.4: Layer 1 fibre bridging stress distributions for various crack lengths. G2A-5/4-0.4 MOHTB specimen with $\sigma_{app}=100\text{MPa}$.

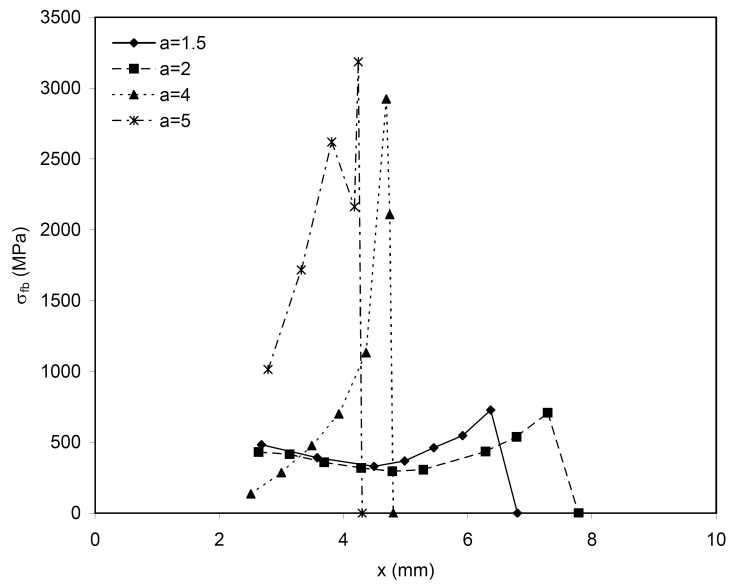


Figure C.5: Layer 2 fibre bridging stress distributions for various crack lengths. G2A-5/4-0.4 MOHTB specimen with $\sigma_{app}=100\text{MPa}$.

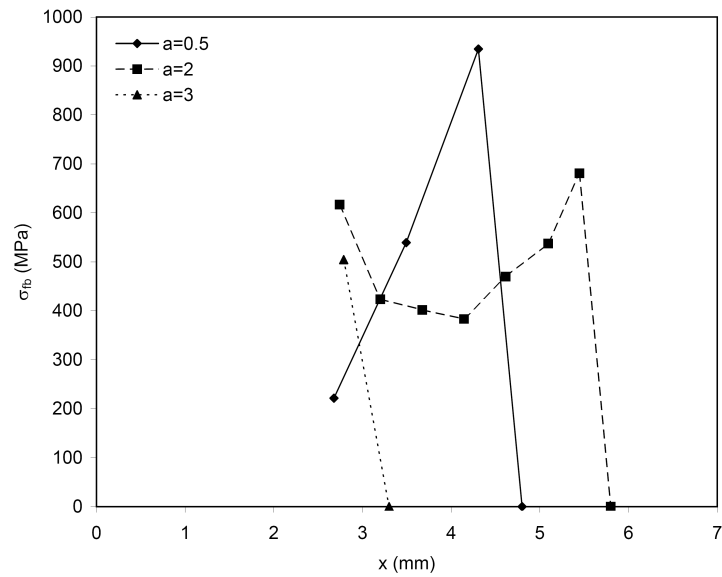


Figure C.6: Layer 3 fibre bridging stress distributions for various crack lengths. G2A-5/4-0.4 MOHTB specimen with $\sigma_{app}=100\text{MPa}$.

C.2.3. MOHTB G2A-6/5-0.4 @ 100MPa

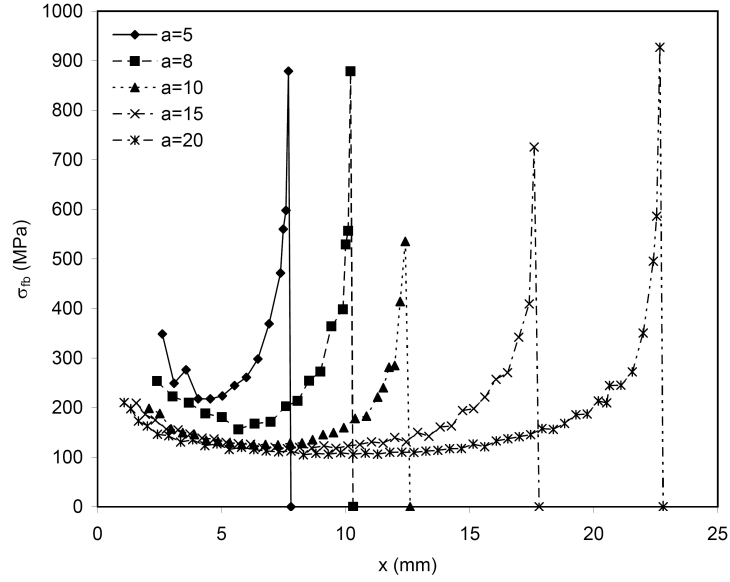


Figure C.7: Layer 1 fibre bridging stress distributions for various crack lengths. G2A-6/5-0.4 MOHTB specimen with $\sigma_{app}=100\text{MPa}$.

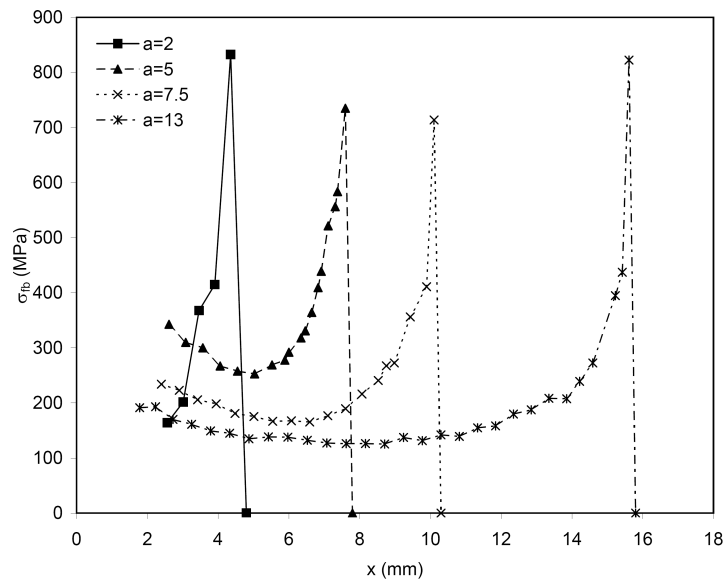


Figure C.8: Layer 2 fibre bridging stress distributions for various crack lengths. G2A-6/5-0.4 MOHTB specimen with $\sigma_{app}=100\text{MPa}$.

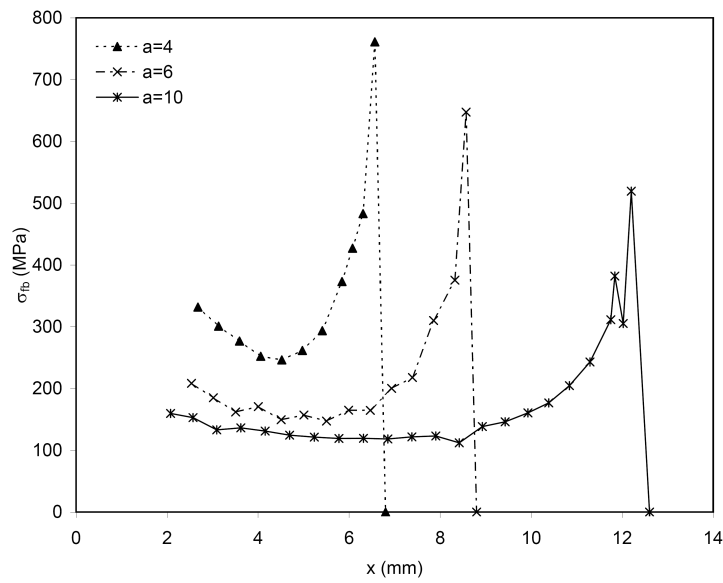


Figure C.9: Layer 3 fibre bridging stress distributions for various crack lengths. G2A-6/5-0.4 MOHTB specimen with $\sigma_{app}=100\text{MPa}$.

C.2.4. Four Point Bend G2A-11/10-0.4

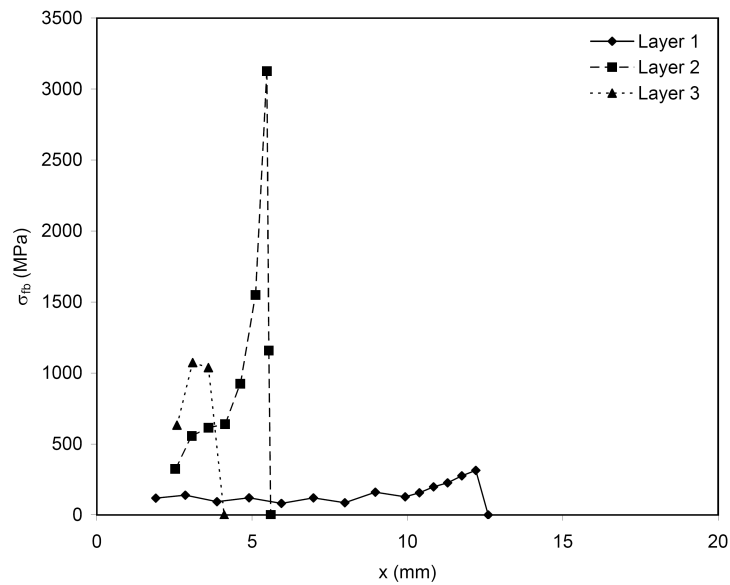


Figure C.10: Fibre bridging stress distributions for surface crack length of 10mm. G2A-11/10-0.4 4 point bend specimen with $\sigma_{max}=200\text{MPa}$.

C Finite Element Results

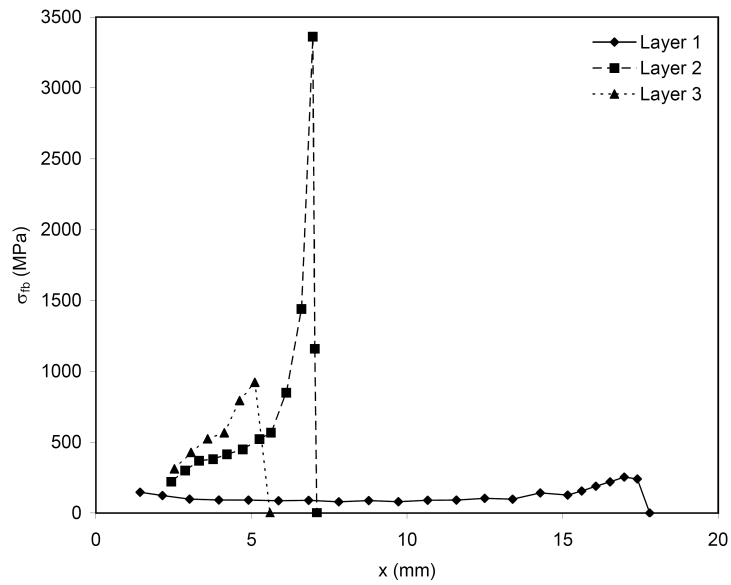


Figure C.11: Fibre bridging stress distributions for surface crack length of 15mm. G2A-11/10-0.4 4 point bend specimen with $\sigma_{max}=200\text{MPa}$.

C.3. Glare 3

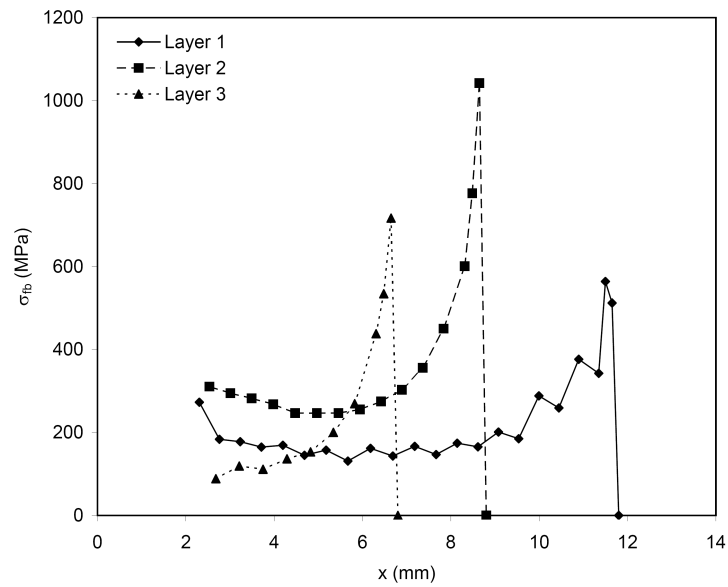


Figure C.12: Fibre bridging stress distributions for surface crack length of 9mm. G3-7/6-0.3 MOHTB specimen with $\sigma_{app}=100\text{MPa}$.

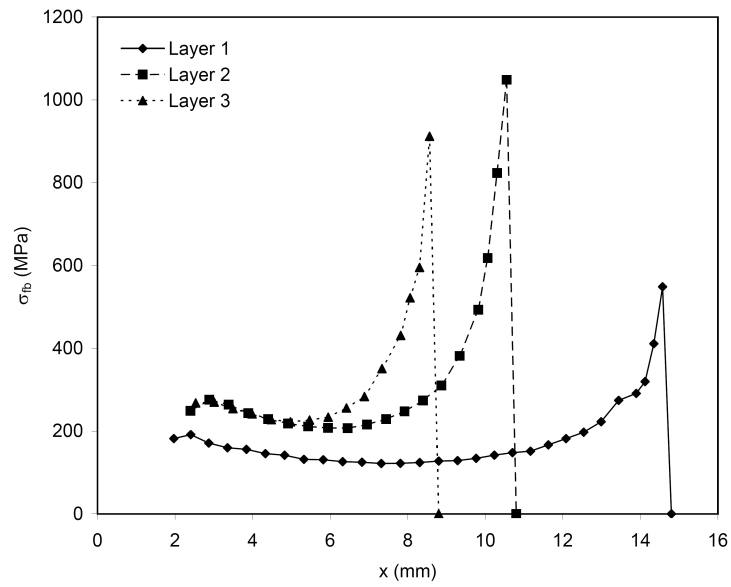


Figure C.13: Fibre bridging stress distributions for surface crack length of 12mm. G3-7/6-0.3 MOHTB specimen with $\sigma_{app}=100\text{MPa}$.

D

Experimental Results



D.1. Introduction

The experimental results of the test specifications detailed in Chapters 3 and 6 are presented here. Each specimen has fatigue data presented in a versus N format for three cracked aluminum plies, and in da/dN versus a format for the surface aluminum ply. The hybrid analytical/numerical model is included for comparison.

The data is arranged in the same order as presented in the main body of the manuscript. Starting with Glare 2A specimens, the first to be presented are the 5/4 lay-ups tested at 80 and 100MPa. Next is the 6/5 lay-up tested at 100MPa, followed by the four point bend specimens. The last portion of data is for the Glare 3-7/6-0.3 specimens tested at 100MPa.

D.2. Glare 2A

D.2.1. MOHTB G2A-5/4-0.4 @ 80MPa

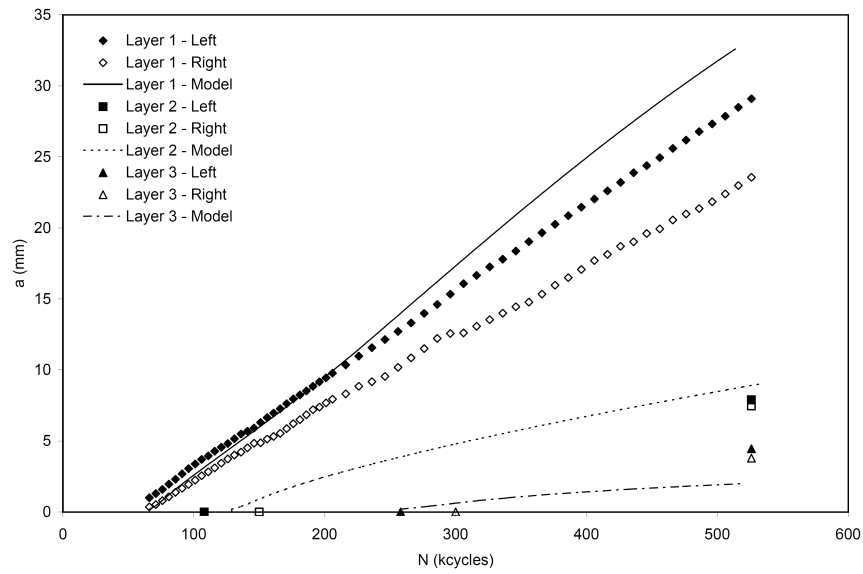


Figure D.1: MOHTB-1, a versus N , G2A-5/4-0.4, $\sigma_{app}=80\text{MPa}$.

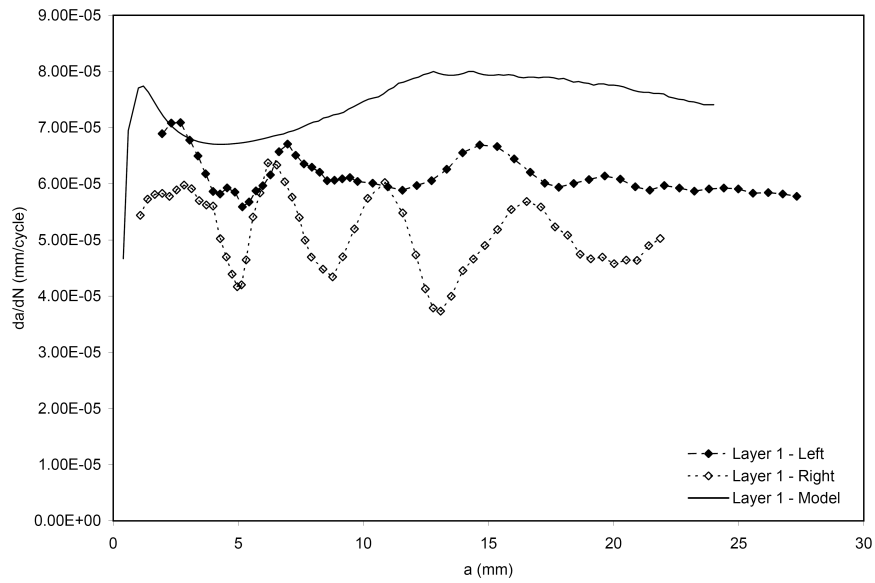


Figure D.2: MOHTB-1, da/dN versus a , G2A-5/4-0.4, $\sigma_{app}=80\text{MPa}$.

D Experimental Results

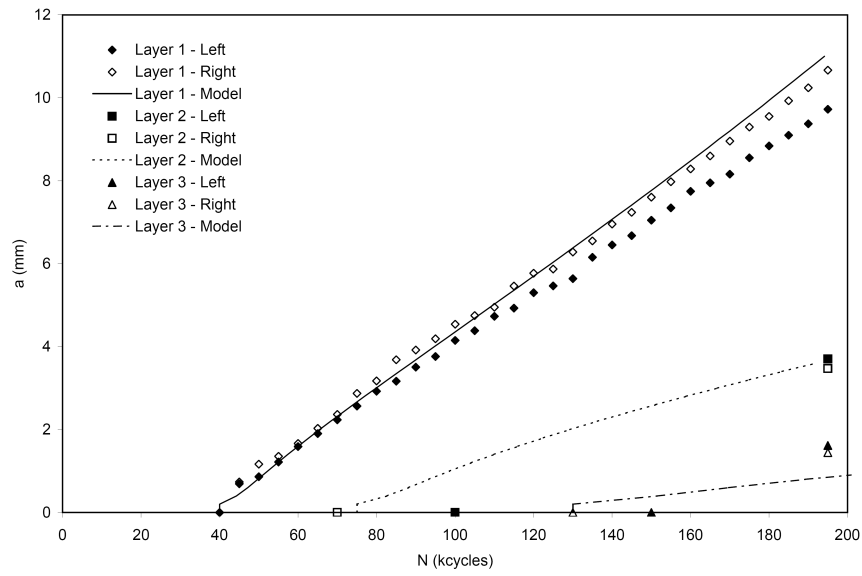


Figure D.3: MOHTB-2, a versus N , G2A-5/4-0.4, $\sigma_{app}=80\text{MPa}$.

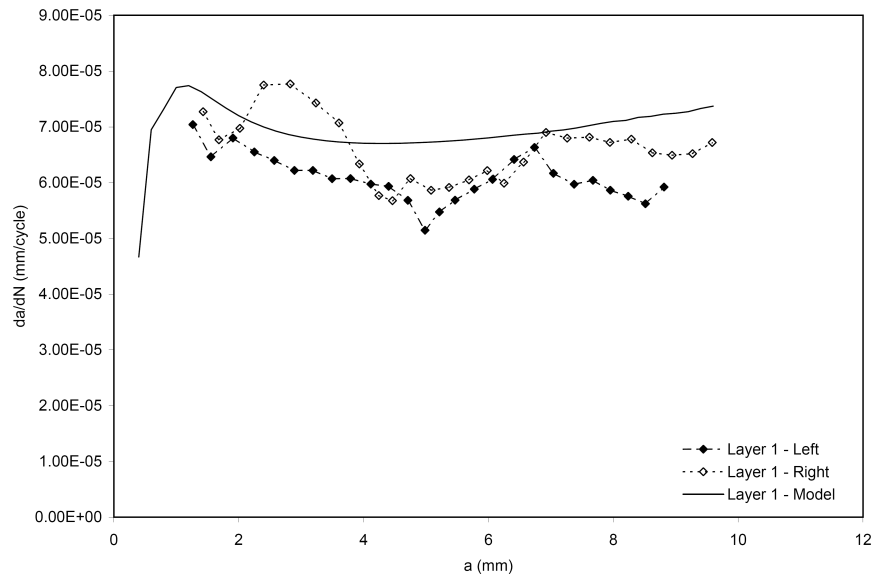


Figure D.4: MOHTB-2, da/dN versus a , G2A-5/4-0.4, $\sigma_{app}=80\text{MPa}$.

Subsurface Fatigue Crack Growth in Glare Fibre Metal Laminates

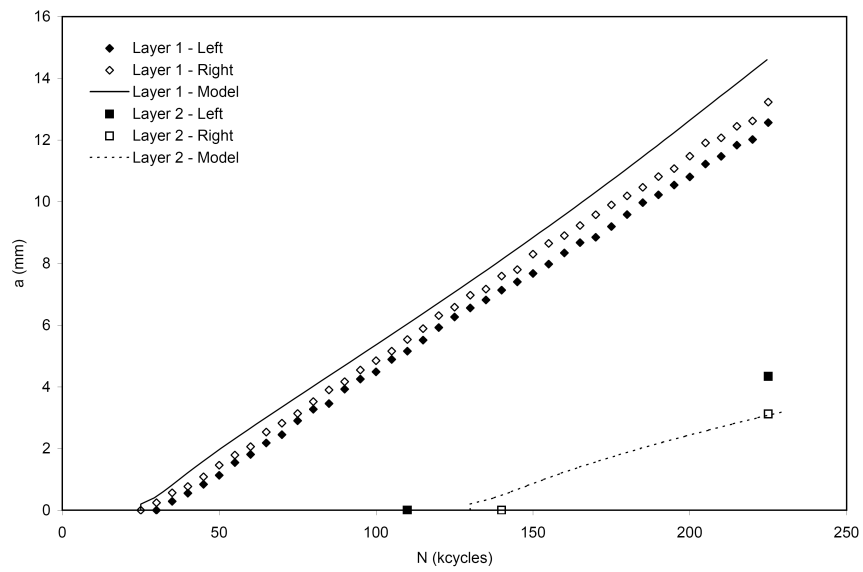


Figure D.5: MOHTB-4, a versus N , G2A-5/4-0.4, $\sigma_{app}=80\text{MPa}$.

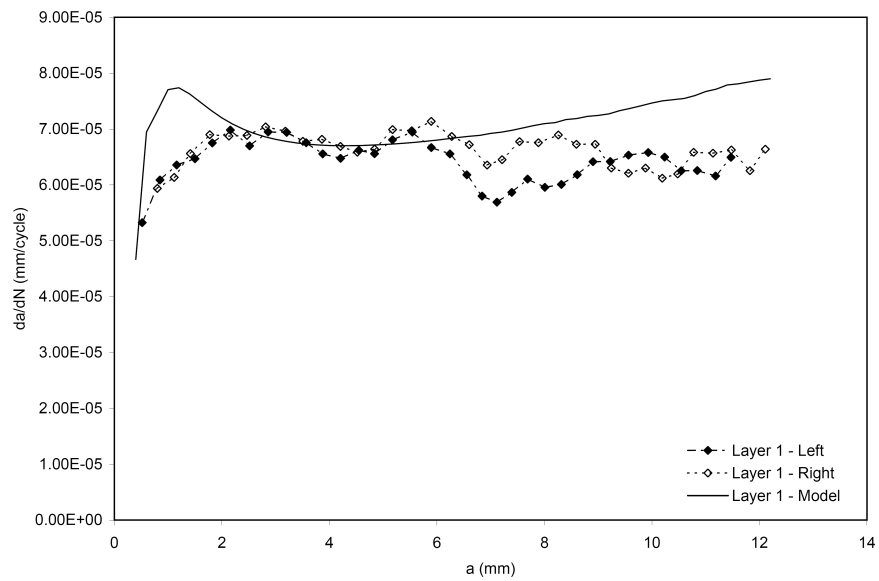


Figure D.6: MOHTB-4, da/dN versus a , G2A-5/4-0.4, $\sigma_{app}=80\text{MPa}$.

D.2.2. MOHTB G2A-5/4-0.4 @ 100MPa

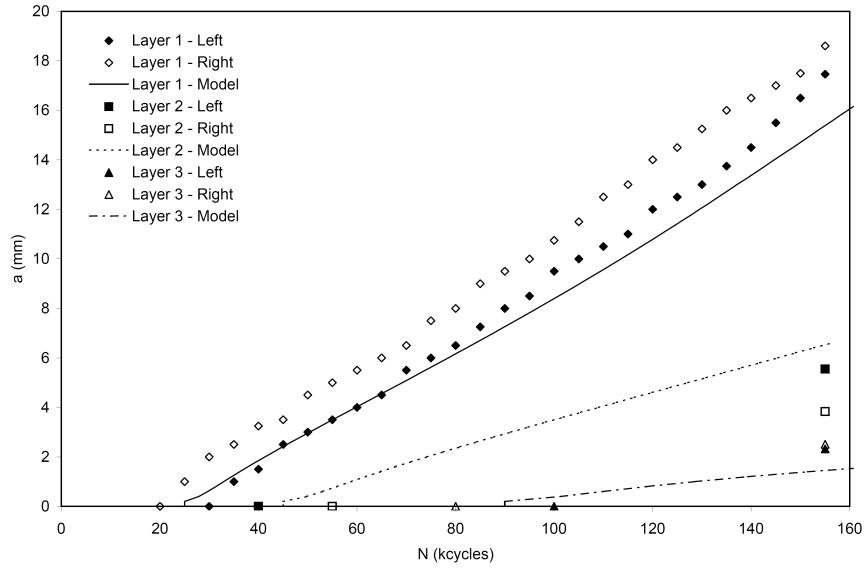


Figure D.7: MOHTB-5, a versus N , G2A-5/4-0.4, $\sigma_{app}=100\text{MPa}$.

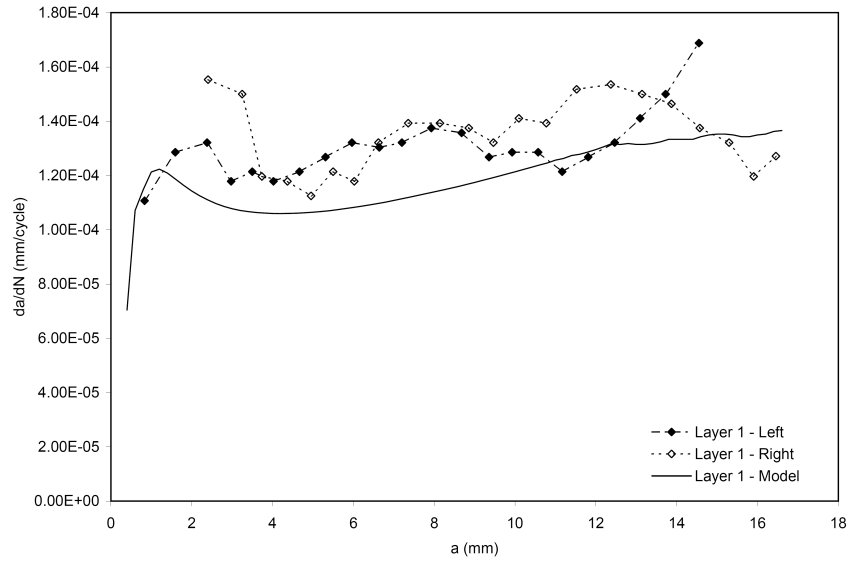


Figure D.8: MOHTB-5, da/dN versus a , G2A-5/4-0.4, $\sigma_{app}=100\text{MPa}$.

Subsurface Fatigue Crack Growth in Glare Fibre Metal Laminates

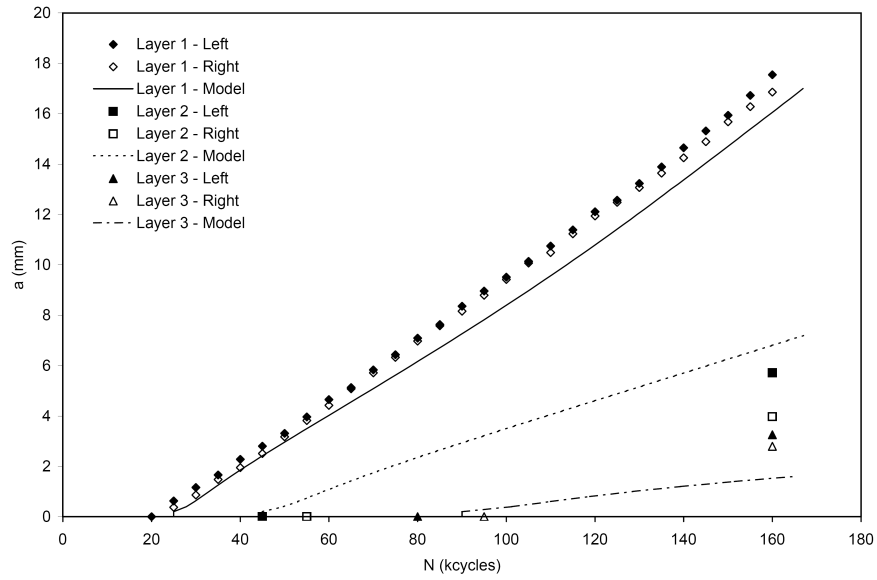


Figure D.9: MOHTB-6, a versus N , G2A-5/4-0.4, $\sigma_{app}=100\text{MPa}$.

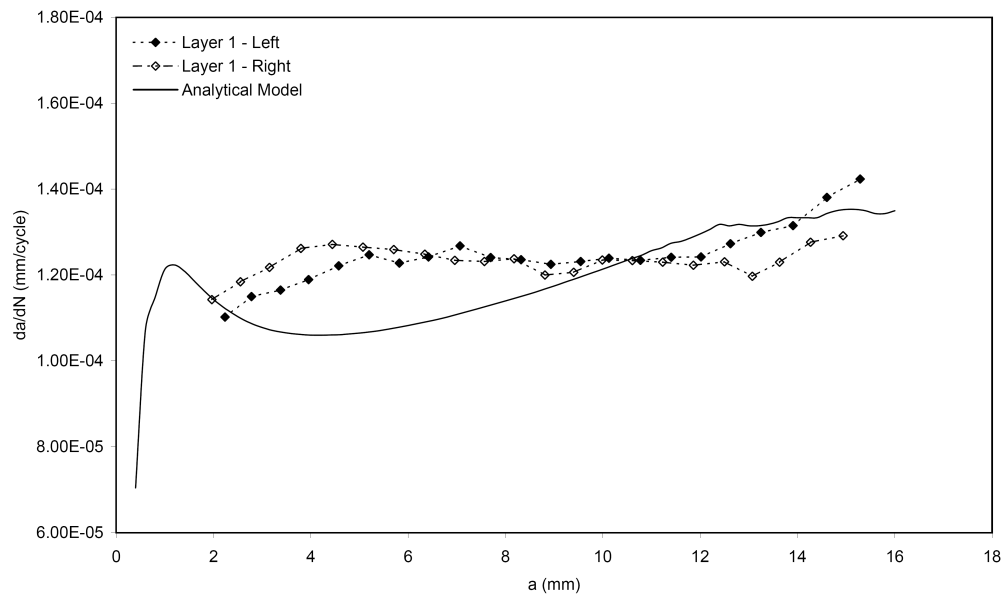


Figure D.10: MOHTB-6, da/dN versus a , G2A-5/4-0.4, $\sigma_{app}=100\text{MPa}$.

D.2.3. MOHTB G2A-6/5-0.4 @ 100MPa

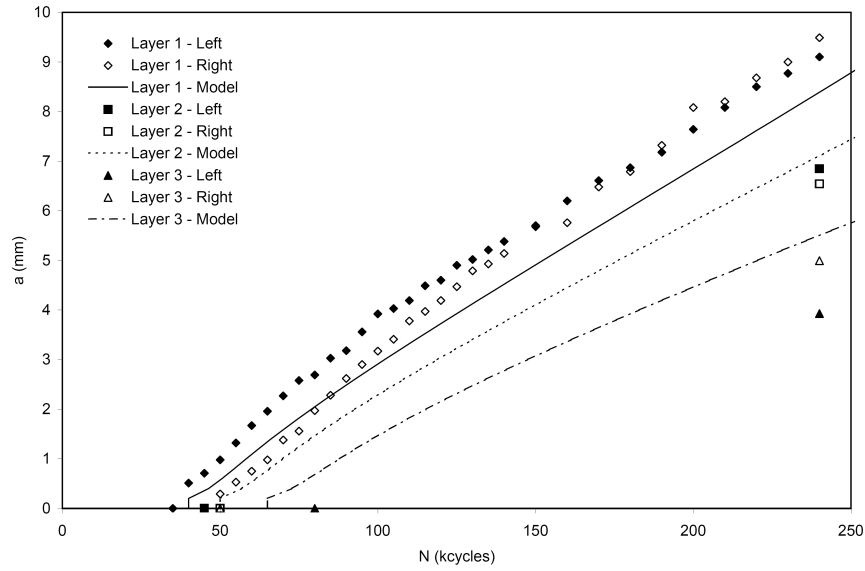


Figure D.11: MOHTB-7, a versus N , G2A-6/5-0.4, $\sigma_{app}=100\text{MPa}$.

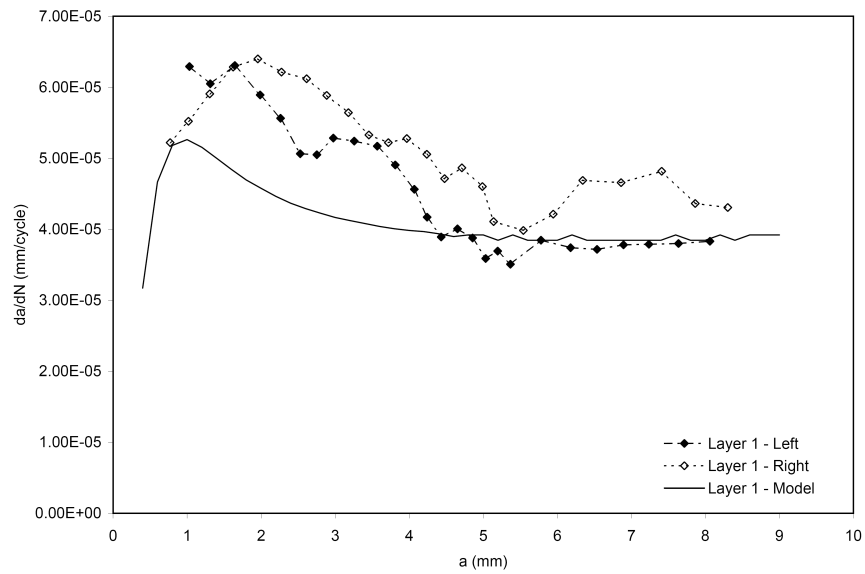


Figure D.12: MOHTB-7, da/dN versus a , G2A-6/5-0.4, $\sigma_{app}=100\text{MPa}$.

Subsurface Fatigue Crack Growth in Glare Fibre Metal Laminates

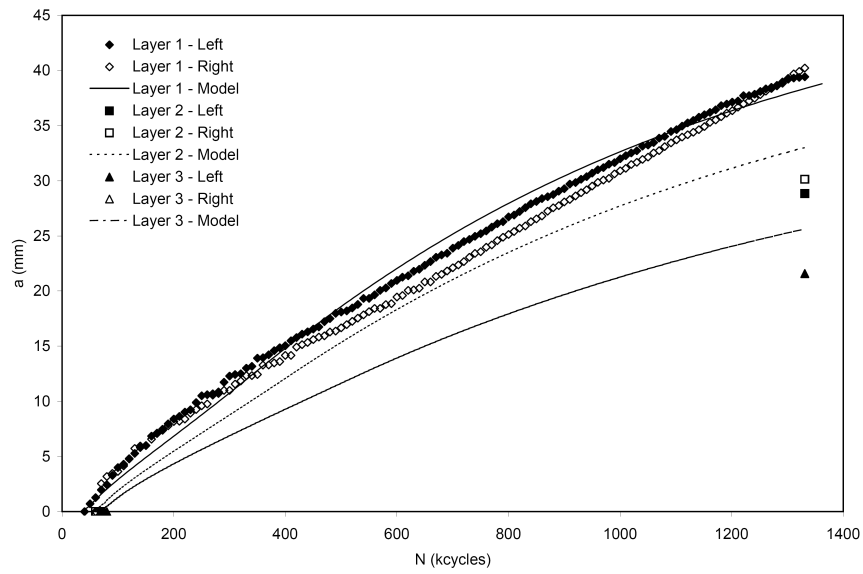


Figure D.13: MOHTB-8, a versus N , G2A-6/5-0.4, $\sigma_{app}=100\text{MPa}$.

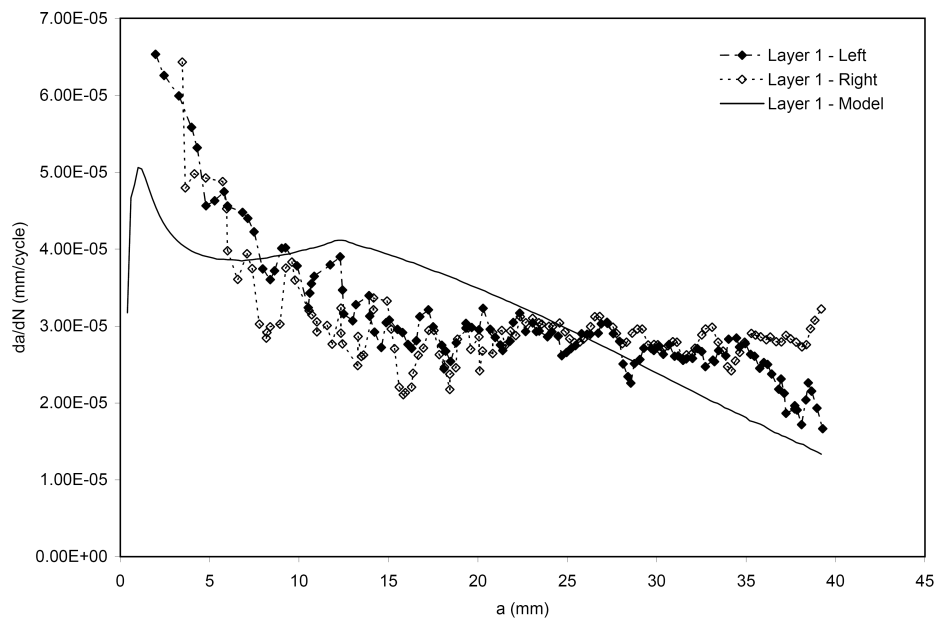


Figure D.14: MOHTB-8, da/dN versus a , G2A-6/5-0.4, $\sigma_{app}=100\text{MPa}$.

D Experimental Results

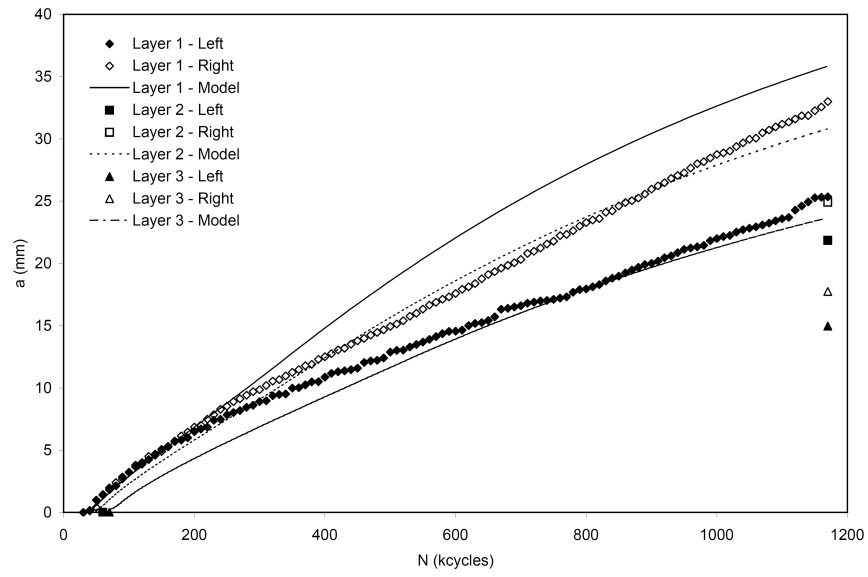


Figure D.15: MOHTB-9, a versus N , G2A-6/5-0.4, $\sigma_{app}=100\text{MPa}$.

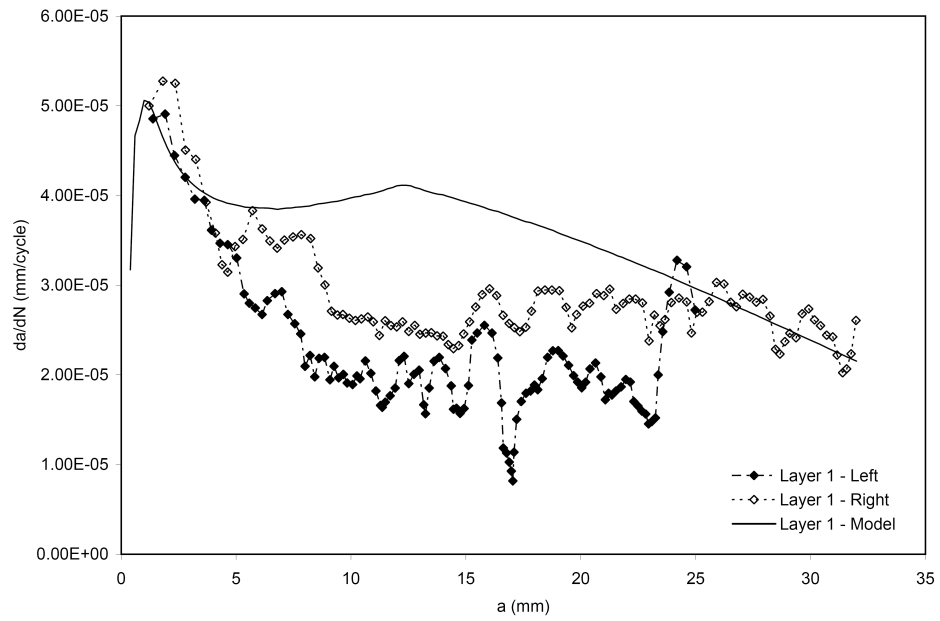


Figure D.16: MOHTB-9, da/dN versus a , G2A-6/5-0.4, $\sigma_{app}=100\text{MPa}$.

D.2.4. Four Point Bend G2A-11/10-0.4

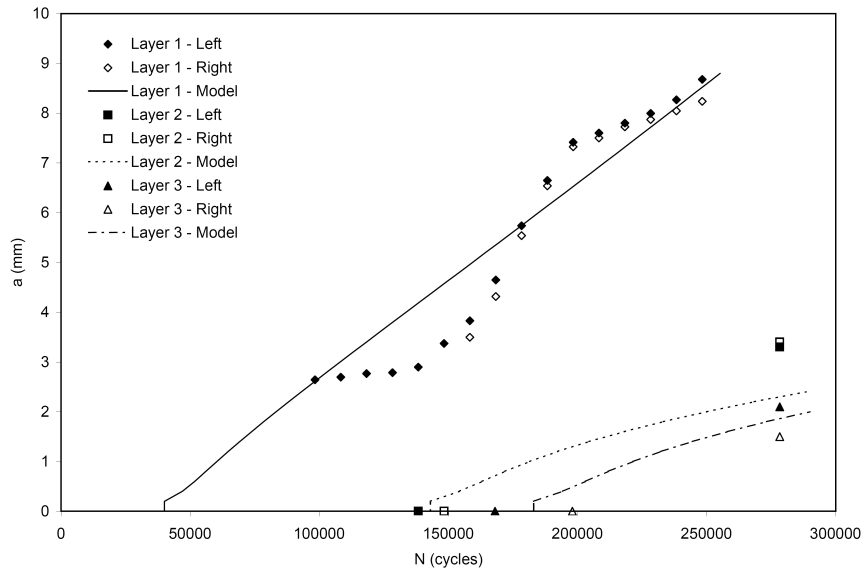


Figure D.17: 4PtBnd-01, a versus N , G2A-11/10-0.4, $\sigma_{max}=200\text{MPa}$.

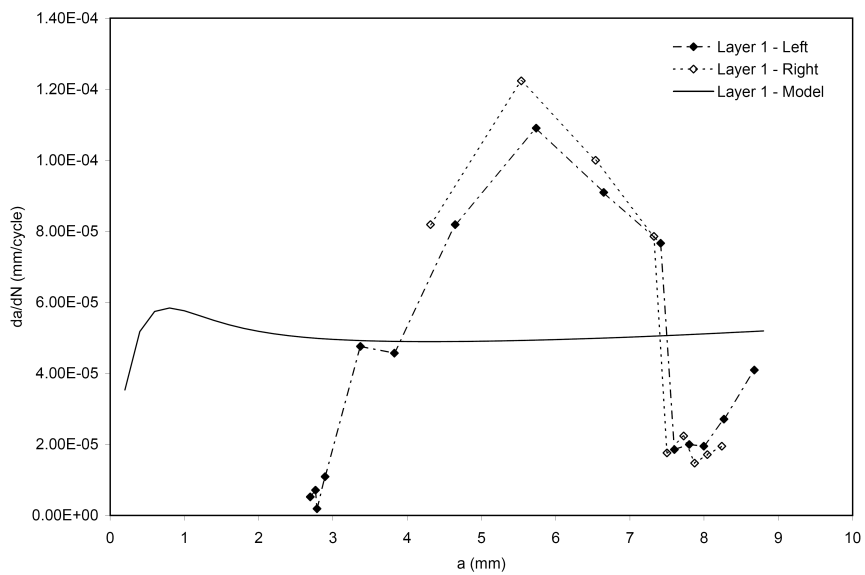


Figure D.18: 4PtBnd-01, da/dN versus a , G2A-11/10-0.4, $\sigma_{max}=200\text{MPa}$.

D Experimental Results

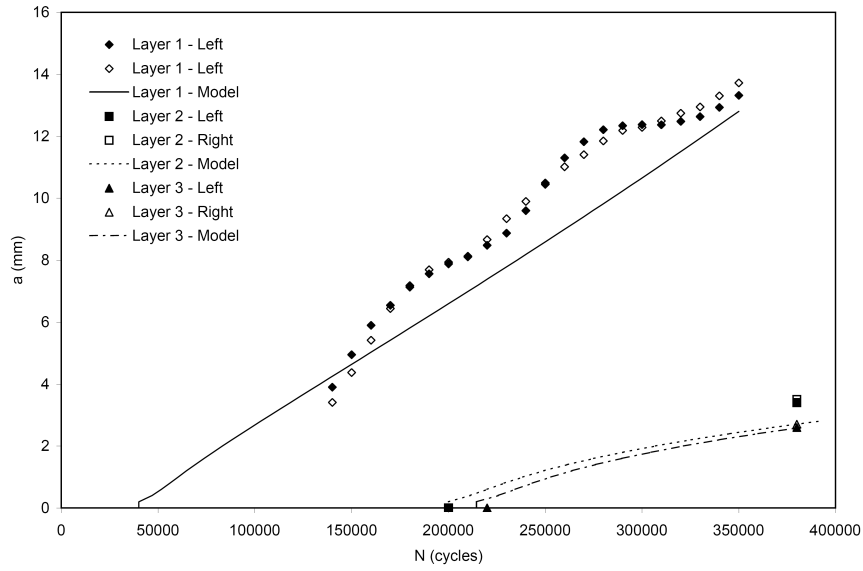


Figure D.19: 4PtBnd-02, a versus N , G2A-11/10-0.4, $\sigma_{max}=200\text{MPa}$.

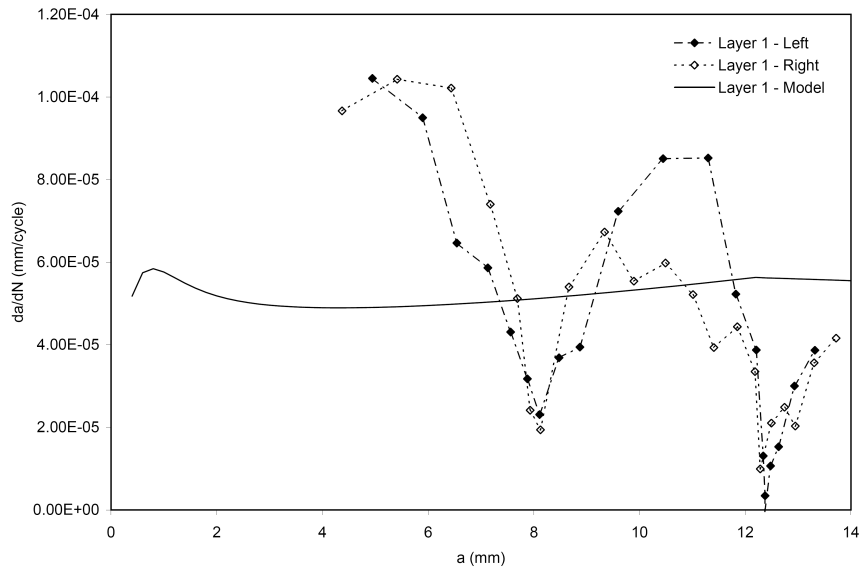


Figure D.20: 4PtBnd-02, da/dN versus a , G2A-11/10-0.4, $\sigma_{max}=200\text{MPa}$.

Subsurface Fatigue Crack Growth in Glare Fibre Metal Laminates

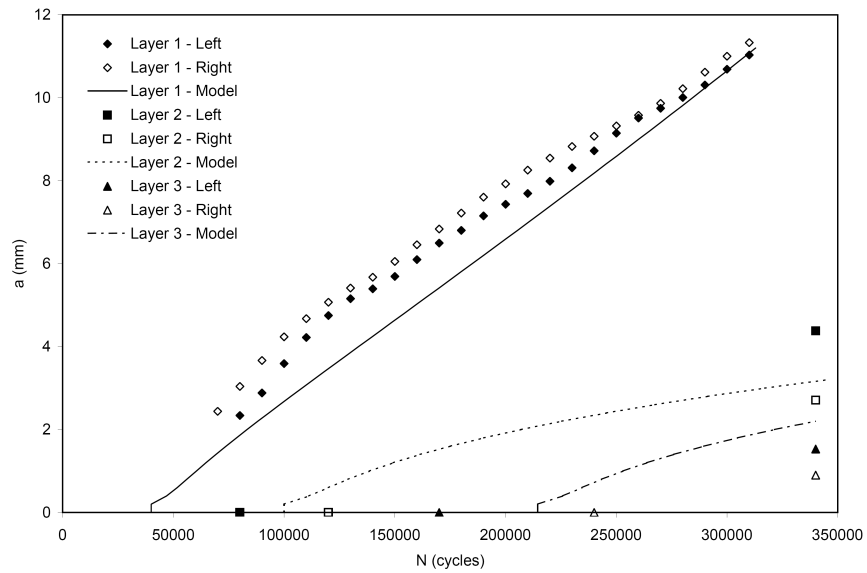


Figure D.21: 4PtBnd-03, a versus N , G2A-11/10-0.4, $\sigma_{max}=200\text{MPa}$.

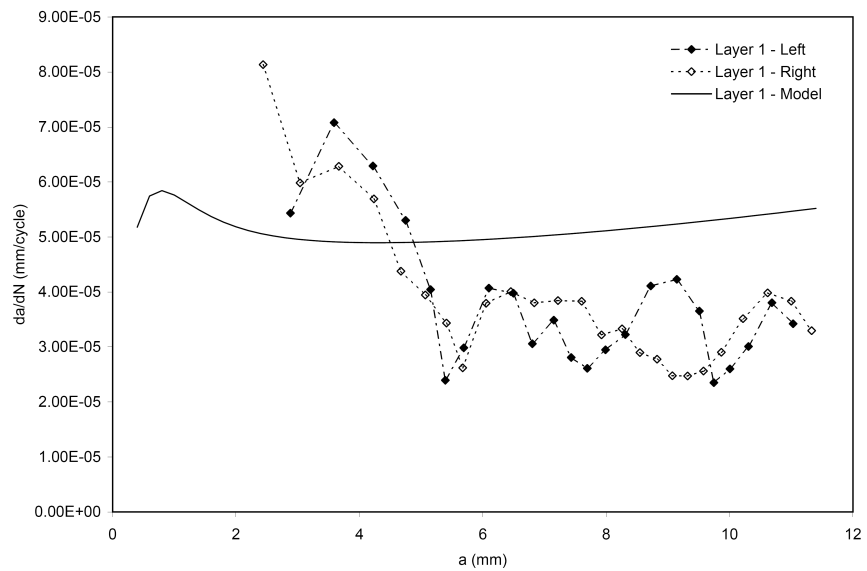


Figure D.22: 4PtBnd-03, da/dN versus a , G2A-11/10-0.4, $\sigma_{max}=200\text{MPa}$.

D Experimental Results

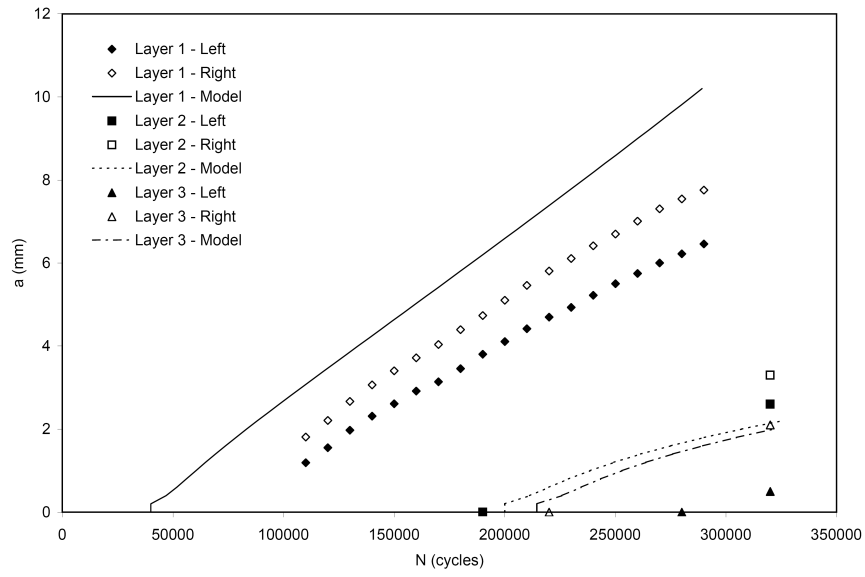


Figure D.23: 4PtBnd-04, a versus N , G2A-11/10-0.4, $\sigma_{max}=200\text{MPa}$.

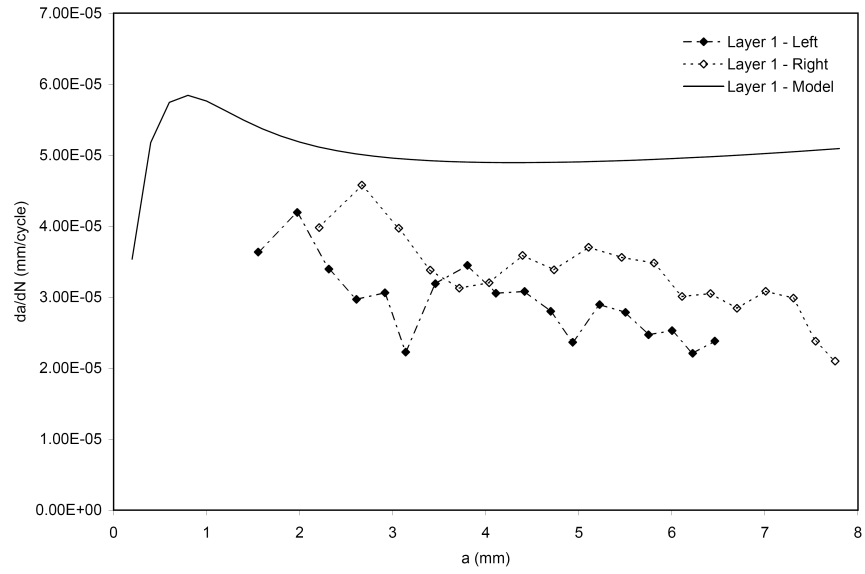


Figure D.24: 4PtBnd-04, da/dN versus a , G2A-11/10-0.4, $\sigma_{max}=200\text{MPa}$.

D.3. Glare 3 MOHTB G3-7/6-0.3 @ 100MPa

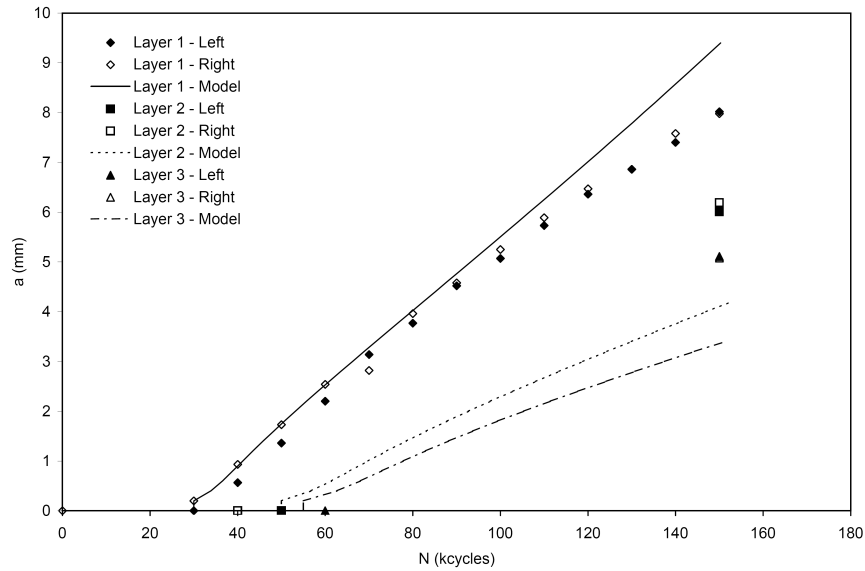


Figure D.25: MOHTB-10, a versus N , G3-7/6-0.3, $\sigma_{app}=100\text{MPa}$.

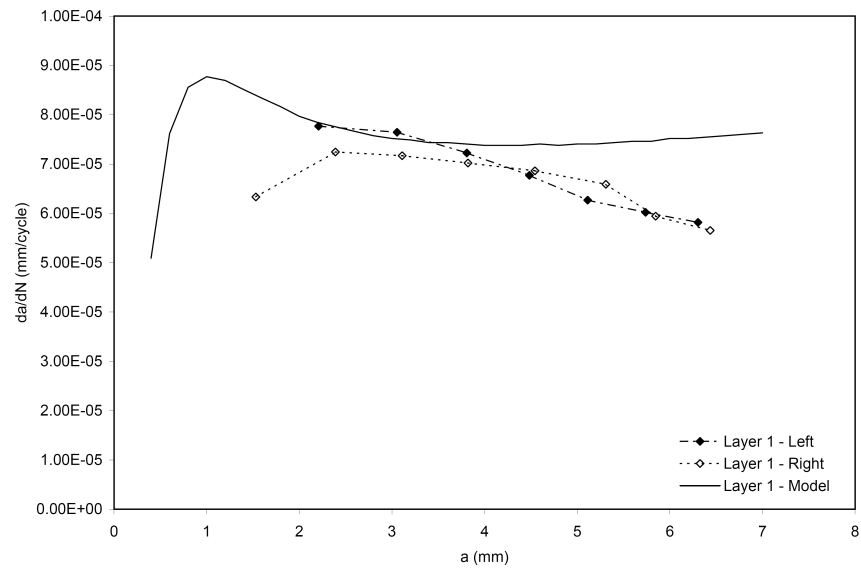


Figure D.26: MOHTB-10, da/dN versus a , G3-7/6-0.3, $\sigma_{app}=100\text{MPa}$.

D Experimental Results

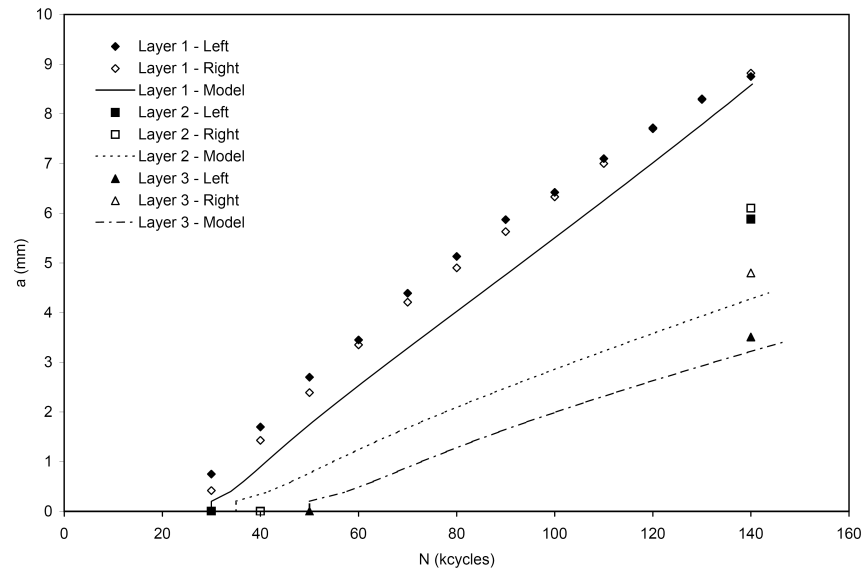


Figure D.27: MOHTB-11, a versus N , G3-7/6-0.3, $\sigma_{app}=100\text{MPa}$.

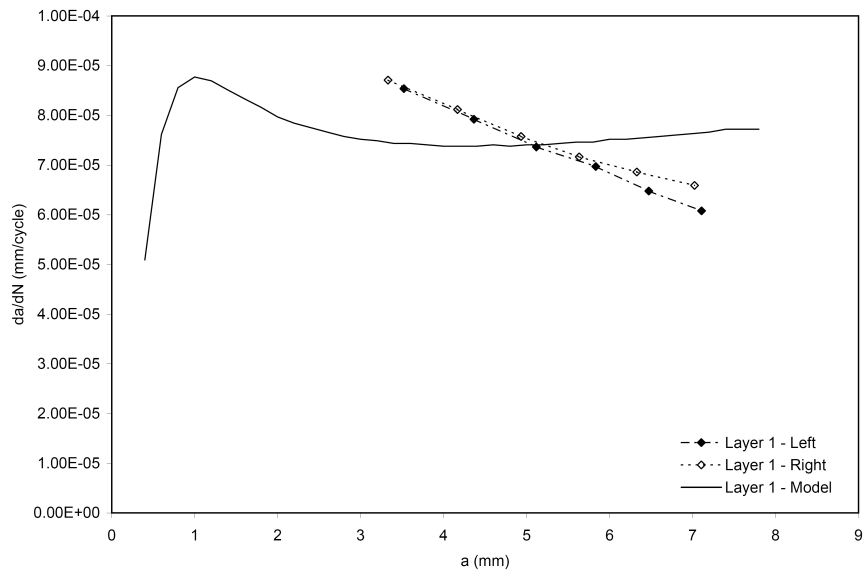


Figure D.28: MOHTB-11, da/dN versus a , G3-7/6-0.3, $\sigma_{app}=100\text{MPa}$.

Subsurface Fatigue Crack Growth in Glare Fibre Metal Laminates

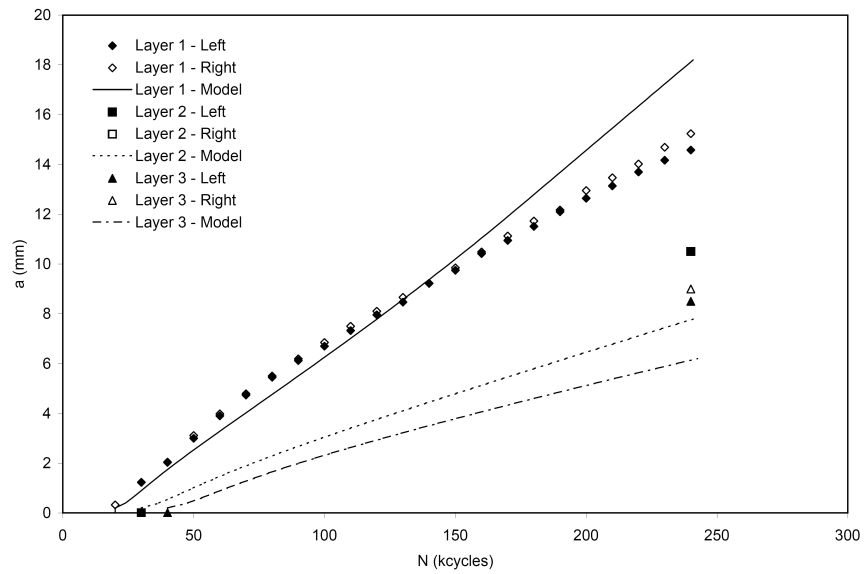


Figure D.29: MOHTB-12, a versus N , G3-7/6-0.3, $\sigma_{app}=100\text{MPa}$.

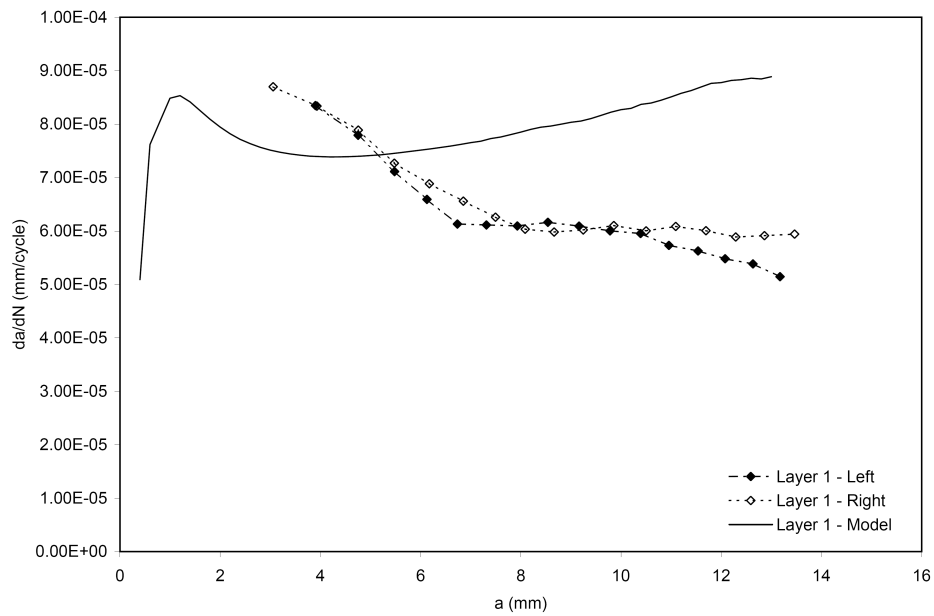


Figure D.30: MOHTB-12, da/dN versus a , G3-7/6-0.3, $\sigma_{app}=100\text{MPa}$.

D Experimental Results

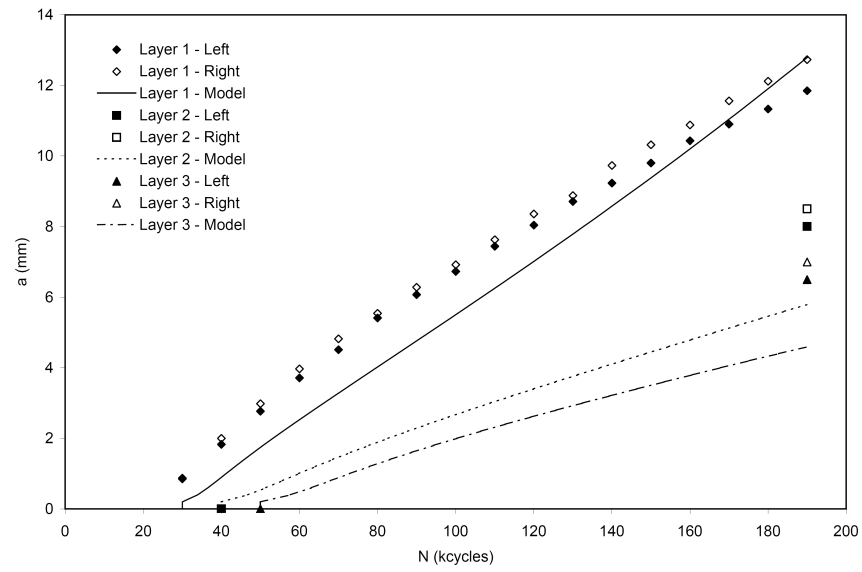


Figure D.31: MOHTB-13, a versus N , G3-7/6-0.3, $\sigma_{app}=100\text{MPa}$.

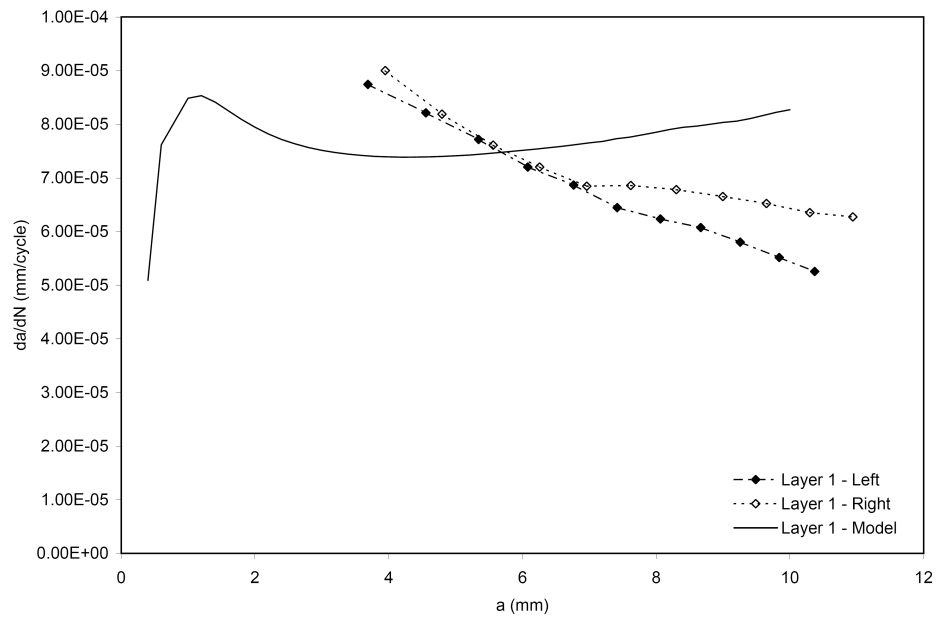


Figure D.32: MOHTB-13, da/dN versus a , G3-7/6-0.3, $\sigma_{app}=100\text{MPa}$.

Subsurface Fatigue Crack Growth in Glare Fibre Metal Laminates

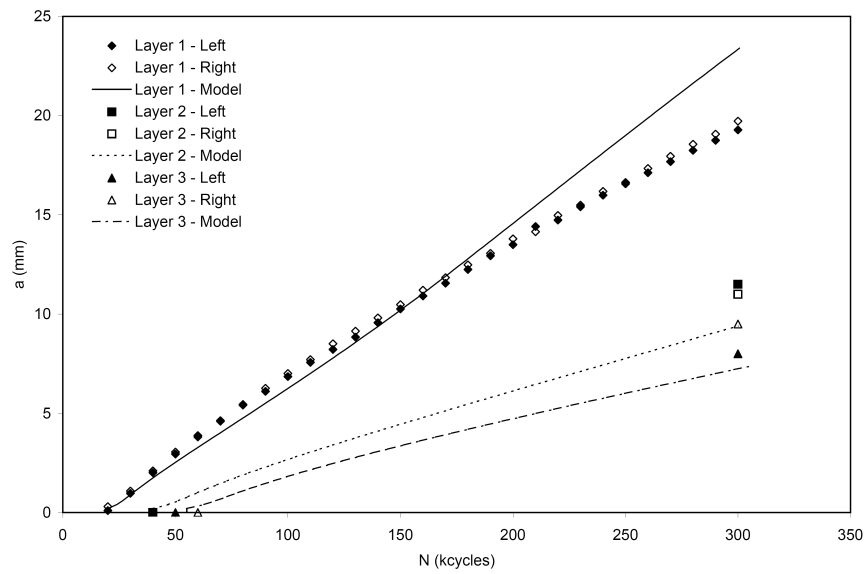


Figure D.33: MOHTB-14, a versus N , G3-7/6-0.3, $\sigma_{app}=100\text{MPa}$.

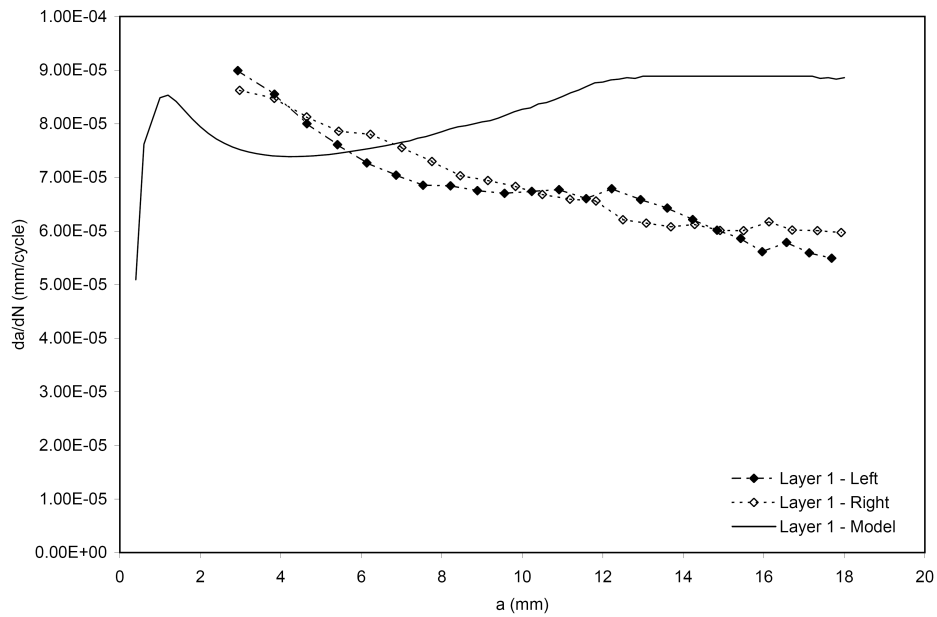


Figure D.34: MOHTB-14, da/dN versus a , G3-7/6-0.3, $\sigma_{app}=100\text{MPa}$.

D Experimental Results

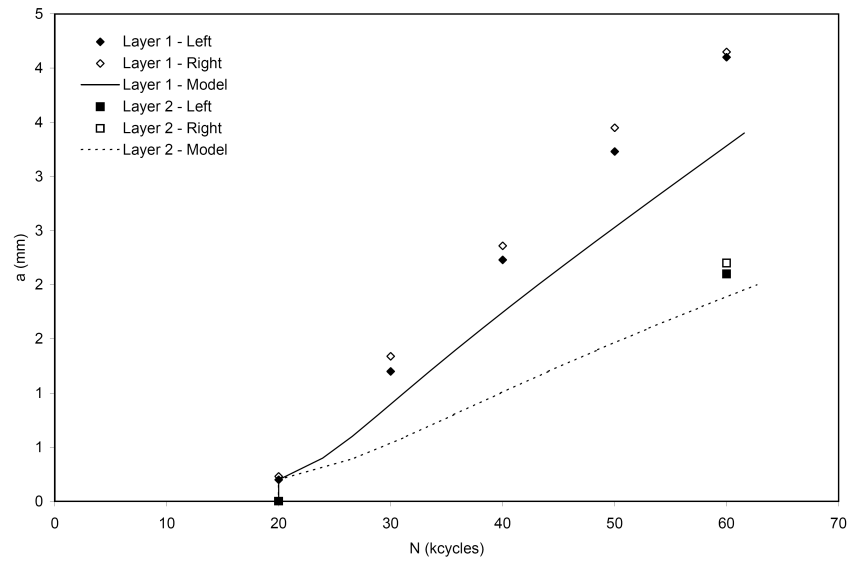


Figure D.35: MOHTB-15, a versus N , G3-7/6-0.3, $\sigma_{app}=100\text{MPa}$.

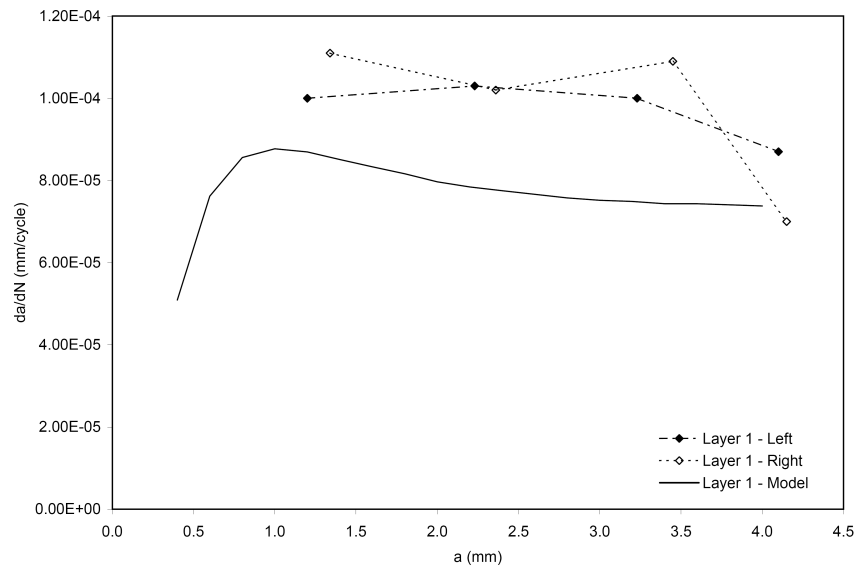


Figure D.36: MOHTB-15, da/dN versus a , G3-7/6-0.3, $\sigma_{app}=100\text{MPa}$.

Subsurface Fatigue Crack Growth in Glare Fibre Metal Laminates

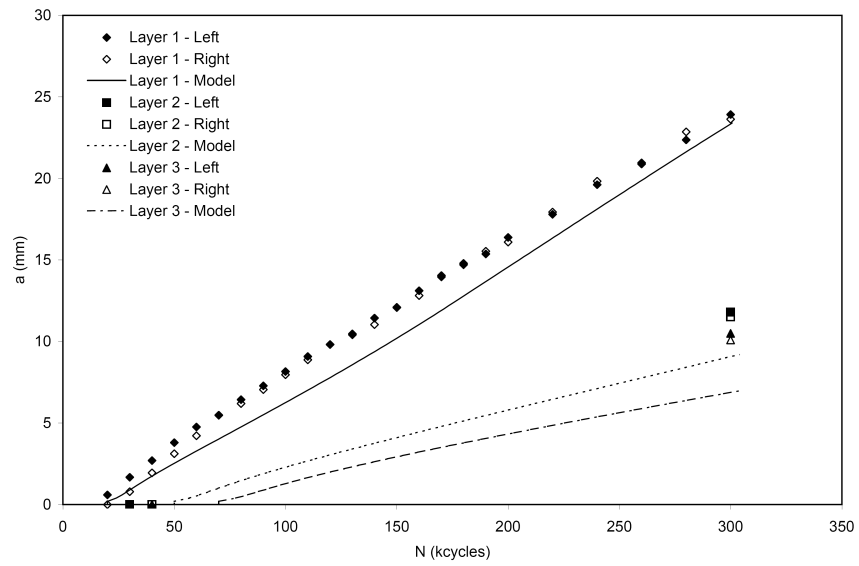


Figure D.37: MOHTB-16, a versus N , G3-7/6-0.3, $\sigma_{app}=100\text{MPa}$.

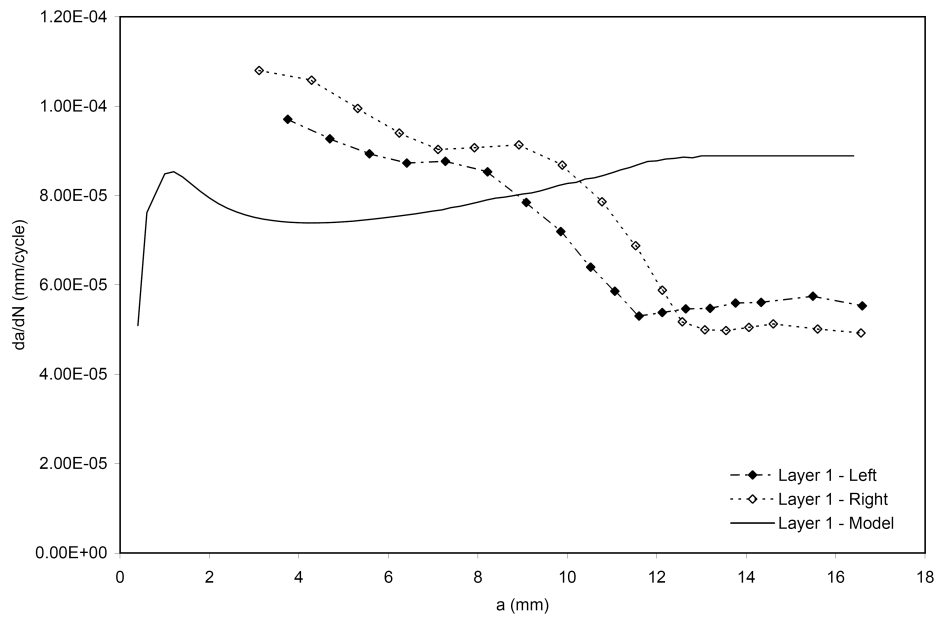


Figure D.38: MOHTB-16, da/dN versus a , G3-7/6-0.3, $\sigma_{app}=100\text{MPa}$.

D Experimental Results

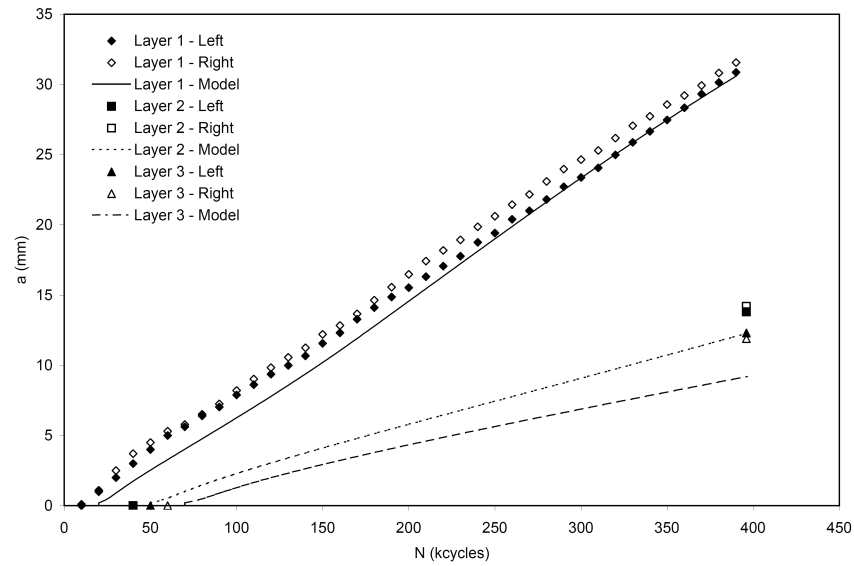


Figure D.39: MOHTB-17, a versus N , G3-7/6-0.3, $\sigma_{app}=100\text{MPa}$.

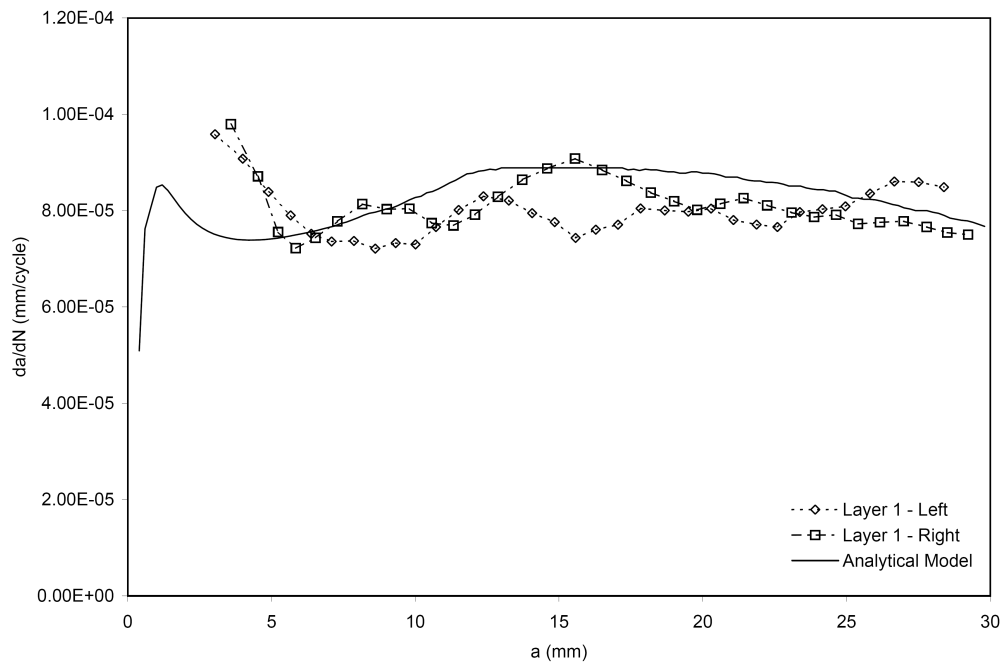


Figure D.40: MOHTB-17, da/dN versus a , G3-7/6-0.3, $\sigma_{app}=100\text{MPa}$.

Curriculum Vitae

The author was born on 11 January 1968 in Fremont, Nebraska. After graduating from high school in 1986, he started his studies at Nebraska Wesleyan University in Lincoln, Nebraska. He graduated with a Bachelor of Science degree in Physics in May 1990. He then attended Washington University in St Louis, Missouri. He graduated with both Bachelor and Master of Science degrees in Mechanical Engineering and was commissioned a Regular Officer in the United States Air Force in May 1993.

As a Second Lieutenant, he was assigned to the Wright Patterson Air Force Base in Dayton, Ohio. There he served as a schedule manager for the EF-111A System Improvement Program, where he conducted schedule and cost risk assessments of contractor and government agency activities. He was then transferred to the Aeropropulsion Directorate of the Wright Laboratories where he was program manager for the High Cycle Fatigue Science and Technology Program, an Air Force and Department of Defence initiative on high cycle fatigue in turbine engines.

Upon promotion to Captain, he was assigned to the 509th Bomb Wing at Whiteman Air Force Base in Knob Noster, Missouri. There he served as Lead Mechanical Systems Engineer for the B-2A Spirit bomber. His responsibilities included evaluation of systems durability and development of corrective actions for mechanical systems. He was then elevated to Commander for the B-2 Research Engineering Flight, where he supervised four engineers and four technicians in an engineering consulting flight to the Logistics Group commander. He directed and managed a wide range of activities in support of B-2 operations, including reliability and maintenance analyses, radar cross-sectional analysis, and repair development.

He was then assigned to the United States Air Force Academy in Colorado Springs, Colorado. He served as an Instructor and later an Assistant Professor in the Department of Engineering Mechanics. He had several additional duties with the cadets including Officer-in Charge of a 30-member cadet chapter of the American Society of Mechanical Engineers and as Associate Air Officer Commanding for Academics for a 120-cadet squadron.

In 2002, he moved to Delft, The Netherlands to begin his doctoral studies in the chair of Aerospace Materials under the sponsorship of the Air Force Institute of Technology and supervision of prof.dr.ir. S. van der Zwaag and prof.dr.ir. J. Schijve. His thesis work is on the topic of “Subsurface Fatigue Crack Growth in Glare Fibre Metal Laminates”.

The author is married to the former Michele Lyn Kauffold of Dodge, Nebraska and they have three children, Jessica Lyn, Spencer Christian, and Emelie Kathleen.

Acknowledgements

The spirit of collaboration within the chair of Aerospace Materials is phenomenal. The positive attitude that runs through the organization is evident as any idea proposed is met with serious consideration and serious discussion. It is an environment that is conducive to research, and a quality to be preserved.

I wish to express my deepest thanks to my co-promoters, Prof.dr.ir. S. van der Zwaag and prof.dr.ir. J. Schijve, without whom this would not have been possible. Prof van der Zwaag's remarkable ability to focus on the core issues of a topic kept my research from running adrift. His experience and curiosity ensured that even challenges in the project were viewed with an attitude of what could be learned and how those issues built upon the whole topic of my research. Prof Schijve's interest, knowledge and wisdom were invaluable in guiding my research. I consider myself fortunate indeed to have had the opportunity to learn from him.

I am very grateful to all the colleagues within the chair of Aerospace Materials. Your contributions, whether technical or motivational, were invaluable. In particular I would like to thank Johannes Homan, who acted as an additional co-promoter for my research in all but name. His knowledge of fatigue and Glare has been instrumental to the success of this work.

Special thanks to my officemate, Reinout van Rooijen. In the world of give and take, I certainly was the beneficiary. I cannot thank you enough for all the help, the ideas, and particularly, the camaraderie. To my fellow promovendi, Reinier de Rijck, Pieter van Nieuwkoop, Arjan Woerden, Mario Vesco, René Alderliesten, Tjarko de Jong, Jens de Kanter, and all the rest, it has been a privilege to work with each of you. The friendships I have found here will always be treasured.

The technical staff within the Hall is fantastic. I wish to thank especially Hans Weerheim for his expertise in instrumentation and Serge van Meer for his assistance with non-destructive inspection. Without them, I would have had no idea what I was measuring. I also need to thank Kees Paalvast and Jeroen Los for their extreme patience in teaching me the intricacies of the fatigue test machines. Their advice kept my experiments on track and me out of the hospital. To the machine shop and particularly Bertus van der Stok and Herman Werges, I am indebted to them for their craftsmanship in fashioning the fatigue specimens that were central to this research. The quality and timeliness of their work were unequalled. Thanks also to Bertil Grashof and Niels Jalving for all their assistance in the laboratory.

I wish to thank the United States Air Force Academy, and particularly Colonel Cary Fisher, head of the Department of Engineering Mechanics for sponsoring my PhD studies at the Technical University of Delft. I am also grateful to Air Force Institute of Technology for managing my academic program from the military side.

Saving the last words to the most important people in my life, I thank my loving wife, Michele, and my children Jessica, Spencer and Emelie. Your patience and support throughout this adventure has made it worthwhile.

